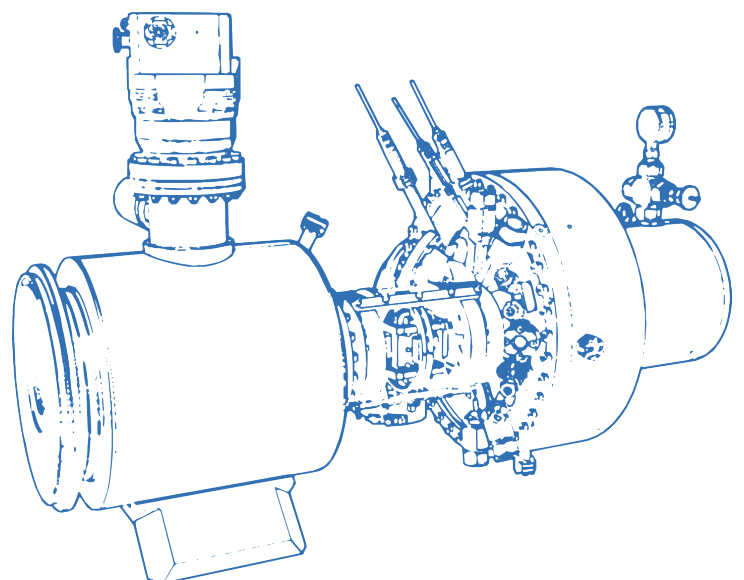


# Development and commissioning of a novel compact X-ray source for preclinical microbeam radiotherapy

Christian Petrich





# Development and commissioning of a novel compact X-ray source for preclinical microbeam radiotherapy

**Christian Petrich**

Vollständiger Abdruck der von der TUM School of Natural Sciences der Technischen Universität München zur Erlangung des akademischen Grades eines

**Doktors der Naturwissenschaften (Dr. rer. nat.)**

genehmigten Dissertation.

**Vorsitz:**

Prof. Dr. Martin Zacharias

**Prüfende der Dissertation:**

1. Prof. Dr. Jan J. Wilkens
2. Prof. Dr. Franz Pfeiffer

Die Dissertation wurde am 16.12.2024 bei der Technischen Universität München eingereicht und durch die TUM School of Natural Sciences am 08.04.2025 angenommen.



*Meinen Eltern gewidmet*



# Danksagungen

Diese Arbeit wäre ohne die Menschen, die mich fachlich und persönlich unterstützt haben und von denen ich in den vergangenen Jahren viel lernen durfte, nicht möglich gewesen. An dieser Stelle möchte ich daher meinen tief empfundenen Dank all jenen aussprechen, die meinen Weg geprägt und begleitet haben. Ihr habt diese Zeit nicht nur lehrreich, sondern auch bereichernd und unterhaltsam gemacht.

Zunächst gilt mein besonderer Dank Stefan Bartzsch, dem Leiter der Arbeitsgruppe für experimentelle medizinische Physik am Helmholtz Zentrum München und dem geistigen Vater des Konzepts der Linienfokus Röntgenröhre (LFXT). Danke, dass du mir die Möglichkeit geboten hast an diesem unglaublich interessanten und thematisch breit gefächerten Projekt mitzuwirken, für das hohe Maß an Vertrauen, dass du in mich gesetzt und die Freiheiten, die du mir gewährt hast, und dafür, dass du für jedes Problem ein offenes Ohr und meist auch eine Lösung oder zumindest einen neuen Denkanstoß hattest.

Besonderer Dank gilt auch meinem Doktorvater Jan Wilkens, dem Leiter der Medizinphysik an der Strahlentherapie des Klinikums rechts der Isar. Ich danke dir für die hervorragende fachliche Betreuung, für die Möglichkeit mich während der Doktorarbeit weiterzubilden und besonders dafür, dass du mir gegen die Universitätspolitik beigestanden bist und dich für mich eingesetzt hast.

Des Weiteren möchte ich meine Dankbarkeit dem gesamten  $\mu$ Flash Team aussprechen, allen voran Johanna Winter, Anton Dimroth und Christoph Matejcek, die in ihren Arbeiten die Entwicklung des LFXT Prototypen begonnen und tatkräftig bei der Vollendung mitgewirkt haben. Die Zusammenarbeit mit euch hat Spaß gemacht und gemeinsam haben wir viel erreicht. Auch möchte ich Monika Dehn, Kurt Aulenbacher und Thomas Beiser von der Johannes Gutenberg Universität Mainz, Marek Galek von der Hochschule München, Michael Butzek und den Kollegen vom Forschungszentrum Jülich, sowie Yunzhe Zhang, Markus Zimmermann, Karl-Ludwig Krämer, Mahadevan Ravichandran und Sebastian Rötzer von der Technischen Universität München danken.

Ich möchte mich herzlich bei Tobias Bausenwein von der Infrastrukturgruppe des Forschungsreaktors München (FRM) bedanken. Obwohl deine Aufgabe eigentlich nur die Organisation der Laborertüchtigung war, hast du mich stets tatkräftig besonders bei Problemen rund um die Elektronik in unserem Labor unterstützt. Ohne dich weiß ich nicht wie ich mich durch die Bürokratie am FRM, die man vor allem am Anfang mit dem Haus das Verrückte macht verwechseln könnte, durchkämpfen hätte sollen. Auch möchte ich Dominik Bausenwein, dem "Klassensprecher" des Techpools am FRM danken. Ich habe unwahrscheinlich viel von euch beiden gelernt und bin euch für jeden Vortrag dankbar. Mein Dank erstreckt sich weiter auf alle Kollegen vom FRM für die immerwährende Hilfsbereitschaft.

Ich bedanke mich bei allen aus den Arbeitsgruppen experimentelle medizinische Physik und Strahlenbiologie für die lehrreichen fachlichen Diskussionen und die angenehme Arbeitsatmosphäre. Bei Susanne Raulefs möchte ich mich besonders für die Unterstützung bei administrativen Aufgaben bedanken. Besonderer Dank gilt auch Rainer Lindner, für seine tatkräftige Unterstützung bei jedwedem technischen Problem.

Abschließend möchte ich mich bei meinen Eltern Renate Petrich und Martin Petrich, meiner Schwester Andrea Petrich, sowie meiner Partnerin Angela Scherle für die immerwährende Unterstützung bedanken und dafür, dass ihr meinen Redeschwall über die Arbeit mal mehr, mal weniger interessiert über euch ergehen habt lassen.



# Abstract

The central challenge in modern radiotherapy lies in widening the therapeutic window by increasing tumour control probability and mitigating normal tissue toxicity. Microbeam radiotherapy (MRT) is a promising novel approach breaking with one of the main paradigms of conventional radiotherapy by irradiating with micrometre-wide planar beamlets of exceptionally high doses instead of a homogeneous irradiation field. Numerous preclinical studies have proven that MRT yields superior normal tissue tolerance while maintaining tumour control. For the generation of a clinically viable MRT irradiation field, X-ray beam qualities commonly only available at third-generation synchrotron light sources are required, which are not clinically compatible due to their size and financial demands.

The line-focus X-ray tube (LFXT) concept promises to provide the required beam qualities for MRT from a compact machine, enabling first clinical trials and potentially a translation of MRT into clinical routine. In this work, the design of the first prototype of a LFXT, which was started in prior works, is concluded, and the commissioning process of it culminating in the first beam is presented. After a short introduction to the topic and an overview of the theoretical background in part I, the design of the LFXT prototype is illustrated in part II of this work from a systems engineering perspective. The systems developed within the scope of this work are organised according to their functions and presented separately. The main requirements imposed upon the systems are identified as providing a method for temperature monitoring of the target, dissipating excess heat, supplying and containing the required acceleration voltage and auxiliary power, ensuring personal safety, and controlling and monitoring the LFXT prototype. While the developed systems are still in the prototype stage, the overall LFXT prototype is operational.

Part III of this work begins with an overview of the three main steps in the commissioning process of the LFXT prototype. The balancing of the target rotor complex, the bake-out of the vacuum system, and the high-voltage (HV) conditioning procedure of the electron accelerator are explained in detail. During the commissioning process, problems caused by the design of the LFXT prototype were encountered, which limited the final performance of the machine. The roots of the encountered problems are identified, and potential future improvements are discussed. As preparation for the characterisation of the X-ray beam, two methods for measuring the focal spot intensity distribution are adapted to the specific requirements of the LFXT prototype. The performances of the adapted edge and pinhole methods are assessed in Monte Carlo simulations, showing the superiority of the edge method. This work culminates in the first X-ray beam produced by the LFXT prototype, during which a series of initial experiments were conducted. The focal spot dimensions were measured using the aforementioned methods, and the depth-dependant peak-to-valley dose-ratio (PVDR) of the MRT irradiation field produced by the LFXT prototype was assessed using phantom measurements and compared to a conventional X-ray source and a synchrotron light source. Additionally, first preclinical *in vitro* MRT irradiations of human lung cancer cells were performed, and deoxyribonucleic acid (DNA) double-strand breaks were visualised by fluorescent staining of the  $\gamma$ H2AX histone. Measurements of the focal spot dimensions showed a width of  $(72.3 \pm 0.3) \mu\text{m}$  and a length of about 6 mm. The measured PVDR in higher depths was clearly superior at the LFXT prototype compared to the conventional X-ray source, and the first preclinical cell experiments validated the functionality of the LFXT prototype.

In conclusion, this work completes the design of the first LFXT prototype and presents the first X-ray beam produced with it, together with the major challenges encountered on the path leading to it. In doing so, this work lays the foundation not only for future exploitation of the LFXT prototype but for the development of a clinical LFXT version facilitating first clinical trials of MRT and potentially a future translation of MRT into clinical routine.



# Kurzfassung

Die zentrale Herausforderung in der modernen Strahlentherapie besteht darin, das therapeutische Fenster zu erweitern, indem die Tumorkontrolle verbessert und die Normalgewebstoxizität verringert wird. Die Mikrostrahltherapie (MRT) ist ein vielversprechender, neuartiger Ansatz, der mit einem der Hauptparadigmen der konventionellen Strahlentherapie bricht, indem anstelle eines homogenen Strahlenfeldes mit einer Serie von Mikrometerbreiten, planaren Strahlenbündeln von ungewöhnlich hoher Dosis bestrahlt wird. Zahlreiche präklinische Studien haben gezeigt, dass MRT überlegene Normalgewebsschonung bei gleichbleibender Tumorkontrolle bietet. Zur Erzeugung eines klinisch anwendbaren MRT-Bestrahlungsfeldes werden Strahlqualitäten benötigt, die üblicherweise nur an, aufgrund ihrer Größe und Kosten nicht mit einer klinischen Anwendung verträglichen, Synchrotron-Lichtquellen verfügbar sind.

Das Konzept der Linienfokus-Röntgenröhre (LFXT) verspricht, die für MRT nötigen Strahlqualitäten in einem kompakten Maßstab zu liefern und dadurch die ersten klinischen Studien und potenziell die Translation von MRT in die klinische Routine zu ermöglichen. In dieser Arbeit wird die Entwicklung des ersten Prototyps einer LFXT, welche in vorangegangenen Arbeiten begonnen wurde, abgeschlossen und der Inbetriebnahmeprozess, welcher in den ersten Strahl mündet, präsentiert. Nach einer kurzen Einführung in das Thema und einem Überblick über die theoretischen Grundlagen in Abschnitt I wird in Abschnitt II dieser Arbeit der Entwurf des LFXT-Prototyps systematisch beschrieben. Die im Rahmen dieser Arbeit entwickelten Systeme werden gemäß ihrer Funktionalitäten geordnet und individuell präsentiert. Die Hauptanforderungen umfassen die Überwachung der Temperatur des Röntgentargets, die Kühlung der Maschine, die Versorgung mit Beschleunigungsspannung und elektrischer Leistung, das Sicherstellen von Personensicherheit und die Kontrolle und Überwachung des LFXT-Prototyps. Obwohl die entwickelten Systeme noch im Prototypenstadium sind, ist der LFXT-Prototyp insgesamt funktionstüchtig.

Teil III beginnt mit einem Überblick über die drei Hauptschritte im Inbetriebnahmeprozess des LFXT-Prototyps. Das Wuchten des Target-Rotor-Komplexes, das Ausheizen des Vakuumsystems und die Hochspannungs (HV)-Konditionierung des Beschleunigers werden im Detail erläutert. Während des Inbetriebnahmeprozesses traten Probleme auf, die durch die Bauweise des LFXT-Prototyps verursacht wurden, die schließlich die Leistung limitierten. Die Ursprünge der Probleme werden identifiziert, und potenzielle Verbesserungen diskutiert. Als Vorbereitung zur Strahlcharakterisierung werden zwei Methoden zur Vermessung des Brennflecks an den LFXT-Prototypen angepasst. Die Leistungsfähigkeit der angepassten Lochblenden- und Kanten-Methoden werden mittels Monte-Carlo-Simulationen beurteilt. Diese Arbeit kulminiert im ersten durch den LFXT-Prototypen erzeugten Röntgenstrahl, während dem eine Serie an Experimenten durchgeführt wurde. Die Ausmaße des Brennflecks wurden mit den zuvor genannten Methoden vermessen, und die tiefenabhängige Peak-to-valley dose-ratio (PVDR) des MRT-Bestrahlungsfeldes wurde in Phantommessungen beurteilt und mit einer konventionellen und einer Synchrotron-Röntgenquelle verglichen. Zusätzlich wurden erste präklinische *in vitro* MRT-Bestrahlungen von menschlichen Lungenkrebszellen durchgeführt, und DNA-Doppelstrangbrüche durch Fluoreszenzfärbung des phosphorylierten  $\gamma$ H2AX-Histons sichtbar gemacht. Die Vermessung der Brennfleckausmaße ergab eine Breite von  $(72.3 \pm 0.3) \mu\text{m}$  und eine Länge von ungefähr 6 mm. Die am LFXT-Prototyp gemessene PVDR in höheren Tiefen war signifikant besser im Vergleich zur konventionellen Röntgenquelle, und die ersten präklinischen Zellexperimente bewiesen die Funktionalität des LFXT-Prototyps.

Zusammenfassend schließt diese Arbeit die Entwicklung des ersten LFXT-Prototyps ab und präsentiert die ersten damit erzeugten Ergebnisse, zusammen mit den wichtigsten währenddessen aufgetretenen Herausforderungen. Dadurch legt diese Arbeit den Grundstein nicht nur für die zukünftige Nutzung des LFXT-Prototyps, sondern für die Entwicklung einer klinischen LFXT-Version, die erste klinische Studien zu MRT und womöglich die Translation von MRT in die klinische Routine ermöglichen wird.



# Contents

<b>Danksagungen</b>	<b>vii</b>
<b>Abstract</b>	<b>ix</b>
<b>Kurzfassung</b>	<b>xi</b>
<b>I Introduction and Background</b>	<b>1</b>
1 Introduction	3
2 Aim of the thesis	7
3 Background	9
3.1 Microbeam radiotherapy . . . . .	9
3.1.1 Physical and technical aspects . . . . .	10
3.1.2 Biological and medical aspects . . . . .	11
3.2 The Line-focus X-ray tube concept . . . . .	12
<b>II Design and setup of the line-focus X-ray tube prototype</b>	<b>17</b>
4 Introduction to the line-focus X-ray tube prototype	19
5 Focal track temperature monitoring system	23
5.1 Requirements . . . . .	23
5.2 Point measurement of surface temperature . . . . .	23
5.3 Measurement of temperature distribution in focal spot . . . . .	26
5.4 Overview and discussion . . . . .	28
6 Cooling system	31
6.1 Requirements . . . . .	31
6.2 Theoretical background . . . . .	32
6.3 Cooling of target and axis . . . . .	34
6.4 Cooling of vacuum chamber . . . . .	35
6.5 Cooling of target motor . . . . .	37
6.6 Heat buffering and dissipation . . . . .	39
6.7 Overview and discussion . . . . .	41
7 High-voltage system	45
7.1 Requirements . . . . .	45
7.2 High-voltage generation . . . . .	47
7.3 Energy transmission . . . . .	48
7.4 Insulation . . . . .	49
7.4.1 Cold-deck . . . . .	49
7.4.2 Hot-deck . . . . .	51
7.5 Overview and discussion . . . . .	54

<b>8</b>	<b>Safety system</b>	<b>59</b>
8.1	Requirements . . . . .	59
8.2	Radiation protection . . . . .	60
8.3	Protection from drive train malfunction . . . . .	63
8.4	Protection from high-voltage . . . . .	65
8.5	Overview and discussion . . . . .	66
<b>9</b>	<b>Control system</b>	<b>69</b>
9.1	Requirements . . . . .	69
9.2	Software . . . . .	70
9.3	Hardware and network architecture . . . . .	74
9.4	Overview and discussion . . . . .	75
<b>10</b>	<b>Overview and discussion of entire system</b>	<b>79</b>
<b>III</b>	<b>Commissioning of the line-focus X-ray tube prototype</b>	<b>85</b>
<b>11</b>	<b>Introduction to commissioning process</b>	<b>87</b>
<b>12</b>	<b>Balancing, bake-out and high-voltage conditioning</b>	<b>89</b>
12.1	Balancing of target rotor complex . . . . .	89
12.2	Bake-out of vacuum chamber . . . . .	91
12.3	High-voltage conditioning of electron accelerator . . . . .	91
12.4	Summary and discussion of commissioning process . . . . .	94
<b>13</b>	<b>Preparation for focal spot characterisation</b>	<b>97</b>
13.1	Introduction . . . . .	97
13.2	Materials and methods . . . . .	97
13.2.1	Pinhole method . . . . .	97
13.2.2	Edge method . . . . .	98
13.2.3	Validation simulations . . . . .	100
13.3	Results . . . . .	101
13.3.1	Pinhole method . . . . .	101
13.3.2	Edge method . . . . .	101
13.4	Discussion . . . . .	103
<b>14</b>	<b>First Beam</b>	<b>105</b>
14.1	Introduction . . . . .	105
14.2	Materials and methods . . . . .	105
14.2.1	Focal spot characterisation . . . . .	105
14.2.2	Dosimetry . . . . .	106
14.2.3	Cell experiments . . . . .	106
14.3	Results . . . . .	106
14.3.1	Focal spot characterisation . . . . .	107
14.3.2	Dosimetry of MRT field . . . . .	109
14.3.3	First preclinical experiments . . . . .	110
14.4	Discussion . . . . .	111
<b>IV</b>	<b>Summary and Outlook</b>	<b>113</b>
<b>15</b>	<b>Summary</b>	<b>115</b>

<b>16 Outlook</b>	<b>119</b>
<b>List of Abbreviations</b>	<b>121</b>
<b>List of Figures</b>	<b>123</b>
<b>List of Tables</b>	<b>125</b>
<b>Own publications</b>	<b>127</b>
<b>Bibliography</b>	<b>129</b>



## **Part I**

# **Introduction and Background**



# 1 Introduction

Soon after the discovery of X-rays by Wilhelm Conrad Röntgen in 1895, they were already applied in medical diagnostics for their ability to visualise the inner structure of the human body [1]. With the widespread adoption of this new type of radiation, the first signs of tissue reactions soon appeared, sparking initial efforts to harness X-rays for therapeutic applications. Although historical records disagree on who was the first to consciously perform therapy with X-rays, it is consensual that it happened within about only one year after their discovery by W. C. Röntgen. In 1896, Leopold Freund performed the potentially first documented treatment using X-rays on a five year old patient with a melanocytic nevus [2]. At that point, the era of radiotherapy began and has since then been characterised by a constant gain of knowledge and technological possibilities [3].

Today, linear accelerators are conventionally used, allowing for photon energies up to several million electron-volt and thus reaching deeper seated tumours while sparing the skin of the patient. The X-ray beam is rotated around the patient, and its intensity and field shape are dynamically modulated to irradiate the targeted volume as conform as possible while sparing the surrounding healthy tissue. By fractionating treatment into a multitude of irradiation sessions separated by up to a day, the therapeutic window is widened. Additionally, irradiations are planned, considering the sensitivities and resistances of different organs and tumours. Highly accelerated electrons, protons, and rarely even neutrons and heavy ions are available for external beam radiotherapy, each with its own advantages and disadvantages. For localised brachytherapy, radioactive sources are utilised by encapsulating them and positioning them within the body of the patient, and for systemic nuclear therapy by binding them to molecules that naturally accumulate within the target volume and injecting them. In addition to these treatments based on ionising radiation, modern cancer treatment rests on surgical resection of the tumour and non-radiative systemic treatments like chemotherapy and immunotherapy, often combined with each other and with nuclear and radiotherapy.

Despite all of the advancements in treating cancer, it is still one of the leading causes of death, with the risk of dying from it before the age of 75 being nearly 10% and about 10 million deaths worldwide in 2022 [4]. Every second patient diagnosed with cancer receives external beam radiotherapy, often in conjunction with other treatment modalities, but the applicable dose and, therefore, the treatment outcome is often limited by the damage inflicted by the traversing beam on healthy tissue surrounding the tumour [5]. The difference in damage done to tumorous tissue in comparison to healthy tissue by treatment with ionising radiation is called the differential effect and is the very foundation of radiotherapy. Depending on the kind of tumour and its localisation, this can be beneficial to the treatment if a radio-sensitive tumour is surrounded by less radio-sensitive tissue or detrimental if the opposite is the case. Therefore, one of the central research topics in radiotherapy is finding ways to enhance the differential effect and thus widen the therapeutic window, either by increasing damage done to radio-resistant tumours or by protecting healthy tissue from it.

One approach to enhancing the differential effect is spatially fractionated radiotherapy (SFRT), which was first investigated in 1909 by Alban Köhler, who placed a chequerboard-like  $3\text{ mm}^2$  grid of woven iron on the skin of the patient during orthovoltage irradiations, resulting in reduced skin toxicity [6]. Today, SFRT has been further developed, and different forms are investigated preclinically, mainly categorised by the size of the individual beams and the used type of radiation. Both X-rays and protons are used for minibeam radiotherapy, in which blade-like sub-millimetre beams are applied. In microbeam radiotherapy (MRT), which is the focus of this work, only X-rays can be used due to the stronger scattering of protons. A MRT irradiation field consists of a series of blade-like planar beams with thicknesses in the range of 25 - 100  $\mu\text{m}$  spaced 100 - 400  $\mu\text{m}$  apart [7]. This creates a dose profile characterised by alternating high-dose regions, so-called peaks, with doses of up to several 100 Gy and low-dose regions, so-called valleys, with doses well below the tissue tolerance.

This breaks with one of the main paradigms of modern radiotherapy by not trying to deliver the highest possible dose homogeneously to the tumour but instead deliberately creating a highly inhomogeneous dose distribution within the tumorous tissue. Nevertheless, MRT has shown in a multitude of preclinical studies to be able to enhance the differential effect by reducing normal tissue toxicity while maintaining tumour control probability [8]. One of the first *in vivo* studies on MRT was published by Slatkin et al. in 1995, showing that peak-doses of up to 5000 Gy could be delivered to the brain of a rat without causing necrosis [9]. In the year 1998, Laissue et al. showed the ability of microbeams to control and even ablate gliosarcomas, a type of aggressive brain tumour, within rats and significantly increase their survival time [10]. The cerebella of weaning piglets were irradiated in 2007 with up to 600 Gy peak dose by Laissue et al., resulting in only minimal structural and neurological effects [11]. Another study published in the year 2008 by Serduc et al. found that microbeam irradiation of about 25% of the volume of the brain of mice with peak doses of up to 1000 Gy did not lead to severe damage on the cerebral vasculature [12]. The superior efficacy of MRT compared to conventional broad beam irradiation was shown in 2016 by Bouchet et al. irradiating the brains of rats bearing glioma with broad beam doses of 17.9 Gy and MRT with valley doses comparable to broad beam irradiation and peak doses of up to 400 Gy [13]. In the year 2024, the first veterinary study using conformal multi-port MRT irradiations of tumour-bearing pet dogs in a clinical setting by Eling et al. proved that MRT does not induce acute radiotoxicity in healthy brain tissue while leading to significant tumour volume reductions and improving the overall quality of life [14].

While there are studies on MRT that have been done using conventional X-ray sources [15, 16], most studies - including the aforementioned - were and are done at 3rd generation synchrotron light sources like the European Synchrotron Radiation Facility (ESRF) in France. The reason for that lies in how a microbeam irradiation field is produced and in the requirements on beam quality that arise from it. For creating the stripe-pattern characteristic for MRT, a multi-slit collimator (MSC) consisting of a highly absorbing body with micrometre-wide slits is placed in a homogeneous X-ray beam. While most of the X-ray beam is absorbed within the material of the MSC, photons can pass through the slits resulting in planar radiation fields. For this to work, the spatial coherence of the original homogeneous X-ray beam needs to be high enough, or in other words, the source spot the beam originates from needs to be small enough, perpendicular to the slits of the MSC in order to minimise beam penumbras and maintain a sufficiently high peak-to-valley dose-ratio (PVDR) in some distance to the collimator. The energy of the used X-ray beam needs to be high enough to penetrate into tissue and low enough to limit the range of secondary electrons scattering and smearing the microbeam dose pattern within it. Additionally, the dose rate must be high enough to deliver the required peak doses quickly, limiting the smearing due to movement in living targets. A more thorough explanation of MRT is given in chapter 3. While already important for preclinical studies, especially *in vivo*, these requirements become even more strict when considering clinical application. A patient is significantly thicker than a mouse or rat used in preclinical studies, emphasising the need for small beam penumbras and sufficiently high X-ray energies. Additionally, anaesthesia and irradiation over the course of hours are impractical, and organ motion within the human body is larger, rendering a dose rate in the range of at least tens of Gy/s vital.

Synchrotron light sources can deliver the beam qualities necessary for preclinical and also clinical MRT but are too large and expensive for routine clinical treatments. Conventional X-ray tubes and linear accelerators are compact and comparably inexpensive but fail to deliver the necessary dose rate within the required energy range and with a sufficiently small source spot. Therefore, novel compact X-ray sources must be developed to translate MRT to clinical studies. Different technologies have been proposed, including carbon nanotube sources [17] and inverse Compton scattering sources [18], but to date, none of them can provide the needed beam qualities for clinical MRT.

In 2017, Bartzsch et al. proposed the concept of the line-focus X-ray tube (LFXT) as a compact source for clinical MRT [19]. The LFXT is based on the principle of conventional rotating anode X-ray tubes, with the difference that it uses a highly asymmetric line-like electron focal spot impinging on a rapidly rotating target with a significantly higher surface speed than conventional sources exhibit. Due to this, the LFXT operates within the heat-capacity limit, and the temperature increase within the focal spot, which is what conventionally limits the achievable dose rate and source spot size, becomes independent of the focal spot

width. Therefore, the LFXT can achieve dose rates of more than 100 Gy/s originating from a focal spot as thin as 50  $\mu\text{m}$  and with mean X-ray energies of 150 keV, according to Monte-Carlo simulations [20]. The theoretical concept of the LFXT is presented in more detail in chapter 3. The LFXT concept is the most promising source to facilitate the first clinical trials of MRT and potentially a translation into clinical routine, but its feasibility has not yet been proven experimentally. The design and setup of the first prototype of a LFXT has been started within other works [21, 22]. This work is focused on bringing the LFXT from the design phase into reality.



## 2 Aim of the thesis

This work aims to conclude the design and development of the first prototype of a line-focus X-ray tube (LFXT), which was started in prior works, and bring it into operation. The LFXT is a concept for a novel compact X-ray source based on the heat-capacity limit able to deliver beam qualities as necessary for microbeam radiotherapy (MRT). In chapter 3, the background to MRT and the LFXT is presented for a more in-depth explanation. The main purpose of the LFXT prototype is to act as a proof-of-concept for the LFXT and potentially lay the foundation for the advancement of the concept and the development of future clinical LFXT versions. While not performing high enough for clinical applications, the LFXT prototype will additionally help to demystify the working mechanisms of MRT by providing a source for preclinical *in vitro* and *in vivo* studies aside from sparsely available third generation synchrotron light sources. In part II containing chapters 4 to 10, the design and setup of the LFXT prototype is presented with a focus on the systems developed within the scope of this work. The commissioning process and first results of the operation of the LFXT prototype are presented in part III ranging from chapter 11 to 14. In part IV, containing chapters 15 and 16, a summary of the complete work and an outlook to potential future developments is given.

The aim of part II of this work is to conclude the design and setup of the LFXT prototype. Part II starts in chapter 4 with an introduction to the main parameters of the LFXT prototype and a presentation of the core systems developed within prior works. Additionally, the basic requirements needing to be fulfilled by the systems developed within the scope of this work are presented from a systems engineering point of view in chapter 4. The systems developed within the scope of this work are dubbed support systems as they are not directly concerned with creating the X-ray beam but instead fulfil the requirements of the core systems, e.g. the electron accelerator, the rotating target, and the vacuum system, and provide means for control, monitoring and safety. The first system that will be presented in chapter 5 is concerned with monitoring the temperature of the target of the LFXT prototype during operation. Due to the high power of the LFXT prototype and the low efficiency of X-ray generation by Bremsstrahlung of only about 1%, the temperature of the target is a critical parameter that needs to be monitored both for reasons of machine safety and for characterising the performance of the LFXT prototype in respect to temperature. The purpose of the cooling system presented in chapter 6 is to disperse not only the heat allocated within the target by the electron beam but also that which is generated within the vacuum chamber due to back-scattering electrons from the focal spot and that produced by power losses of the electric motor propelling the target. In chapter 7, the high-voltage (HV) system is presented. The purpose of the HV system is to supply the necessary acceleration voltage as well as the needed power for beam control and cathode heating to the electron accelerator. Additionally, the HV system contains the components needed for insulating the acceleration voltage as well as the means for supplying electrical power through a voltage barrier. Due to the different threats the LFXT prototype poses to personnel residing in the vicinity of it, including ionising radiation, high voltage, and high amounts of kinetic energy, a dedicated safety system is required. The safety system presented in chapter 8 is closely intertwined with other systems, and, therefore, some components are shared between multiple systems. The concerned components will generally be presented within all systems to which they belong, with a focus on their functionality in each respective system. The control system presented in chapter 9 contains all components, both hardware and software, needed for controlling and monitoring the LFXT prototype and future experimental setups during operation. Finally, in chapter 10, an overview of the entire LFXT prototype and all its support systems is given. The advantages and disadvantages of the chosen approaches are discussed together with potential improvements.

The aim of part III of this work is to bring the LFXT prototype from a finished setup to an operational machine, culminating in the first X-ray beam. Part III aims to give an overview of the main steps in the commissioning process of the LFXT prototype, discuss the issues faced, and present the first X-ray beam

together with the experiments conducted during it. In chapter 11, motivation and introduction to the commissioning process of the LFXT prototype are given. The following chapter 12 briefly presents the main commissioning steps required for putting the LFXT prototype into operation. This includes balancing the target-rotor complex before the final assembly of the vacuum chamber, baking out the vacuum chamber to achieve the required ultra-high vacuum (UHV) conditions, and conditioning the electron accelerator for the required high acceleration voltage. The challenges and respective solutions encountered during the commissioning of the LFXT prototype will be presented here. For the adjustment of the electron optics and for later characterisation of the performance of the LFXT prototype, methods for visualising the focal spot are required. Chapter 13 presents two methods conventionally used for characterising the focal spot of an X-ray tube adapted to the specific requirements of the LFXT prototype. The adapted methods are presented together with simulations evaluating their performance and a comparison of their respective advantages and disadvantages. In chapter 14, the first experimental results achieved with X-rays generated by the first LFXT prototype constituting the culmination point of this work are finally presented. Chapter 14 concludes part III of this work and symbolises the transition from the commissioning phase of the LFXT prototype into the operation phase, which lies beyond the scope of this work.

Part IV aims to conclude this work by giving a summary of the design, setup and commissioning process presented in parts II and III in chapter 15. In chapter 16, an outlook of the operation phase of the LFXT prototype and future experiments that will be conducted is given. Additionally, an outlook on potential future developments, including a clinical prototype, is given.

### 3 Background

In the following chapter, the background to microbeam radiotherapy (MRT) and the concept of the line-focus X-ray tube (LFXT) are presented. For MRT, the physical and technical aspects are explained with a focus on the requirements for the X-ray source and the potential biological mechanisms underlying the observed enhancement of the differential effect. The theoretical background to the heat capacity limit is explained as the underlying concept for the LFXT, together with the technical basics of the LFXT.

#### 3.1 Microbeam radiotherapy

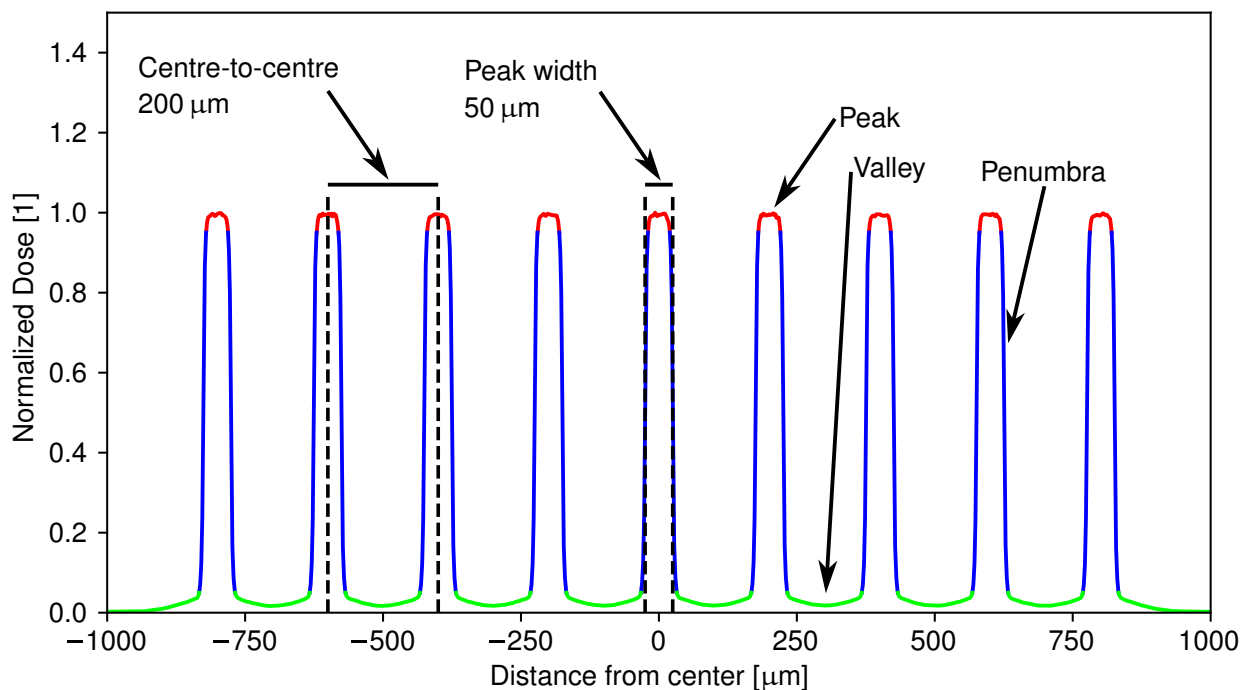


**Figure 3.1** Exemplary MRT dose profile. The centre-to-centre distance of 200  $\mu\text{m}$  and the peak width of 50  $\mu\text{m}$  are highlighted. Additionally, an exemplary peak, a valley and a beam penumbra are marked. The x-axis depicts the distance from the beam centre in  $\mu\text{m}$  and the y-axis dose normalised to peak dose. The peaks are drawn in red, the penumbras in blue, and the valleys in green.

Based on spatially fractionated radiotherapy (SFRT) introduced in 1909 by Alban Köhler [6], different types of radiation therapies utilising heterogeneous dose distributions and various types of radiation have been developed. Out of these, MRT using X-rays modulates the beam on the finest scale. A MRT irradiation field is characterised by a series of planar blade-like beamlets with thicknesses in the range of 25 - 100  $\mu\text{m}$  spaced 100 - 400  $\mu\text{m}$  centre-to-centre apart [7]. A Monte Carlo simulated exemplary dose profile produced by MRT with a thickness of an individual beamlet of 50  $\mu\text{m}$  and a centre-to-centre distance of 200  $\mu\text{m}$  in a water phantom is presented in fig. 3.1. The arising high-dose regions within the target volume are called peaks, while the intermediary low-dose regions are called valleys. The peak doses used in preclinical studies range up to several 100 Gy, while the valley doses are lower by a factor of up to 100 [20]. The proportion between peak and valley dose is called the peak-to-valley dose-ratio (PVDR) and is

an important parameter characterising a MRT irradiation field. Due to different effects that will be explained in the following, the transition between peaks and valleys is not ideal, and the resulting transition region often defined as 10% - 90% of peak dose is called penumbra [23].

### 3.1.1 Physical and technical aspects

In order to generate a MRT irradiation field, a specialised multi-slit collimator (MSC) is used. As depicted in fig. 3.2, a MSC conventionally consists of a body made from a highly absorbing material (e.g. Tungsten) with slits allowing parts of the incoming homogeneous X-ray beam to pass. The design of a MSC depends on the used beam geometry, either parallel or divergent, the X-ray spectrum, and the desired characteristics of the MRT field. Within the range of X-ray energies used for MRT, the MSC needs to be about 10 mm thick in order to be sufficiently attenuating and provide a high PVDR, rendering the manufacturing process difficult. Manufacturing is mostly done using electrical discharge wire erosion, a process in which a thin wire is inserted through the material and a high voltage is applied [24]. The occurring electrical discharges from the wire to the surrounding material gradually erode it, allowing for very high precision and complex geometries by slowly moving the wire. Due to limitations of this process concerning the thickness of the cut material and of the used wire, MSCs often consist of several stacked plates with individually wider slits, shifted to achieve the desired slit width [16, 25]. Another method of realising a MSC is by stacking alternating foils of highly absorbing and less absorbing material, but this only allows for parallel beam geometries and leads to a loss of dose rate and PVDR due to absorption and scattering [26, 27].

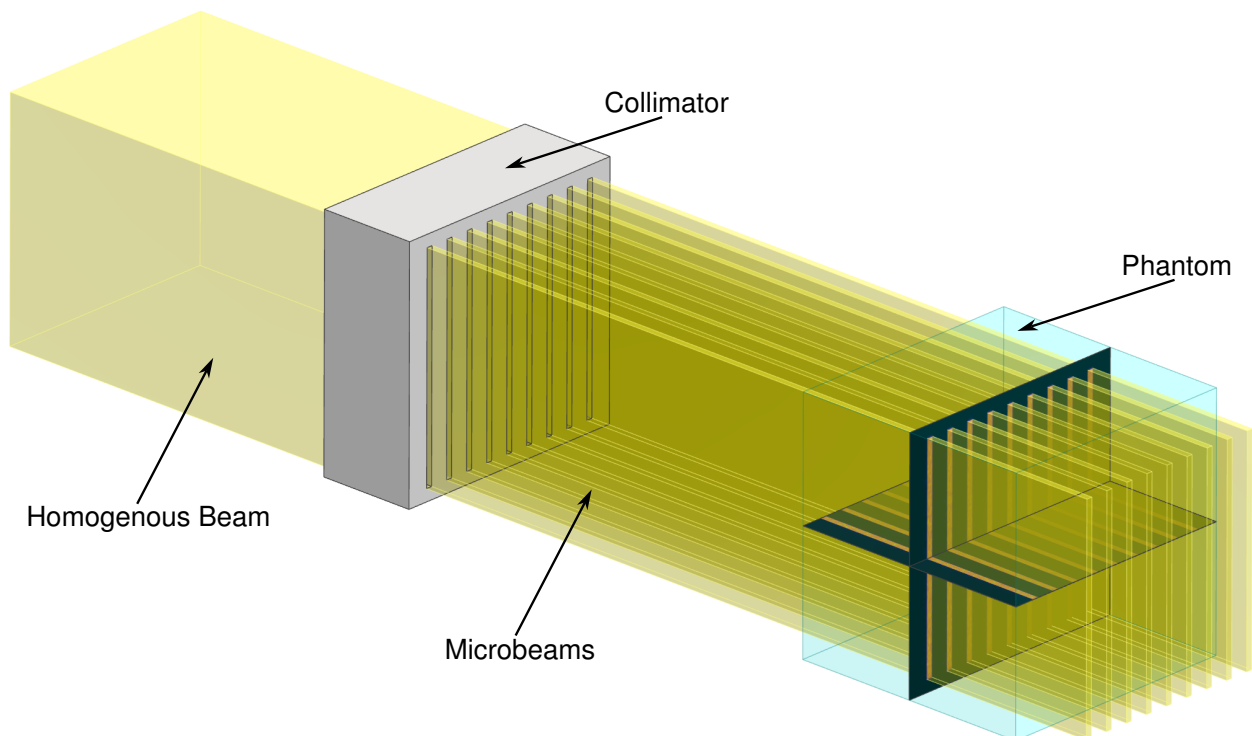


**Figure 3.2** Sketch of the basic principle of MRT. An incoming homogeneous X-ray beam (depicted in translucent yellow) is formed by a collimator (depicted in grey) into a series of microbeams. The microbeams penetrate through a phantom (depicted in translucent blue), depositing dose. Within the phantom, a horizontal and a vertical slice of the 3D dose distribution are shown.

As already mentioned, only X-rays can be used for MRT in contrast to other SFRT modalities. The reason for that is the higher scattering probability of particles (e.g. protons), which would lead to a deterioration of the very fine MRT dose pattern. For the same reason, MRT is limited to significantly lower X-ray energies than conventional radiotherapy using linear accelerators. X-ray photons deposit the largest part

of their dose indirectly via secondary electrons, which travel and scatter further, depositing their dose in a volume around the original interaction site. This effect is one of the main influences creating the penumbra in a MRT field. In the relevant energy range, secondary electrons are created by the photo effect transferring the full photon energy and the Compton effect transferring a fraction of it, with the Compton effect being dominant at photon energies above about 100 keV. For 100 keV photons, the mean energy of the secondary electrons is about 13 keV, allowing them to travel up to about 7  $\mu\text{m}$ , while for 200 keV photons, travel ranges of up to about 35  $\mu\text{m}$  are possible increasing non-linearly with X-ray energy [23]. Below about 100 keV photon energy, the influence of the photo effect increases and with it, the mean kinetic energy and travel range of the produced secondary electrons. Therefore, low X-ray energies in the range of around 100 keV are optimal for steep penumbras. However, low X-ray energies also lead to increased attenuation within a material, limiting penetration depth and, thus, irradiation possibilities for deeper seated target volumes. Therefore, the X-ray energy used for MRT is a trade-off between sharp penumbras and penetration depth that needs to be decided based on the respective application.

Another parameter severely influencing the penumbra of a MRT pattern and, therefore, the achievable PVDR, especially in higher distances from the collimator, is the spatial coherence of the X-ray beam perpendicular to the collimator slits. In conventional X-ray sources based on a beam of accelerated electrons impinging on a metal target, the spatial coherence is defined by the dimensions of the focal spot from which the X-ray photons emerge: The smaller the focal spot under a specific angle, the higher the respective spatial coherence. For synchrotron sources, the effective focal spot can be approximated as a point source at an infinite distance. The influence of the focal spot size perpendicular to the collimator slits on the MRT pattern is a purely geometric one, as the resulting dose pattern is mathematically a convolution of the intensity distribution of the focal spot with the collimator, which can be modelled by a series of box functions. Due to this, the focal spot size perpendicular to the collimator slits needs to be smaller than the width of the collimator slits, as otherwise partial shadows behind the collimator would lead to the dose pattern deteriorating with increasing distance.

In preclinical *in vivo* or potential future clinical studies, the dose rate with which the MRT irradiation is conducted plays a vital role in addition to the parameters discussed before. Due to the heartbeat, the peristalsis, and the breathing of a living organism, all tissues within it are moving with a more or less pronounced amplitude. This is called organ motion and can heavily impact the MRT dose pattern, as already movement in the range of 10  $\mu\text{m}$  during the irradiation would lead to severe smearing. To counteract this, the required dose of up to several 100 Gy needs to be delivered within a time frame small enough to limit the influence of organ motion to a minimum, e.g. within a fraction of the heartbeat. This would lead to a required dose rate in the range of several  $\text{kGys}^{-1}$  for clinical applications, which is, to date, only achievable at 3rd generation synchrotrons [20]. An approach to mitigate the requirements on the dose rate is to do multiple irradiations from different directions with individually lower peak doses, similar to conventional multi-port irradiation. That way, a lower dose rate is sufficient to deliver a single MRT field in a short time, and as the individual fields do not overlap within healthy tissue, the sparing effect is conserved. Within the target volume, however, the individual fields overlap either in an interlaced or cross-planar geometry, leading to a more complex dose distribution [23].

### 3.1.2 Biological and medical aspects

The reduced normal tissue toxicity observed after irradiation with any type of SFRT is based on the dose-volume effect, stating that the tolerance of non-tumorous tissue to radiation increases when the irradiated volume is decreased [23]. In other words, the smaller the irradiated volume, the more dose can be delivered to that volume without increasing side effects. The dose-volume effect was experimentally shown in 1961 by Zeman et al [28] by irradiating the brains of mice with deuteron beams of varying diameters to evaluate the effects of cosmic radiation. They saw that the tolerance of brain tissue increased from 140 Gy when irradiating with a 1 mm beam to about 4000 Gy at a beam diameter of 25  $\mu\text{m}$ . As MRT utilises the smallest individual beams of all SFRT modalities and, therefore, irradiates the smallest contiguous volumes, it utilises the dose-volume effect to the highest extent. In tumorous tissue, the dose-volume effect is significantly less pronounced or even reversed, such that fractionation may lead to an increase in sensi-

tivity to radiation. The causes for the observed difference in the reactions of healthy and tumorous tissue to MRT and SFRT in general are not yet fully understood, but several effects playing a vital role have been identified, which are presented in the following.

As presented by Crosbie et al [29], the response of healthy and tumorous tissue after MRT irradiation differs significantly on a cellular level. Healthy tissue retains its structure and is able to efficiently repair the damaged peak regions by removing apoptotic cells and undergoing cell proliferation. However, in tumorous tissue, cells from the peak and valley regions intermix quickly after irradiation due to migration, and no removal of apoptotic cells or coordinated repair occurs. The capabilities of cells within healthy tissue that only received a low dose to repair neighbouring highly damaged regions is the main factor leading to the increased tolerance of normal tissue to MRT. The rapid intermixing of cells from the peak with cells from the valley regions in tumorous tissue potentially enhances the so-called radiation-induced bystander effect that could play a significant role in the increased sensitivity of tumorous tissue to MRT. [29]

The radiation-induced bystander effect describes the phenomenon that unirradiated cells in close proximity to irradiated cells behave as if they had been irradiated [30]. This is due to chemical signalling processes from the irradiated to the unirradiated cells, either directly by gap junctions or through the extracellular fluid. The bystander effect varies in strength among different cell types, depending on their degree of differentiation, with less differentiated cells exhibiting a more pronounced response [31]. Generally, cells of malignant tumours are less differentiated than those forming healthy tissue, rendering them more susceptible to the bystander effect. Together with the high mobility of cells within tumorous tissue, this is one of the effects that lead to the entire tumour being damaged by MRT despite only a fraction of the cells being irradiated.

A beneficial effect of MRT improving tumour control that can only be observed in *in vivo* studies is the amplification of immune responses after irradiation [32]. Different studies have shown a clustering of immune cells and the up-regulation of transcriptomic factors related to immune and inflammatory responses within tumorous tissue irradiated by MRT in contrast to conventional radiotherapy [33, 34, 35]. Not only does this improve tumour control within the irradiated volume, but it has been proposed that following systemic abscopal effects could combat metastasis at distant sites, especially in combination with immunotherapy [36].

Additionally to the aforementioned more bio-medical effects, MRT has a physical effect on microvasculature differing in healthy and tumorous tissue. The mature and well-structured vasculature of healthy tissue can withstand MRT irradiation with peak doses up to 1000 Gy without suffering functional impairment [37, 12]. The microvasculature within tumorous tissue is significantly more chaotic and immature and, therefore, more sensitive to the high peak doses of MRT [38]. This can lead to hypoxia and malnutrition due to reduced perfusion of the tumorous tissue [39], and enhance the efficacy of e.g. chemotherapy by increasing vascular permeability [40].

### 3.2 The Line-focus X-ray tube concept

The design of X-ray tubes has changed significantly since the gas-filled discharge tubes Röntgen used in his experiments, but the physical principles they rely on did not. An electron source, conventionally a thermionic cathode, produces free electrons, which are accelerated in an applied electric field towards an anode. The accelerated electron beam impinges on a metal target, which is sometimes called the anticathode and can simultaneously be the anode, leading to the emission of X-ray photons by Bremsstrahlung and characteristic fluorescence. Different types of X-ray sources operating on this principle exist, but they all suffer from the highly inefficient conversion process in which only about 1% of the power in an accelerated electron beam is converted into X-ray photons, and the residual 99% remains as heat in the target and the surrounding structures [41]. Ultimately the temperature within the focal spot of the electron beam on the target limits the possible performance of every X-ray tube. Depending on the application, different types of X-ray tubes exist, ranging from stationary anode X-ray tubes if only low power is required, over rotating anode X-ray tubes mitigating the temperature problem and achieving a higher fluence, to

liquid metal jet X-ray tubes and other experimental forms for specific applications. However, none of the presently available compact X-ray sources is able to deliver the required beam properties for MRT as presented in section 3.1.

The line-focus X-ray tube (LFXT) is a novel type of X-ray tube proposed by Bartzsch and Oelfke in 2017 [19], promising to deliver up to  $180 \text{ Gys}^{-1}$  from a focal spot that is only  $50 \mu\text{m}$  wide at an acceleration voltage in the orthovoltage regime. The LFXT is based on the principle of rotating anode X-ray tubes but operates within a physical domain of target heating first described by Bartzsch and Oelfke, who termed it the heat capacity limit in contrast to the heat conduction limit conventional rotating anode X-ray tubes operate in. The basic principle of a LFXT is visualised in fig. 3.3. In a LFXT, a beam of accelerated electrons is produced by a dedicated electron source comprising both cathode and anode. The target and the anode are, therefore, separate components in contrast to most conventional rotating anode X-ray tubes. The electron beam is then focused by a series of magnets acting as electron optics creating a line-like focal spot on the target, eponymous for the concept. The length of the focal spot  $l$  is in the range of 20 mm, while the width  $b$  is only about  $50 \mu\text{m}$ . The target of a LFXT rotates with a significantly higher surface speed compared to conventional rotating anode X-ray tubes with the velocity vector  $v$  parallel to the width of the focal spot. The high surface velocity, combined with the small width of the focal spot, leads to a change in heat deposition mechanisms and, therefore, to the heat capacity limit, which will be shortly deduced in the following. [19]

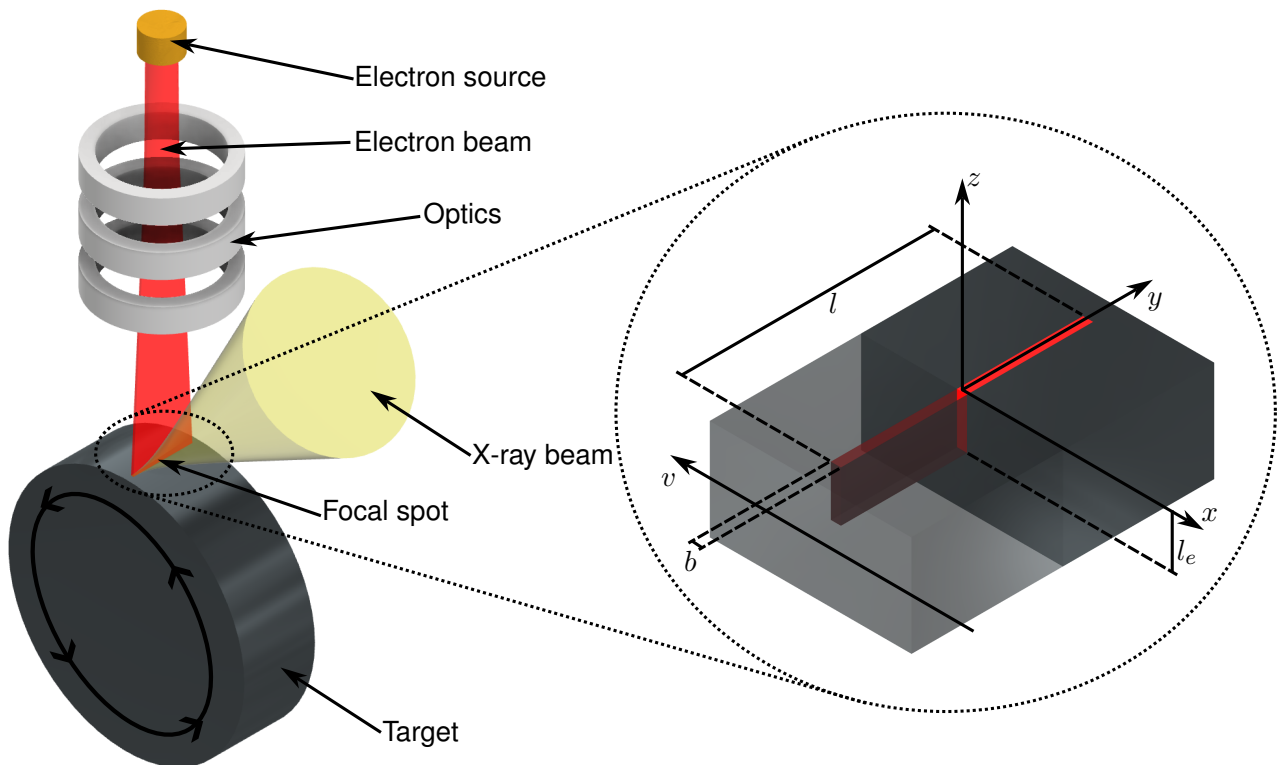


**Figure 3.3** Sketch of the basic principle of the LFXT as a special type of rotating anode X-ray tube. On the left, the main components incorporating the electron source, optics and target are depicted together with the electron beam, the line-like focal spot and an exemplary X-ray beam. On the right, a zoom-in of the focal spot on the target is presented, with part of it translucent to visualise the electron penetration into the target. Incribed are the coordinate axes, the length  $l$  and width  $b$  of the focal spot, the electron penetration depth  $l_e$ , and the velocity vector of the target  $v$ . The depictions are only exemplary and not to scale.

Assuming a steady planar target and an electron focal spot moving along the positive  $x$ -axis, the three-dimensional temperature change at time  $t$  of a volume element in the target at position  $\vec{r}$  is given by the heat equation

$$\frac{\partial T(\vec{r})}{\partial t} = \frac{f(\vec{r}, t) + \kappa \Delta T(\vec{r})}{\rho c} \quad (3.1)$$

with the thermal conductivity  $\kappa$ , the mass-density  $\rho$  and the heat capacity  $c$  of the target material, the Laplace-operator  $\Delta$  and a function  $f(\vec{r}, t)$  modelling the volumetric heating power of the electron beam [42]. From eq. 3.1, it can be seen that two effects influence the temperature within the target: The direct deposition of energy by the electron beam modelled by  $f(\vec{r}, t)$  and the heat conduction within the target represented by  $\kappa \Delta T(\vec{r})$ . The effects can be measured by the heat conduction length  $l_c$  defined by

$$l_c = 2\sqrt{\frac{\kappa \Delta t}{\rho c}} \quad \text{with} \quad \Delta t = \frac{b}{v} \quad (3.2)$$

with the focal spot width  $b$  and surface velocity  $v$  representing the distance a heat-front can travel into the target during the time  $\Delta t$  the focal spot takes to traverse the target, and the electron penetration depth  $l_e$  dependant on the electron energy and the stopping power of the target material representing the depth electrons can penetrate into the target to deposit energy [19].

In a conventional rotating anode X-ray tube, the time  $\Delta t$  is high due to a low surface velocity combined with a conventionally larger focal spot. Therefore, the heat conduction length  $l_c$  is significantly higher than the electron penetration depth  $l_e$ , and thus electron penetration into the target can be neglected. Due to this, heating by the electron beam can be assumed to only occur at the surface of the target, and the heating function  $f(\vec{r}, t)$  can be expressed by

$$f(\vec{r}, t \in [0, \Delta t]) = \frac{P_e}{bl} \cdot \Theta(x - (vt - b))\Theta(vt - x) \cdot \Theta(y - \frac{l}{2})\Theta(\frac{l}{2} - y) \cdot \delta(z) \quad (3.3)$$

with the total heating power of the electron beam  $P_e$ , the length and width of the focal spot  $l$  and  $b$ , the Heaviside function  $\Theta$  and the Dirac function  $\delta$  [42]. This assumption is the so-called heat conduction limit and allows eq. 3.1 to be solved, resulting in the maximum temperature rise during a single passing of the electron beam:

$$\Delta T_{cond} = \frac{2P_e}{l\sqrt{\pi\kappa\rho cbv}} \quad (3.4)$$

This equation was deduced by Oosterkamp in 1948 to model the temperature behaviour of rotating anode X-ray tubes [43]. Important to note in eq. 3.4 is the dependence on the focal spot width  $b$ , as this implies that with decreasing focal spot width and, therefore, increasing power density in the focal spot, the maximum temperature increases. Effectively this leads to the established behaviour of rotating anode X-ray tubes, where the width of the focal spot and the achievable electron beam power are a trade-off.

In a LFXT, the surface velocity  $v$  is significantly higher, and the focal spot width  $b$  is significantly smaller than in a conventional rotating anode X-ray tube. Therefore, the heat conduction length  $l_c$  as described by eq. 3.2 is, in this case, significantly smaller than the electron penetration depth  $l_e$  and heat conduction can be neglected by assuming  $\kappa \Delta T(\vec{r}) = 0$  in eq. 3.1. As electron penetration into the target is not neglectable here, the heating function  $f(\vec{r}, t)$  needs to be expressed as the loss of power from the electron beam per volume element [19]:

$$f(\vec{r}, t \in [0, \Delta t]) = \frac{\partial P_e}{\partial \vec{r}}(\vec{r}) \quad (3.5)$$

Following the definition of electron penetration depth given by Bartzsch and Oelfke as  $l_e = E_e / \langle \frac{\partial E_e}{\partial z}(z) \rangle$  with the primary electron energy  $E_e$  and the maximum energy loss per depth interval in statistical average  $\langle \frac{\partial E_e}{\partial z}(z) \rangle$ , the resulting temperature increase is given by [19]:

$$\Delta T_{cap} = \frac{P_e}{l_e v l \rho c} \quad (3.6)$$

It can be seen that the temperature increase in this approximation is only dependent on the heat capacity of the target material and not the thermal conductivity, thus the name heat capacity limit. Additionally, the

temperature is independent of the focal spot width  $b$ , allowing the focal spot width to be decreased ad libitum without temperature limitations.

Both the heat conduction and the heat capacity limit are approximations for extreme scenarios. In practice, heat conduction within the target and electron penetration into it influences the temperature behaviour simultaneously, but to a varying extent, depending on the characteristics of the source. In fig. 3.4 simulations done by Winter et al [42] using Monte-Carlo and finite element analysis (FEA) for the two limiting cases and a realistic case are shown. For the simulations, an electron beam with 90 kW power at 300 kV acceleration voltage and a tungsten target with a surface speed of  $200 \text{ ms}^{-1}$  were assumed.

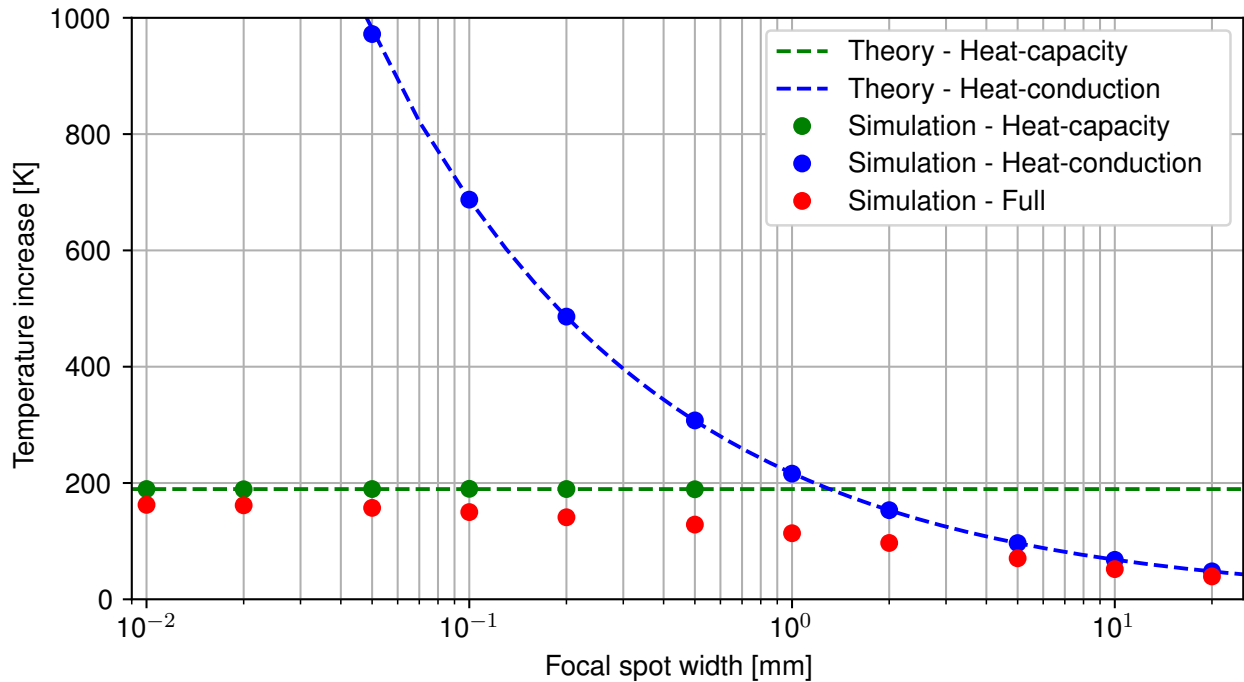


**Figure 3.4** Simulated maximum temperature increase in the focal spot depending on focal spot width. The dashed lines represent analytical results calculated using eq. 3.4 and 3.6 and the round markers simulated results. In blue, the results assuming pure heat conduction, and in green, the ones assuming pure heat capacity are shown. In red the results of a realistic simulation taking both effects into account are shown. *Adapted from [42].*

When comparing the results for the heat capacity and heat conduction cases in fig. 3.4, the behaviour discussed before is clearly visible. As predicted by eq. 3.4, the temperature increase is higher the smaller the focal spot width in the heat conduction limit. In the heat capacity limit as modelled by eq. 3.6, the temperature increase is independent of focal spot width. In the realistic simulation, it can be seen that for a large focal spot and, therefore, a large traversal time  $\Delta t$ , the temperature increase is similar to that in the heat conduction limit, as heat conduction is the dominant process. For small focal spots, electron penetration is the dominant process, and the temperature increase is asymptotic to that in the heat capacity limit. Every real rotating anode X-ray tube will, in theory, show this behaviour, but the temperature at which the asymptote defined by the heat capacity limit lies is dependent on the surface speed of the target  $v$  according to eq. 3.6. For conventional rotating anode X-ray tubes, this maximum temperature is above the tolerable range of target temperatures. A LFXT is characterised by a sufficiently high surface speed  $v$ , such that the maximum temperature at small focal spot widths  $b$  is reduced to acceptable levels. Thereby, the LFXT is able to achieve high power while maintaining a focal spot sufficiently small for MRT.



## **Part II**

# **Design and setup of the line-focus X-ray tube prototype**



## 4 Introduction to the line-focus X-ray tube prototype

The concept of the line-focus X-ray tube (LFXT), as set out above in chapter 3, has to date been verified mathematically and in simulations but not experimentally. Within the collaboration this work is part of, the aim is to build the first prototype of a LFXT and prove its feasibility for preclinical microbeam radiotherapy (MRT). Based on the theoretical concept of the LFXT presented in chapter 3, the design for the first prototype has been started in prior works within the collaboration. Before presenting in the following chapters 5 to 9 the systems developed within the scope of this work, the core systems developed within prior works are shortly presented for a complete overview. The LFXT prototype is meant as a proof-of-concept for the underlying principle and for later preclinical studies but is not yet suitable for clinical trials. As mentioned before, it is based on a conventional rotating anode X-ray tube with an accelerator producing and focusing the electron beam onto a rapidly rotating target, where X-ray photons are produced by means of Bremsstrahlung and emission of characteristic radiation. A multi-slit collimator (MSC) is used to split the resulting homogeneous radiation field into a field for MRT. In fig. 4.1, a horizontal cut through the computer aided design (CAD) model of the vacuum chamber encasing the core systems is presented.

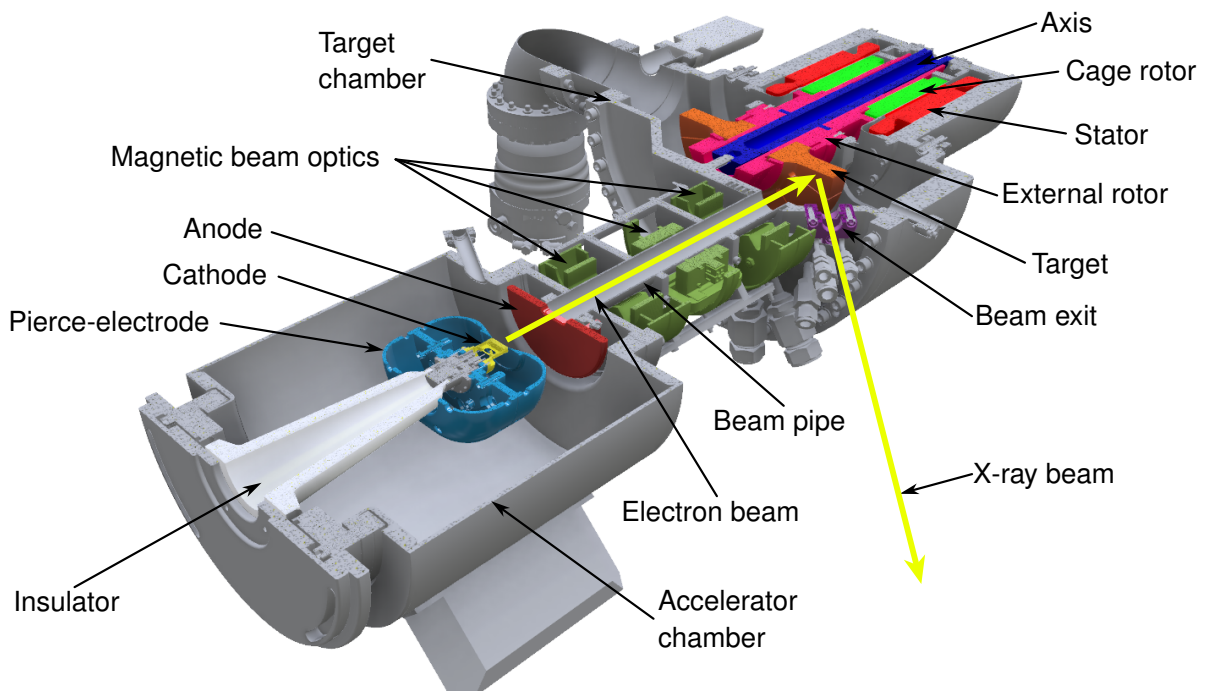


**Figure 4.1** Horizontal cut through the CAD model of the vacuum chamber of the LFXT prototype. The core components within the vacuum chamber are highlighted and labelled. Additionally, the electron and X-ray beams are denoted.

The electron beam of the LFXT prototype is produced by a dedicated accelerator as presented by Matejcek et al. [44]. Electrons are emitted from an electrically heated thermionic cathode of a rectangular shape surrounded by a Pierce-electrode for beam control and shaping. The assembly of the cathode and the pierce electrode is called the electron source complex and is held by a ceramic insulator. The free electrons are accelerated by the applied high-voltage towards a slotted anode and pass through it into the

beam pipe. In contrast to conventional X-ray tubes, the anode is not simultaneously the target in the LFXT prototype but a distinct part of the accelerator. The maximum beam current and acceleration voltage for which the LFXT prototype is designed are 300 mA and 300 kV. While traversing through the beam pipe, the electron beam is focused by an array of a quadrupole magnet, a steerer magnet, and a second quadrupole magnet into its final focal spot on the target surface. The magnetic optics are designed such that the focal spot has a length in the horizontal direction of 20 mm and a width in the vertical direction of 50  $\mu\text{m}$ .

The target of the LFXT prototype needs to withstand high thermal and mechanical stresses due to the unconventionally high-powered and narrow electron beam as well as the high surface velocity necessary for operation within the heat capacity limit. It consists of a tapered cylindrical disk with a diameter of 240 mm and a thickness of 27 mm at the outer edge and is made of titanium–zirconium–molybdenum alloy (TZM) for its high mechanical and thermal stability, as presented by Winter et al. [42]. As relief for stress within the target, it is segmented by radial slits such that material expansion is possible. The relief slits are tilted in a way that the electron beam can not penetrate through and potentially damage structures behind the target. On the frontal surface of the target, in the area where the electron beam impinges, a 1 mm thick inlay made of a tungsten-rhenium alloy is forged onto the TZM body as focal track. In X-ray tubes, tungsten-rhenium is a conventionally used conversion material for its beneficial thermal and mechanical properties and its high atomic number, increasing the efficiency of X-ray conversion [45].

A core requirement for operation within the heat capacity limit is a high surface velocity of the target in the area of the focal spot. To achieve the necessary surface velocity, the target is mounted on a dedicated external rotor revolving around a steady axis, as explained by Dimroth A. [21]. A dynamic liquid metal bearing is used to ensure low friction and abrasion as well as sufficient heat and electrical conduction. Rotation is induced by a high performing electrical motor with its cage rotor pressed onto the external rotor the target is mounted on and its stator within the surrounding structure. The drive train is designed for rotational frequencies of up to 200 Hz resulting in a surface velocity of about  $150 \text{ ms}^{-1}$ .

The electron accelerator, the target and the rotor are encased within a vacuum chamber meant for ultra-high vacuum (UHV) conditions. The UHV is necessary as the cathode of the accelerator and the surface of the target would be damaged by residual gas at high temperatures. Additionally, insulation of the high acceleration voltage of 300 kV is only possible within UHV and the accelerated electrons would scatter with residual gas molecules, rendering focusing of the electron beam impossible. Another reason for the necessity of UHV is that under the presence of oxygen, the liquid metal within the bearing would oxidise, forming a solid. Two turbo-molecular pumps are used to evacuate the vacuum chamber and achieve UHV conditions. The vacuum chamber is segmented into the accelerator chamber and the target chamber, connected only by a narrow pipe through which the electron beam traverses from one to the other. The beam exit window is made of industrial diamond for its low X-ray absorption and thermal properties [22].

In order for the core systems developed within prior works to operate and experiments to be conducted using the LFXT prototype, a multitude of interdependent requirements needs to be fulfilled, as presented in fig. 4.2. For example, for experiments to be conducted, an X-ray beam as well as electrical power for devices like detectors and movement stages are required, and personal safety needs to be ensured. The requirement of an X-ray beam is fulfilled by the target, which itself has requirements that need to be fulfilled by other systems. The components fulfilling the requirements of the core systems are grouped into separate support systems developed within the scope of this work and presented in detail in chapters 5 to 9.

The focal track temperature monitoring system presented in chapter 5 enables measurement of the temperature within the focal track and focal spot on the target surface. This is necessary both for safety reasons and for the characterisation of the thermal behaviour of the LFXT prototype, potentially experimentally proving the heat capacity limit. Not only does the electron beam heat up the surface of the target, but about half of the accelerated electrons are scattered from the target surface back onto the inner surface of the vacuum chamber, depositing their kinetic energy in the form of heat. In order to keep the temperature of the vacuum chamber within safe margins, the cooling system presented in chapter 6 removes excess heat. In addition, the cooling system cools the electric motor propelling the target and indirectly the target through the steady axis of the drive train.

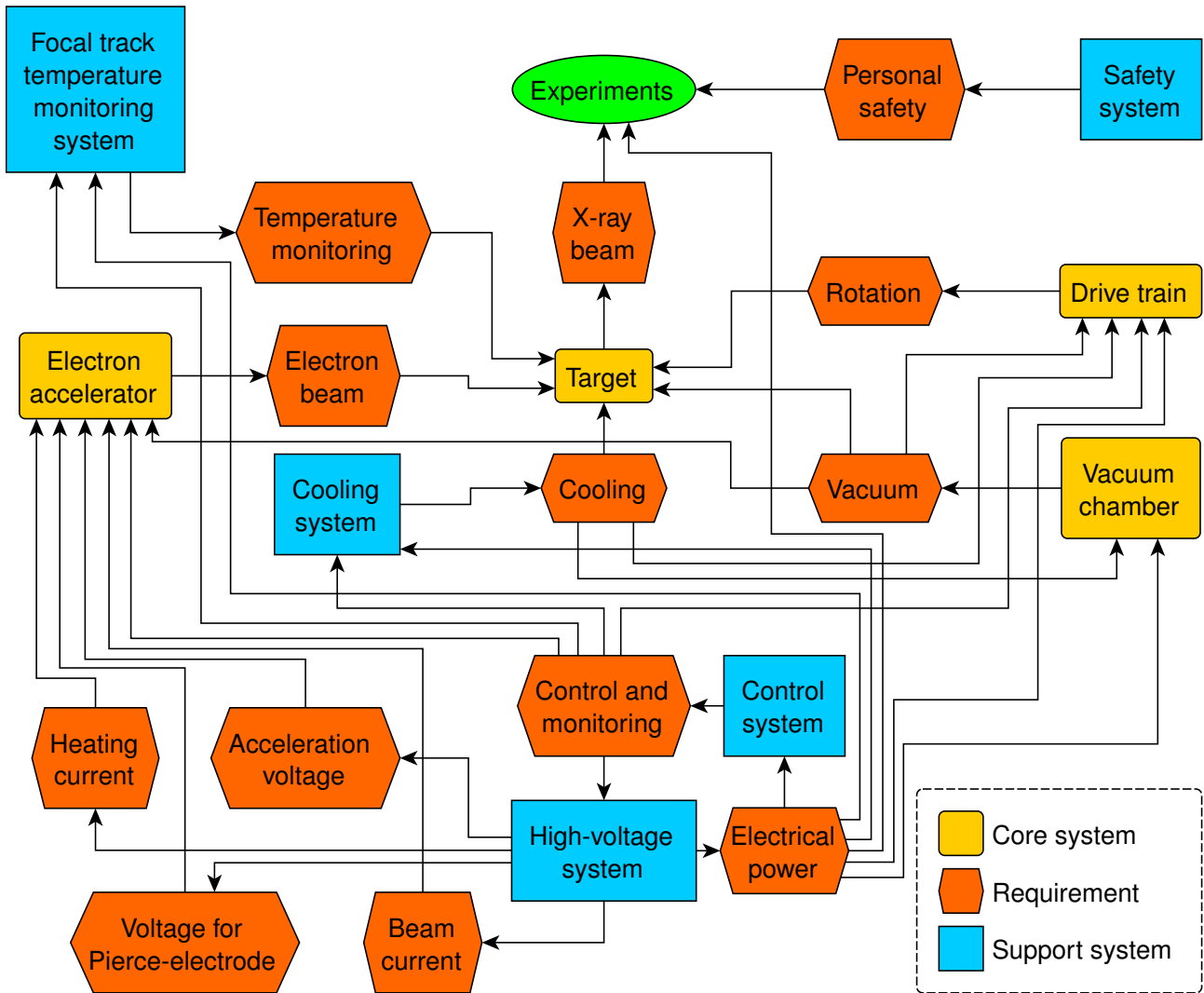


**Figure 4.2** Requirement diagram for experiments at the LFXT prototype. Presented are the core systems with their respective requirements for operation and the support systems fulfilling them. Arrows symbolise either the need for or the fulfilment of a requirement.

Within the high-voltage (HV) system presented in chapter 7, all components concerned with generating, insulating or otherwise affecting the acceleration voltage of the electron accelerator are gathered. This includes the HV sources used for generating the acceleration voltage and beam current, the means of insulating it, and the cables transmitting it. Additionally, the supply components needed for the electron source complex of the accelerator and the means of transmitting electrical power through the emerging voltage barrier are included in the HV system.

The safety system presented in chapter 8 is concerned with ensuring personal safety during the operation of the LFXT prototype, including radiation protection as well as protection from the acceleration voltage and mechanical protection from the rapidly rotating target. In chapter 9, the control system is presented, gathering all components on the hardware and software side needed for controlling and monitoring the sensors and actuators of the LFXT prototype.



## 5 Focal track temperature monitoring system

In the following the focal track temperature monitoring system is presented. The purpose of this system is to measure the temperature within the focal track and focal spot on the target of the LFXT prototype during operation for reasons of machine safety and for characterisation of the thermal behaviour of the LFXT prototype. For that, three infrared (IR) pyrometers and an IR camera in conjunction with an optical system are used. At first the requirements for the system will be presented, followed by the setup of the pyrometers for point measurements. Next, the IR camera and the design of the optical system are discussed and finally, an overview of the whole system will be given.

### 5.1 Requirements

As stated in chapter 4, the main requirement the focal track temperature monitoring system needs to fulfil is to measure the temperature of the target surface in the area heated by the electron beam. According to simulations, the temperature can rise to more than 2000 °C in the focal spot when heated by an electron beam of 90 kW power focused into a focal spot of 50 µm width by 20 mm length. Therefore, the temperature range of the system needs to be wide enough to accommodate the range of possible target temperatures, especially at the upper limit, with a sufficient buffer. Additionally, it is desirable to be able to assess the spatial temperature distribution in the focal spot. For this, a resolution of about 5 µm is required, corresponding to 10 data points across the width of the focal spot.

Several boundary conditions limit the design of the focal track temperature monitoring system. First of all, only non-contact measurements are possible due to the rotating target and the vacuum requirements. Next, it is highly preferable to position the sensors outside of the vacuum chamber, as thereby conventional devices can be used instead of specialised ones fit for UHV conditions. Integration of the sensors and the required viewports into the vacuum chamber is rendered challenging due to the multitude of other components present, e.g. the magnetic optics, the integrated circuits of the cooling systems, and the X-ray window. Additionally, the backscattering of electrons produces a significant heat load on components facing the focal spot, which needs to be considered [42]. Last, X-ray radiation can heavily damage electrical devices and therefore, no complex electrical components (e.g. all components containing semiconductors) may be positioned within a direct line of sight to the focal spot of the LFXT prototype [46]. Even if not positioned in the primary X-ray beam, potentially sensitive devices should be shielded from stray and scattered radiation.

### 5.2 Point measurement of surface temperature

The conventional option for performing non-contact spot measurements of surface temperature is by using so-called IR pyrometers [47]. In principle, an IR pyrometer measures the fluence of IR light being emitted from the surface of an object and infers, according to Planck's law, the temperature of the object from it [48, 49]. Planck's law gives the spectral intensity of IR light emitted by an ideal emitter, a so-called black body, at a given temperature [50]. To correct for the differing emission efficiency of a real object, the spectral emissivity, defined as the ratio between the IR fluence emitted by the object and that of a black body at the same wavelength and temperature, is required [48, 51]. As an equation, Planck's law as applied to IR measurements can be written as

$$I(\lambda, T) \propto \frac{\epsilon(\lambda, T)}{\lambda^5} \cdot \frac{1}{\exp(\frac{hc}{\lambda k_B T}) - 1} \quad (5.1)$$

with the IR fluence emitted by an object  $I(\lambda, T)$  dependant on wavelength  $\lambda$  and temperature  $T$ , the emissivity  $\epsilon(\lambda, T)$ , the Planck constant  $h$ , the speed of light  $c$  and the Boltzmann constant  $k_B$  [50].

Different types of IR pyrometers exist, depending on their temperature range, the size of their measurement spot, the wavelength they are sensitive to, and the measuring principle they rely on. Concerning measuring principles, the two main types that can be distinguished are single-wavelength measurements and two-wavelength measurements. In single-wavelength measurements, the IR fluence in a narrow band around a specific wavelength is analysed, and the temperature is directly calculated from the measured intensity according to eq. 5.1. In two-wavelength measurements, as the name suggests, the IR fluence is analysed around two specific wavelengths, and the temperature is inferred from the ratio of the measured intensities [52]. Pyrometers operating on this ratio principle are less prone to measuring errors due to attenuation or objects not completely filling the measurement spot, as is the case for the focal spot of the LFXT prototype. Additionally, ratio pyrometers are more robust against imprecise emissivity values as long as the ratio between the emissivities at the two wavelengths can be assumed to be independent of temperature [52]. Due to these advantages and the improved flexibility of getting the two single-wavelength temperatures in addition to the ratio temperature, it was decided to use pyrometers based on the two-wavelength principle for usage with the LFXT prototype.

When deciding on the wavelengths the pyrometers should be sensitive to, the material of the target surface needs to be considered to maximise emissivity. If the measured object has a higher emissivity at the wavelength the pyrometer is sensitive to, more IR intensity is gathered by the sensor and the statistical measurement error is decreased. Generally, metallic objects, including the tungsten surface of the LFXT prototype, exhibit low emissivity, especially towards longer wavelengths [53, 51]. Therefore, the measurement wavelengths of the used two-wavelength pyrometers should be as short as possible to maximise precision.

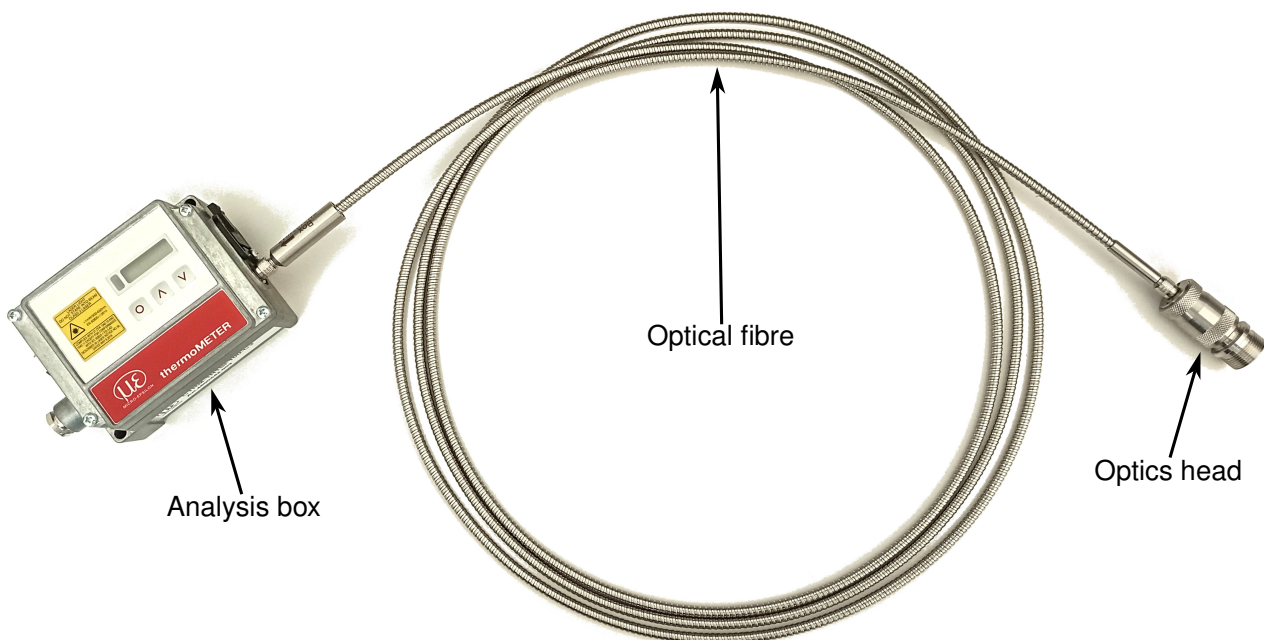


**Figure 5.1** Photograph of an exemplary pyrometer used with the LFXT prototype. The pyrometer consists of the analysis box containing the electronics, the optics head containing a lens system for adjusting the point of measurement, and the optical fibre connecting both.

For the LFXT prototype, it was decided that the temperature should be measured in two spots: The focal spot exhibiting the maximum temperature of the surface and the opposite side of the focal track where the median temperature of the target surface is present. In the focal spot, a small measurement spot and a wide temperature range with a maximum temperature of more than 2000 °C is required, while requirements on the focal track measurement are more relaxed. However, no pyrometer could be found on

the market exhibiting a sufficiently wide temperature range for the focal spot measurement, and therefore, it was decided to use two pyrometers with differing temperature ranges.

Ultimately, three pyrometers specialised for high-temperature measurements of metals manufactured by the company Micro-Epsilon (Micro-Epsilon Messtechnik GmbH & Co. KG, Ortenburg, Germany) were chosen. The chosen pyrometers utilise the two-wavelength principle and consist of an optics head containing a lens system for adjusting the measurement spot, an optical fibre for guiding the IR light gathered by the head, and an analysis box containing the evaluation electronics as presented in fig. 5.1. The optics head does not contain any electrical components and can, therefore, be placed in direct line of sight to the focal spot without risking damage, while the analysis box can be positioned away from the primary beam and shielded against stray and scattered radiation.

Name	Temperature range	Wavelengths	Spot size
Pyrometer 1	275 °C - 1000 °C	1.45 $\mu\text{m}$ - 1.75 $\mu\text{m}$	7.9 mm
Pyrometer 2	1000 °C - 3000 °C	0.8 $\mu\text{m}$ - 1.1 $\mu\text{m}$	3.0 mm
Pyrometer 3	400 °C - 1500 °C	1.45 $\mu\text{m}$ - 1.75 $\mu\text{m}$	6.0 mm

**Table 5.1** Properties of pyrometers

In tab. 5.1 the properties of the used pyrometers are presented, where the two pyrometers directed at the focal spot are termed pyrometer 1 and 2, and the pyrometer aimed at the focal track opposite of the focal spot is termed pyrometer 3. All three pyrometers are sensitive to wavelengths in the near IR range, optimising precision, but differ in their temperature ranges and minimal spot sizes. By combining the temperature ranges of pyrometers 1 and 2, a range of 275 °C to 3000 °C is achieved for the measurement of focal spot temperature, meeting the demands of the range of possible temperatures.

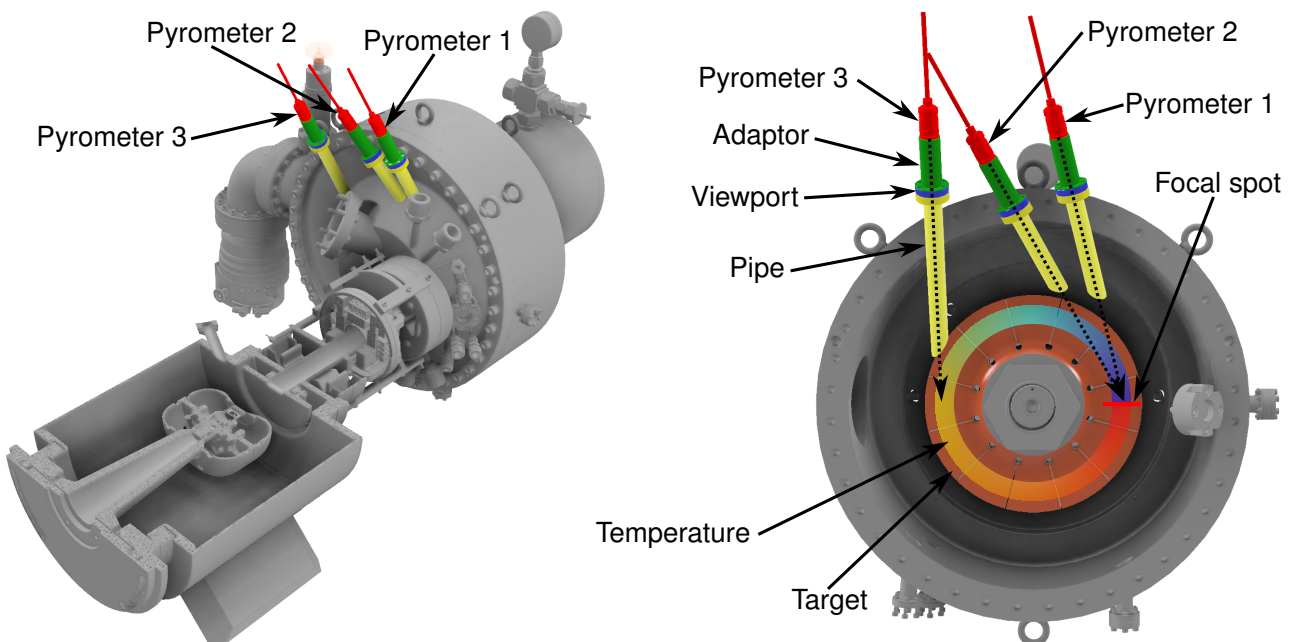


**Figure 5.2** CAD rendering of the setup for point measurements using three pyrometers. On the left, an overview of the vacuum chamber of the LFXT prototype in which the pyrometers are highlighted is depicted for orientation. On the right, a view in the direction of the electron beam onto the target is presented with the cover of the vacuum chamber removed (except for the pyrometer pipes and the primary beam exit for orientation). The three pyrometers, the adaptors for fixation, the vacuum viewports, and the respective pipes are highlighted. For each pyrometer, the respective direction of view onto the target is marked. The target is highlighted, and on the target, the focal spot and the temperature gradient of the focal track are exemplary signified.

In fig. 5.2, the setup of the pyrometers as connected to the vacuum chamber of the LFXT prototype is depicted. Using custom adaptors, the pyrometers are fixed to the ends of pipes protruding from the vacuum

chamber. The distance from the pyrometer heads to the respective measurement spots is the same for all three pyrometers and adjusted such that the smallest possible measurement spots are achieved. Between the ends of the pipes and the adaptors, a viewport acts as a vacuum barrier and seals the chamber. The window within the viewport is made from industrial Sapphire for its high transmittance in the near IR range.

### 5.3 Measurement of temperature distribution in focal spot

For measuring the temperature distribution of a surface, IR cameras can be used. An IR camera contains a pixelated sensor, of which each pixel functions similarly to a pyrometer discussed before in that it infers the temperature of the measured object from the IR light emitted by it. In general, IR cameras can be categorised into cooled and uncooled cameras, with cooled cameras achieving a significantly higher accuracy but requiring a cryogenic cooling system and being substantially more expensive, and uncooled cameras being less accurate but cheaper and easier to use [54]. For the measurement of the temperature distribution on the target surface of the LFXT prototype, accuracy in the range offered by cooled IR cameras was not necessary and, therefore, it was decided to use an uncooled IR camera.

Other characteristic parameters of an IR camera influencing the choice are the frame rate, resolution, and field-of-view (FOV) achieved by it and, similar to pyrometers, the range of wavelengths it is sensitive to and its temperature range. As the tungsten surface of the target emits for the greater part light in the near IR regime, the camera needs to be sensitive to short wavelengths of about 1  $\mu\text{m}$  to maximise accuracy. The temperature range should accommodate the range of possible temperatures of the focal spot to the highest extent possible, and the resolution of the system should reach down to about 5  $\mu\text{m}$  on the target surface. The frame rate is desired to be high, enabling the visualisation of quick temperature changes when toggling the electron beam, and the FOV should be large.

During the search for a suitable IR camera, no commercially available solution achieving a sufficiently high resolution or wide temperature range could be found. Therefore, it was decided to use an IR camera fitting the temperature range as closely as possible and combine it with a dedicated optical setup as presented in fig. 5.3. A specialised high-temperature camera produced by the company Micro-Epsilon (Micro-Epsilon Messtechnik GmbH & Co. KG, Ortenburg, Germany) for the metalworking industry was chosen, and the optical system was designed with respect to it. The chosen IR camera has a temperature range from 450  $^{\circ}\text{C}$  to 1800  $^{\circ}\text{C}$  and a spectral range from 0.85  $\mu\text{m}$  to 1.1  $\mu\text{m}$ . The maximum resolution is approximately 55  $\mu\text{m}$  at a distance of 90 mm to the object, and the maximum frame rate is up to 1 kHz.

For the optical system, the light path had to be defined first, considering the spatial constraints posed by components like the electron optics or the pyrometer pipes. A perpendicular line of sight onto the focal spot, although preferable, was not possible. Instead, a shallow angle from the top, as presented on the left in fig. 5.3, had to be chosen. Additionally, the Rayleigh criterion limits the highest achievable resolution [55]. The Rayleigh criterion defines the highest distance two details can be apart to be resolved  $\Delta x_{max}$  of an optical system in the diffraction-limited case as

$$\Delta x_{max} = 1.22\lambda \cdot \frac{g}{D} \quad (5.2)$$

with the wavelength  $\lambda$ , the distance between the object and the objective lens  $g$ , and the size of the limiting aperture  $D$  [56]. The limiting aperture can either be the objective lens itself or, for example, a pipe limiting the maximum aperture angle  $\alpha$  defined by

$$\tan\left(\frac{\alpha}{2}\right) = \frac{D}{2g} \quad (5.3)$$

In conventional high-resolution systems, e.g. optical microscopes, a large aperture angle is achieved by positioning the objective lens close to the object. However, in the case of the LFXT prototype, this would lead to a substantial heat load on the lens due to backscattered electrons from the focal spot. Instead, the objective lens needs to be positioned further away from the focal spot and, therefore, needs to be of a larger diameter  $D$  to fulfil the Rayleigh criterion. Within the vacuum chamber, not enough space

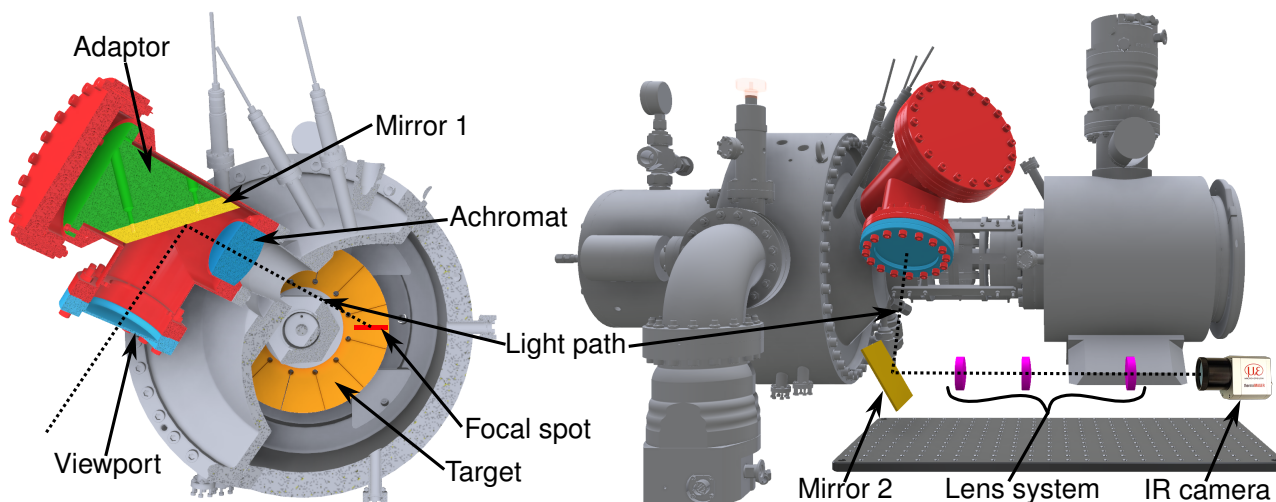


**Figure 5.3** CAD rendering of the optical setup for the measurement of focal spot temperature distribution using an IR camera. On the left, the initial part of the optical system within the vacuum chamber is presented, comprising the target with an exemplary focal spot and the so-called mirror holder drawn in red housing an achromat, a specialised mirror fixed to an adaptor, and the viewport as a vacuum barrier. On the right, the atmospheric part is shown with a second mirror, an exemplary lens system, and the IR camera, all mounted on an optical breadboard. The light path through the optical system, starting at the focal spot and ending at the IR camera, is signified on both sides.

was available to fit a sufficiently large pipe, and instead, a cone-like pipe pointed at the focal spot was used, minimising the required space. The objective lens is positioned at the end of the cone-like pipe at a distance of 230 mm from the focal spot, and the final diameter of the pipe acting as the aperture is 66 mm. Together with the longest wavelength the IR camera is sensitive to of  $1.1 \mu\text{m}$ , this allows for a theoretical resolution of about  $4.7 \mu\text{m}$  taking only the Rayleigh criterion into account.

Following the objective lens, labelled "Achromat" in fig. 5.3, a custom-built mirror made from copper with a highly reflective gold surface deflects the IR beam downwards. Both the objective lens and the mirror, which are positioned using an adaptor block, are contained within the so-called mirror holder, which is an annex of the vacuum chamber. The deflected IR beam exits the mirror holder through a 100 mm diameter viewport made from Sapphire for its high transmittance.

After leaving the vacuum chamber, the IR beam is again deflected by a second mirror into a horizontal path parallel to the longitudinal axis of the vacuum chamber as shown on the right in fig. 5.3. At the end of the horizontal stretch, the IR camera is positioned, and between it and the second mirror, a lens system is installed. All components outside the vacuum chamber are built onto an optical breadboard for straightforward positioning. The lenses used in the optical system, including the objective lens, need to be achromatic lenses, also called achromats. An achromatic lens conventionally consists of two or three separate lenses made from materials with different refractive indices combined together and is able to mitigate, but not fully prevent, chromatic and spherical aberrations that would otherwise deteriorate the resulting image. The required magnification of about 11 is mainly facilitated by the lens system installed on the breadboard next to the vacuum chamber, while the purpose of the achromat within the mirror holder is to gather the IR light emanating from the focal spot and compress it to a narrow beam that can be guided to the lens system. Additionally, a compressed narrow beam allows the usage of smaller lenses without the loss of numerical aperture.

The usage of the two mirrors has not only the advantage of bending the light path into a horizontal line, rendering the positioning of the optical components less complex, but additionally removes the IR camera from the direct line of sight to the focal spot and, therefore, the primary X-ray beam. On the optical breadboard, the camera can be shielded from scattered and stray radiation, effectively protecting the sensitive electrical components inside. The only exception is the lens, as no shielding can be applied in front of it.

In addition to damage from X-ray radiation, the IR camera could be damaged by too intense IR light as emitted by an object hotter than the maximum temperature the camera is meant for. To protect the camera against damage from IR radiation, a flag mechanism already integrated with the camera can be repurposed. Under normal operation, the flag mechanism is used to zero the camera signal as the type of sensor used within the IR camera suffers from a drifting signal, which would lead to wrong measurements if not corrected. For the correction, the flag mechanism is triggered every couple of seconds and shields the sensor for a short duration from IR light, during which the signal the unexposed sensor produces is measured and then used to correct for signal drift. Using an external digital signal to the camera, the flag mechanism can be forced to remain active, effectively shielding the sensor for an undefined duration from IR radiation. This signal can be provided by the pyrometers presented in sec. 5.2 using a specialised process interface, over which the pyrometer emits a signal if the measured temperature is above a specified threshold. That way, the pyrometer will send a signal triggering the flag mechanism of the camera as soon as the focal spot temperature is above a threshold and will only release the flag mechanism as soon as the temperature decreases below the threshold, effectively protecting the IR camera from potential damage.

## 5.4 Overview and discussion

As presented, the usage of two IR pyrometers pointed at the focal spot and one at the focal track opposite the focal spot of the LFXT prototype allows the point measurement of maximum and mean target surface temperature. This fulfils the primary requirement for which the focal track temperature monitoring system is meant. The used pyrometers are split into an optics head without any electronics and an analysis box connected via an optical fibre, allowing the electronics to be removed from the primary X-ray beam and shielded against scattered and stray radiation. The pyrometers are based on the two-wavelength principle, mitigating the influence of potential inaccuracies in the emissivity of the target surface and allowing for temperature measurements even if the focal spot is not filling the measurement spot. It was attempted to experimentally determine the temperature dependant emissivity of the target surface by heating a small test object made from the same material and with the same processes as the real target to known temperatures and calibrating the emissivity of the pyrometers such that the correct temperature is measured. Due to the lack of a suitable vacuum oven, the experiment was conducted with a conventional high-temperature oven. However, due to the oxidation of the surface, no usable results could be achieved, and it was decided to use tabulated values instead, as the complexity of a more elaborate experimental approach would have been disproportionate to the potential gain. This leads to uncertainties in the absolute temperature measurements that are extremely challenging to assess due to the unknown emissive properties of the target surface. These uncertainties can be handled by applying a sufficient safety margin to the maximum tolerable temperatures of the target and by using only relative assessments of temperature for experimental statements, e.g. comparing the temperatures measured for two different target velocities to each other instead of viewing them individually as absolute values.

For measuring the temperature distribution in the focal spot of the LFXT prototype, a system consisting of a specialised IR camera and a complex optical system was presented. Within a mirror holder, an objective lens gathering IR light emanating from the focal spot and a custom-made metallic mirror deflecting the IR beam are incorporated. The deflected IR beam is intercepted by a second mirror and guided into a horizontal path through a lens system. The lens system magnifies the focal spot by a factor of about 11, increasing the effective resolution of the IR camera to about  $5\ \mu\text{m}$ . By combining information gathered by the pyrometers with the camera image, the quantitative temperature distribution can be measured. Above, the basic setup for the optical system is presented. However, due to time restrictions and sub-projects with a higher priority, the detailed design of the optical system, including the choice of lenses, was not finished. A working lens setup remains to be designed, and its validity needs to be tested within simulations, especially regarding chromatic and spherical aberrations.

Overall, the focal track temperature monitoring system in its present state is able to quantitatively measure the temperature in the focal spot and on the opposite side of the focal track over the full range of possible temperatures. The spatial temperature distribution within the focal spot can be visualised using

the IR camera and the custom-made metallic mirror, although only with a substantially inferior resolution in comparison to the planned resolution of 5  $\mu\text{m}$ . With this, it is possible to monitor the temperature of the target for safety concerns and potentially validate the heat capacity limit. In a later work, the optical system for the IR camera could be completed. The IR pyrometers have been installed and tested, although not yet at higher temperatures. The IR camera has been tested by aiming through the primary beam exit made of diamond, but to date, not in conjunction with the metallic mirror due to practical reasons.



## 6 Cooling system

In the following chapter, the cooling system of the LFXT prototype is presented. The purpose of this system is to dissipate heat produced by the accelerated electron beam due to the inefficient conversion process into X-ray photons and the loss of power of the electric motor driving the target. The system can be split into three sections according to their functionality: The section cooling the vacuum chamber and the target, the section cooling the electric motor, and the section buffering and finally dissipating the heat. First, the requirements the system needs to fulfil and the constraints posed on it will be presented, followed by a short introduction to the theoretical background of heat and fluid transport. Next, the setup of the three sections of the cooling system is presented. In the last part of this chapter, an overview of the complete cooling system will be given, and its current state will be discussed. The cooling system has been developed jointly with another work within the scope of the overarching project and is, therefore, also described by Dimroth A. [21].

### 6.1 Requirements

As mentioned in chapter 4, the purpose of the cooling system is to remove excess heat from the LFXT prototype, including that produced by the accelerated electron beam in the target, by backscattered electrons in the vacuum chamber and by power loss in the electric motor propelling the target. About 99 % of the power within a beam of accelerated electrons impinging on a metallic target is converted into heat instead of X-ray photons [41]. A significant amount of that heating power is not deposited within the target itself but transported by scattered electrons into the half-space in front of the target, an effect called backscattering that is dependent on the electron energy and the target material [57, 58]. For the specific case of the LFXT prototype with a tungsten target and an assumed electron energy of 300 keV, 61.2 % of the heating power remains within the target, and the remaining 38.8 % are distributed within the vacuum chamber according to Monte-Carlo simulations [22]. At the maximum power of 90 kW the LFXT prototype is designed for this corresponds to a heating power of about 55 kW in the target and about 35 kW in the surrounding vacuum chamber. The only part of the vacuum chamber receiving a relevant amount of heating power is the so-called lid together with the primary beam exit, as it spans nearly the full half-space in front of the target, especially in the area closest to the focal spot. In fig. 6.1, the backscattering of electrons is illustrated together with the results of combined Monte-Carlo and finite element analysis (FEA) simulations depicting the temperature distribution on the inner surface of the lid of the vacuum chamber without cooling after irradiating with a primary electron beam power of 90 kW for 20 s, which is the maximum pulse duration the LFXT prototype is designed for. As presented in fig. 6.1, the heating power is concentrated mainly around the entry of the electron beam pipe and the primary beam exit, resulting in a maximum temperature of nearly 700 °C [22]. Such high temperatures would damage sensitive components of the machine directly heated by backscattered electrons, like the primary beam exit that can only bear up to 250 °C before the vacuum sealing is lost [59], and ones that are adjacent to hot surfaces, like the quadrupole magnets whose insulation would melt. Additionally, high temperatures would lead to a severe deterioration of the vacuum within the chamber, potentially damaging parts of the machine, e.g. the thermionic cathode. Therefore, the critical parts of the vacuum chamber close to the focal spot need to be actively cooled to limit the temperature increase.

The target is designed to withstand the significant amount of heating power remaining within it during the pulse duration and buffer it. After the pulse, however, the heat energy needs to be removed from the target during the cooling phase of 20 min before being able to begin with the next cycle. Heat transport away from the target is based on the combination of heat radiation shifting the heat onto the vacuum chamber

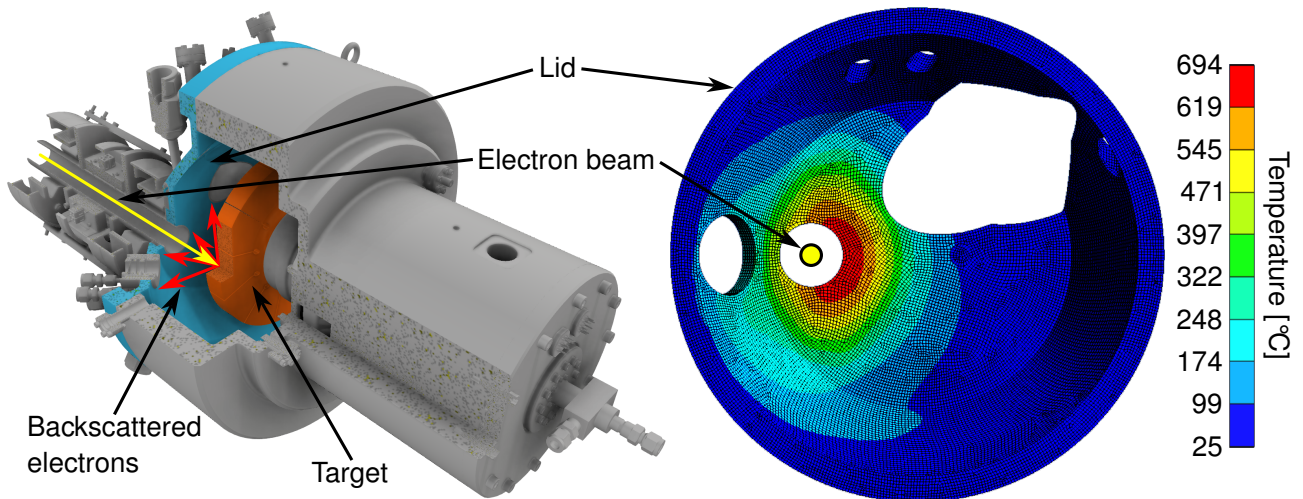


**Figure 6.1** Deposition of heat on the inner surface of the vacuum chamber by backscattered electrons. On the left side, a CAD rendering of the relevant parts of the vacuum chamber is presented with the target highlighted in orange and the lid of the vacuum chamber in blue. The primary electron beam hitting the target within the focal spot is denoted in yellow, and the resulting backscattered electrons originating from the focal spot and impinging on the lid are exemplarily drawn in red. On the right, simulated results for the temperature distribution without cooling on the inner surface of the lid after 20 s of activity with a 90 kW electron beam are presented. *Results of temperature simulations are adapted from Dimroth A. [21]*

and heat conduction through the target, rotor and bearing into the steady axis. To dissipate the heat from the steady axis within the cooling phase lasting 20 min, active cooling is required as only heat conduction through the steady axis would not be sufficient [42]. Additionally, the maximum temperature of the liquid metal bearing is limited due to fears the used liquid metal alloy (called Galinstan) could inflict corrosion damage on the rotor and axis at high temperatures as shown for pure Gallium in combination with different metals.

The electric motor propelling the target is neither directly nor indirectly heated by the electron beam. Instead, it accumulates heat due to a not ideal efficiency of the electromagnetic coils and due to eddy currents within the separation tube constituting the vacuum barrier between the stator and the rotor [21]. The nominal power of the motor is 7.85 kW at an efficiency of 73.7%, meaning that about 2 kW of heating power is produced that needs to be cooled [60]. The maximum temperature of the motor is limited to about 80°C due to the cable insulation within the coils. An additional requirement posed on the cooling of the motor is that only an electrically non-conductive cooling medium may be used in order to not short-circuit the motor.

In addition to the requirements for cooling the mentioned components, the complete cooling system needs to be electrically insulated from the ground sufficiently for 150 kV of HV. This is necessary as the vacuum chamber of the LFXT prototype and, therefore, all components not insulated from it in a manner suitable to HV, is charged with an electrical potential of up to 150 kV during operation as explained further in chapter 7.

## 6.2 Theoretical background

In accordance with the first and second laws of thermodynamics, heat can neither be erased nor transformed into a different type of energy to a greater extent [61, 62]. Instead, heat flows from the hotter to the cooler medium until thermal equilibrium is reached due to a combination of heat conduction and heat radiation. Heat radiation is the process by which an object with a temperature above absolute zero emits energy in the form of electromagnetic waves, e.g. photons. The amount of energy emitted by an ideal emitter, a so-called black body, of temperature  $T$  and surface area  $A$  is given by the Stefan-Boltzmann law as

$$P = \sigma AT^4 \quad (6.1)$$

where  $P$  is the emitted power and  $\sigma$  is the Stefan-Boltzmann constant [63]. Heat conduction describes the transport of heat through a medium or the boundary between two media in contact and can, in its most general case, be represented by Fourier's law of thermal conduction as

$$\vec{q}(\vec{r}) = -\lambda \cdot \vec{\nabla}T(\vec{r}) \quad (6.2)$$

where  $\vec{q}(\vec{r})$  is the vectorial heat flux density at position  $\vec{r}$  dependant on the thermal conductivity  $\lambda$  of the material and the gradient of the temperature within the material denoted by  $\vec{\nabla}T(\vec{r})$  [64]. In the case of heat conduction through the boundary between two media, e.g. a flow of cooling fluid along a hot solid surface, Fourier's law can be expressed in a one-dimensional form for conduction only perpendicular through the boundary surface as

$$\dot{q} = \alpha(T_W - T_F) \quad (6.3)$$

with the heat transfer coefficient  $\alpha$  and the temperature difference between the hot surface  $T_W$ , e.g. a heated wall, and the cooler medium  $T_F$ , e.g. a cooling fluid [64]. Contained within the heat transfer coefficient  $\alpha$  are all parameters defining the amount of heat transferred between the two media, including their physical parameters like thermal conductivity and heat capacity, as well as other properties, such as to which extent the flow is turbulent. Therefore, a multitude of different cases need to be distinguished when calculating the heat transfer coefficient, and often, only empirical approximation equations are available [65].

In the case of a cooling liquid, e.g. water, being actively pumped through dedicated conduits within a heated component, the most important parameters are the volumetric flow rate and the turbulence of the flow. The Reynolds number  $Re$  is a dimensionless measure for the extent to which a flow is either laminar or turbulent and, in general, defined by

$$Re = \frac{\omega L}{\nu} \quad (6.4)$$

with the kinematic viscosity of the fluid  $\nu$ , the characteristic flow velocity  $\omega$ , and the characteristic length  $L$  [64]. For Reynolds numbers below 2320, pure laminar flow, and for Reynolds numbers above 8000, pure turbulent flow can be assumed, while in the region between both conditions contribute [66]. In laminar flows, only the boundary layer is in contact with the walls of the conduits and can, therefore, absorb heat. In turbulent flows, all of the cooling fluid comes into contact with the walls. Due to this, the heat transfer coefficient  $\alpha$  is higher and turbulent flows are, in most cases, to be preferred for cooling applications.

However, a high Reynolds number and, therefore, a turbulent flow also increases the pressure drop along the cooling cycle, including the afferent and efferent supply pipes. This pressure drop needs to be counterbalanced by the pump, forcing the cooling fluid through the cycle. The pressure drop  $\Delta p$  within a pipe of circular cross-section, e.g. a typical supply pipe, can be calculated as

$$\Delta p = \zeta \cdot \frac{l\rho u^2}{2d} \quad (6.5)$$

with the drag coefficient  $\zeta$ , the length  $l$  and inner diameter  $d$  of the pipe, the density of the cooling liquid  $\rho$ , and the flow velocity  $u$  [66]. The drag coefficient  $\zeta$  is dependent on the turbulence of the flow and can, assuming a hydro-dynamically smooth inner surface, be approximated from [66]

$$\zeta = \begin{cases} 0.3164 \cdot Re^{-\frac{1}{4}} & 3000 \leq Re \leq 10^4 \\ (1.8 \cdot \ln(Re) - 1.5)^{-2} & 10^4 \leq Re \leq 10^6 \end{cases} \quad (6.6)$$

For lower Reynolds numbers, a separate equation for laminar conditions needs to be applied, and for Reynolds numbers above  $10^6$ , more elaborate approaches are required.

### 6.3 Cooling of target and axis

The greater fraction of the heating power produced by the electron beam remains within the target and is buffered over the pulse duration. Within a single 20 s pulse, about 1.1 MJ of heat energy is accumulated that needs to be dissipated over the 20 min long cooling phase. A fraction of the heat energy is transported from the target to the vacuum chamber via heat radiation. However, for a conservative case under the assumption of heat radiation having no influence on target heat dissipation, the minimal cooling power required to remove the accumulated energy within the cooling phase is about 0.92 kW.

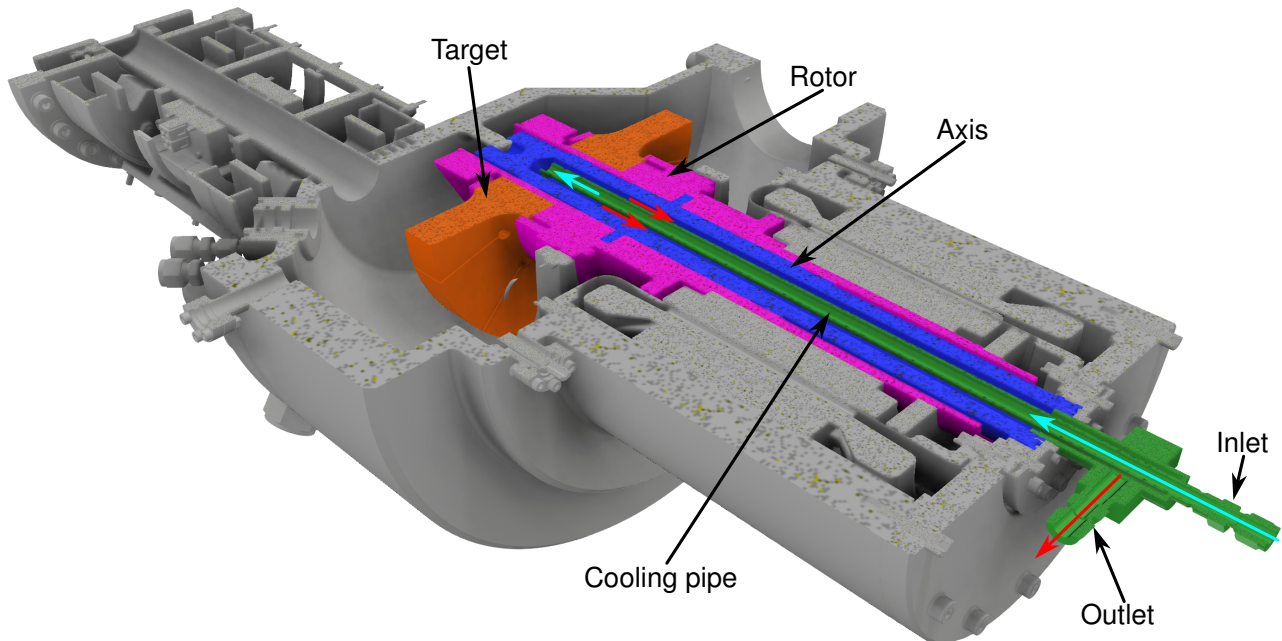


**Figure 6.2** Horizontal cut through the CAD model of the vacuum chamber depicting the cooling cycle within the steady axis. The Target is visualised in orange, the rotor in violet, the steady axis in blue and the cooling pipe within the axis in green. Additionally, the flow of water is indicated as coloured arrows, with blue signifying cold water flowing in and red hot water flowing out.

Within the target and rotor, no direct cooling in the form of, for example, a cooling cycle traversed by water is possible as both parts rotate rapidly, and additionally, the mechanical stability of the parts would be impaired. Instead, the heat front travels from its origin in the focal track through the bulk material of the target and the rotor into the steady axis. Within the steady axis, a cooling cycle can be integrated, as presented in fig. 6.2. For the cooling cycle, the steady axis is manufactured hollow with a blind hole and a cooling pipe is inserted, resulting in a coaxial cycle [21]. As a cooling fluid, deionised water was chosen for its availability and good cooling capabilities. Cold water is pumped into the steady axis through the inside of the cooling pipe and flows back out through the gap between the cooling pipe and the inner surface of the axis, taking up heat. By defining the direction of flow as described and additionally presented in fig. 6.2, the water temperature at the tip of the cooling cycle is minimised and, therefore, the heat uptake is maximised in the vicinity of the target according to eq. 6.3.

In order to achieve the required cooling power and limit the water temperature to below 80 °C with a sufficient margin of safety, a minimal volume flow rate of about 2.4 m<sup>3</sup>/h is required, for which a pressure drop of about 2 bar within the cycle is to be expected [67]. For selecting a suitable water pump, the pressure drop within the supply pipes, depending on their length and inner diameter, also needs to be taken into account. The water pumps for the cooling system are positioned outside the X-ray cabinet, and therefore, the supply pipes need to have a combined length of about 13 m. For the water supply, rubber pipes with a smooth inner surface and an inner diameter of 19.3 mm were chosen. With the density of water of 1000 kg/m<sup>3</sup> and its dynamic viscosity of  $797 \times 10^{-6}$  sPa at 30 °C, the Reynolds number within the pipes is about  $5.8 \times 10^4$  according to eq. 6.4. From the Reynolds number and the length of the pipes, the

additional pressure drop produced by the supply pipes can be calculated using eq. 6.5 and 6.6, resulting in  $\Delta p = 0.06$  bar. In order to accommodate for the pressure drop produced by the connections of the pipes to the pump and the cooling pipe within the steady axis and by bends in the pipe, an additional pressure drop of 0.5 bar is assumed. In sum, the water pump for the target cooling cycle, therefore, needs to provide at least a pressure of about 2.6 bar at a volume flow rate of  $2.4 \text{ m}^3/\text{h}$ . In the end, a high-performance multi-staged pump manufactured by the company KSB (KSB SE & Co. KGaA, Frankenthal, Germany) was chosen that produces a pressure of about 4.5 bar at the required flow rate, leaving a sufficient margin for safety [68].

## 6.4 Cooling of vacuum chamber

Due to the backscattering of electrons from the focal spot, a heating power of about 35 kW is produced on the inside of the lid of the vacuum chamber as presented in sec. 6.1. The heating power is not distributed uniformly but rather focused around the entry point of the electron beam pipe and the primary beam exit, including the lateral surface of the lid next to it [42]. Without cooling, these spots would reach critical temperatures within a single pulse. Therefore, active cooling is required to limit the maximum temperatures already during the pulse and remove the remaining heat in the succeeding cooling phase.

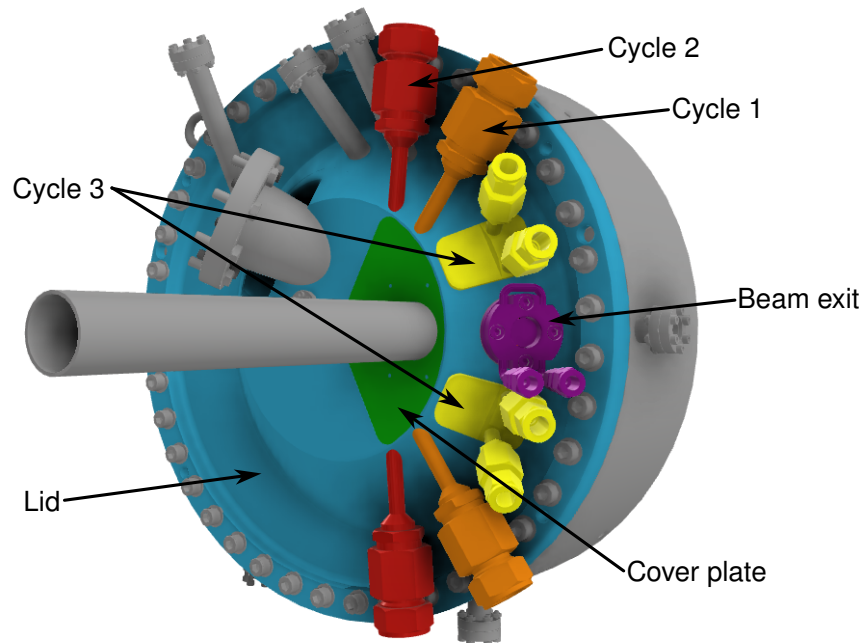


**Figure 6.3** Overview of the cooling cycles of the vacuum chamber. The lid of the vacuum chamber is drawn in blue and the primary beam exit in purple. The cooling cycle integrated into the lateral surface of the lid, denoted cycle 3, is depicted in yellow. The cover plate above the cooling cycles integrated around the entry of the electron beam pipe, called cycles 1 and 2, is represented in green, and the connectors of cycles 1 and 2 are shown in orange and red, respectively.

As the heating power distribution on the inside of the lid of the vacuum chamber is non-uniform, it was decided to split the cooling system into four separate cycles as presented in fig. 6.3. Each cooling cycle is adjusted to the required cooling power in its area and supplied by its own water pump. Cycle 1 is meant to cool the area directly around the entry point of the electron beam pipe, as well as the wall of the beam pipe itself and is burdened with the highest heating power of all cycles. The area on the frontal surface of the lid further away from the electron beam pipe is cooled by cycle 2. On the lateral surface of the cone-like part of the lid close to the primary beam exit, cycle 3 is positioned. Cycle 3 is split into two symmetric parts that are connected in parallel to a single water pump. The fourth cooling cycle is integrated into the beam

exit and removes heat both from the beam window itself and from the vacuum flange integrated into the chamber.

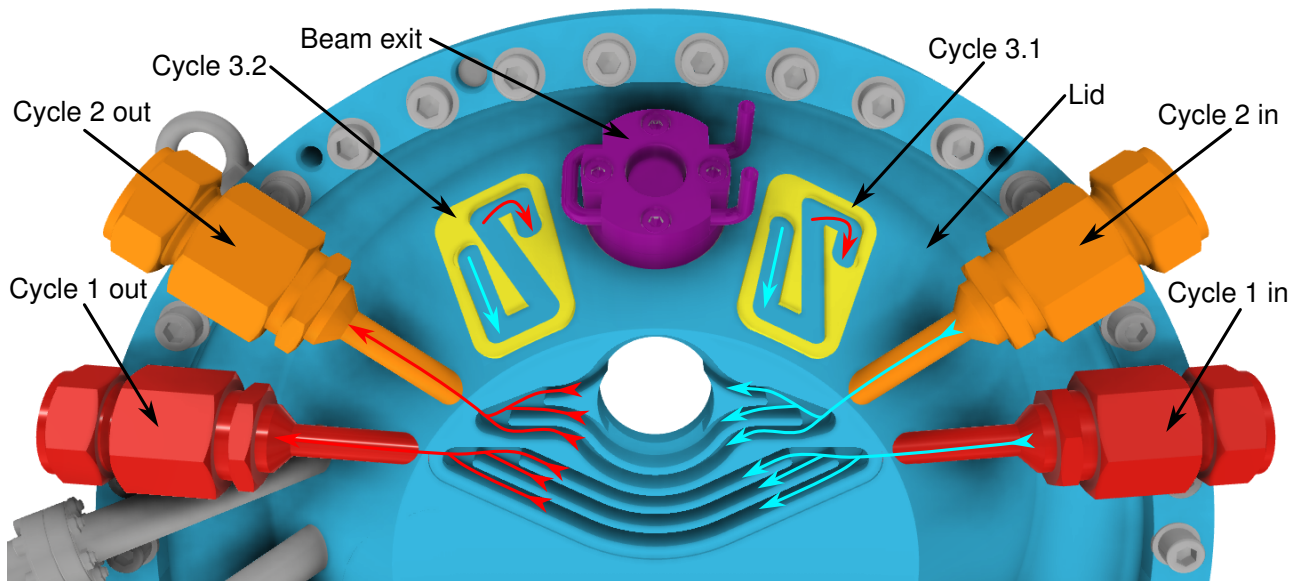


**Figure 6.4** Detailed depiction of the three cooling cycles integrated into the lid of the vacuum chamber. The different components are coloured equal to fig. 6.3, and the depiction is rotated by 90° counterclockwise such that the bottom side of the vacuum chamber is on the right. The cooling cycles are cut open such that the channels within are visible, and the direction of flow within the cycles is signified, with blue representing cold water flowing in and red representing hot water flowing out.

In fig. 6.4, the three cycles directly integrated with the lid of the vacuum chamber are presented in detail. Cycles 1 and 2 are designed in conventional rib geometry with 3 channels each and geometrically adjusted in order to minimise the pressure drop. In cycle 1, the water flows directly along the wall of the electron beam pipe, partly constituting the wall of two of the cooling channels. The cooling channels of cycles 1 and 2 are milled directly into the lid of the vacuum chamber and closed off by a metal plate welded on top. For both cycles, the direction of flow is upward in order to avoid pumping against the natural convection of hot water. The two symmetric parts of cycle 3 are designed as single channels within a component welded onto the vacuum chamber, such that the cooling water flows directly over the surface of the vacuum chamber. The two sub-cycles constituting cycle 3 are connected in parallel by external piping.

The cooling cycle of the primary beam exit is presented in fig. 6.5. The beam exit consists of an industrial diamond window integrated into a conventional vacuum flange for a sealed connection to the vacuum chamber [22]. The window is made from diamond for its high temperature resistance and, more importantly, its high heat conductivity. On top of the vacuum flange, a copper cooling element with a single integrated cooling channel is placed. The heat from the vacuum chamber and the diamond window travels through the vacuum flange and into the cooling element, from where it can be removed by a flow of water through the cooling channel.

Cycle	Flow rate [m <sup>3</sup> /h]	Pipe diameter [mm]	Pressure drop [bar]
1	7.2	25.4	10.0
2	2.5	25.4	2.5
3	1.4	12.7	2.0
Beam exit	0.15	12.7	2.0

**Table 6.1** Minimum flow rate, inner pipe diameter and expected pressure drop of cooling cycles [67, 21]

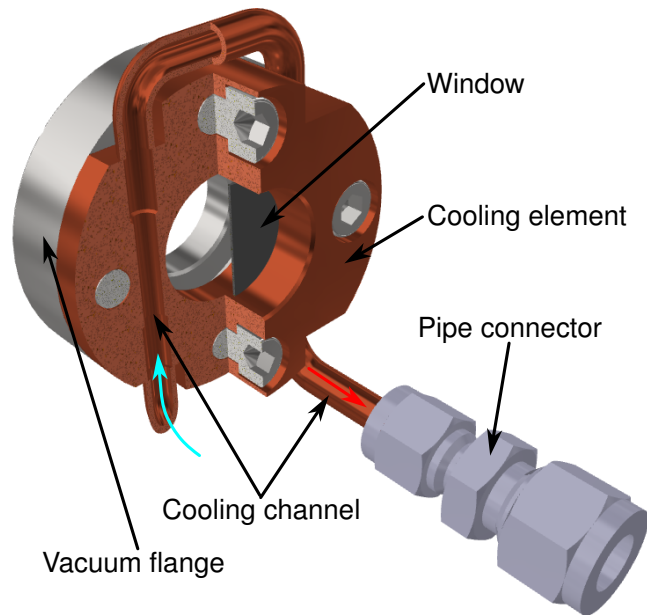


**Figure 6.5** CAD rendering of primary beam exit with integrated cooling channel. The beam exit is rendered partly cut open to visualise the cooling cycle running through the copper cooling element sitting on top of the vacuum flange. The in-flow of cool water is signified by a blue arrow, and the out-flow by a red arrow.

In tab. 6.1, the flow rates of cooling water through the cycles required to limit the water temperature below 80°C and achieve sufficient cooling power are presented. Additionally, the pressure drop expected within the cooling cycles, including that within the supply pipes approximated by eq. 6.5, and the inner diameter of the supply pipes leading from the water pumps outside the X-ray cabinet to the vacuum chamber is listed in tab. 6.1.

For the final realisation, an adjustable multi-staged high-pressure water pump was chosen for cycle 1, achieving at maximum power a volume flow rate of 7.5 m<sup>3</sup>/h at a pressure of about 15 bar [68]. An adjustable pump was chosen instead of a conventional pump that can only be toggled on or off to be able to control the pressure and flow rate within cycle 1 and thereby mitigate the risk of leakage or components failing under too high pressure. Additionally, the power of the pump can be adjusted to the momentary thermal load, e.g. the pump can be throttled down during the cooling phase when no full cooling power is required. For cycles 2 and 3 and the cooling cycle of the beam exit, the same pump model is used three times. At the required flow rate for cycle 2 of 2.5 m<sup>3</sup>/h it achieves a pressure of about 2.8 bar, at a flow rate of 1.4 m<sup>3</sup>/h, corresponding to cycle 3, it delivers 3 bar, and for the beam exit requiring a flow rate of 0.15 m<sup>3</sup>/h it provides about 3.2 bar. All pumps are manufactured by the company KSB (KSB SE & Co. KGaA, Frankenthal, Germany) and were chosen such that a sufficient margin of safety is present both in pressures and volume flow rates. Additionally, all components within the respective cycles were chosen considering the maximum possible pressure the water pumps can produce in case of a blockade to minimise the risk of components bursting.

## 6.5 Cooling of target motor

Within the electric motor propelling the target and the separation tube between the rotor of the motor in the vacuum and the stator outside of it, heat is deposited due to eddy currents and ohmic losses. About 2 kW of heating power is produced when the motor is operated at full power, which is mainly during the acceleration and deceleration of the target. However, for a conservative calculation, it is assumed that the motor constantly operates at its maximum power. The separation tube would quickly heat up and potentially undergo structural failure due to its thickness of only 0.8 mm, and the insulation of the motor coils would melt, leading to a short-circuit at temperatures above about 80°C [21]. As the motor is an

electric component, cooling with water as for the other components would lead to a short-circuit and is therefore not possible. Instead, a special low-viscosity oil is used as cooling fluid within the motor. A low viscosity is necessary to minimise the pressure drop within the cooling cycle and achieve a sufficient flow rate.

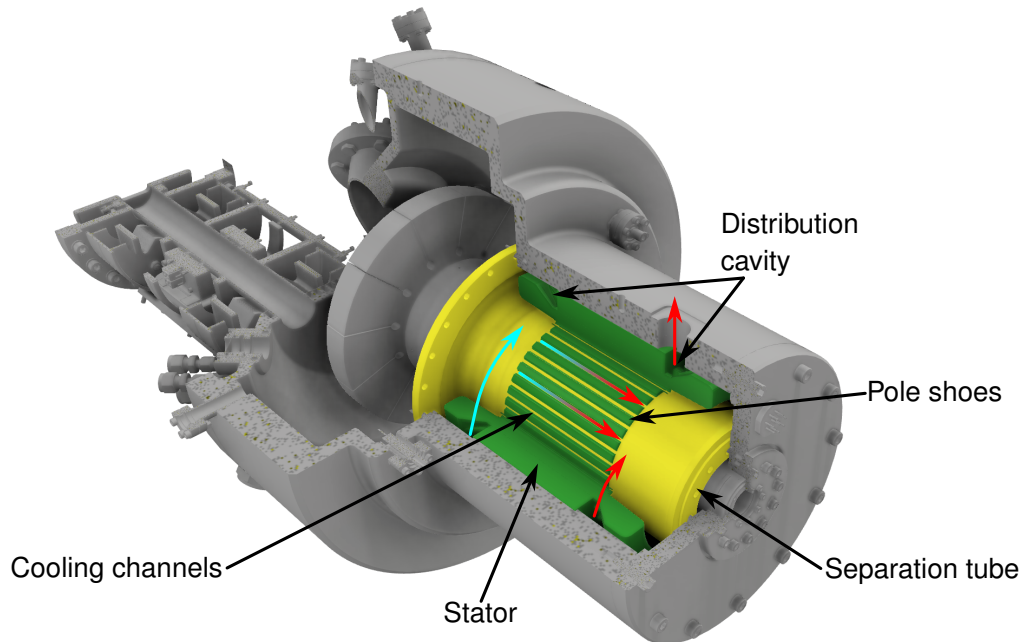


**Figure 6.6** CAD rendering of cooling channels within motor. The separation tube is depicted in yellow, and the stator of the electric motor in green. Part of the stator and the motor chamber are removed to allow the depiction of the cooling channels between the separation tube and the stator. The flow of oil from the bottom left to the port on the top right is depicted, and the temperature of the oil is hinted, with blue representing cooler temperatures and red hotter temperatures.

Within the stator of the motor, cooling channels are integrated, as shown in fig. 6.6. Cold oil is pumped into the part of the vacuum chamber housing the stator from a port at the bottom on the target side and enters a toroidal distribution cavity formed by the separation tube and the vacuum chamber [21]. The cold oil from the distribution cavity then gets pressed into a multitude of small cooling channels between the pole shoes of the stator, the separation tube and the coils of the stator, where it takes up heat from the separation tube and the stator. Leaving the cooling channels, the now hot oil gets gathered in a second distribution cavity and leaves the chamber through a port at the top. By defining the direction of flow from the bottom to the top following the direction of natural convection, a minimal reduction of the pressure drop is achieved. Oil is a less efficient cooling fluid than water, and although the heating power is low compared to the other components, a volume flow rate of about  $0.4 \text{ m}^3/\text{h}$  is required, which leads to an expected pressure drop of about 4 bar within the motor due to the higher viscosity of oil [67].

To cool the oil down again, a fluid-fluid heat exchanger is used to transfer the heat from the oil to a secondary water circuit, as presented in fig. 6.7. The chosen heat exchanger is manufactured in cross-flow design by the company Schwämmle (Schwämmle GmbH & Co. KG, Aspach, Germany). The two circuits within the heat exchanger are different, with one designed for higher flow rates and lower pressure drops than the other. Due to the higher viscosity of oil compared to water, the oil circuit is connected to the high flow rate circuit of the heat exchanger, minimising the pressure drop [69]. Following the heat exchanger, the oil flows into a tank acting as a buffer. From the oil tank, the oil is pumped into the motor again using a gear pump specifically designed for oil, achieving a maximum pressure of 10 bar at a volume flow rate of  $0.54 \text{ m}^3/\text{h}$ . The high static pressure of the oil pump could potentially rupture the thin separation tube, posing a significant threat to the LFXT prototype. Therefore, the pressure needs to be reduced using a bypass built into the pump, allowing a part of the oil to flow directly from the outlet back to the inlet of the pump. The oil cycle needs to be kept as short as possible, as extended lengths of pipes would

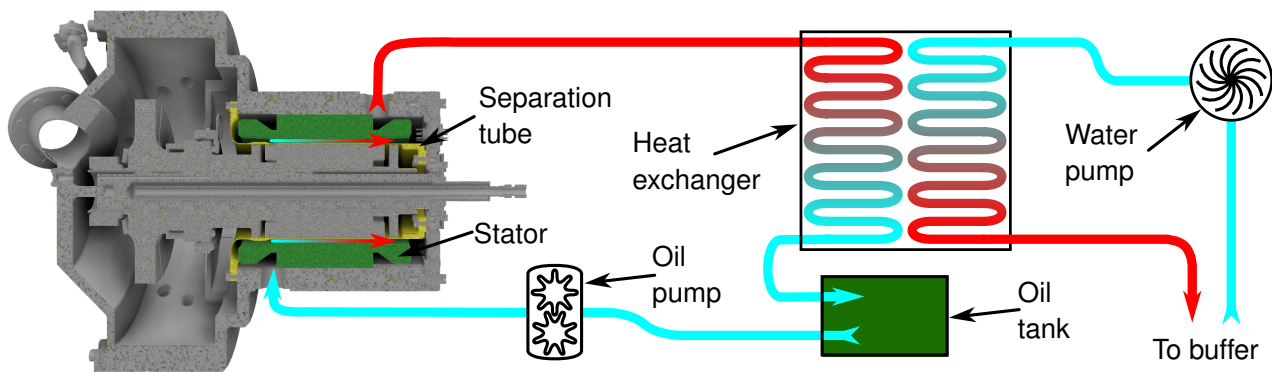


**Figure 6.7** Schematic drawing of the cooling cycle through the target motor. On the left, a vertical section view through the CAD drawing of the chamber of the LFXT prototype with the separation tube highlighted in yellow and the stator drawn in green is shown. The oil and water pumps, the oil tank, and the fluid-fluid heat exchanger are exemplarily depicted. Additionally, the flow of oil and water through the cycles is depicted and coloured according to the fluid temperature, with blue referring to low and red referring to high temperatures.

drastically increase the pressure drop within the cycle. Therefore, the complete oil cycle, including the heat exchanger, the tank, and the pump, is positioned within the X-ray cabinet closely adjacent to the motor. From the heat exchanger, long pipes then transport the water out of the X-ray cabinet, similar to the circuits of the other components.

Within the water circuit, a volume flow rate of  $0.3\text{ m}^3/\text{h}$  is sufficient to remove the heat from the oil, leading to a pressure drop of about 0.4 bar within the heat exchanger circuit [67, 69]. Out of simplicity, the same water pump as used in some of the other water circuits was chosen, achieving a pressure of up to 5.5 bar at low flow rates [68]. The high margin of safety within the water circuit cooling the heat exchanger ensures that no heat is buffered within the oil and should effectively limit the maximum temperature in the oil circuit. For temperature monitoring within the oil cycle, a thermometer is positioned within the oil tank, measuring the starting temperature before the oil enters the motor, and one is positioned directly at the exit of the motor, measuring the maximum temperature within the cycle. Additionally, thermometers are incorporated within the motor, allowing the monitoring of the coil temperature.

## 6.6 Heat buffering and dissipation

The heat gathered by the aforementioned cycles needs to be dissipated from the cooling system. Conventionally, in a laboratory, a cooling cycle provided by the building could be used with a heat exchanger, and the cooling cycle of the building would then handle the heat dissipation. However, as explained in sec. 6.1, the vacuum chamber of the LFXT prototype and, therefore, also the cooling system as water is electrically conductive, is on up to 150 kV during operation and therefore needs to be insulated from ground. Consequently, running a water pipe from the cooling system to the cooling circuit of the building is impossible, and the gathered heat needs to be dissipated differently.

A fluid-air heat exchanger consisting of a fan blowing air through a cooling element traversed by the heated water from the cooling system is used. That way, the heat from the water is transferred into the air within the laboratory, which in turn gets cooled by the ventilation system. Instead of using a very large heat exchanger with sufficiently high cooling power to directly dissipate the heat energy gathered by the cooling cycles, a small heat exchanger with just enough power to dissipate the heat energy gathered during the pulse duration within the cooling phase is applied. The chosen heat exchanger is manufactured by the company Schwämmle (Schwämmle GmbH & Co. KG, Aspach, Germany) and achieves a cooling power of up to 180 W per Kelvin temperature difference between water and air at a volume flow rate of  $1\text{ m}^3/\text{h}$  or more [70]. According to the datasheet of the heat exchanger, for a volume flow rate of  $1\text{ m}^3/\text{h}$ , a pressure of about 0.5 bar is required [70]. The heat exchanger is placed outside the X-ray cabinet, and therefore, the pipes leading to and from it are only about 2 m in length, minimising the pressure drop within them. Out

of simplicity, the same water pump as used for the cooling cycle of the steady axis presented in sec. 6.3 is also used for the supply of water to the heat exchanger. The pump is significantly over-designed for the heat exchanger as it produces a pressure of up to 5 bar at 1 m<sup>3</sup>/h flow rate, meaning a much higher flow rate will be achieved.

During the 20 s pulse, the heat from the cooling cycles is buffered within the water volume of the cooling system, including the water within the cycles, the pumps and, most importantly, the water tank from which the individual cycles are fed. After a pulse, the heat from the water gets dissipated by the heat exchanger. The water temperature in the cooling system is given by the differential equation

$$\dot{T}_{Water}(t) = \frac{P(t) - Q \cdot (T_{Water}(t) - T_{Air})}{\rho V c} \quad (6.7)$$

with the time dependant water temperature  $T_{Water}(t)$  and its derivation  $\dot{T}_{Water}(t)$ , the air temperature  $T_{Air}$ , the heating power transferred into the water  $P(t)$ , the cooling power of the heat exchanger  $Q$ , the water volume  $V$ , and the density and specific heat capacity of water  $\rho$  and  $c$ . The heating power  $P(t)$  can, due to its time dependency, be used to model the difference between the pulse and cooling phases. The amount of energy removed from the water, modelled by the second term in the numerator in eq. 6.7, is dependent on the temperature difference between water and air, and therefore, the water temperature will only go asymptotically towards the air temperature within a long time-frame. Consequently, the water temperature in a continuous cyclic operation with 20 s pulses followed by 20 min cooling phases will reach a steady state after a couple of cycles, in which it alternates between a maximum temperature reached directly at the end of the pulse and a minimum temperature at the end of the cooling phase. In fig. 6.8A, a numeric solution for eq. 6.7 depicting the temperature increase relative to a starting temperature of 20 °C is presented depicting the described behaviour. The simulation was conducted assuming a heating power  $P(t)$  of 90 kW during the pulses and 0 kw during the cooling phases, a cooling power  $Q$  of 180 W/K, a water volume  $V$  of 100 L, and an air temperature  $T_{Air}$  of 20 °C. For the simulations, a step size of 1 s was chosen, but simulations with shorter step sizes down to 1 ms were also conducted for validation without any significant deviations.

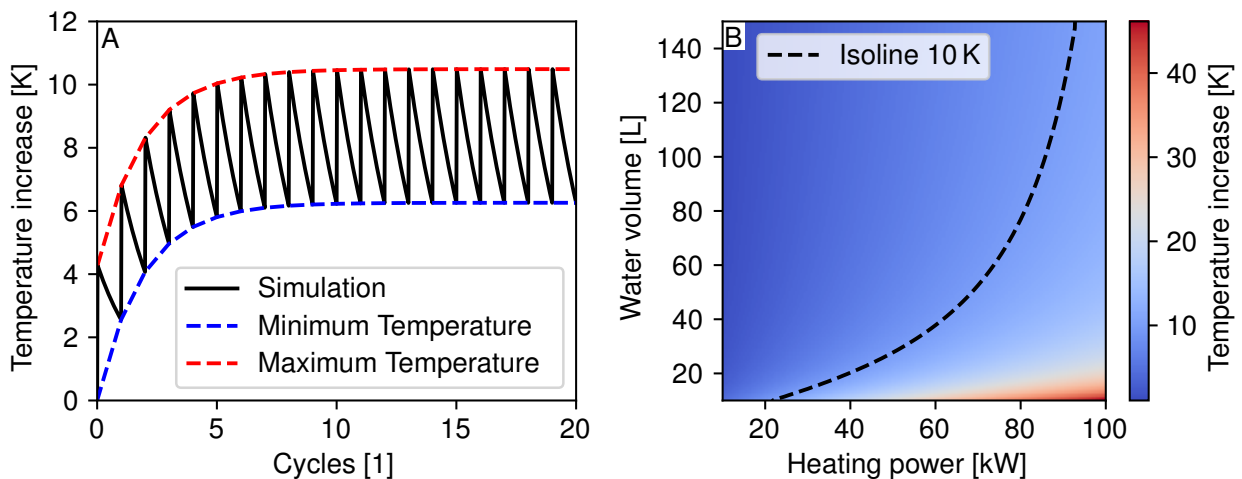


**Figure 6.8** Results of simulations for the temperature within the water tank of the cooling system. In **A**, the temperature increase relative to a starting temperature of 20 °C over 20 cycles is plotted for a heating power of 90 kW and a water volume of 100 L. Additionally, the minimum temperature increase directly at the end of the cooling phase and the maximum temperature at the end of a pulse is presented. In **B**, the maximum temperature increase after 20 cycles is visualised in dependence of heating power and water volume, and the isoline for a temperature increase of 10 K is registered.

The temperature increase within the water tank needs to be limited to about 10 K above room temperature, as the cooling power achieved by the other cycles is dependent on the temperature difference be-

tween the cooling water and the component to be cooled, as apparent from eq. 6.3. This can be achieved by a sufficiently large volume of the water tank, as a higher volume leads to a lower maximum temperature in the steady state. In fig. 6.8B, the maximum temperature of the cooling water in dependence on the heating power during a pulse and the water volume within the system is presented. Under the conservative assumption of no heat dissipation from the vacuum chamber by radiation or contact with air, a heating power of about 90 kW needs to be buffered, for which a water volume of about 120 L is sufficient. The water tank was designed to fit a volume of about 100 L, which is, together with the volume in the pipes and pumps, sufficient.

## 6.7 Overview and discussion

In the preceding chapter, the cooling system of the LFXT prototype was presented. The purpose of the cooling system is to remove excess heat from the LFXT prototype produced by the primary electron beam, backscattered electrons, and the power loss of the electric motor propelling the target. In fig. 6.9, a schematic overview of the whole cooling system is given, incorporating the main components.

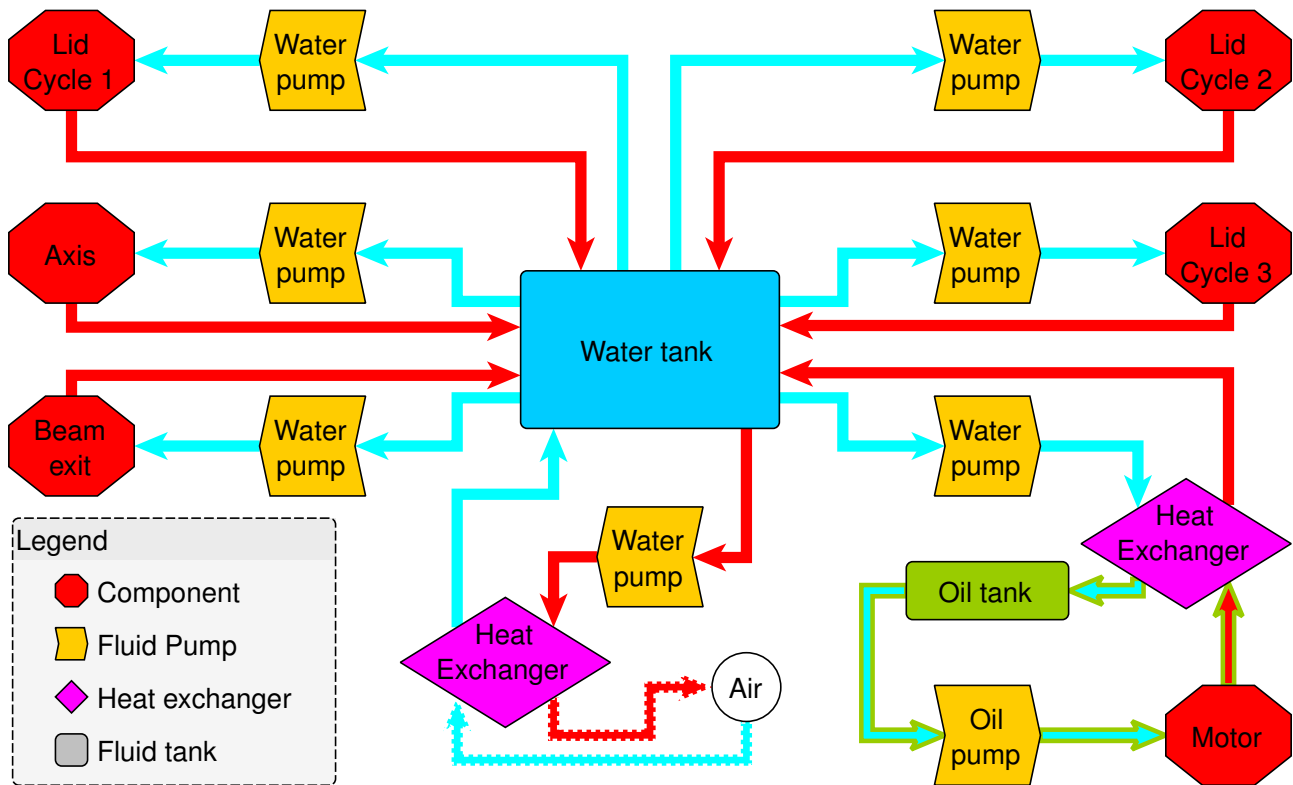


**Figure 6.9** Overview graph depicting full cooling system. Arrows symbolise the flow of water, oil, and air through the system and are coloured according to the temperature of the medium, with red representing hot and blue representing cold medium in respect to the cycle. The components that need cooling, the pumps supplying the cooling medium, the water and oil tanks, and the two heat exchangers are visualised. Heat is transported from the components to the water tank and from there through the air-water heat exchanger into the laboratory air.

The cooling system is split into seven water cycles and one oil cycle. The purpose of the oil cycle is the cooling of the electric motor propelling the target, as cooling with water would lead to a short circuit. The oil cycle is powered by a gear pump specialised for oil and supplied from a small oil tank filled with special low-viscosity cooling oil. The heat generated by the motor and gathered by the oil cycle is transferred to one of the seven water cycles over a fluid-fluid heat exchanger and the respective water cycle is designed sufficiently powerful to remove all heat from the oil, effectively minimising the oil temperature. The seven water cycles are all driven by their own dedicated water pumps but supplied from a single water tank containing about 100 L of deionised water. The usage of pure deionised water without any additives is

possible, as all metal parts in the cooling system are made from stainless steel and copper, which have similar electronegativity, preventing corrosion. All pumps within the cooling system, including the oil pump, have been chosen according to the needed volume flow rates of their respective cycles and with the pressure drops within the perfused components and the piping in mind. The pipes transporting the cooling fluids through the cycles have also been chosen according to the required flow rates, mainly in concern to their length and inner diameter, to minimise the pressure drop and, therefore, the static pressure the pumps need to provide. Six of the water cycles transport heat into the water tank, with five directly cooling the vacuum chamber and the steady axis and one indirectly cooling the motor via the oil cycle. The water tank is designed with sufficient volume to buffer the heat energy gathered during a 20 s pulse of 90 kW electron beam power. In the 20 min cooling phase following a pulse, the seventh water cycle cools down the water in the cooling system by transferring the heat into the laboratory air via an air-water heat exchanger. The volume of the water tank and the cooling power of the heat exchanger cycle are designed such that the temperature of the cooling water in the system never increases to more than 10 K above room temperature in cyclic operation. The usage of an air-water heat exchanger instead of the cooling system of the building enables the cooling system of the LFXT prototype to be fully electrically insulated from the surrounding components, which is a requirement as stated in sec. 6.1 due to the high voltage of up to 150 kV that the cooling system is subjected to.

A series of thermal sensors are positioned at strategic points to monitor the temperature within the cooling system. Within the oil cycle, a thermal sensor is built into the oil tank to measure the entry temperature of the oil into the motor, another four sensors are built into the motor for monitoring the temperature of the stator coils, and one sensor is placed at the motor outlet, measuring the temperature of the heated oil leaving the motor. For the water cycles, a thermal sensor is placed inside the water tank to monitor the starting temperature of each cycle, and one sensor is placed in each pipe coming from the components directly before the pipe is connected to the tank to measure the maximum temperature of the respective cycle.

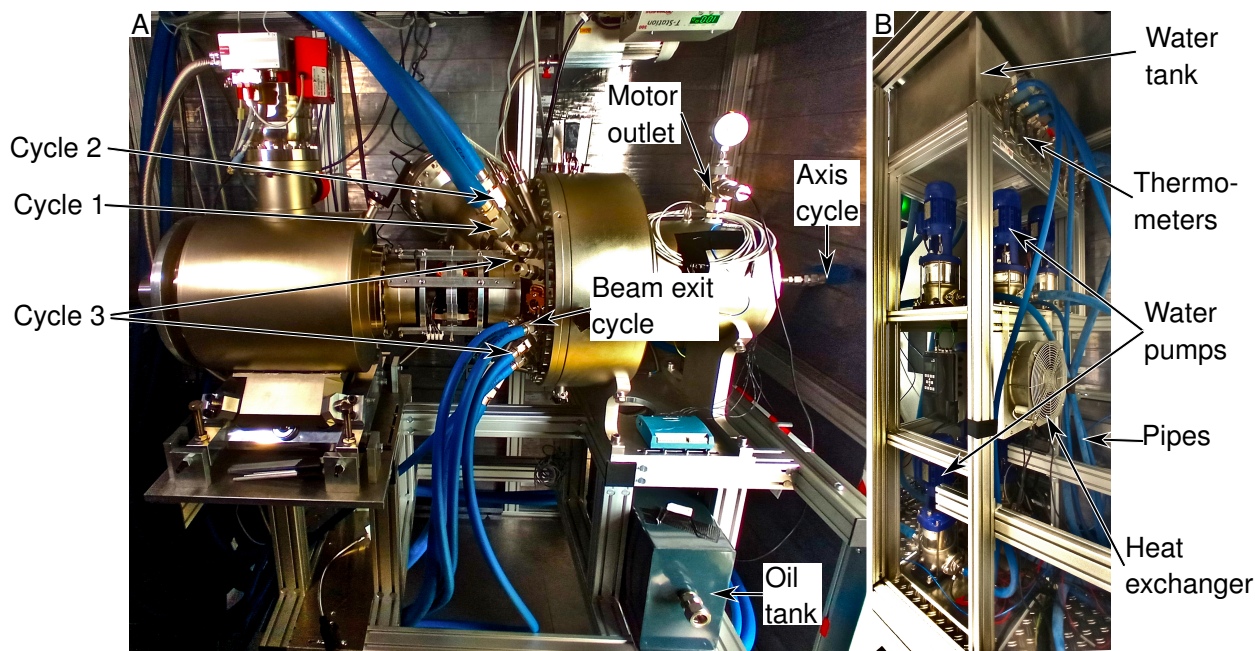


**Figure 6.10** Annotated photographs of the two parts of the cooling system. In **A**, the vacuum chamber of the LFXT prototype is shown as it is positioned within the X-ray cabinet. The visible parts of the cooling system are labelled. The oil pump, oil-water heat exchanger, and the inlet of the motor cooling cycle are not visible from the perspective in the photograph. In **B**, the part of the cooling system positioned outside the X-ray cabinet is shown. Visible are a part of the water pumps, the air-water heat exchanger, the water tank, the thermometers within the tank inlets, and the pipes leading to and from the vacuum chamber inside the cabinet.

In fig. 6.10, two photographs of the cooling system in its current state are presented. At the time of writing, the cooling system had not been filled with water and tested in full operation, as the LFXT prototype has not been operated at such high powers that active cooling would have been required. It was decided against filling the cooling system purely for testing purposes, as that would have rendered other work significantly more complex. Overall, the cooling system is, in most parts, significantly over-designed and more powerful than necessary, which can be attributed to a lack of experience and associated large margins of safety and conservative calculations. Additionally, heat dissipation by radiation or direct contact of the heated components with air was neglected during the design of the cooling system as a conservative approach, while in reality, these effects would also significantly contribute to the cooling of the LFXT prototype and reduce the necessary cooling power to far below the anticipated 90 kW. Concluding, the cooling system is designed to be able to remove all excess heat from the LFXT prototype generated during operation and is electrically insulated for high voltage, fulfilling all requirements posed on it.



# 7 High-voltage system

In the following chapter, the HV system is described. As presented in chapter 4, the HV system has three main purposes to fulfil: The generation of the required electrical voltages and currents for the electron accelerator, the electrical insulation of the high acceleration voltage, and the provision of electrical power through electrical potential barriers. To satisfy these requirements, two HV generators, two insulation transformers, a fence acting as a Faraday cage, and a so-called hot-deck and cold-deck are used. At first, the requirements for the HV system will be laid out in detail, followed by sections describing the HV generation, the designs used for electrical insulation, and the technology used for supplying electrical power. Finally, an overview of the whole system will be given together with the state of the system at the time of writing and a discussion.

## 7.1 Requirements

As mentioned in chapter 4, the HV system has three main requirements to fulfil. The first is the supply of electrical power to the electron accelerator, consisting of the cathode as the electron source and the negative pole of the direct current accelerator, the anode as the positive pole, and the Pierce electrode for controlling and initial focusing of the electron beam as depicted in fig. 7.1. For the operation of the electron accelerator, an acceleration voltage of up to 300 kV needs to be applied between the electron source complex, formed by the cathode and the pierce electrode, and the anode. The anode is conductively fixed to the beginning of the electron beam pipe and, thereby, the vacuum chamber. A ceramic insulator holds the electron source complex in place to insulate it from the vacuum chamber and ensure the correct position relative to the anode.

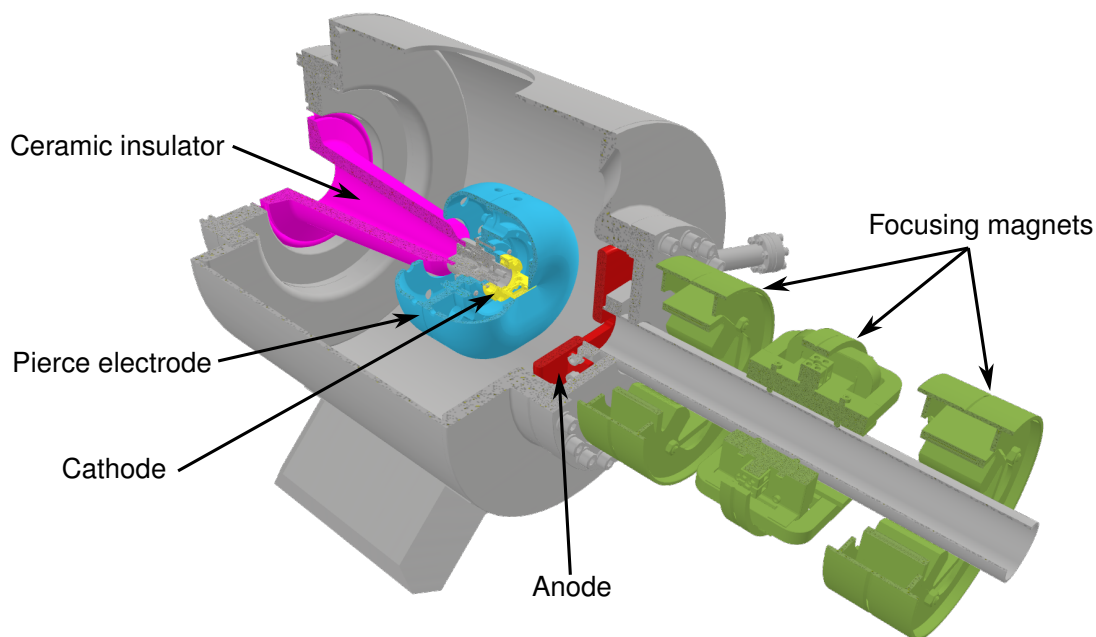


**Figure 7.1** CAD rendering of electron accelerator with main components highlighted. The cathode is drawn in yellow, the surrounding pierce electrode in blue, and the ceramic insulator holding both in place is depicted in magenta. The anode fixed to the electron beam pipe is coloured red, and the focusing magnets are green.

At the maximum acceleration voltage, an electron beam current of up to 300 mA is demanded, meaning the sources for the generation of the acceleration voltage need to be able to deliver a power of up to 90 kW. To allow electrons to escape from the thermionic cathode into the vacuum and turn into an electron beam, a current of about 4-5 A flowing through and heating it up is required. By heating up the cathode, the kinetic energy of some of the electrons is statistically increased above the work function of the material, allowing them to escape into the surrounding vacuum as free electrons [71]. The free electrons are then accelerated away from the cathode and towards the anode by the strong electrical field between the two, forming the initial electron beam.

While it would theoretically be possible to limit the electron beam current at a specific acceleration voltage by reducing the temperature of the cathode and, thereby, the number of electrons with sufficient kinetic energy to overcome the work function, this method would have several practical implications. The three main limitations are that changing the temperature of the cathode is a slow process, that the electron beam current would be very sensitive to minimal temperature differences, and that at lower heating currents, the temperature of the cathode would be inhomogeneous, leading to an altered emittance behaviour. Instead, the so-called pierce electrode is used to control the electron beam current, including blocking it fully while switching the acceleration voltage when the cathode is heated so as not to risk an uncontrolled electron beam forming in the transient electrical field. For that, a voltage of up to several 100 V is applied between the cathode and the pierce electrode, with the pierce electrode being more negative in comparison to the cathode. The applied voltage distorts the electrical field between the cathode and the anode. It can figuratively be seen as a valve opening with decreasing and closing with increasing voltage until the electrical field lines from the cathode are completely blocked and no electrons can leave the area around the cathode, effectively switching off the electron beam. By modifying the electrical acceleration field, the pierce electrode additionally leads to an initial focusing of the electron beam.

In summary, the first requirement the HV system needs to fulfil is to supply an acceleration voltage of up to 300 kV between the cathode and the anode at a maximum electron beam current of 300 mA. On top of the acceleration voltage, it needs to provide a heating current of about 4-5 A for the thermionic cathode and a voltage of up to several 100 V between the cathode and the pierce electrode for beam control. For the process of HV conditioning, it should additionally be possible to increase the acceleration voltage to about 10% above the nominal acceleration voltage without current flowing. During HV conditioning, the acceleration voltage is slowly increased without heating the cathode to prepare the LFXT prototype for later operation. For HV conditioning, special HV resistors additionally need to be integrated into the circuit to limit the amount of discharged energy in case of an electrical arc and protect the LFXT prototype from damage. The HV conditioning process is presented in detail in chapter 12 of part III.

The second requirement the HV system needs to fulfil is closely connected to the first one, as due to the high acceleration voltage, it is impossible to deliver electrical power to devices on potential, e.g. the power supplies for the cathode and the pierce electrode, in a conventional manner using conductive cabling. Due to the high power demand of some of the components, the elongated presence of HV during conditioning, and the additional hazards posed by them, the usage of batteries for buffering the required electrical power during operation and recharging during the cooling phase is not suitable. Instead, a method for transmitting sufficiently high electrical power through the potential barriers in a galvanically insulated manner is required.

The third purpose of the HV system follows from the need for the high acceleration voltage. Depending on the way the acceleration voltage is generated, not only the electron source complex is on potential during operation but also other components, e.g. the power supplies for delivering the heating current and the pierce electrode voltage. All components on electrical potential need to be insulated from components on other potentials, including the ground, both for technical and safety reasons. For the electron source complex, this is achieved by the ceramic insulator and the UHV conditions, as a vacuum is a very good insulator. However, for other components, adapted solutions need to be found, which is rendered non-trivial due to practical restrictions on space and handling of the source and due to the high acceleration voltage of up to 300 kV. Additionally to pure insulation, a method for safely discharging any remaining potential from components before personnel comes into proximity is required.

## 7.2 High-voltage generation

The main function of the HV system is supplying electrical power to the electron accelerator in the form of acceleration voltage, electron beam current, cathode heating current and pierce electrode voltage. The LFXT prototype is designed for a maximum acceleration voltage of 300 kV at an electron beam current of 300 mA, resulting in a maximum electron beam power of 90 kW. The acceleration voltage of an X-ray tube is defined as the difference in electrical potential between the cathode and the anode, producing the electrical field in which the electrons are accelerated. As only the voltage difference between the two parts of the accelerator but not towards the ground is of interest, different configurations are possible for achieving an acceleration voltage of 300 kV. The electrically easiest solution would be to utilise a single HV generator, achieving -300 kV connected to the cathode and connecting the anode to the ground. That way, the anode and, therefore, the vacuum chamber would be on ground potential, and only the electron source complex and the respective power supplies would need to be insulated. As a single HV generator providing an electron beam power of 90 kW at the required acceleration voltage would have been very expensive, it was decided out of financial reasons to instead use two lower powered HV generators with positive and negative polarities respectively. The chosen HV generators achieve a maximum voltage of  $\pm 150$  kV respective to ground potential at a maximum current of 300 mA, corresponding to an output power of 45 kW per generator [72]. The output of the positive HV source is connected via the vacuum chamber to the anode of the electron accelerator. The negative HV source is connected through the so-called cold-deck to the electron source complex. In fig. 7.2, a wiring diagram of the part of the HV system responsible for the provision of the electron accelerator is presented.

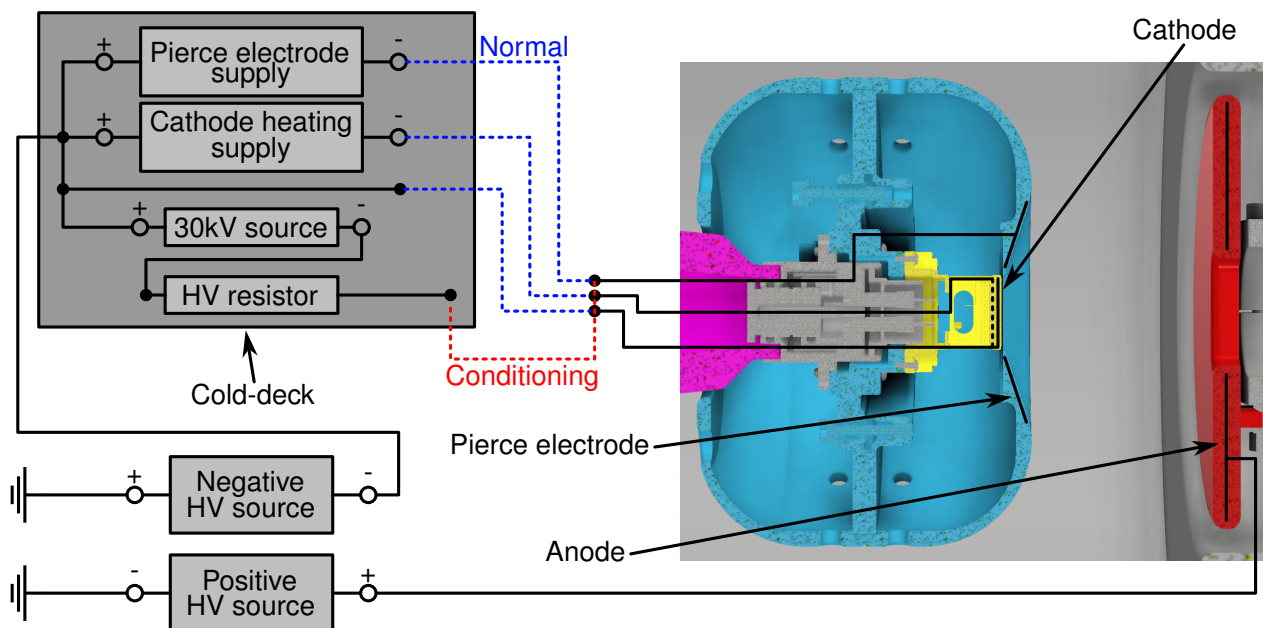


**Figure 7.2** Wiring diagram of HV generation including the HV sources, the cold-deck containing the power supplies for the electron source complex, and the electron accelerator. A horizontal section view of the electron accelerator depicting the cathode, the pierce electrode, and the anode is shown in addition to the electrical schematics for better visualisation. The wiring for normal operation is depicted in blue, and the wiring for HV conditioning is drawn in red.

The power supplies delivering the cathode heating current, as well as the pierce electrode voltage, are positioned within the cold-deck. They are connected on one side to the negative HV source and on the other side to the cathode and pierce electrode. That way, the heating current and pierce electrode voltage are provided on top of the acceleration voltage. The pierce electrode supply can achieve a voltage of up to 3500 V at a very low current of 10 mA and is connected with its positive output to the acceleration voltage and with its negative output to the pierce electrode, leading to the pierce electrode being more negative than the cathode [73]. The low maximum current of the power supply is sufficient as the pierce electrode

is insulated from the cathode, and the maximum voltage allows to fully switch off the electron beam even when an acceleration voltage of 300 kV is applied by repelling the electrons freed from the cathode [74].

The thermionic cathode consists of the heating coil through which the heating current flows and the emitter from which electrons are freed when heated [44]. The heating coil is connected on one side directly to the negative HV source and thereby the acceleration voltage and on the other side to the negative output of the cathode heating supply. The positive output of the power supply is, in turn, connected to the acceleration voltage as presented in fig. 7.2. The emitter is connected to the heating coil on the side, where it is directly connected to the acceleration voltage. In this configuration, the heating coil of the cathode can be traversed by the heating current and is charged with a potential that is more negative or equal to the acceleration voltage to which the emitter of the cathode is connected. The heating coil needs to be more negative with respect to the emitter to elongate the lifespan of the emitter material [75].

The connections between the cold-deck and the electron source complex presented up to this point are the configuration used for the normal operation of the LFXT prototype with an electron beam. For HV conditioning of the LFXT prototype, which is presented in chapter 12, the inputs to the electron source complex are purposefully short-circuited as depicted in red in fig. 7.2, and connected through a series of four HV resistors to the negative output of a small 30 kV source integrated in the cold-deck. That way, the maximum voltage applied between the electron source complex and the anode can be increased up to 330 kV and the maximum current that can flow in case of an electrical discharge is limited by the four HV resistors with a combined resistance value of 320 M $\Omega$ . The 30 kV source can be controlled via a relay built into its power supply, which is in turn controlled by a micro-controller over a network interface.

### 7.3 Energy transmission

During the operation of the LFXT prototype, the cold-deck containing the power supplies of the electron source complex is on a potential of -150 kV, and the vacuum chamber containing the anode is on +150 kV together with all components connected to it, including sensors, computers, the cooling system and many more devices. The X-ray protection cabinet the LFXT prototype is positioned in is also charged with up to 150 kV during operation, as for spatial and practical reasons, insulation of the vacuum chamber and connected components from the X-ray cabinet would not have been possible. Matching the cold-deck, the synopsis of the X-ray cabinet with all devices electrically connected to it is called the hot-deck. Both in the cold-deck and the hot-deck, electrical power is required for a multitude of devices, such as the power supplies for the electron source complex or the electric motor driving the target. A conventional connection via conductive cabling to the electrical infrastructure of the laboratory room is, however, impossible due to the HV potential the components are charged with. Instead, a method of transmitting sufficiently high electrical power over the potential barrier in a galvanically insulated manner is required. In the cold-deck, only low power of up to about 1 kW with a single phase is required for the power supplies. However, on the hot-deck, devices consuming significantly more power, such as the target motor, the vacuum pumps and the cooling system, are present, leading to a power requirement of up to 25 kW over three phases for a short duration.

The solution to the problem of energy transmission is the use of so-called insulation transformers. An insulation transformer is, in principle, a conventional transformer with the same number of coil windings on the secondary side as on the primary side, leading to output and input having the same voltage. The primary and secondary coils are placed in a tank filled with insulation oil and, thereby, insulated from each other for the required voltage. As long as only a continuous voltage is present between the input and output sides of the transformer, it can transmit an alternating current. For the power provision of the cold-deck, a small insulation transformer delivering up to 5 kW over a single phase is used. For the hot-deck, a high-powered three-phase insulation transformer delivering up to 20 kW continuously is used. As the power rating of a transformer is mainly based on heat generated within it over time, overloading the insulation transformer of the hot-deck to 25 kW for a short duration is acceptable as long as it has time to cool down afterwards at a lower power, according to the manufacturer.

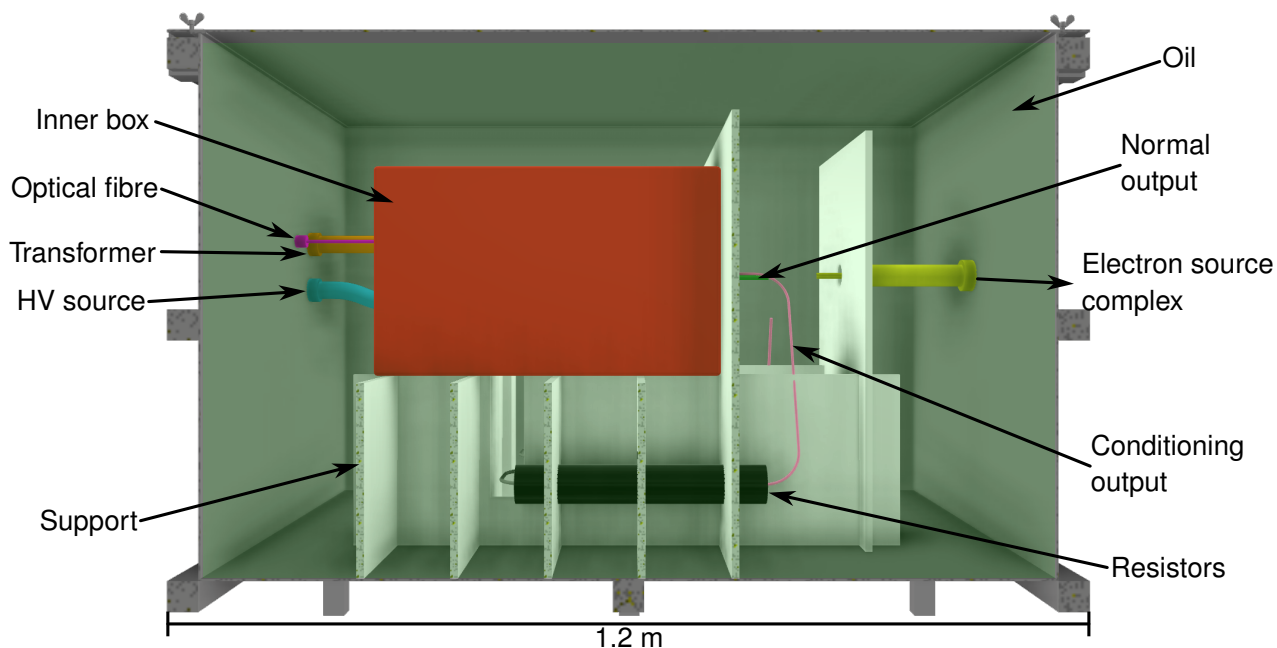
## 7.4 Insulation

As mentioned, the third purpose of the HV system is the insulation of the two polarities of the high acceleration voltage from each other and the ground. During operation, the primary components on HV potential include the electron source complex and the cold-deck containing the associated power supplies and the 30 kV source on -150 kV and the hot-deck containing the vacuum chamber with the anode and all connected devices on +150 kV. For the insulation of electrical voltage between two electrodes in general and especially for HV, two effects that can potentially lead to a loss of insulation need to be considered. The first effect is the direct discharge through the medium between the two electrodes as an electrical arc. The breakdown voltage an electrical arc forms at is mainly dependent on the dielectric strength of the medium, the shape of the electrodes, with pointy electrodes concentrating the electrical field and increasing the ionisation probability, and the distance between the electrodes. Therefore, the insulation against an electrical arc can be optimised by homogenising the electrical field by rounding the outer surface of the electrodes, increasing the distance between them and filling the gap between the electrodes with a dielectrically strong medium, e.g. oil or rubber. The second important effect is the development of so-called creeping currents along the surface of an insulator in the electrical field between two electrodes. Creeping currents can form due to impurities on the surface, deposition of pollutants, and humidity. Over time, they can alter the surface of an insulator, increasing its conductivity and eventually leading to a spontaneous discharge. For protection against creeping currents, the choice of insulation materials, the distance on the surface between the electrodes and the environmental conditions are important.

### 7.4.1 Cold-deck

For the cold-deck, insulation is achieved by nesting two metallic boxes within each other and filling the volume between them with specialised transformer oil, as presented in fig. 7.3. Transformer oil has a dielectric strength ranging from about 10 kV/mm to more than 100 kV/mm, mainly depending on moisture and impurities within the oil [76]. The outer box is made of aluminium sheet metal and has inner dimensions of 110 cm x 75 cm x 70 cm (length x width x height). The lid of the outer box contains a rubber sealing that gets pressed onto the corpus, closing the box airtight to limit the amount of dust and humidity from the air polluting the oil. The inner box is made from 8 mm to 15 mm thick steel plates, weighs around 70 kg when empty and has outer dimensions of 50 cm x 39 cm x 30 cm (length x width x height). The inner box is sealed airtight in order to stop oil from intruding. The high thickness of the steel plates is necessary, as the outer corners and edges of the box are rounded with a radius of 5 mm to homogenise the electrical field, as explained before, for which enough material is required. Additionally, the thickness and the material choice lead to the high weight, which prohibits the air-filled inner box from floating and leads to sufficient friction between it and the structure it is resting on to keep the inner box in place. The inner box rests on a support structure made from polyoxymethylene (POM) for its high mechanical and electrical stability and oil resistance.

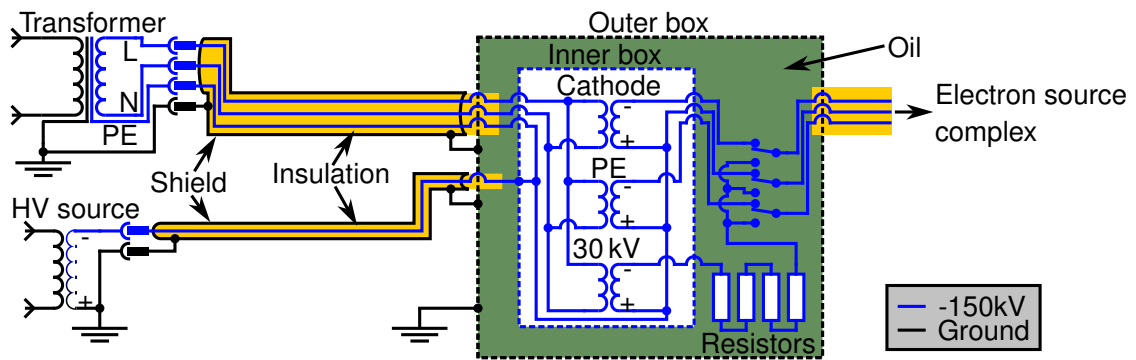
The inner box is charged with an electrical potential of up to -150 kV during operation, together with the devices contained in it. That way, no electrical field is present within the inner box that could damage the sensitive devices inside. The outer box is directly connected to ground as depicted in fig 7.4, homogenising the electrical field and allowing the cold-deck to be positioned in close proximity to other components on ground. For the function of the cold-deck electrical power, acceleration voltage and a way to send commands to the devices inside the inner box are required. The transmission of commands is achieved over a network connection facilitated by non-conductive optical fibres running through the outer box and the oil into the inner box, as visible on the left in fig. 7.3. The optical fibre cable can lead into the inner box in the shortest way, as within the oil, the risk of creeping currents forming is minimal. As presented in section 7.3, electrical power is provided to the cold-deck by a single-phase insulation transformer and the acceleration voltage of up to -150 kV is provided by the negative HV source as presented in section 7.2. Transmitting the current and voltage from the insulation transformer and the HV source into the inner box of the cold-deck requires the usage of specialised HV cables, as the outputs of both devices are on potential during operation. An HV cable consists, in general, of one or several inner wires, equivalent to a



**Figure 7.3** CAD rendering depicting insulation principle of cold-deck. In red, the inner box containing the power supplies is depicted resting on the support structure, which is drawn in white. In black, one of the HV resistors embedded in the support structure is visible. On the left, the HV cable coming from the insulation transformer in orange, the HV cable coming from the HV source in blue, and the optical fibre in magenta are shown. On the right, the normal output cable coming from the power supplies within the inner box is depicted in green, and the conditioning output cable coming from the 30 kV source is drawn in pink going into the first HV resistor and returning from the last. The HV cable running from the cold-deck to the electron source complex in the vacuum chamber on the hot-deck is rendered yellow. The transformer oil filling the volume between the boxes is visualised in translucent green.

normal cable, transporting the respective currents and voltages, surrounded by a thick insulation layer, a woven metallic shield, and an outer mantel for mechanical protection. The combination of the inner wires on potential with the surrounding shield on ground acts as a coaxial cable, homogenising the electrical field between them and shielding the outside from any unwanted electrical fields. A voltage up to the maximum rated voltage of the cable can be applied between the inner wires and the shield, in the case of the supply cables for the cold-deck up to 225 kV [77]. On the side of the insulation transformer and the HV source, the HV cables are connected with specialised HV plugs, connecting the inner wires to the output and the shield to the housing and thereby ground of the respective device, while ensuring protection against electrical breakdowns due to arcs or creeping currents. On the side of the cold-deck, the HV cables are hardwired as sketched in fig. 7.4. The shield of the HV cables is on ground potential and may, therefore, not come into proximity of the inner box of the cold-deck. Instead, it is connected on the outside to the outer box of the cold-deck, ensuring insulation and shielding up to the point where the cable enters into the transformer oil. The inner wires surrounded by the insulation layer intrude into the outer box through a sealed port, where the insulation layer ends before the inner wires protrude through another port into the inner box, where they are connected.

As mentioned in section 7.2, the cold-deck has two output configurations for normal operation and for HV conditioning, and corresponding, the inner box has two output ports. Through the port for normal operation, one cable transports the negative output of the cathode heating power supply, one transports the negative output of the pierce electrode power supply, and one transports directly the voltage from the HV source and simultaneously the positive outputs of the two power supplies. Through the output port for HV conditioning, only a single cable leaves the inner box, transporting the output of the 30 kV source. The output of the 30 kV source is fed directly into the series of HV resistors embedded underneath the inner box within the support structure and then again upwards close to the other output port, as shown in



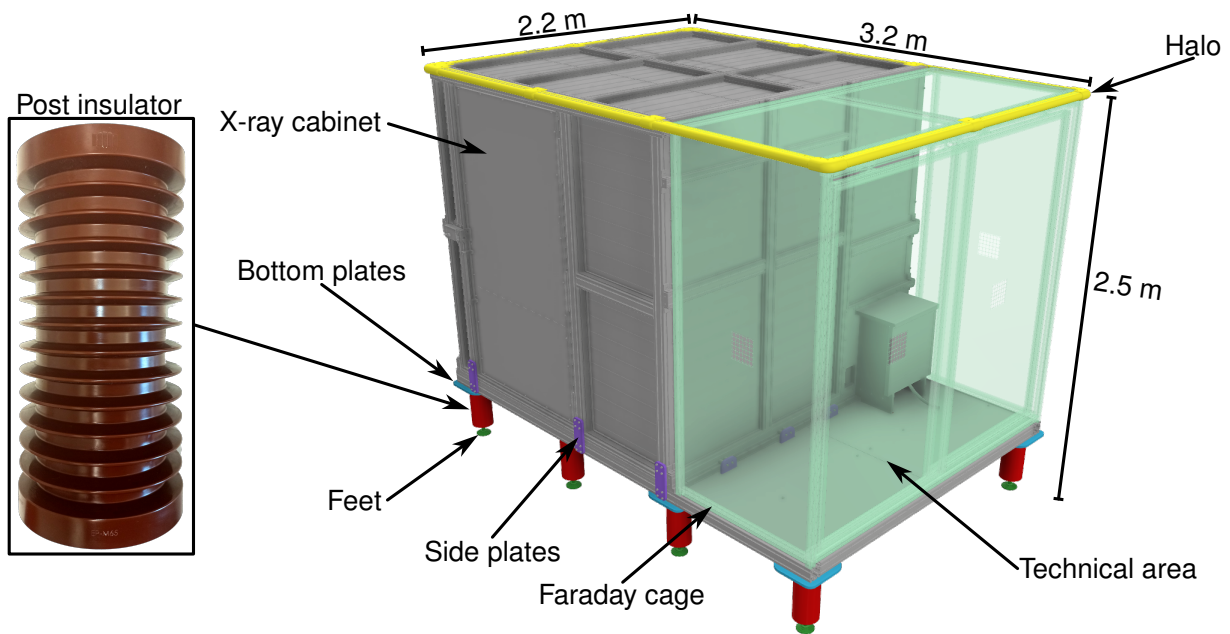
**Figure 7.4** Simplified circuit diagram of cold-deck including insulation and shielding. All power supplies, including the HV source, are depicted as transformers for simplicity. On the left, the insulation transformer and the negative HV source are depicted receiving electrical power from the room infrastructure on their input side. The output side of the transformer and the HV source are connected via two HV cables to the cold-deck. The HV cables are drawn with their inner wires, their thick insulation in yellow entering the outer box, and their outer shield connected to the outer box. The inner box of the cold-deck containing the two power supplies and the 30 kV source is shown within the outer box, and the volume in between is filled with oil visualised in green. The HV cable running from the cold-deck to the electron source complex is depicted on the right. The HV resistors are shown between the inner and outer box, and three switches represent the switching point between normal operation and conditioning. All conductive parts are colour-coded according to their electrical potential, with black lines representing ground and blue lines representing -150kV.

fig. 7.3. The HV resistors are positioned in the transformer oil between the inner and outer box, as they are on -150kV during conditioning but can be on up to +150kV in case of an electrical arc. Therefore, they need to be insulated both from the inner box on -150kV and the outer box on ground. Within the transformer oil, close to the two outputs of the inner box, an HV cable with three inner wires starts that runs to the electron source complex on the hot-deck. Depending on the operation mode, the three wires of the normal output are connected within the oil to the output HV cable or the single wire coming from the series of resistors is connected to all three wires of the output HV cable. By positioning the switching point in the transformer oil between the inner and outer box, electrical insulation is ensured, and switching is possible without having to open the sealed inner box.

### 7.4.2 Hot-deck

The hot-deck consists of the X-ray cabinet with an inner size of a little less than 2 m by 2 m and a free height of about 1.8 m and a technical area sharing the same electrical potential. Within the X-ray cabinet the vacuum chamber of the LFXT prototype and experimental setups are positioned. In the technical area, the cooling system, parts of the control system, and in general devices that need to be conductively connected to the experimental setup and the vacuum chamber are positioned. Therefore, devices in the technical area are protected from radiation damage while being on the same potential as the devices inside the X-ray cabinet. A Faraday cage built from aluminium profiles, metallic meshes and metal sheets surrounds the technical area on all sides to eliminate electrical fields that would damage sensitive devices. The X-ray cabinet acts, due to its walls consisting of lead bricks, also as a Faraday cage, protecting the devices inside of it from electrical fields.

As the hot-deck needs to be easily accessible, insulation from the surrounding space using transformer oil or any other insulant similar to the cold-deck is not an option. Instead, insulation needs to be achieved by homogenising the electrical fields and by increasing the distance within the restrictions posed by the available space. To increase the distance from the floor, the hot-deck rests on 11 industrial post insulators with a height of 30 cm as presented in fig. 7.5. The used post insulators are made of a material with a high mechanical strength to carry the weight of the hot-deck of about 8 tons and a high dielectric strength for insulation. Additionally, the material has a high resistance against the formation of creeping currents and a ripped outer surface to maximise the distance a creeping current would need to overcome. The post



**Figure 7.5** CAD rendering of hot-deck with components important for insulation highlighted. In translucent green, the Faraday cage surrounding the technical area next to the X-ray cabinet is depicted. Surrounding the top of the hot-deck on all sides, the so-called halo is rendered in yellow, and on the sides of the cabinet, the rounded side plates are shown in violet. The 11 stilts the hot-deck rests on consist of the bottom plates in blue, the post insulators in red and the adjustable feet in green.

insulators are connected to the hot-deck using specially shaped bottom plates that are rounded towards the floor with a radius of 15 mm and towards the sides with a radius of 5 mm. The bottom plates are large enough to surmount the aluminium profiles of the hot-deck, shielding the sharp corners within their field shadow. To adjust for the unevenness of the floor and to increase the distance of the hot-deck to the floor, the post insulators are placed on adjustable feet instead of standing directly on the ground. The design of the stilts consisting of the bottom plates, the post insulators and the adjustable feet was validated in a model experiment at an HV test station. Additionally, the minimum height of the stilts was evaluated with the result that for 150 kV, at least a height of 35 - 40 cm is required. On the top, insulation of the hot-deck is realised by the so-called halo. The halo consists of a series of bent metal sheets and specially shaped metal parts forming a closed ring around the top edge of the cabinet and rounding the edge with a radius between 21 mm and 26 mm, again homogenising the electrical field. On the top, approximately the same distance is required for insulation as at the bottom. To achieve a sufficient free height of the room, the upper layers of the floor had to be removed, such that the cabinet is standing on the base-plate of the storey. In addition to the measures taken for rounding off the edges and corners of the cabinet at the top and bottom, the sides of the hot-deck were also optimised. This mostly concerns the side plates holding the vertical aluminium profiles of the X-ray cabinet, which were manufactured with a round shape at the edges. Additionally, the cut ends of all profiles were closed off by metallic caps with smooth edges, and the cables for the lock of the door of the X-ray cabinet were wrapped with conductive tape.

As presented in fig. 7.6, the hot-deck is surrounded on all sides except for the right side by a metallic fence made from aluminium beams and metal meshes serving two purposes. On the one hand, the fence is an important part of the safety system, as explained later in chapter 8. On the other hand, the fence acts as the counter electrode to the hot-deck and homogenises the electrical field due to its flat design, equivalent to the outer box of the cold-deck. Therefore, it improves the insulation and acts as a Faraday cage, shielding the infrastructure of the building and adjacent rooms from being disturbed by strong electrical fields or, in case of an insulation breakdown, from electrical arcs. The fence is connected to the electrical ground at various positions with thick cables, ensuring a quick discharge in case of an electrical arc transporting charge from the cabinet into the fence. On the right side, the fence is not

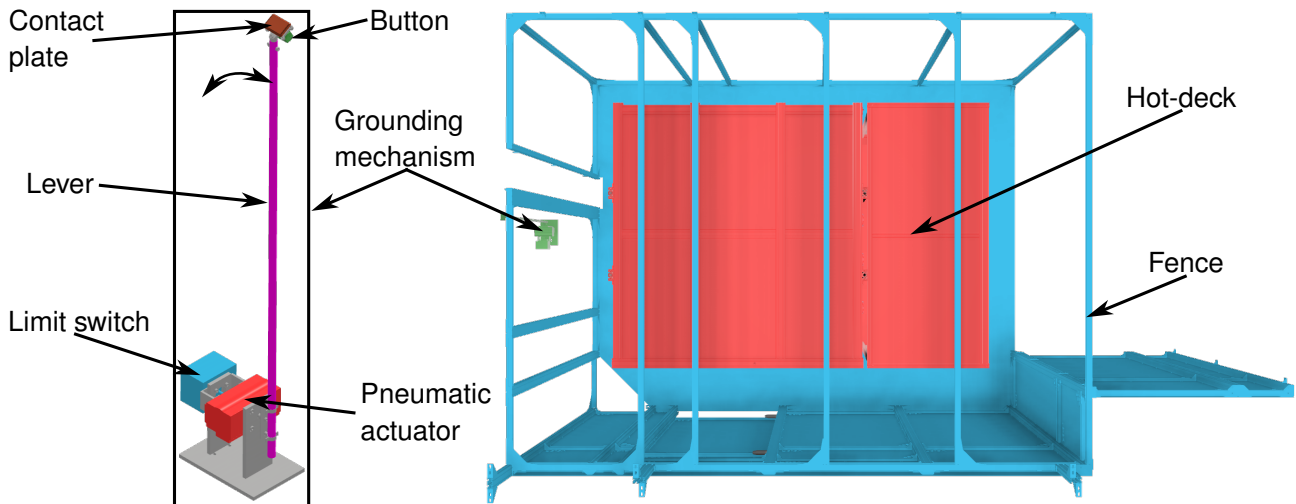


**Figure 7.6** CAD rendering of the fence surrounding the hot-deck in top-down view and the pneumatic grounding mechanism. On the right, the fence is drawn in blue, the grounding mechanism outside the fence in green, and the cabinet in red. The metallic mesh the areas between the beams of the fence are filled with on the left, top, and back sides of the cabinet are not rendered. On the left, the grounding mechanism is shown with the pneumatic actuator in red, the limit switch in blue, the lever in magenta, the contact button in green and the contact plate in copper colour. Additionally, the movement direction of the lever is sketched.

closed for reasons of practicability, as the HV sources, the insulations transformers and the cold-deck are positioned there and need to be connected to the hot-deck. Instead, the distance from the hot-deck to other components is high enough to ensure insulation.

As mentioned in section 7.1, a method to safely discharge any remaining potential from the hot-deck before personnel comes into proximity of it is required in addition to pure insulation. To be able to fully discharge the hot-deck, it needs to be ensured during the building of the hot-deck that all parts are conductively connected to each other, such that charge can flow freely. For that, the aluminium profiles from which the skeleton of the hot-deck is built are connected using specialised connectors, and during the building process, conductivity was validated repeatedly. In the case that the hot-deck is one single conductive component, any remaining potential can be discharged by connecting the hot-deck to the electrical ground. For safety reasons, this is done using an automatic grounding mechanism as presented in fig. 7.6 on the left. The grounding mechanism consists of a pneumatic single-action rotary drive moving a copper contact plate fixed to the end of a lever into contact with the side wall of the hot-deck. The contact plate is connected to ground via a dedicated cable running through the metal pipe acting as the lever and connects the hot-deck to ground when in contact to it. A single-action rotary drive has been chosen for safety reasons, as only for breaking contact with the hot-deck pressurised air is required. In case of a failure in the pneumatic system or a power outage, the spring in the drive will automatically discharge the hot-deck. As feedback for the safety system, the contact plate is fitted to a spring-loaded button, which is pressed when in contact with the hot-deck and otherwise released. Additionally, a limit switch is connected to the pneumatic actuator, signalling if the lever is in the connected or disconnected position. As presented in fig. 7.6, the base of the grounding mechanism is positioned just outside the fence such that the lever can be moved through a slot in the fence into contact with the hot-deck. That way, the grounding mechanism is outside the electrical field during operation, ensuring that it has no influence on the insulation. In addition to the automatic grounding mechanism, a grounding rod, as conventionally used in the maintenance of railway cables, is used for manual grounding for redundancy.

The hot-deck requires electrical power, the positive acceleration voltage, a connection to the control system, and a connection to the cold-deck for the supply of the electron source complex. As presented in fig. 7.7, the connections to the insulation transformer and the positive HV source are facilitated using HV cables, equivalent to the cold-deck. As mentioned before, the connection from the cold-deck to the electron source complex is also facilitated with an HV cable, with the difference that one rated for up to 300 kV is

used. The shields of the HV cables coming from the insulation transformer and the HV source end at the fence, and only the insulations reach the hot-deck. This is important as the shields are on ground, and bringing them into proximity to the hot-deck on +150 kV would lead to an electrical arc. The shield of the HV cable originating in the cold-deck is completely removed in the area outside the hot-deck, as the cold-deck is placed very close to the fence, and the part of the HV cable that could be shielded is only very short. Inside the hot-deck, the shield is present and on +150 kV during operation. On the hot-deck, the neutral wire of the insulation transformer is connected to the output of the HV source via a so-called PEN bridge to ensure that the coils of the insulation transformer are not on a floating potential. That way, the electrical system in the hot-deck is equivalent to a TN-S system as used in conventional installations, and safety devices like ground fault interrupters can be used. The connection to the control system is facilitated using optical fibres, equivalent to the cold-deck. All connections running from the hot-deck to other components are guided in waves through the air instead of using the shortest connection in order to maximise the distances creeping currents would need to bridge.

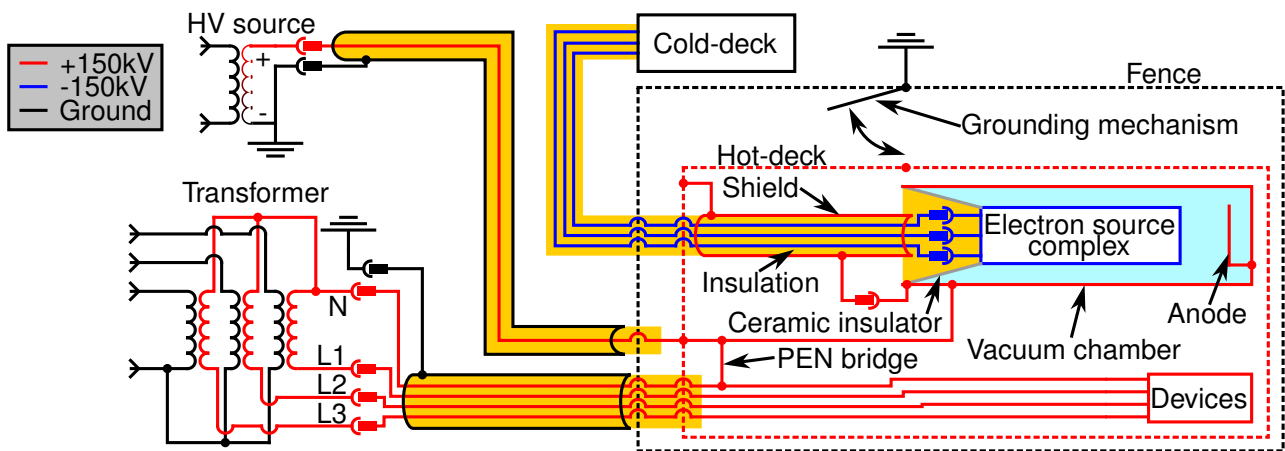


**Figure 7.7** Simplified circuit diagram of hot-deck including insulation and shielding. The positive HV source is depicted as a transformer for simplicity. On the left, the three-phase insulation transformer and the positive HV source are depicted receiving electrical power from the room infrastructure on their input side. The output side of the transformer and the HV source are connected via two HV cables to the hot-deck. Additionally, the HV cable running from the cold-deck to the electron source complex within the hot-deck is depicted. The HV cables are drawn with their insulations in yellow, and their shields are coloured according to the electrical potential. For simplicity, the four HV cables coming from the insulation transformer are shown as only a single one with four wires. The fence and the hot-deck are sketched, and on the hot-deck the vacuum chamber is outlined, containing the anode and the electron source complex held by the ceramic insulator. The box labelled "Devices" represents all electrical devices on the hot-deck, that are supplied by the insulation transformer. All conductive parts are colour-coded according to their electrical potential, with black representing ground, blue representing -150 kV, and red representing +150 kV.

## 7.5 Overview and discussion

In the preceding chapter, the HV system of the LFXT prototype was presented. The HV system fulfils three interconnected requirements for the operation of the LFXT prototype. The main purpose is to provide the acceleration voltage, the cathode heating current and the pierce electrode voltage to the electron accelerator, which consists of the cathode, the pierce electrode and the anode. The second requirement the HV system satisfies is supplying electrical power to components aside from the electron accelerator that are on electrical potential during operation, e.g. the power supplies for the cathode and the pierce electrode or the cooling system. The third purpose of the HV system is to electrically insulate the high acceleration voltage of up to 300 kV and provide a mechanism to safely discharge any remaining potential before personnel comes into proximity.

In fig. 7.8, the main components making up the HV system are depicted as they are positioned in the laboratory room. The acceleration voltage for the electron accelerator is provided by two HV sources,

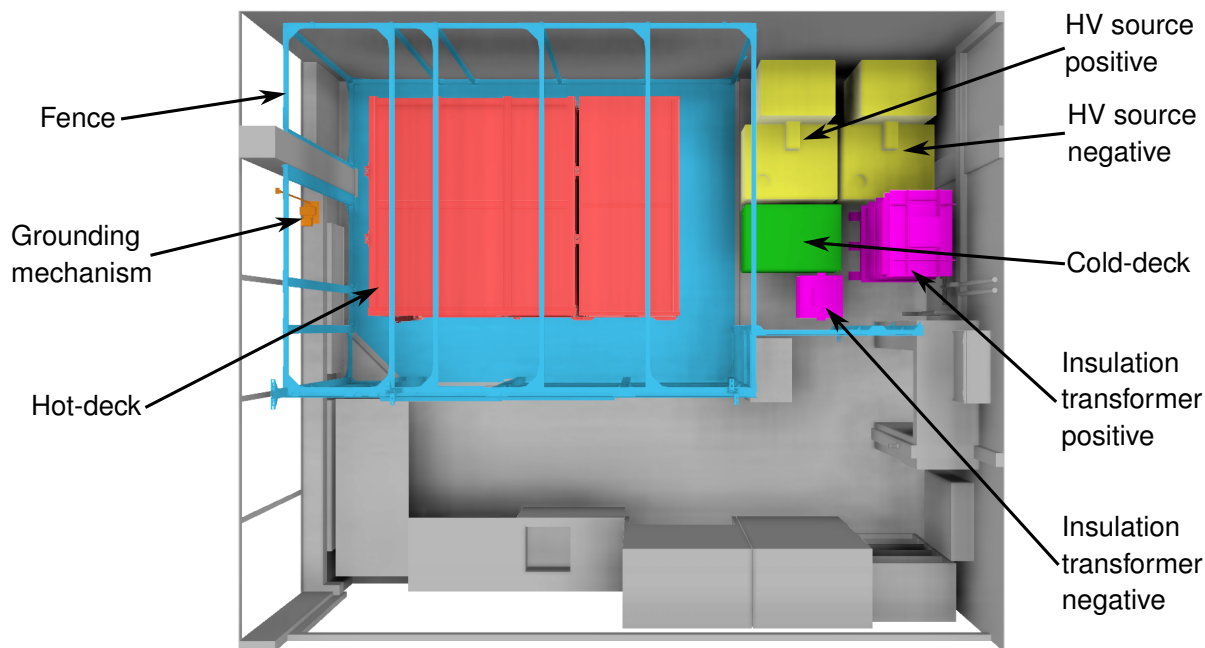


**Figure 7.8** CAD rendering of laboratory with parts of the HV system highlighted in top-down view. The positive and the negative HV sources are depicted in yellow, the insulation transformers in magenta, and the cold-deck in green. The hot-deck is depicted in red, and the fence is in blue. On the left side of the fence, the grounding mechanism is drawn in orange on the windowsill.

generating 150 kV at a maximum current of 300 mA with negative and positive polarity, respectively. The positive HV source is connected directly to the hot-deck and via that to the vacuum chamber and the anode of the LFXT prototype. The hot-deck consists of the X-ray cabinet and a technical area surrounded by a Faraday cage. To insulate the hot-deck, it is positioned on stilts consisting of adjustable feet, industrial post insulators, and specially shaped metallic bottom plates. The so-called halo rounds the outer edge on the top of the hot-deck to homogenise the electrical field towards the ceiling. To increase the available insulation distances at the top and the bottom of the hot-deck to about 35 cm, the upper layers of the floor were removed. Surrounding the hot-deck on all except for the right side, a fence acting as a Faraday cage is built to homogenise the electrical field further and shield the rest of the building from it. Next to the hot-deck, the grounding mechanism is positioned outside the fence on the windowsill. It consists of a pneumatic rotary drive controlled by the safety system, pressing a connection plate made from copper that is connected to the electrical ground onto the side of the cabinet. Electrical power for the multitude of devices on the hot-deck is provided by a large three-phased insulation transformer positioned on the right side of the room.

The negative portion of the acceleration voltage is not directly provided to the electron source complex but through the so-called cold-deck containing the power supplies for heating the cathode and controlling the electron beam using the pierce electrode. Additionally, the cold-deck contains a 30 kV source and a series of HV resistors for HV conditioning explained later on in chapter 12. From the cold-deck, the electron source complex is supplied via an HV cable rated for up to 300 kV. The cold-deck consists of two metallic boxes nested within each other. The inner box contains the electrical devices, and the gap between the two boxes is filled with transformer oil for insulation. Electrical power is provided to the devices within the cold-deck from a small single-phase insulation transformer positioned directly next to the cold-deck. As the inner box, which is the potentially charged component of the cold-deck, is fully contained within the sealed outer box that is continuously connected to ground, a grounding mechanism similar to the hot-deck is not required.

In fig. 7.9, photographs of the realisations of the hot-deck, the grounding mechanism, and the cold-deck as positioned within the laboratory are shown, with the main components important for the HV system highlighted again. At the time of writing, the supply of the electron accelerator through the two HV sources

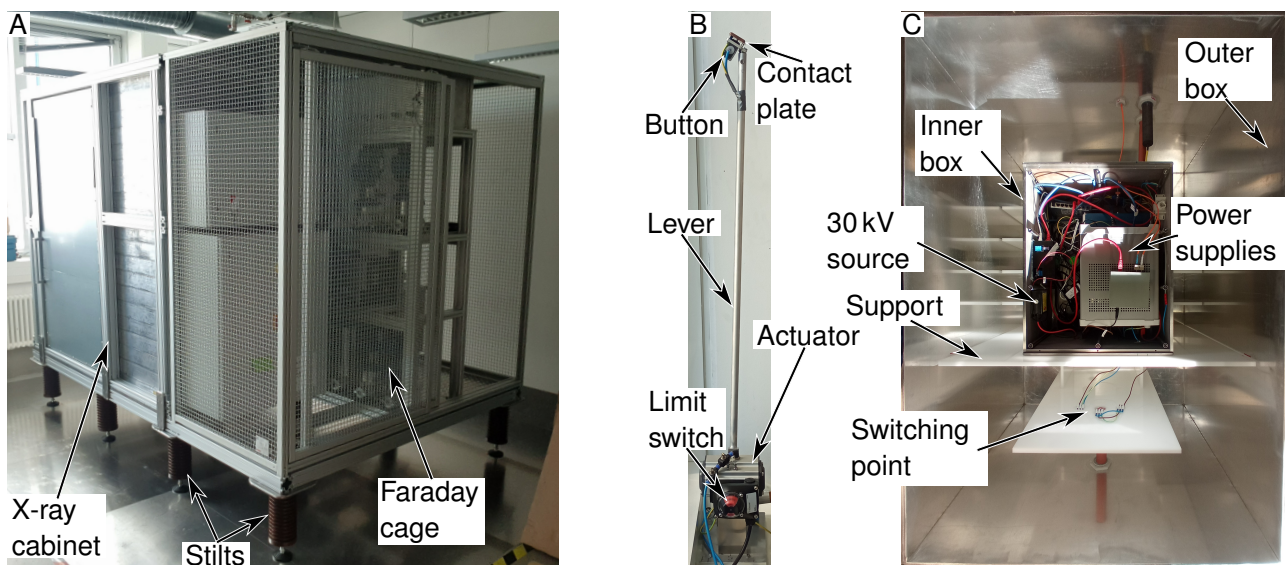


**Figure 7.9** Annotated photographs of the central parts of the HV system. In **A**, the hot-deck is presented with the X-ray cabinet, the Faraday cage and the stilts marked. The stilts consist of the adjustable feet, the post insulators and the bottom plates. In the photograph, the halo on top of the hot-deck is missing, as it was only installed after the fence was closed, and no photograph depicting the whole hot-deck could be taken anymore. In **B**, the grounding mechanism is shown, with the main parts highlighted. In **C**, a photograph of the cold-deck is presented in a top-down view and without the lid of the inner box. The power supplies in the inner box are stacked on top of each other, and the 30 kV source is fixed to the wall of the inner box. From the top, the HV cables from the HV source and the insulation transformer and the optical fibres enter. On the bottom, the switching point and the exiting HV cable running to the electron source complex are visible.

and the power supplies within the cold-deck has been fully tested. The HV sources are fully functional up to their maximum voltage of  $\pm 150$  kV and stable above a voltage of about  $\pm 10$  kV. The provision of cathode heating current and pierce electrode voltage to the electron source complex is working even when HV is applied. At the start of testing, the delivery of the additional 30 kV by the smaller HV source within the cold-deck was also functional, but at some point during the HV conditioning explained later on in chapter 12 the microcontroller controlling the 30 kV source was damaged. The transmission of electrical power to the hot-deck and cold-deck through the two insulation transformers has also been fully tested. The insulation transformers are working as intended and are stable during operation. One problem with the insulation transformers arises from the electrical installation on their input sides, as due to the high starting currents, the fuses are triggered, and it usually takes numerous attempts to start a transformer. This could be improved by exchanging the fuses with stronger and more inert types.

The insulation of the negative and of the positive portion of the acceleration voltage against the electrical ground by the hot-deck and the cold-deck has also been fully individually tested at the time of writing. Insulation between the inner and the outer box of the cold-deck is fully working as intended without a single breakdown so far. The insulation between the HV resistors and both boxes in the case of an electrical arc between electron source complex and anode has involuntarily also been tested at up to about 265 kV and is functional. During the design of the cold-deck, unnecessarily large margins of safety have probably been applied due to a lack of experience with HV insulation. In future iterations, the cold-deck could potentially be designed in a more compact way. On the positive side, corona discharges in the air originating from the hot-deck are audible, starting at about 80 kV. From the experiments at the HV test station, the occurrence of corona discharges was to be expected and is, on its own, not critical. However, corona discharges can be a precursor for a nearing electrical arc, as they are, on the one hand, a symptom of a sharp edge or spike leading to a concentrated electrical field and, on the other hand, can act as an ionisation seed. With the original design of the hot-deck, only about 115 kV could be reached before electrical arcs towards the ceiling of the fence led to insulation breakdowns. It is assumed that the combination of the modular design of the halo, leading to slight edges, and the very limited free height of the laboratory room was to blame for

the insufficient insulation at the top of the hot-deck. To increase the breakdown voltage between the top of the hot-deck and the ceiling of the fence, four layers of 1 mm thick elastic Polyvinylchlorid (PVC) sheets were stacked onto the hot-deck above the halo. The PVC sheets are large enough that they overhang the sides of the hot-deck for about 20 cm to 30 cm. As material PVC was chosen due to its availability and price, as well as its high dielectric strength ranging from 13.8 kV/mm to 19.7 kV/mm [76]. Additionally, PVC is not flammable and, therefore, not a safety concern. By stacking four individual layers of PVC sheets on top of each other instead of using a single thicker layer, the probability of flaws in the plastic sheets that could lead to an insulation breakdown to be aligned on top of each other is minimised. With the addition of the PVC sheets, the insulation of the hot-deck was improved sufficiently to reach the maximum voltage of +150 kV. The grounding mechanism of the hot-deck has also been tested and is, at the time of writing, already used in operation, where it has proven to be fully functional and reliable.

The maximum voltage difference and, therefore, acceleration voltage that was tested at the time of writing was about 265 kV. Within the HV system, the voltage difference is only of importance for the HV cable running from the cold-deck over the hot-deck to the electron source complex and the associated HV plug. Within the HV cable itself, no insulation problems were registered up until the time of writing. However, due to a design problem concerning the fixation of the HV plug in the ceramic insulator, the plug loosened over time, leading to the formation of a creeping current between the plug and the ceramic insulator as the receptacle. At about 265 kV, the creeping current led to an insulation breakdown that destroyed both the plug and the ceramic insulator. The design of the fixation for the HV plug was reworked, and the destroyed components were replaced.

Overall, the HV system is fully functional after some minimal amendments to the original design and has been nearly fully tested and put into operation. The electron accelerator can be provided with the required cathode heating current, pierce electrode voltage and acceleration voltage through the cold-deck. Both the hot-deck and the cold-deck can be supplied with power independently of the applied acceleration voltage through the two insulation transformers. The insulation of the negative portion of the acceleration voltage by the cold-deck and the insulation between the HV resistors and both boxes of the cold-deck is functional without restrictions. The insulation between the hot-deck and the fence is also functional, although corona discharges are present at higher voltages. Although the HV system is fully functional, the initial decision to use two HV sources and accelerate from -150 kV to +150 kV did not only lead to significantly higher complexity of the system and increased safety risks, but also to a higher price, effectively reverting the initial argument for it. Therefore, for the next iteration of the LFXT, acceleration from a negative voltage to ground using a single HV generator should be favoured.



## 8 Safety system

In the following chapter, the safety system is described. As presented in chapter 4, the central purpose of the safety system is to ensure personal safety in the laboratory during the operation of the LFXT prototype. This includes protection from X-ray radiation, the acceleration voltage, and the high kinetic energy contained within the target rotor complex. To fulfil this purpose, the safety system is associated with most components in one way or the other, but dominantly with the X-ray cabinet on the hot-deck and the fence. In the following, the requirements for the safety system will be explained in detail, followed by the principles applied to ensure protection from the three major danger sources. Finally, an overview of the safety system will be given together with its realisation at the time of writing and a discussion. The safety system was developed in cooperation with the company Seitec (Seitec GmbH, Königsee, Germany), who built the control cabinets and programmed them, the company retrag (retrag GmbH, Erfurt, Germany), responsible for the X-ray cabinet, and the company SSP (SSP Safety System Products GmbH & Co. KG, Spaichingen, Germany) who manufactured the fence.

### 8.1 Requirements

As mentioned in chapter 4, the central purpose of the safety system is to guarantee personal safety during the operation of the LFXT prototype. Aside from conventional hazards in a laboratory environment like chemicals, tripping, electricity, and impact on low-hanging components, there are three significant sources of danger that arise during operation.

The first danger source originates from the overall purpose of the LFXT prototype to generate ionising X-radiation. While X-rays can be used for a myriad of applications in science, industry and medicine, ranging from spectroscopy for material studies to the treatment of cancer, their damaging properties with respect to biological materials are well known. Within biological cells, X-radiation leads to the ionisation of molecules and can, thereby, directly or indirectly damage the deoxyribonucleic acid (DNA). On the most basic level, damage from ionising radiation can be categorised into deterministic and stochastic effects. Deterministic effects include symptoms of radiation damage that occur promptly after exposition to a dose above a certain threshold and whose severity scales with the dose. For example, a homogeneous full-body exposition of an adult human to a dose below 1 Gy leads to minor changes in the haemogram and a mortality risk below the detection limit, while exposition to a dose of about 10 - 15 Gy leads to severe symptoms of radiation sickness and a mortality risk of 90 - 100 % [78]. Stochastic effects arise from mutations after radiation-induced DNA damage that lead to the development of cancerous diseases where the exposition dose increases the probability but not the severity. Stochastic effects can not be ruled out even at doses well below the thresholds for deterministic effects. In the context of radiation protection, dose is conventionally not given in units of Gy but as equivalent dose in units of Sv, incorporating the biological effects of different types of ionising radiation and the vulnerabilities of different tissues. However, for X-radiation and under the assumption of accidental full-body exposition, a dose of 1 Gy equals 1 Sv [78]. According to German law, different radiation protection areas are defined according to the equivalent dose a person staying there could be exposed to. Due to the research facility the laboratory containing the LFXT prototype is located on, the area surrounding the room is already classified as a surveillance area. In contrast to a normal area, where a person continuously staying there may only receive up to 1 mSv over the course of one year in addition to natural and medical exposition, a person working 40 hours per week for 50 weeks per year in a surveillance area may be exposed to up to 6 mSv [78, 79]. Within the laboratory, a control area can be established, if necessary, where working personnel may be exposed to up to 20 mSv per year. However, if possible, the design of structural radiation protection measures

should always reduce the dose exposition to below 1 mSv/a. Overall, German radiation protection laws are significantly more complex than those introduced here. In principle, the safety system has to minimise the exposition of personnel, whether involved in the operation of the LFXT prototype or not, to ionising radiation and ensure that any potential exposition stays below the thresholds. This is the so-called ALARA ("as low as reasonably achievable") principle.

The second danger source is connected to the heat capacity limit the LFXT prototype is based upon. For operation within the heat capacity limit, high surface speeds of the target are required, leading to a significant amount of rotational energy. The drive train of the LFXT prototype is designed to propel the about 40 kg heavy target rotor-complex to a rotation frequency of about 200 Hz, corresponding to a rotational energy of about 476 kJ [21]. For comparison, a normal car with a mass of 1500 kg going 90 km/h has about the same amount of kinetic energy. Under normal circumstances, the rotating components are encased within the vacuum chamber. Still, in case of a malfunction of the bearings, the rotational energy could spontaneously be conferred to the chamber, posing a significant threat. Additionally, the probability of the target bursting into fragments due to the high thermal and mechanical stresses is low but not negligible. The safety system needs to ensure that, in case of a malfunction, the released rotational energy is contained and dispersed such that no personnel is harmed.

The third danger source is closely related to the HV system as presented in chapter 7. The safety system needs to guarantee that the HV generators can not be activated while any personnel is in the proximity of them or potential-carrying components. Additionally, it needs to be ensured that no personnel can come into proximity before the whole system is fully discharged and secured again. In case of an electrical malfunction, e.g. an electrical arc, any currents flowing need to be safely dispersed and insulated from personnel to avoid harm.

## 8.2 Radiation protection

As mentioned, one of the major sources of danger during the operation of the LFXT prototype the safety system needs to protect personnel from is the produced ionising X-radiation. According to simulations, the LFXT prototype produces a dose rate of 10 Gy/s in water within the primary beam at a distance of 20 cm from the focal spot, which corresponds to an equivalent dose-area product of 0.4 Sv<sup>m</sup>/s [42]. In order to shield personnel from this high amount of radiation, the LFXT prototype is encased within an X-ray protection cabinet built from lead bricks held in place by an aluminium profile skeleton. For practical reasons, the X-ray cabinet can not be fully sealed but requires a door to allow personnel to enter and a so-called shielding maze as a feed-through for cables, pipes and similar conduits. Both the door and the shielding maze are designed such that no direct line of sight from inside the cabinet to the outside is available, and a single X-ray photon would need to be scattered at least twice to leave the cabinet. The interfaces between the lead bricks that make up the walls, floor, and ceiling of the cabinet follow the same design principle.

In fig. 8.1, the layout of the building the LFXT prototype is situated in is depicted. The LFXT prototype is contained within the X-ray cabinet, which, in turn, is positioned in the laboratory. As mentioned before, the LFXT prototype produces three primary beams, with two of them in the horizontal plane and the third going downwards. Additionally, stray radiation is present due to other ports on the vacuum chamber (e.g. the Pyrometer pipes) or transmission through the chamber (e.g. through the weakly absorbing electron source complex). Within the cabinet, the LFXT prototype is oriented such that no primary beam is directed at the door of the cabinet or the shielding maze, as these are potential weak spots in the shielding. Surrounding the X-ray cabinet, a danger zone exists where no personnel can be present during operation due to the required high acceleration voltage as presented in chapter 7 and later discussed in more detail in section 8.4 of this chapter. Enclosing the danger zone are the operator area, the catwalk, the hallway and the adjacent laboratory. The catwalk and the hallway are circulation areas where personnel not involved in the operation of the LFXT prototype may be present for limited amounts of time. In the operator area, personnel involved in operating the LFXT prototype resides during irradiations. In the adjacent laboratory, uninvolved

personnel may be present for extended amounts of time, making it the most critical area, especially as it is partly in the direction of one of the primary beams.

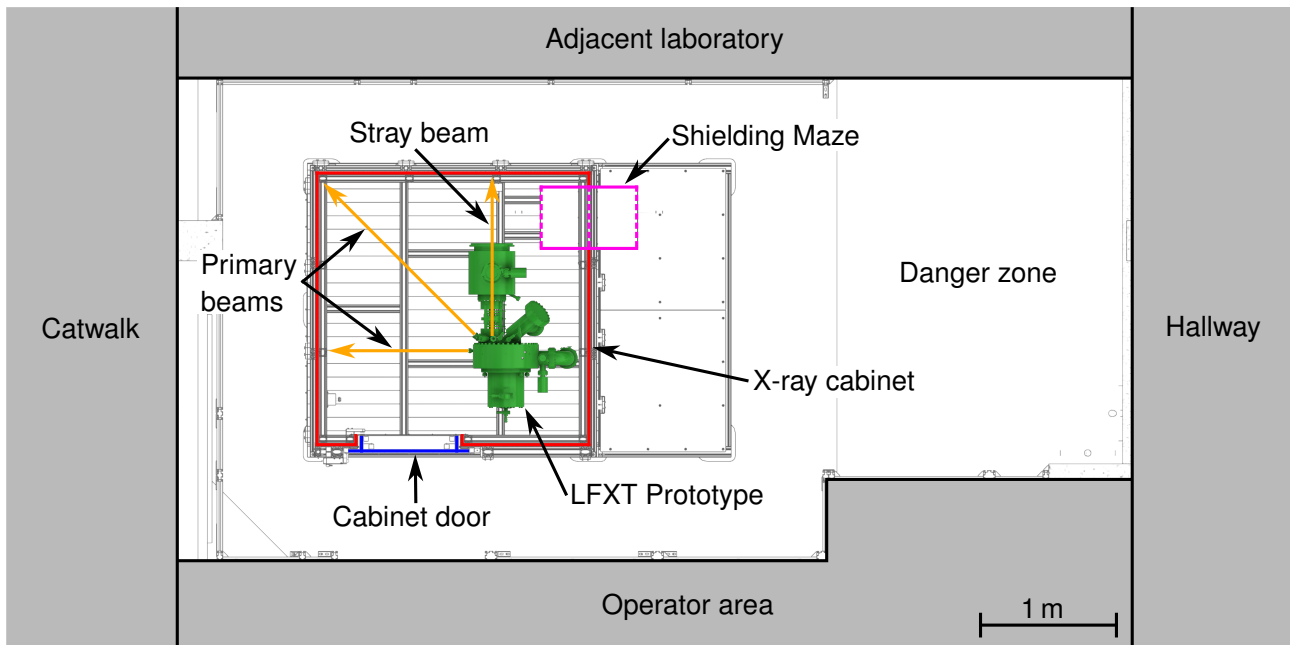


**Figure 8.1** Laboratory layout depicting the different areas surrounding the X-ray cabinet containing the LFXT prototype. Areas in which personnel can be present during operation are marked in grey. In white, the danger zone surrounding the X-ray cabinet, where no personnel can be present during the operation, is depicted. The lead walls of the X-ray cabinet are sketched in red, and the door and the maze of the cabinet are drawn in blue and magenta, respectively. In orange, the two horizontal primary beams and the horizontal stray beam through the electron accelerator are signified. The depiction is to scale defined by the scale bar in the lower right corner.

Attenuation factors from radiation protection literature are used to calculate the required thickness of the lead walls of the cabinet. As reference position, a distance of 2.5 m to the focal spot along the primary beam with the highest dose rate is assumed, and geometric influences due to angled walls are neglected. Overall, these assumptions are conservative and lead to overestimating the required shielding thickness. Without shielding, the dose rate in the reference position would amount to 64 mSv/s during an active pulse, corresponding to an accumulated dose of 7 554 Sv over the course of one work year with maximum cyclic utilisation of the LFXT prototype defined by 20 s pulses followed by 20 min intervals. According to German radiation protection laws, a work year is defined as 50 weeks with 40 hours per week [78]. From the accumulated dose without shielding and the maximum dose, the required inverse attenuation coefficient and the required shielding thickness can be calculated. To reduce the accumulated dose below the threshold for surveillance areas of 6 mSv, an inverse attenuation coefficient of less than  $7.9 \times 10^{-7}$  and, to achieve that, a lead thickness of about 25 mm is required [78]. It is important to mention here that the lead thickness derived from the literature is meant for a 300 kVp spectrum pre-filtered by a 3 mm thick copper filter, but the simulated dose rate is given for an unfiltered spectrum [78, 22]. Due to this, the spectrum used in the literature is significantly harder than the simulated spectrum, which leads to an additional overestimation of the required lead thickness.

To validate the calculated lead thickness, Monte-Carlo simulations using TOPAS [80, 81] for the dose-to-water distribution in three dimensions around the X-ray cabinet were conducted. For reasons of efficiency and due to restrictions of the simulation tool, the simulations were split into several steps. In the first step, multiple Monte-Carlo simulations were performed in which a beam of electrons with kinetic energies of 300 keV was directed into a 20 mm long and 50  $\mu$ m wide focal spot on a model of the target. The target model consisted of a 2 cm thick layer of Molybdenum with a 1 mm thick tungsten conversion layer on top where the electrons impinged. A spherical phase space scorer encasing the target then registered the photons generated from the interactions of the electrons with the target. In the resulting phase spaces,

every photon was saved with its exact position, impulse vector and energy to act as a source in the next simulation step. Overall,  $28 \times 10^9$  electrons were simulated in the first step, resulting in more than  $560 \times 10^6$  scored photons. In the second step, the phase spaces generated before were used as photon sources in Monte Carlo simulations and placed within a simplified model of the vacuum chamber of the LFXT prototype made from steel. In a  $5 \times 5 \times 5 \text{ m}^3$  box made of air around the vacuum chamber, the dose-to-air was then scored in  $512 \times 512 \times 512$  voxels. The lead shielding of the cabinet could not be directly modelled in the simulations as, due to the high attenuation, not enough statistics could have been gathered outside the cabinet within a reasonable amount of simulation time. For the simulations in the second step, every phase space generated during the first step was repeated ten times, and the scored doses were summed up, resulting in the scored dose corresponding to an irradiation time of  $1.5 \times 10^{-7} \text{ s}$  at an electron beam current of 300 mA. Overall, the simulations for the first and second steps took over one week to conclude on a high-powered computer.

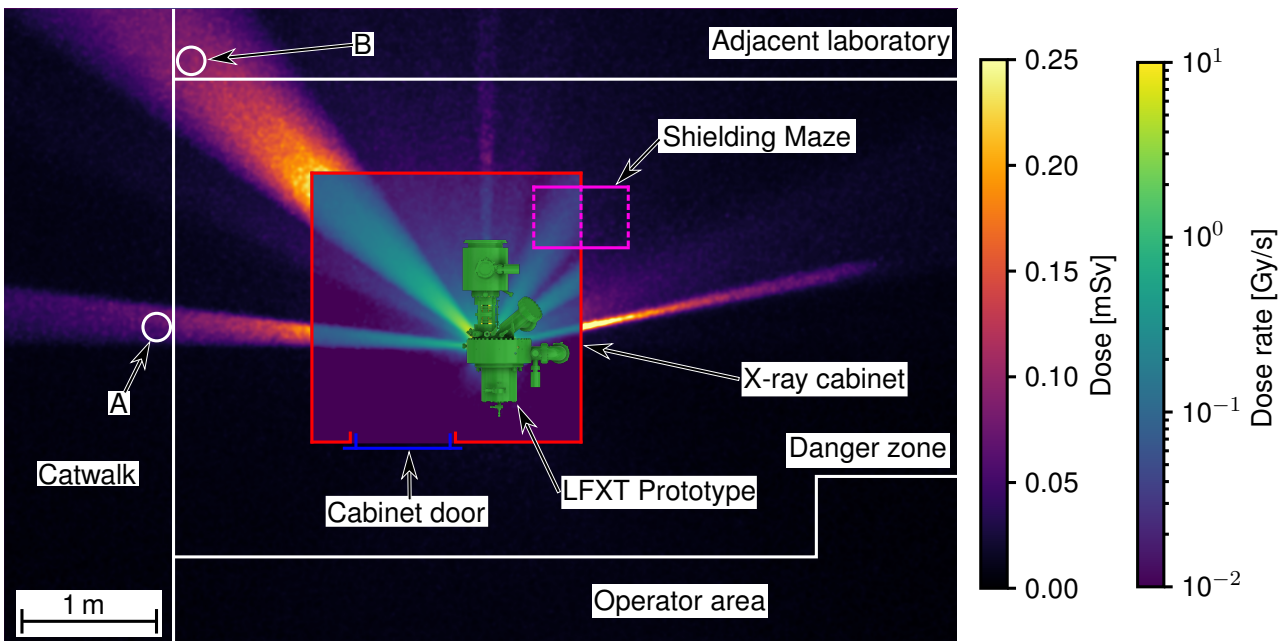


**Figure 8.2** Simulated dose-to-water distribution around the LFXT prototype and the X-ray protection cabinet. The simulated dose distribution is overlaid over the laboratory layout (equivalent to fig. 8.1) incorporating the different areas and the X-ray cabinet with its door and shielding maze containing the LFXT prototype. The dose distribution is shown as a maximum-intensity projection along the vertical dimension for an electron beam current of 300 mA at an acceleration voltage of 300 kV. Inside the cabinet, the maximum dose rate during a pulse in units of Gy/s is depicted on a logarithmic scale corresponding to the right colour bar. Outside the 25 mm thick lead shielding of the X-ray cabinet, the dose accumulated over the course of one work year, as defined by German radiation protection laws, is depicted under the assumption of cyclic operation at maximum utilisation. The dose distribution outside the cabinet is given in units of mSv according to the left colour bar. In area **A**, situated on the catwalk within one of the primary beams, a person would be exposed to a dose of  $(0.0552 \pm 0.0013) \text{ mSv}$  over the course of one work year. In area **B**, in the corner of the adjacent laboratory hit by the other primary beam, the accumulated dose would amount to  $(0.0901 \pm 0.0009) \text{ mSv}$ .

In the third step, the X-ray energy spectrum was calculated from the phase spaces simulated in the first step and filtered by 25 mm lead using spectral interaction cross-sections from the xraylib [82]. This resulted in the unfiltered spectrum, the spectrum after filtering with 25 mm of lead, and the mean attenuation factor of 25 mm of lead for the exact spectrum of the LFXT prototype. The calculated mean attenuation factor was  $6.7 \times 10^{-9}$ , which is significantly lower than the value from the radiation protection literature mentioned before by about two orders of magnitude due to the softer spectrum without the copper filtering. In the fourth step, Monte Carlo simulations for the conversion between the scored dose-to-air and the desired dose-to-water were performed. For that, three simple simulations consisting of a parallel beam photon source emitting either the filtered or the unfiltered X-ray spectrum and a block of either air or water within

which the dose was scored were conducted. By comparing the dose deposited by the unfiltered spectrum in a block of air to the doses deposited by the unfiltered and the filtered spectra in a block of water, conversion factors from dose-to-air scored in the second step to dose-to-water inside and outside the X-ray cabinet were derived. For the dose outside the cabinet, the mean attenuation factor was additionally factored in. The scoring block used in the simulations was chosen large enough that scattering out of the volume could be neglected and with a thickness of 20 cm, mimicking the cross-section of a human body. In the fifth and last step, the three-dimensional dose-to-air distribution scored in step two was split into regions inside and regions outside the X-ray cabinet and converted into dose-to-water according to the conversion factors derived in step four. Using the overall number of simulated electrons, the resulting absolute dose values were converted into dose rates under the assumption of the maximum beam power the LFXT prototype is designed to deliver.

In fig. 8.2, the resulting dose distribution inside and around the X-ray cabinet is depicted as a maximum-intensity projection along the vertical axis. Inside the X-ray cabinet, close to the primary exit window of the vacuum chamber, the simulated dose rate amounts to about 10 Gy/s, which is in very good accordance with the former simulations given by Winter et al. [42] and therefore validates the simulations conducted here. Outside the X-ray cabinet, the dose accumulated by a person standing a full work year at a specific position while the LFXT prototype operates in its maximum duty cycle is given. In the two most critical points where a person could be standing as close as possible to the X-ray source within one of the primary beams, the accumulated doses would be  $(0.0552 \pm 0.0013)$  mSv and  $(0.0901 \pm 0.0009)$  mSv according to the simulations, given on a confidence interval of  $\sigma$ . These values are significantly below the threshold for a surveillance area of 6 mSv and even below the threshold for a normal area of 1 mSv, therefore validating the functionality of the 25 mm lead shielding. The difference to the values calculated from the radiation protection literature can be traced back to spectral effects and the, in general, very conservative calculations done before. Overall, a shielding of 25 mm lead leaves a sufficient margin of safety and is highly effective in minimising the exposition of personnel to ionising radiation.

### 8.3 Protection from drive train malfunction

As mentioned before, the quickly rotating target rotor complex weighing about 40 kg and containing a rotational energy of about 476 kJ at maximum velocity poses a significant threat in case of malfunction not only to the machine itself but also to personnel in its vicinity. The safety system needs to ensure that the high amount of rotational energy remains encapsulated and is safely dispersed in case of malfunction without posing a threat to persons involved or uninvolved with the operation of the LFXT prototype. In general, two types of malfunctions were identified that could lead to the uncontrolled release of rotational energy from the target rotor complex. Firstly, a malfunction of the bearings between the target rotor complex and the steady axis could lead to a blockage of the bearings and, therefore, to the rotational energy being transmitted spontaneously into the steady axis and, from that, potentially into the vacuum chamber. The second type of malfunction is the target losing its structural integrity due to the high temperature gradients and the high rotational forces and bursting into fragments. The individual fragments could potentially carry high amounts of kinetic energy and act as shrapnel.

Different measures have been taken to minimise the threat ensuing from the rapid rotation. The steady axis of the LFXT prototype is connected to the vacuum chamber only on one side, and there are only eight M3 screws. In case of a blockade of the bearings, the rotational energy would be transmitted into the steady axis, which would lead to the screws between the axis and the vacuum chamber breaking and the axis rotating more or less freely within the chamber, dispersing its energy over friction with the inside of the chamber. Therefore, the rotational energy from the target rotor complex would comparably slowly be transferred onto the vacuum chamber. The vacuum chamber, in turn, weighs about 500 kg and is fixed to the X-ray cabinet, allowing it to transfer the energy further onto the cabinet, weighing about 8 tons, which will not significantly move due to it.

The first measure taken to minimise the threat posed by highly energetic fragments of a bursting target is the thickness of the walls of the vacuum chamber. Surrounding the target, the walls of the vacuum chamber

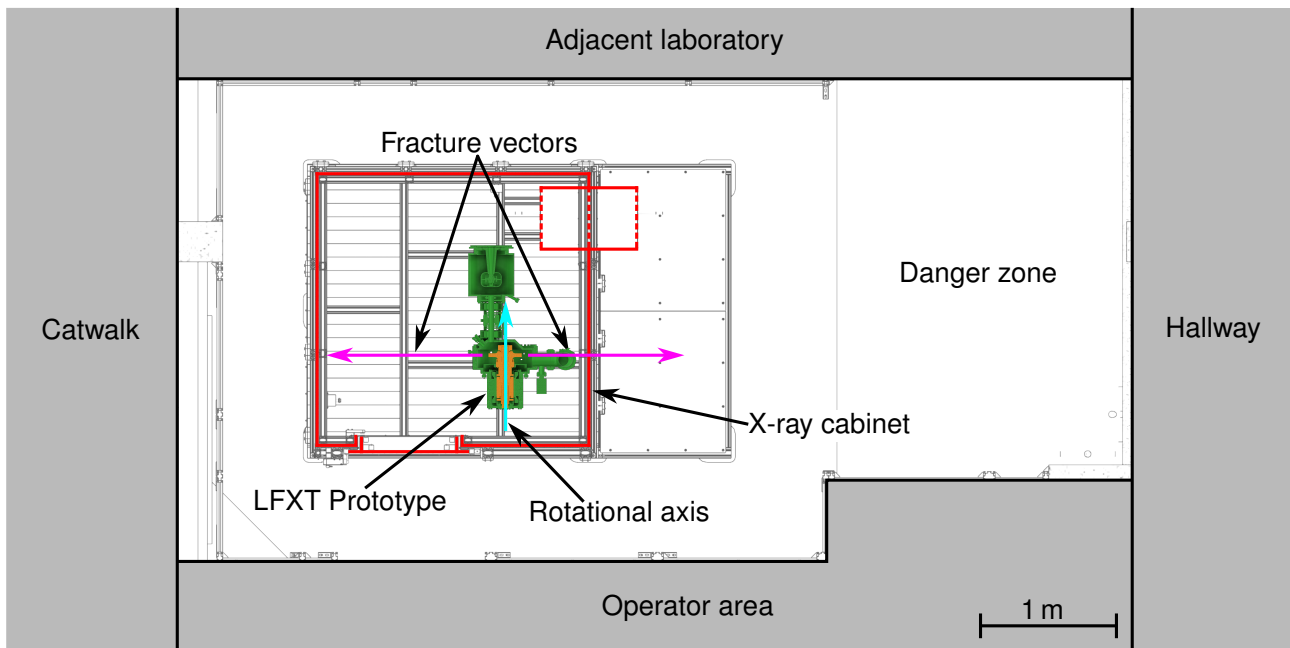


**Figure 8.3** Laboratory layout depicting the different areas surrounding the LFXT prototype and the quickly rotating target rotor complex as danger source. In green, the vacuum chamber of the LFXT prototype is depicted, containing the target rotor complex in orange. The rotational axis of the target rotor complex is drawn in blue, and the potential fracture vectors in the horizontal plane in case of the target fracturing are sketched in magenta. Surrounding the LFXT prototype, the lead walls of the X-ray cabinet are shown in red. In the danger zone depicted in white, no personnel can be present during the operation of the LFXT prototype, but in the grey areas, personnel may be present for varying amounts of time.

are made of 35 mm thick stainless steel, effectively blocking most potential fragments from leaving the vacuum chamber according to unpublished experience gathered by a cooperation partner from fracturing neutron choppers. Only smaller fragments with a diameter below about 16 mm and, therefore, lower energy could leave the vacuum chamber through the ports meant for the X-ray beams or the pyrometers. These smaller, less energetic fragments would then hit the 25 mm thick lead walls of the cabinet and, as lead is ductile, would quickly lose their energy.

In fig. 8.3, the last measure taken is sketched. The LFXT prototype is oriented such that the rotational axis is directed at the operator area and the adjacent laboratory, and, therefore, the potential impulse vectors of fragments or the whole chamber are parallel to these areas. Within the danger zone around the X-ray cabinet, no personnel can be present during the operation of the LFXT prototype for reasons explained in section 8.4. The motor driving the target rotor complex is only activated during the operation if the danger zone is sealed. In the operator area and the adjacent laboratory, personnel may be present for considerable amounts of time, and therefore, these areas have the highest priority. The catwalk and the hallway, where the potential fracture vectors are directed, are circulation areas where persons only spend very limited amounts of time, reducing the risk probability. The catwalk is especially used only in case of fire alarms and by security personnel a couple of times per day. Between the catwalk and the X-ray cabinet, there is only a window and no additional material that could act as a shield against fragments, but between the hallway and the X-ray cabinet, a thick stone wall is present.

Overall, the probability of any released rotational energy posing a significant threat to personnel outside the X-ray cabinet or the danger zone surrounding it is very low due to the vacuum chamber and the X-ray cabinet absorbing most, if not all, of the potential kinetic energy. The probability of personnel damage is further reduced by orienting the impulse vectors such that they face areas where no personnel is continuously present and partly where additional walls that act as kinetic shields exist. However with a very high probability, the machine would be fully destroyed in case of a bearing malfunction or a bursting target.

## 8.4 Protection from high-voltage

The third major hazard ensuing from the operation of the LFXT prototype is the HV applied for electron acceleration. Due to the insulation concept, as detailed in chapter 7, the whole X-ray cabinet is on up to 150 kV during operation, and it needs to be ensured by the safety system that no personnel can be in proximity of charged components when the HV system is being activated or can get into proximity while not all components are fully discharged again. Additionally, the safety system needs to ensure that all charge is safely dispersed in case of a malfunction without posing a threat to persons residing in the laboratory.

In fig. 8.4, the main components important for the HV part of the safety system are depicted. The laboratory room is separated into the danger zone and the operator area by the front of the fence, as already mentioned in chapter 7. Within the danger zone, the X-ray cabinet and the different devices that are part of the HV system are located, and no personnel may be within the danger zone during the operation of the LFXT prototype. In the operator area, normal laboratory equipment can be placed and used by personnel also when the HV system is active. The front of the fence is designed in a double-layered manner, where the side facing the danger zone is made from a metallic mesh connected on several points to electrical ground, thereby acting as an antipole to the X-ray cabinet, as explained in chapter 7. The side of the fence facing the operator area is layered with transparent Polymethylmethacrylate (PMMA) plates, so no metallic parts of the fence can be touched by accident. Without this double-layered design, a person accidentally touching the fence when an electrical arc from the X-ray cabinet to the fence occurs would be circuited in parallel to the inner resistance of the fence, leading to an electrical current through the body. The electrical current would be minimal but nonetheless present and could potentially lead to harm. With the double-layered design, the touchable surface of the fence is fully insulated from the metallic and potentially current-carrying parts. Additionally, it is impossible to accidentally reach through the metallic mesh and provoke an electrical arc. The door of the fence is fitted with a specialised locking mechanism to render it impossible to enter into the danger zone while charge is present.

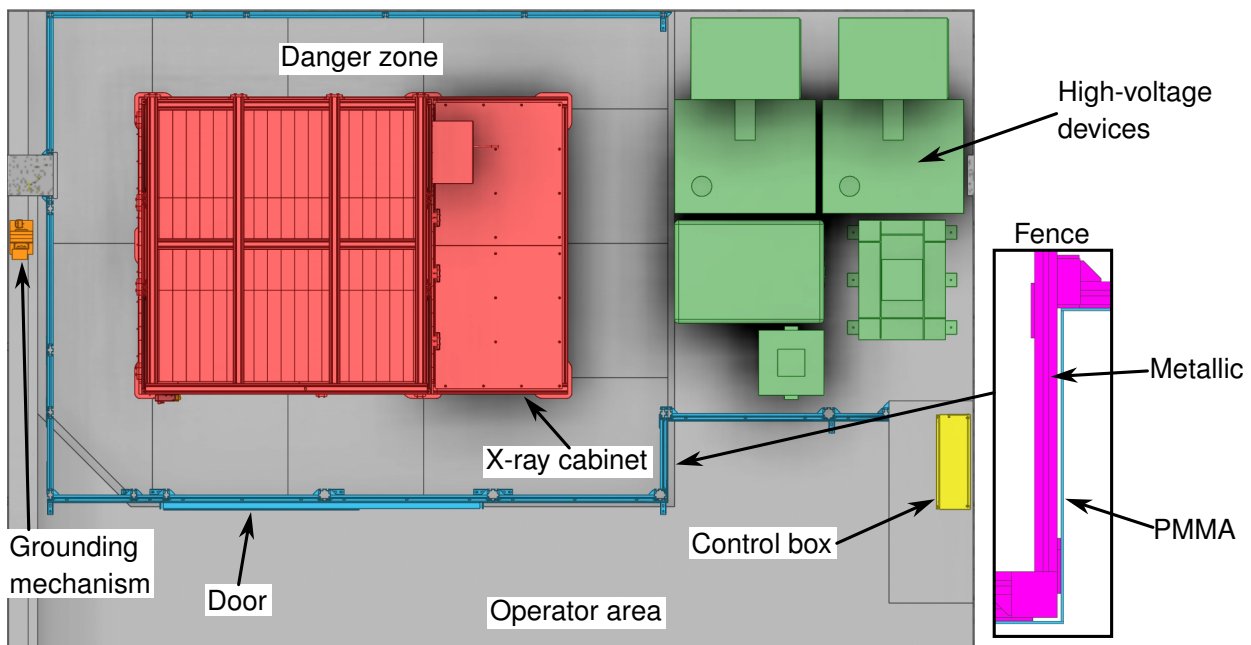


**Figure 8.4** Laboratory layout depicting the HV danger zone containing the X-ray cabinet in red and the HV devices in green. The danger zone is separated from the operator area by the fence drawn in blue, and on the windowsill on the left, the grounding mechanism is shown in orange. On the right, a section of the fence is depicted in a magnified view to visualise the double-layered design with the metallic parts drawn in magenta and the PMMA parts drawn in blue. Above the laboratory entrance, the main control box of the safety system is depicted in yellow.

Before entering the danger zone after the HV system was active, it needs to be ensured that all remaining electrical charge stored within the capacities of the HV system is fully dissipated. For that, the

automatic grounding mechanism, presented in detail in chapter 7, connects the X-ray cabinet to the electrical ground and thereby discharges it. The grounding mechanism is designed such that an electrical signal and pressurised air are required to disconnect the X-ray cabinet from the electrical ground, but in case of a power outage or a loss of air pressure, the cabinet is automatically discharged without intervention. Two redundant sets of switches monitor the configuration of the grounding mechanism, making sure that the X-ray cabinet is fully disconnected from the electrical ground or fully connected. In addition to the automatic grounding mechanism, a manual grounding rod is available in the laboratory for redundancy and in case of a malfunction of the automatic system. A programmable logic controller (PLC) integrated into the control box depicted in fig. 8.4 controls the automatic grounding mechanism, the locks of the fence and X-ray cabinet, and the safety interlocks of the HV sources.

## 8.5 Overview and discussion

In the preceding chapter, the main components of the safety system have been presented. The purpose of the safety system is the protection of personnel from ionising X-radiation, the high acceleration voltage, and the rapidly rotating target rotor complex. Protection against ionising radiation is achieved by the X-ray cabinet consisting of an aluminium skeleton and 25 mm thick lead walls. In Monte Carlo simulations, it has been proven that the design of the X-ray cabinet is highly effective in minimising the amount of radiation dose personnel involved in the operation of the LFXT prototype and personnel in proximity to the laboratory is exposed to. To minimise the threat ensuing from the rapidly rotating target, the orientation of the rotational axis of the target rotor complex, together with the design of the vacuum chamber of the LFXT prototype and the X-ray cabinet, is important. The rotational axis of the target rotor complex is oriented such that the movement vectors of potential fragments from a bursting target do not face areas where personnel may be present for extended amounts of time. Additionally, any fragment would need to pierce through the 35 mm thick steel wall of the vacuum chamber and the 25 mm thick lead wall of the X-ray cabinet before posing a threat to personnel around the X-ray cabinet. In case of a malfunction of the bearings on which the target rotor complex is mounted, leading to a spontaneous transfer of the rotational energy from the target rotor complex into the steady axis, the weight of the X-ray cabinet is sufficiently high to dissipate the energy without posing a threat to personnel. However, both in the case of a bursting target and a bearing malfunction, the near complete destruction of the LFXT prototype itself and surrounding components is highly probable. To ensure that the high acceleration voltage does not lead to personnel damage, the area around the X-ray cabinet and the HV devices is separated from the operator area by a double-layered fence. The side of the fence facing towards the X-ray cabinet is made of a metallic mesh connected to the electrical ground, acting as a Faraday cage and shielding the operator area from electrical arcs. Towards the operator area, the fence is layered with PMMA plates to prevent accidental contact with the metallic and potentially current-carrying parts and to prohibit anything from reaching through the fence. The fence is fitted with a safety lock, and the sliding door of the fence can only be opened if the X-ray cabinet is fully discharged and safely connected to the electrical ground. For the connection of the X-ray cabinet to the ground, an automatic grounding mechanism is used, and additionally, a manual grounding rod is available for redundancy and in case of a malfunction of the automatic grounding mechanism.

In addition to the main components explained before, the safety system contains a series of emergency stops in strategic locations, a signal lamp depicting the status of the system, a siren and warning lights, as well as several buttons for user interactions. A PLC controls all procedures and components of the safe system, including the door locks and the interlocks of the target motor and of the HV generators. Interlocks are safety features that allow the safety system to prohibit the operation of components that would otherwise threaten personnel. The two most important procedures integrated into the safety system are the search procedure before the HV generators and the target motor are activated and the opening procedure after an operation cycle. The purpose of the search procedure is to ensure no personnel is within the danger zone behind the fence or the X-ray cabinet before releasing the interlocks of the HV generators and the target motor and locking the doors of the X-ray cabinet and the fence. During the search procedure, a loud siren and blinking warning lights alert all personnel within the lab of the imminent

activation of the LFXT prototype, and the interlocks are only released after the doors are locked and the grounding mechanism is fully disconnected. After an operation cycle, the doors remain locked until the opening procedure is finished. The main purpose of the opening procedure is to ensure the X-ray cabinet is fully discharged and the target motor is stopped before the doors are unlocked, and personnel may enter the danger zone and the X-ray cabinet again. In fig. 8.5, photographs of the fence and X-ray cabinet as they are built in the laboratory are presented with the mentioned parts highlighted. The automatic grounding mechanism is not depicted here, as it was already shown in detail in chapter 7.

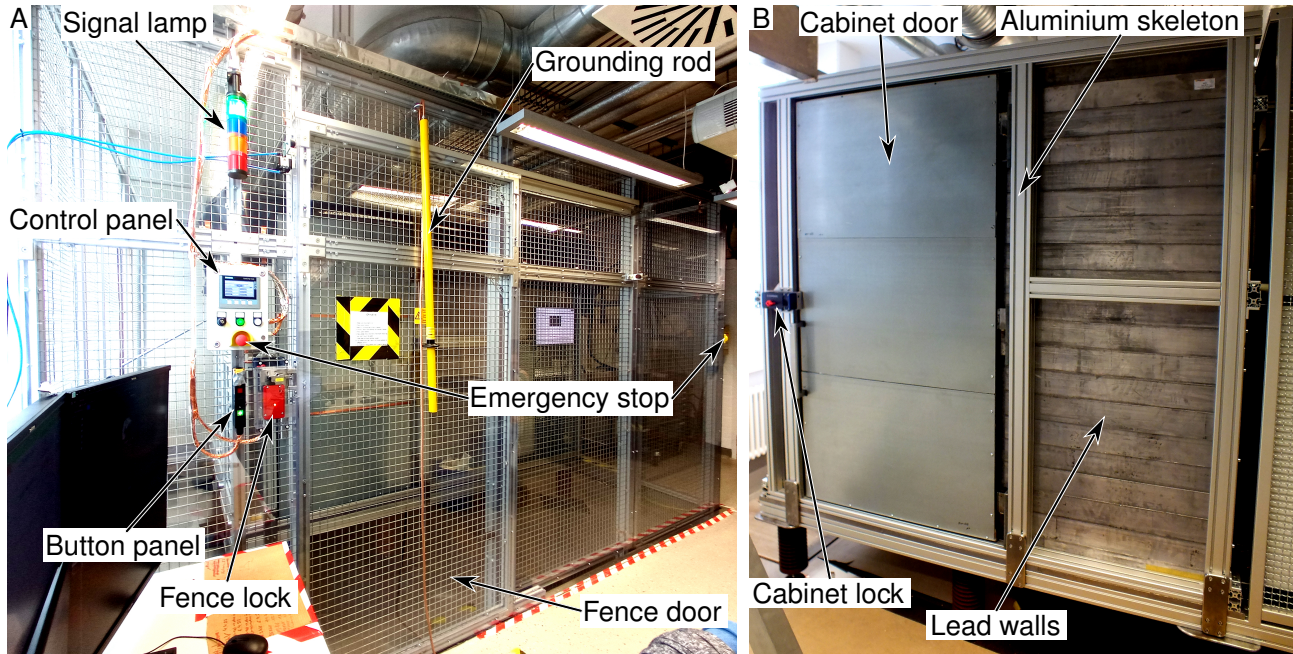


**Figure 8.5** Annotated photographs of the fence and the X-ray cabinet as the most crucial parts of the safety system. In **A**, the double-layered fence consisting of metallic meshes held by aluminium profiles layered with PMMA plates is depicted. The metallic mesh is well visible, and the PMMA plates can be seen from the reflections on the fence. The door of the fence with its lock is labelled, as well as the manual grounding rod hanging in front of it. To the left of the fence door, the button and control panels and the signal lamp are visible. Additionally, two emergency stop buttons are marked. The siren and warning lights used for the search procedure are not visible, as they are located behind the fence within the danger zone for obvious reasons. In **B**, the X-ray cabinet is shown consisting of the 25 mm thick lead walls made from bricks surrounded by a skeleton made from aluminium profiles. The door of the cabinet with its lock is labelled.

At the time of writing this work, the safety system is fully set up and functional. The LFXT prototype has not yet been operated at full power, and therefore, the final conclusion concerning the efficiency of the X-ray cabinet in protecting personnel from ionising X-radiation can not yet be drawn. However, in all experiments conducted up to the time of writing, no radiation above the background noise level could be measured at any point outside of the X-ray cabinet. Concerning the efficacy of the vacuum chamber and the X-ray cabinet in dissipating the energy from a bearing malfunction or bursting target, no conclusion can be made so far, as no such incident occurred until the time of writing and hopefully never will. The protection against the HV has been fully tested up to the maximum voltage of the X-ray cabinet of 150 kV and also in the incident of an electrical arc between the X-ray cabinet and the fence. The fence is able to quickly dissipate any charge in case of an electrical arc, and no metallic parts of the fence can be touched by accident. The automatic grounding mechanism is in regular operation and has, up until the time of writing, not had a single malfunction. The manual grounding rod is easy to use as a redundant method of discharging the X-ray cabinet before entering the danger zone. The search and opening procedures the safety system enforces are also used regularly at the time of writing and are working as intended.



## 9 Control system

In the following chapter, the control system of the LFXT prototype is presented. As explained in chapter 4, the purpose of the control system lies in monitoring and controlling all components needed for the correct operation of the LFXT prototype. The control system can be split into the hardware and the software parts, where the hardware part gathers all physical components, including the network architecture, and the software part contains the program architecture, which consists of a client and server side. Below, the requirements for the control system will be laid out in detail, followed by explanations of the software and hardware parts. At the end of the chapter, an overview of the whole system will be given together with its realisation at the time of writing and a short discussion.

### 9.1 Requirements

As mentioned in chapter 4, the purpose of the control system is to act as the central nexus of the LFXT prototype by controlling and monitoring all components. Monitoring is a mostly passive process and includes gathering the status of all components regularly, logging it where it is appropriate, and potentially reacting to critical conditions to protect the machine from damage. Controlling the LFXT prototype is the active part of the control system, as it includes, in general, the execution of requests from users to change the parameters of the machine, e.g. setting the acceleration voltage or irradiating with a defined amount of dose.

On the software side, there are only a few hard requirements, allowing for a large design space. The software architecture needs to be able to control and monitor a large number of different components simultaneously, rendering a high level of concurrency crucial. For example, it needs to be possible to change the parameters of the beam-focusing components while controlled irradiation is ongoing, for which the dose needs to be closely monitored. To allow for future changes to the control system, e.g. in case of the addition or exchange of a component, to be performed in a straightforward manner and, in general, to allow for easy maintainability, the software architecture should be built in a modular manner adhering to the rules of object-oriented programming. Concerning communication with the components, the control system needs to support a large variety of different interfaces, ranging from simple serial interfaces over network-based interfaces like transmission control protocol (TCP) and user datagram protocol (UDP) to proprietary interfaces. Additionally, it is desirable for the control system to be able to handle inputs from and outputs to several users simultaneously to allow different users to control and monitor different parts of the LFXT prototype during operation, e.g. one user controls the X-ray beam whilst another user controls some experimental setup.

The main requirement for the hardware architecture of the control system is to support the software architecture that needs to run on it. Therefore, the requirements for the hardware architecture partly mimic the requirements for the software architecture. Due to the high level of concurrency required in the software part, the hardware part needs to provide sufficient computational power for it. The general need for a large variety of different interfaces means the hardware of the control system must provide not only a sufficient variety of connection terminals but also a sufficiently high number of them. To support several users concurrently, a number of independent user terminals are required. In addition to these requirements derived from the software architecture, other constraints also apply to the hardware architecture. The design of the HV system presented in chapter 7 heavily influences the design of the hardware architecture of the control system, as direct conductive connections using conventional cables are not possible between areas of different electrical potentials. A conventional connection running from the danger zone behind the fence to the operator area as defined in chapter 8 is also not possible, as it would circumvent the

electrical insulation and safety that the double-layered fence establishes. The last requirement for the hardware architecture originates from security concerns, as an unauthorised external intrusion into the control system could inflict severe and potentially irreparable damage on the LFXT prototype. While the internal network of the research facility, the LFXT prototype is located in, is already highly secured, it is therefore still highly advisable to isolate the control system from the facilities network either physically or by a sufficiently strong firewall blocking all but required and authorised communications.

## 9.2 Software

The software of the control system of the LFXT prototype is designed in server-client architecture. The server-client architecture was chosen to support several clients and, thereby, users simultaneously. The client is designed as an interaction point for the user, comprising a graphical user interface (GUI) and an interface for communication with the server, but no logic for direct control of devices. The server handles all communications with the devices, including monitoring their statuses and handling commands. Communication between client and server is established via a rest-like hypertext transfer protocol (HTTP) interface and is, as such, platform-independent, meaning neither the operating systems nor the programming languages of the server and the clients need to be identical. In the following, the basic architecture of the server is presented. The client consists mainly of a GUI and the HTTP interface and does not contain a significant amount of logic for the operation of the control system. Therefore, the design of the client will not be presented in detail.

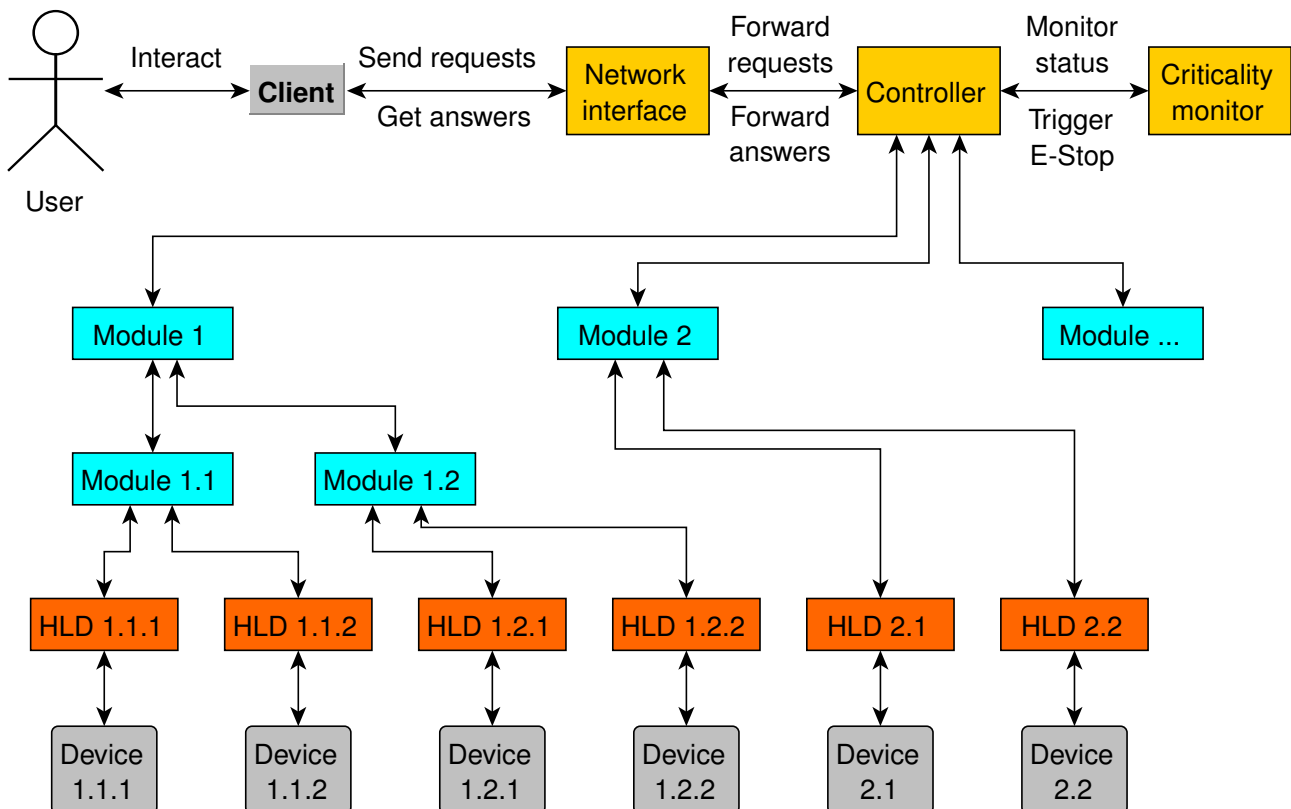


**Figure 9.1** Exemplary overview graph of software architecture depicting the modular tree-like hierarchy of the server. An exemplary user interacting with a client is depicted and the top-level classes of the server existing only once are depicted in yellow. In blue, the module tree defining the structure of the server hierarchy is presented, and in orange, the HLDs are shown. For every HLD, the controlled device is depicted in grey at the very bottom.

In fig. 9.1, an example of the modular tree-like architecture of the server is shown. The server architecture can be split into the top level, the module tree, and the high-level drivers (HLDs). On the top level,

three distinct objects, which are instances of three different classes, are present. The network interface provides the HTTP interface for communication with the clients and forwards formatted client requests for handling by the rest of the server. The so-called controller is the root of the tree-like hierarchy of the server architecture and acts as the central nexus of the server. The main functionality of the controller lies in governing the server startup and shutdown procedures and forwarding requests to and from the module tree. Additionally, the controller executes the emergency stop procedure in case it is required. The last object on the top level is the criticality monitor. The criticality monitor is concerned with machine safety, with its only function being the continuous monitoring of the full status of the LFXT prototype for critical conditions and triggering the emergency stop procedure in the controller in such cases. The module tree is what defines the tree-like hierarchical structure of the server architecture and consists of a multitude of module objects. Every module object is an instance of a corresponding module class and may only exist once. The module classes inherit from an abstract base class containing the functionality common to all modules according to the rules of object-oriented programming. The purpose of an unspecified module is to forward requests and results back and forth through the module tree, giving the server architecture its structure, and to provide a location for complex commands involving several devices. In the HLD layer, communication with the devices of the LFXT prototype is finally handled. Each HLD is responsible for controlling and monitoring exactly one device and is unique within the server architecture. All HLDs inherit their basic functionality from the same abstract base class and augment it with the required functionality for their respective device.

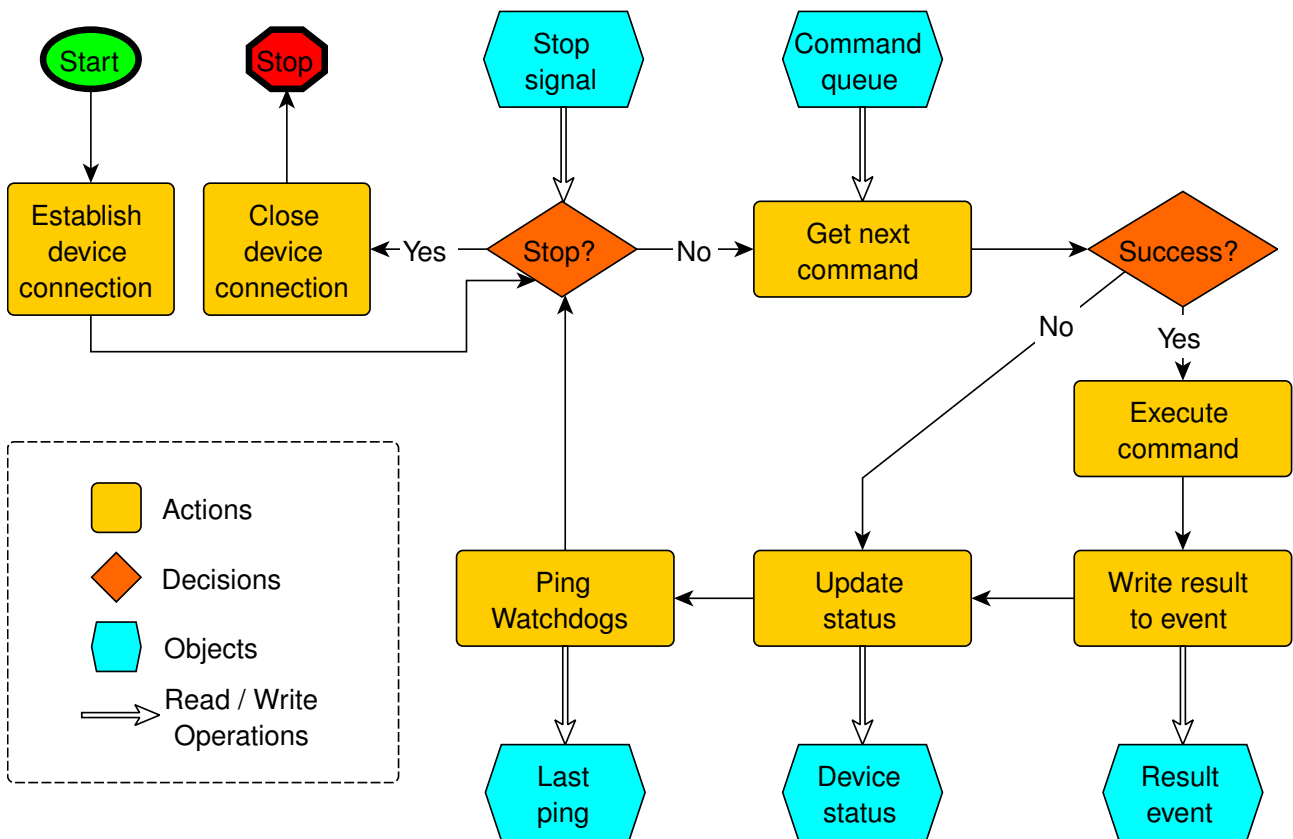


**Figure 9.2** Simplified sequence diagram of command thread in HLD depicting the running command loop. On the top left, the entry and exit points of the command loop are marked as "Start" and "Stop". Actions are depicted in yellow, decisions in orange and objects in blue. Normal arrows indicate the sequence of program parts, while hollow arrows indicate read and write operations affecting objects.

The HLDs contain the main functionality of the software part of the control system. By using an individual HLD for every piece of hardware that needs to be controlled and monitored, the individual interfaces of the devices can be fully supported, allowing for maximum flexibility and fulfilling one of the main requirements of the software. Additionally, the HLDs facilitate the required concurrency by using multithreading

with three separate threads running in continuous loops within each HLD. A thread is a sequence of code that is executed in parallel to code executed in other threads, thus allowing different tasks to be processed concurrently. The three threads running in a HLD are two so-called watchdog threads and a so-called command thread. The watchdog threads are very straightforward, with their purpose being to redundantly monitor the execution of the command thread and raise an alarm in case of a malfunction. The command thread is the most complex part of the HLD and handles all communication with the respective device, including executing commands and querying for status updates. In fig. 9.2, a simplified sequence diagram of the command thread is presented. When the command thread is started, the connection to the respective device is established, and the command loop is entered. The command loop is executed as long as no stop signal is received, in which case the loop is exited, the connection to the device is closed, and the command thread ceases execution. In the command loop, the command thread at first attempts to get a new command from the so-called command queue. A queue is a synchronisation object in multithreading, allowing one thread to put an object into the queue and another thread to get the objects from the queue in a first-in-first-out manner. If the command thread could get a new command from the command queue, meaning the queue was not empty, it executes the command by communicating with the device in one way or another and writes the result of the command into a specialised result event. An event is another synchronisation primitive in multithreading that conventionally contains a single truth value and allows threads to wait for this truth value, or in other words, for the event to be triggered. The result event used in the HLDs was augmented to be able to carry a dictionary in addition to the truth value and thus act as a communication pathway for the results of command execution. The external thread originally adding a command to the command queue receives a reference to the empty result event and can then wait for the result event to be filled and triggered by the command thread after the command was executed. If the command queue was empty when the command thread attempted to get a new command, the execution step is skipped. After a command is executed or the execution step is skipped, the command thread queries the device for its current status and writes the status into a shared variable of the HLD, which is writable by the command thread and read-only by all other threads. After updating the device status variable, a ping is sent to the watchdog threads to let them know the command loop is still functioning correctly, and the stop condition is audited before entering the next cycle of the command loop. As the command loops of all HLDs are executed concurrently, all devices can be controlled and monitored simultaneously.

For a clearer description of how a command sent from a client is executed in the server and the result is returned to the client, fig. 9.3 shows a simplified sequence diagram of exemplary command execution. The execution of a command involves mainly three threads in the server. The HTTP server thread and the command thread of the HLD the command is targeted at are running continuously within the server, and the messenger thread exists only for the time of the execution of the command. In the beginning, a command gets received by the HTTP server thread encapsulated within a HTTP request. The HTTP server thread directly spawns a messenger thread for further handling of the command and hands the HTTP request over to it before continuing its work. The messenger thread converts the HTTP request into a command format understood by the server and routes the command through the module tree to its destination HLD. In the HLD, the messenger thread adds the command to the command queue of the command thread and receives a reference to an empty result event in turn, on which it waits now to be triggered. At some point in its execution, depending on how many other commands are in the command queue, the command thread pulls the command of the observed messenger thread from the command queue and executes it. Afterwards, the command thread fills the result event with the result of the command execution and triggers it. The messenger thread gets notified about the result of its command being available, pulls the result from the result event and routes it back through the module tree to the network interface, where it places the result into the answer buffer of the HTTP network server and ceases operation. The answer buffer of the HTTP server thread functions similarly to a queue. The HTTP server thread pulls the command result from the answer buffer, packages it into an HTTP message, and sends it back to the original client. In theory, an unlimited number of messenger threads can be active simultaneously within the server, waiting for their respective commands to be executed by the command threads of the HLDs. Thus, an unlimited number of commands from a multitude of clients can be handled simultaneously.

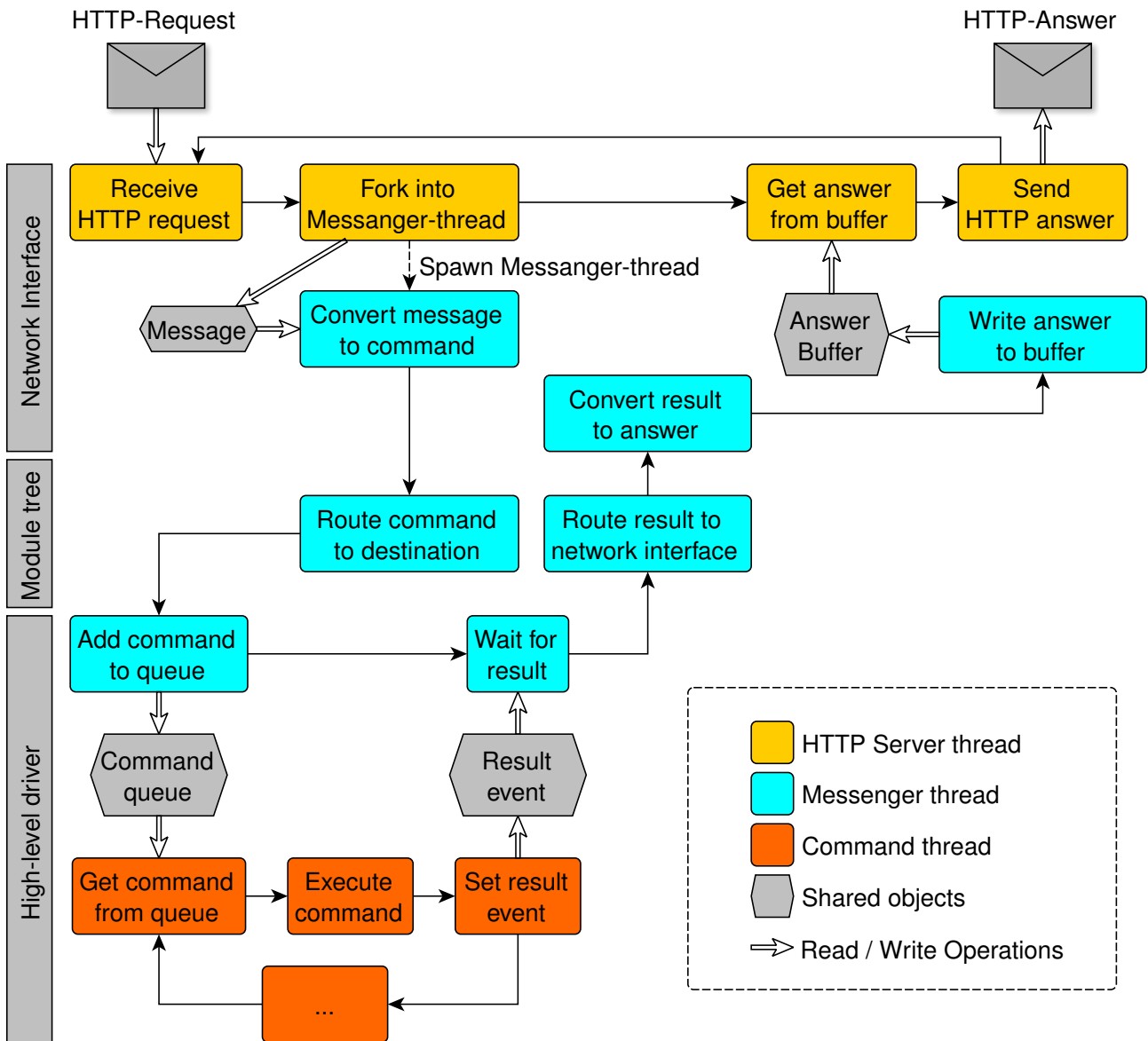


**Figure 9.3** Simplified sequence diagram of command execution in server ranging from receiving a request from a client until sending an answer. The actions carried out by the three different threads taking part in the processing of a command are depicted in yellow, blue and orange according to the legend in the figure. The shared objects acting as communication pathways between the different threads are drawn in grey. On the left, the location of the actions within the modular hierarchy of the server is registered for orientation. Normal arrows symbolise the action sequence and hollow arrows stand for read and write operations.

### 9.3 Hardware and network architecture

The hardware for the control system of the LFXT prototype is mainly designed according to the requirements of the software and under the constraints posed by the HV system and the safety system as presented in chapters 7 and 8. For the control system, a dedicated local area network (LAN) presented in fig. 9.4 was designed that is fully isolated from the network of the research facility where the LFXT prototype is located. The network architecture of the control system can be split into the hot-deck, the cold-deck, the HV area and the operator area equivalent to the areas presented in chapters 7 and 8. As mentioned in the preceding chapters, connections to and from the hot-deck and the cold-deck need to be established using non-conductive methods due to the differences in electrical potential of up to 150 kV. Additionally, any connection between the HV area and the operator area also needs to be facilitated non-conductively to ensure that in case of a malfunction, no electrical pulses can travel through conductive cabling into the operator area and harm personnel. To satisfy these requirements, all connections crossing a border between areas are facilitated using fibre-optical cables and optical converters, allowing the establishment of stable connections without the need for conductive cabling. Within the separate areas, conventional conductive Ethernet and USB/serial connections can be used. Within the separate areas, conventional conductive Ethernet and USB/serial connections can be used.

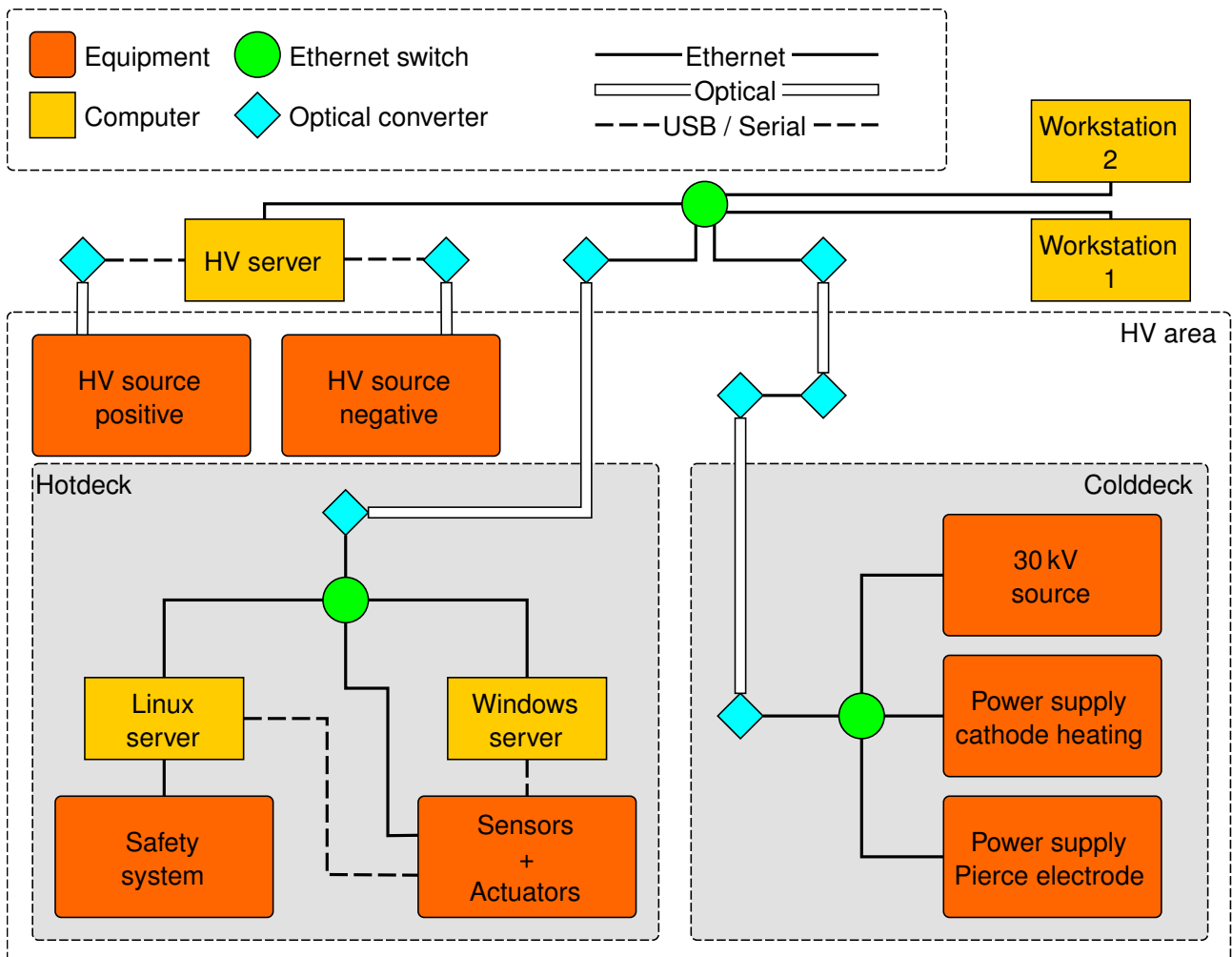


**Figure 9.4** Overview graph of physical network architecture showing main components and connection pathways between them. The hot-deck and the cold-deck are outlined, as well as the HV area surrounded by the operator area. Converters from optical to either Ethernet or USB/serial connection are shown in blue, Ethernet switches in green, computers in yellow and general equipment in orange, according to the legend at the top of the figure. Distinctly styled lines mark the connection types between the devices. The equipment labelled "Sensors + Actuators" on the hot deck is a placeholder for a multitude of different devices.

In the operator area, two workstation computers are located, acting as user terminals for interaction with the control system. The workstations are equipped with two network interfaces for simultaneous connection to the control network and the internet. That way, the control network is still isolated from the facilities network, but the workstations have access to the internet for convenience. Additionally, it is possible to allow the computers in the control network access to the internet (e.g. for firmware updates) by configuring one of the workstations as a router, including a firewall. The central computer of the control system running the main server software is located on the hot-deck and labelled "Linux server" in fig. 9.4. The Linux server is a high-performance computer running a Linux distribution as the operating system for its beneficial stability. In addition to the Linux computer as the main server, two auxiliary servers, termed the Windows server and the HV server, are part of the control system. The Windows server is a high-performance computer running Microsoft Windows as the operating system located on the hot-deck. It is required as, unfortunately, not all equipment needing controlling and monitoring natively supports connections with Linux. The Windows server, therefore, acts as an adaptor connecting to the equipment and exhibiting an interface for the Linux server, maximising flexibility in the choice of equipment. The HV server is a low-performance mini-computer located in the operator area and connected via optical fibres to the HV sources. The HV server is dedicated solely to controlling and monitoring the HV sources, which was deemed necessary as they require a complex interaction protocol to operate properly and pose one of the major safety hazards both concerning the machine and personnel present in the laboratory. By outsourcing the complex interaction with the HV sources to the dedicated HV server, the main server only needs to interact via a simpler protocol with the dedicated server, minimising the risk of software-based malfunctions. Within the cold-deck, no additional auxiliary server is required, as the two power supplies were chosen with the requirement for a network interface in mind, and the interface for the 30 kV source is self-built.

Most of the equipment that needs to be controlled and monitored by the control system is located on the hot-deck. For the connections of a large number of various devices, the two server computers on the hot-deck exhibit a high quantity of USB ports with which adaptors for different interfaces can be connected. One device connected to the control system should be mentioned specifically due to its importance: the safety system. The safety system, as presented in chapter 8, is concerned with personnel safety around the LFXT prototype and, therefore, the most critical system. As the safety system controls the motor driving the target and the cooling pumps, a connection to the control system is required. The connection to the control system is realised via an Ethernet connection directly from a second network interface of the Linux server to the secondary control box of the safety system located on the hot-deck. In doing so, the safety system is physically isolated from the control network, minimising the risk of malfunctions. As the control system can not be assumed to be a safe system without the possibility of malfunctions, it should under no circumstance be able to influence the protocols of the safety system. The safety system ensures this, as any program parts concerning personal safety can not be altered in any way. Instead, the control system can only query the safety system for its status and request, but not force, the change of very specific parameters, e.g. the rotational speed of the target motor. That way, personnel safety is ensured by the safety system also in case of a malfunction of the control system.

## 9.4 Overview and discussion

In the preceding chapter, the control system of the LFXT prototype has been presented. The purpose of the control system is to enable users to control and monitor the machine during operation and continuously examine the status of the LFXT prototype for critical conditions. In addition to the direct requirements, the design of the control system is constrained by the designs of the HV and safety systems presented in chapters 7 and 8. Overall, the control system can be split into a software and a hardware part.

The software of the control system is designed in a server-client architecture, enabling the simultaneous support of several clients and, therefore, users. The clients are designed as GUIs with a network interface for communication with the server and do not contain any means for direct control of the LFXT prototype. The central part of the software is the server, containing all logic required for controlling and monitoring

the LFXT prototype. The server is structured in a hierarchical tree-like manner defined mainly by so-called modules and HLDs, which are based on abstract base classes according to the rules of object-oriented programming. The modular tree-like architecture based on two base classes allows for a high amount of flexibility and expandability. The modules serve mainly as structural elements, gathering sub-modules and HLDs together and providing a location for commands concerning different devices. The HLDs are the most important parts of the server, as they handle all communication with the devices. For every device that is part of the LFXT prototype and that needs controlling and monitoring, exactly one HLD is needed. Each HLD contains a so-called command thread handling the communication with the respective device concurrently to all other threads of the server. By using this highly parallelized multi-threading approach, it is possible to handle the communication and, thereby, control and monitoring of all devices simultaneously instead of sequentially. For communication with the clients, the server exhibits a network interface based on HTTP requests, making it fully platform-independent. A dedicated thread of the server, aside from the modular control structure, continuously examines the overall status of the LFXT prototype for critical conditions and triggers an emergency procedure if required. Therefore, the server design reduces the risk of machine damage. The control system of the LFXT prototype is explicitly not concerned with personnel safety, which is handled by the safety system presented in chapter 8.

The hardware for the control system is designed according to the requirements of the software and within the constraints posed by the HV and safety systems. The hardware consists of two workstation computers acting as user terminals, one main and two auxiliary server computers, and several network devices. On the workstations, the client program of the software part is running while the server part is located on the main server computer. The workstations are located in the operator area as defined in chapter 8, and the main server computer is located on the hot-deck as defined in chapter 7. The positioning of the main server on the hot-deck allows for devices without network capabilities to be connected directly to it using conventional conductive cabling. The auxiliary server computer running Microsoft Windows as the operating system is also positioned on the hot-deck, to enable the easy usage of devices that are incompatible with the Linux-based operating system of the main server. The second auxiliary server is dedicated to controlling and monitoring the HV sources to reduce the risk of malfunction as the main server, which is concerned with a multitude of other tasks, does not need to handle the complex direct communication with the HV sources but only the more simplistic communication with the auxiliary HV server. Connections between the different computers and devices, which are part of the control system, are established via a dedicated LAN. The network is split into four areas according to the constraints of the HV and safety systems laid out in detail in chapters 7 and 8 and fully isolated from the network of the surrounding research facility. Within each area, network connections are established using conventional cabling, while connections crossing the borders between the areas are facilitated using optical fibres and converters. By using fibre optical connections, the areas are electrically insulated against each other, and the functionality of the HV and safety systems are not compromised without reducing the stability of the network, as would be the case for wireless connections.

At the time of writing this work, the hardware part of the control system is fully set up, functional and used in regular operation. The only malfunctions of the hardware up to the time of writing were minor configuration issues with the network and rare failures of network devices due to electromagnetic influences from the HV system. The software part of the control system is not fully implemented yet, due to a severe lack of time and resources. Only a very basic version of the software is being used at the time of writing, not even fully implementing the server-client architecture. However, the principle design of the HLDs for concurrent communication with several devices and the HTTP based network interface are implemented and functional. Additionally, the software for the auxiliary HV server is fully implemented and has been controlling the HV sources from the first HV tests up to the time of writing.

Overall, the control system is not fully set up yet at the time of writing, but the implemented parts have proven to fulfil the requirements posed on the control system and are used in regular operation. The design of the software architecture has been partly implemented and tested but still lacks most of its final functionality. The design of the control system presented here is valid for a preclinical prototype of the LFXT but is widely insufficient for a future commercial and potentially clinical version. Especially for a

clinical version, significantly higher requirements for fault tolerances would be posed on both software and hardware. Additionally, the current design of the control system is not real-time capable due to the usage of conventional computers and operating systems, as well as the choice of Python as the programming language. For a commercial product, dedicated real-time capable hardware and a real-time capable programming language should be used. The modular and highly parallelized design of the software could, however, also be used for future versions, in the author's opinion.



## 10 Overview and discussion of entire system

In the preceding chapters of part II, the systems developed within the scope of this work supporting and enabling the operation of the LFXT prototype have been presented in detail. In the following chapter, an overview of the different systems focused on their main components depicted in fig. 10.1 and functionalities will be given with respect to the requirements posed on them in chapter 4. For a better understanding of the interplay between the different systems and to highlight their interconnections, the procedure of an exemplary irradiation will be laid out. At the end of the chapter, weak points of and potential future improvements to the different systems will be discussed.

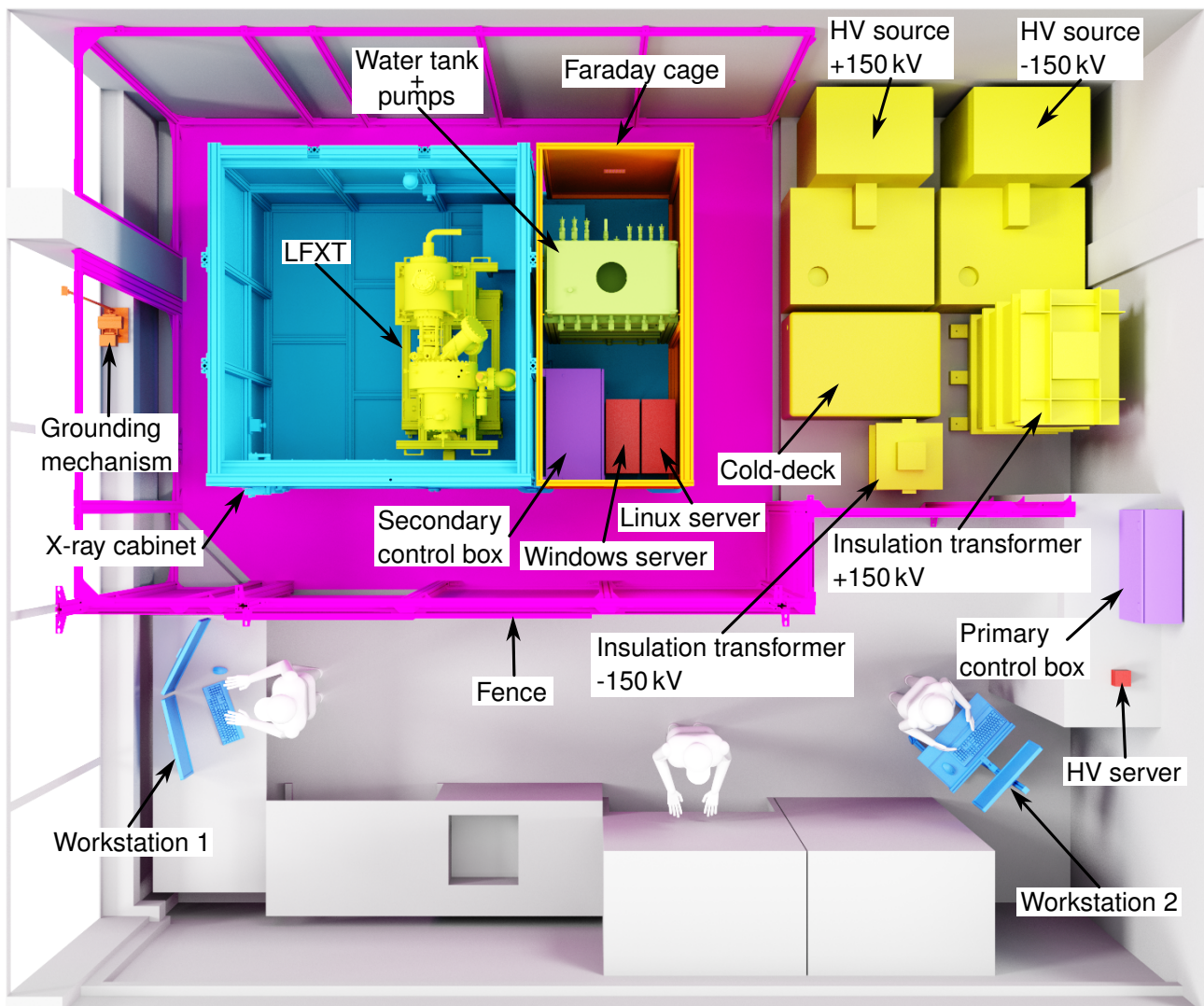


**Figure 10.1** Overview of the laboratory room the LFXT prototype is set up inside with the main components highlighted and labelled. Pipes, cables and other small components are omitted for clarity. Components integrated with the vacuum chamber of the LFXT prototype, e.g. the IR pyrometers and cooling channels, are not depicted due to the scale of the figure. The roofs of the X-ray cabinet, the Faraday cage and the fence are not rendered. Everything is depicted in its operating state with the doors closed and the grounding mechanism disconnected from the X-ray cabinet. For a sense of scale, dummies of personnel working in the operator area have been added to the rendering.

As detailed in chapter 4, two basic requirements need to be fulfilled for any kind of experiment to be conducted at the LFXT prototype. The first requirement is that the protection of personnel involved or not with the operation of the LFXT prototype from threats it poses must be ensured by the safety system. The three major sources of hazard arising from the operation of the LFXT prototype are the ionising X-radiation, the required high acceleration voltage and the high amounts of kinetic energy contained within the rapidly rotating target rotor complex. Protection against ionising X-radiation is mainly facilitated by the X-ray cabinet encasing the LFXT prototype. The walls, floor and ceiling of the X-ray cabinet are made from 25 mm thick lead bricks, effectively limiting the maximum radiation dose personnel would be exposed to under the assumption of maximum utilisation of the LFXT prototype to about 0.09 mSv/a according to Monte Carlo simulations. This is more than a factor of 10 below the German legal limit for the general population and about a factor of 67 lower than the limit for personnel working in radiation surveillance areas. Therefore, the radiation protection function of the safety system is fulfilled exceptionally well according to the theoretical simulations, and although the LFXT prototype has not yet been operated at full power, no amount of radiation whatsoever could be experimentally measured outside the X-ray cabinet during the experiments conducted up to the time of writing. Protection against the high acceleration voltage that charges the X-ray cabinet with up to 150 kV during operation due to the design of the HV system is mainly facilitated by the fence and the grounding mechanism depicted in fig. 10.1. The front of the fence is designed in a double-layered manner and separates the laboratory room the LFXT prototype is set up inside into a danger zone and an operator area. The side of the fence facing the danger zone containing the X-ray cabinet is made from a metallic mesh connected on several strategic points to the electrical ground, effectively shielding the operator area from the strong electrical field and potential electrical arcs. The front of the fence is layered with electrically insulating PMMA plates on the side facing the operator area, preventing personnel from accidentally touching conductive parts and objects from penetrating through the front of the fence. The grounding mechanism is, in principle, a pneumatically driven lever positioned on the windowsill on the left in fig. 10.1 that can automatically connect the X-ray cabinet to the electrical ground, dissipating any remaining charge before personnel enters into the danger zone. The safety system fulfils its function of protecting personnel from being harmed by the HV efficiently, with no malfunctions up to the time of writing, even in the occurrence of electrical arcs. Protection against the high amount of kinetic energy contained within the rapidly rotating target rotor complex is facilitated by the 3.5 cm thick steel wall of the vacuum chamber surrounding the target, the 2.5 cm thick lead walls of the X-ray cabinet and the orientation of the LFXT prototype in respect to the surrounding areas. Calculations or simulations for the protective efficiency of the vacuum chamber and the X-ray cabinet against a bursting target or a blocking bearing were impossible due to the extremely high complexity of the involved principles. Instead, the argumentation is built on unpublished experience from destructive tests of neutron choppers conducted by a cooperating institute. Up to the time of writing, no catastrophic bearing malfunction or target burst occurred, and therefore, no final assessment for the efficiency of the safety system to protect against such malfunctions can be given. To control all processes of the safety system, like locking the doors of the X-ray cabinet and the fence or attaching the grounding mechanism to the X-ray cabinet, two control boxes containing a PLC depicted in fig. 10.1, belong to the safety system in addition to the other mentioned main components.

The second basic requirement for experiments to be conducted with the LFXT prototype is the provision of the X-ray beam. For that, a focused electron beam must impinge on the rapidly rotating target, producing X-ray photons and heat. Due to the high amount of power in the electron beam and the low efficiency of the conversion from electron beam power to X-ray beam power, both the vacuum chamber and the target of the LFXT prototype are exposed to a significant amount of heating power. Therefore, the temperature of the target needs to be monitored, and the LFXT prototype needs to be cooled.

All functionality for monitoring the target temperature is consolidated within the focal track temperature monitoring system. The highest temperature is present in the focal spot on the target and monitored by two IR pyrometers and an IR camera. The IR pyrometers are integrated with the vacuum chamber of the LFXT prototype and have a combined temperature range of 275 °C–3000 °C. The IR camera is designed to use a complex optical system partly integrated with the vacuum chamber to measure the high-resolution

spatial temperature distribution in the focal spot. A third IR pyrometer, also integrated with the vacuum chamber, monitors the temperature of the focal track on the side opposite the focal spot. At the time of writing, the temperature monitoring by the IR pyrometers has been tested and is functional. The design of the optical system for the IR camera is highly complex due to the required high resolution, the sub-optimal viewing angle, the IR wavelength limiting the achievable resolution, and aberrations due to chromatic and spherical effects. Although the design of the optical system has been started, it is not yet finished at the time of writing due to a lack of time and resources in combination with higher priorities of other sub-projects.

The dissipation of heat from the LFXT prototype is handled by the cooling system, which can be split into a part integrated with the LFXT prototype and the mobile frame it is built onto and an external part positioned outside the lead shielding of the X-ray cabinet. The vacuum chamber is fitted with four cooling cycles, extracting the heat deposited by backscattered electrons, and the steady axis of the target drive train is fitted with a single cooling cycle, extracting the heat deposited by the direct electron beam. A sixth cooling cycle is integrated into the electric motor propelling the target rotor complex to extract the heat generated due to the power loss of the motor. As the electric motor can not be directly cooled by water, it is cooled by a dedicated oil cycle integrated with the mobile frame incorporating an oil-water heat exchanger to convey the gathered heat from the oil cycle into a water cycle to be handled equivalent to the other cycles directly cooled by water. The external part of the cooling system incorporates a 100 L water tank and seven industrial water pumps, of which six supply water to the integrated cooling cycles. The seventh water pump supplies a water-air heat exchanger, conveying the heat buffered within the water tank during a 20 s irradiation pulse to the air in the laboratory room during the following 20 min cooling period to be dissipated by the air conditioning of the laboratory. The cooling system is designed to be able to extract and buffer 90 kW of heating power deposited continuously over a period of 20 s and dissipate it during a 20 min cooling phase. The calculations for the cooling system were, in general, performed in a very conservative manner due to a lack of experience, leading to the cooling system being oversized. At the time of writing, the cooling system was fully built but had not been put into operation yet as the applied electron beam powers did not make it necessary. Therefore, no final assessment of the efficiency of the cooling system can be given here.

The focused electron beam required for the generation of an X-ray beam is provided by the electron accelerator. For the electron accelerator to function, it requires UHV, provided by the vacuum chamber, and a very specific set of electrical currents and voltages, provided by the HV system. The HV system provides the required high acceleration voltage and electron beam current from two HV sources, generating  $\pm 150$  kV at up to 300 mA respectively. The output of the positive HV source is directly connected to the slotted anode and the vacuum chamber of the LFXT prototype. As the vacuum chamber can not be insulated from the surrounding X-ray cabinet and future experimental setups, this leads to the entire X-ray cabinet being charged with up to +150 kV during operation. To insulate the X-ray cabinet from the surrounding laboratory, it is built onto post insulators and surrounded by the metallic fence on all sides apart from the one facing the HV sources. The fence acts as a counter-electrode to the X-ray cabinet, homogenising the electrical field to improve insulation and shielding the surrounding areas from electrical fields. Within the X-ray cabinet, no electrical field is present, protecting sensitive devices from being damaged by it. To enable the positioning of devices sensitive to damage from X-radiation that need to be conductively connected to the LFXT prototype outside the lead shielding of the X-ray cabinet, a so-called hot-deck is available next to the X-ray cabinet. The hot-deck is surrounded by a Faraday cage, as depicted in fig. 10.1, to protect devices from electrical fields. The aforementioned grounding mechanism can automatically discharge the X-ray cabinet. The counterpart to the hot-deck is the so-called cold-deck, where the power supplies for the electron source complex are positioned. The cold-deck is connected on one side to the negative HV source and on the other side to the electron source complex through special HV cables and plugs. Insulation of the cold-deck is achieved by nesting a sealed metallic box containing the power supplies and some support devices within a larger metallic box connected to the electrical ground and filling the volume between the boxes with insulation oil. To provide electrical power to the devices in the X-ray cabinet and the cold-deck through the electrical barriers, two insulation transformers are used. At the time of writing, the HV system has been fully tested and is in regular operation. The provision of

the acceleration voltage from the HV sources and the provision of electrical power through the insulation transformers is fully functional. The cold-deck is able to provide for the electron source complex, and the insulation is working down to -150 kV. The insulation of the hot-deck is functional up to +150 kV after some minor adaptations, but corona discharges are present above about 100 kV. The presence of strong corona discharges suggests that the insulation of the hot-deck is very close to a breakdown, which was to be expected due to the very limited available height of the laboratory room and the, therefore, very limited amount of insulation distance.

For all of the aforementioned systems to fulfil their functions and enable the operation of the LFXT prototype, they need to be able to work together as a cohesive unit. For that a central system is required to monitor and control them and enable interactions from operators. This control system can be split into a hardware and a software part. The main components of the hardware part of the control system are depicted in fig. 10.1 and include the so-called Linux server, which is the main server computer of the control system, and the so-called Windows server, which is one of two auxiliary servers. The Linux and Windows servers are positioned on the hot-deck to be able to directly connect devices to them. The second auxiliary server is the so-called HV server, which is positioned in the operator area above the entry to the laboratory room depicted on the right in fig. 10.1. As interaction terminals for operators, two workstation computers are located in the operator area. The position of the primary workstation is fixed, while the secondary workstation is built onto a mobile frame to be positioned freely. On the software side, the control system is designed in a client-server architecture, with a single server supporting one or more clients. The clients consist mainly of a GUI the user can interact with and a network interface for communication with the server and are running on the workstation computers. The server architecture is designed in a modular, hierarchical and highly parallelized manner, making extensive use of multi-threading and abstract base classes. Due to the modular manner based on abstract classes, the server is easily extendable. Using an individual parallelized thread for each controlled device allows the simultaneous monitoring and controlling of all devices, in contrast to a sequential approach. The server is designed to be capable of handling commands from several clients and monitoring the status of the LFXT prototype for critical conditions simultaneously. The major part of the server program is designed to run on the main Linux server, but part of the functionality is outsourced to the auxiliary servers for practical reasons. The communication with the HV sources is, for example, handled by the HV server to unburden the main server from the very complex communication protocol of the HV sources and thus minimise the risk of malfunctions. The basic principles of the control system have been tested and are functional. The full control system is, however, not yet implemented at the time of writing due to a lack of time. Instead, a very crude version is used during the running experiments that incorporates the basic principles but not fully the modular client-server architecture.

To better highlight the interplay between the separate systems, an exemplary irradiation procedure as planned when all systems are fully implemented will be shortly presented in the following. Before starting an irradiation, the LFXT prototype and its supporting systems are in a secured state, where the interlocks of the HV sources and of the target motor are blocked, the grounding mechanism is attached to the X-ray cabinet and the doors of the X-ray cabinet and the fence are unlocked. Even in the secured state, the pumps of the cooling system may be running, the electron source complex is supplied from the cold-deck, and electrical power is supplied to the cold-deck and the hot-deck through the insulation transformers. By performing the search procedure of the safety system, the LFXT prototype can be readied for operation. During the search procedure, it is ensured no personnel is left within the danger zone before the doors of the X-ray cabinet and the fence are closed and locked by the PLC of the safety system. After the doors are secured, the safety system detaches the grounding mechanism from the X-ray cabinet and releases the interlocks of the HV sources and the target motor, allowing them to become active. Using the two workstations, operators can activate the target motor and ramp up the acceleration voltage by interacting with the control system. By lowering the voltage of the Pierce electrode in the electron source complex, the irradiation is started. During irradiation, all parameters of the LFXT prototype can be monitored and controlled from the workstations, including the target temperature, through the focal track temperature monitoring system. The heat produced by the electron beam and the power loss of the electric motor

is buffered within the water volume of the cooling system during the irradiation. After the irradiation is completed and the target motor and HV sources are deactivated, the opening procedure of the safety system can be started. During the opening procedure, the safety system blocks the interlocks of the HV sources and the target motor and waits until the remaining charge of the hot-deck falls below a predefined threshold, after which it attaches the grounding mechanism to the X-ray cabinet and unlocks the doors. When the doors are unlocked, all systems are again in a secured state and the X-ray cabinet can be entered by personnel to prepare the next irradiation. During all this time, the cooling system dissipates the buffered heat through the water-air heat exchanger. Although not all systems are yet fully implemented, the presented procedure is, in most parts, already performed at the time of writing during the first experiments.

Overall, the requirements stated in chapter 4 for the support systems developed within the scope of this work and presented in the preceding chapters are fulfilled, but not all systems are fully implemented at the time of writing. Additionally, several aspects of the presented systems can be improved upon in the future, as established. For the focal track temperature monitoring system, the viewing angle available to the IR camera is extremely sub-optimal, especially if resolutions in the  $\mu\text{m}$ -range are required, as it leads to problems with depth of focus and the increased distance limits the achievable numerical aperture and, thereby, resolution. The position of the viewing window for the IR camera was limited by the electron optics in the LFXT prototype and can not be changed anymore but should be considered in future LFXT versions. The presented cooling system is, as mentioned before, oversized and, due to that, more complex than necessary, which can be attributed to a lack of experience and over-conservative calculations. In a potential future version, the cooling system could potentially be designed more efficiently and with fewer individual pumps and cycles. One of the major aspects that can be improved upon in future versions is the generation of the acceleration voltage in the HV system. The initial decision to use two HV sources producing  $\pm 150\text{ kV}$  to save financial resources turned out to lead to a significantly increased complexity of all other systems, undermining not only the original goal but also leading to safety concerns and an increased risk of malfunction. For a future version, it is highly advisable to use a single HV source with negative polarity to generate the acceleration voltage and keep the vacuum chamber on electrical ground. The safety system is fully functional and adequate for the requirements of the LFXT prototype but could be simplified in a future version if the threat posed by the electrically charged X-ray cabinet is eliminated. The control system is only implemented in a minimal version at the time of writing and can, therefore, not be fully assessed. For a future version, especially if a clinical application is planned, the control system should be programmed in a real-time capable manner and on dedicated hardware instead of conventional computers and operating systems. However, the presented modular client-server architecture would also be suitable for a future version, in the author's opinion.

In summary, the LFXT prototype and the support systems are still in the prototype stage and, therefore, flawed. However, most aspects of the presented systems are working as intended, and the LFXT prototype is able to produce X-rays for the first experiments as presented in the following in part III.



## **Part III**

# **Commissioning of the line-focus X-ray tube prototype**



# 11 Introduction to commissioning process

In the preceding chapters of part II, the overall design and setup of the line-focus X-ray tube (LFXT) prototype was presented. The following part presents the main steps, besides the individual tests of separate systems as presented above, for commissioning the LFXT prototype, culminating in the first successful X-ray beam produced with it. For the commissioning steps, the underlying principles and the reasons they need to be performed are shortly illustrated, and problems encountered along the way are presented together with their respective solutions and potential future improvements.

The commissioning steps that need to be performed before the first operation of the LFXT prototype are presented in chapter 12 and include the balancing of the target rotor complex before the final assembly of the vacuum chamber, the bake-out of the vacuum chamber, and the high-voltage (HV) conditioning of the electron accelerator. At first, balancing of the target rotor complex is required to minimise imbalances leading to vibrations and potential malfunctions of the drive train at high rotational speeds. Balancing must be performed before the other steps, as the target rotor complex is encased within the vacuum chamber. Therefore, the vacuum chamber can only be finally assembled and sealed once all work concerning the target rotor complex has been concluded. After assembly of the vacuum chamber, it must be baked out to achieve the required ultra-high vacuum (UHV) conditions. During the bake-out, the vacuum chamber is heated to accelerate the degassing of its inner surfaces, improving the vacuum conditions once the chamber is cooled down again. Once the UHV conditions are established inside the vacuum chamber, the electron accelerator needs to be conditioned to be able to sustain the required high acceleration voltages of up to 300 kV. During HV conditioning, the voltage applied between the electron source complex and the anode of the electron accelerator is slowly increased, leading to minor discharges cleaning the surfaces of impurities, which would otherwise limit the achievable acceleration voltage and lead to electrical arcs that could potentially damage the LFXT prototype. The processes of the separate commissioning steps are presented chronologically, starting with a basic approach evolving after each encountered problem.

After performing the main commissioning steps, the LFXT prototype is ready for its first operation, during which the focus of the focal spot needs to be adjusted by adapting the parameters of the magnetic optics. During the focal spot adjustment and also for later characterisation of the focal spot of the LFXT prototype, a method for quantitatively measuring the dimensions and spatial intensity distribution of the focal spot is required. In chapter 13, two standard methods for characterising the focal spot of an X-ray source are adapted to the specific requirements of the LFXT prototype and their performances are validated in Monte Carlo simulations.

Finally, in chapter 14, the results of the very first experiments conducted with a LFXT are presented. The experiments conducted during the first beam include a preliminary characterisation of the focal spot, the generation and assessment of a first microbeam irradiation field, and an *in vitro* irradiation of cancer cells with microbeam radiotherapy (MRT).



## 12 Balancing, bake-out and high-voltage conditioning

The following chapter presents the three main steps performed during the commissioning process of the LFXT prototype. At first, the balancing of the target rotor complex is presented, followed by the bake-out of the vacuum chamber and the HV conditioning of the electron accelerator. For the individual commissioning steps, a short explanation about the reasons they are necessary is given, followed by a chronological presentation of the process, including the major encountered problems. The commissioning process was executed twice due to major problems during the first attempt and necessary repairs. At the end of the chapter, a summary of the commissioning process is given, and the remaining problems and future improvements are discussed.

### 12.1 Balancing of target rotor complex

Before the final assembly of the LFXT prototype, the target rotor complex needs to be mechanically balanced. Balancing any type of rotor includes adding or removing weight from it, and as the target rotor complex of the LFXT prototype is fully encased within the vacuum chamber, this is only possible before the final assembly. The target rotor complex consists of two mechanical units assembled around the steady axis and connected by screws as depicted in fig. 12.1. The left part of the target rotor complex is mainly composed of the target fixed to the left rotor by two large nuts, and the right part consists of the right rotor carrying the cage rotor of the electric motor [21].

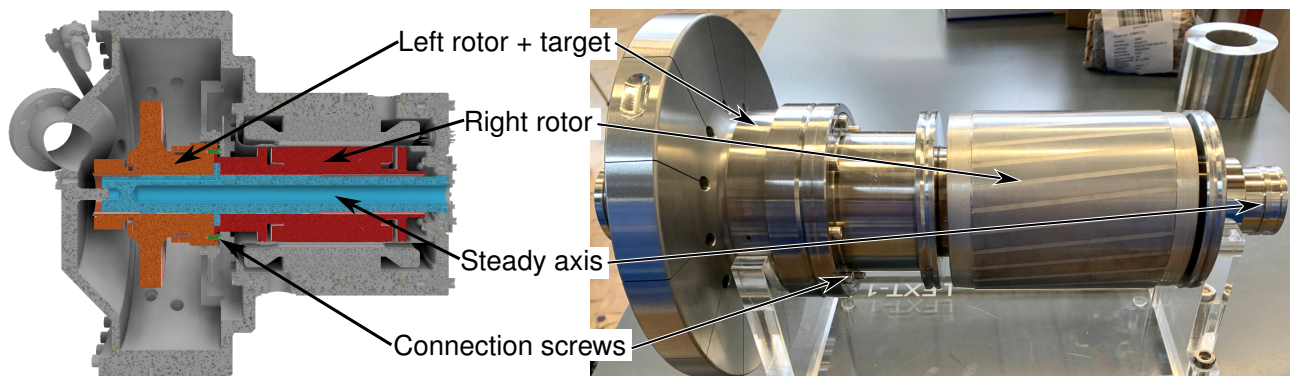


**Figure 12.1** Annotated computer aided design (CAD) rendering and photograph of target rotor complex. On the left, a vertical section view through the CAD model of the target chamber of the LFXT prototype is presented, depicting the two mechanical groups of the target rotor complex in orange and red, the connection screws binding them together in green and the steady axis in blue. On the right, a photograph of the target rotor complex assembled around the steady axis is shown.

Balancing means, in general, the minimisation of asymmetries in the weight distribution of a rotor, called unbalances, that would lead to periodic forces exerted during rotation by the rotor on its bearings and through them on all connected components [83]. Unbalances can not be fully avoided as they are, for example, caused by tolerances during rotor manufacturing. Forces exerted by a rotating rotor would lead to vibrations of varying magnitudes, potentially causing damage up to a catastrophic failure. Rotors can be classified into rigid and flexible, depending on their mechanical stability at rotational speeds up to their maximum designed speed [83]. While flexible rotors deform and change their weight distribution depend-

ing on the rotational speed, the unbalance of rigid rotors can be approximated as speed-independent, rendering the corresponding balancing process significantly less complex. The unbalance of a rigid rotor is, in most cases, a combination of its static and dynamic unbalances, where static unbalance describes a displacement of the centre of mass of the rotor away from the rotational axis, and dynamic unbalance is a misalignment between the principle inertia axis of the rotor and its rotational axis [84]. The addition of balancing weights in a single plane is sufficient to counteract a static unbalance, while the correction of a dynamic unbalance requires two separate balancing planes [84].

The two mechanical sub-units of the target rotor complex of the LFXT prototype were balanced separately by their respective manufacturers. For the first commissioning attempt, an external company balanced the assembled target rotor complex separately from the steady axis and the vacuum chamber before the final assembly. Due to unresolved issues with the liquid metal bearing, which caused a blockage and prevented the target rotor complex from rotating, the validity of the initial balancing attempt could not be confirmed. To resolve the issues quickly, the liquid metal bearing was exchanged for two conventional roller bearings by a cooperation partner, which meant the balancing had to be redone. For the second attempt, it was decided to balance the target rotor complex *in situ* on its steady axis inside the vacuum chamber to consider potential displacements of the steady axis and the influence of the whole system, e.g. resonances.

The basic principle of the applied *in situ* balancing approach includes two measurements of the vibrations produced by unbalances, one with a test weight placed on a known position of the rotor and one without. For the measurements, a signal from which the position of the rotor can be derived is required to correlate the measured displacements with the phase shift of the rotation. From the two measurements conducted with a specialised measurement tool for *in situ* balancing, a first guess for the mass and placement of a counterweight is calculated. After adding the counterweight to the target rotor complex, the vibrations are again measured to validate it, and the process can be repeated to improve the balancing further.

During the balancing process, several problems with the design of the LFXT prototype became apparent. Due to the target rotor complex being fully encased within the vacuum chamber, the sensor for measuring the vibrations could only be positioned on the outer surface of the vacuum chamber and not, as it should be, close to the bearings. In combination with the steady axis being only loosely connected to the vacuum chamber by eight M3 screws on one side and by a floating bearing on the other side, the sub-optimal placement of the sensor led to a significant deterioration of the measured displacement signals. Additionally, the design of the vacuum chamber rendered the process of changing the balancing weights highly time-consuming, with about one hour required to e.g. add or remove a test weight. In the design of the target rotor complex, balancing was planned to be done by removing material from balancing discs incorporated into it, which should only be done once the correct weight distribution is found. A better approach for balancing would have been to incorporate threaded holes in which balancing screws made from tungsten could be inserted or removed. For the initial balancing attempts, it was decided to add weights to the connection screws between the two units to evade making irreversible changes.

The *in situ* balancing approach explained above was repeated numerous times over the course of about two days, but no stable balancing solution could be found due to the mentioned problems with the sensor signals, and the approach was discarded. Instead, a combination of a brute force and least squares approach was contrived, in which the measured absolute amplitude of the vibrations was plotted against the position of the respective balancing weight in polar coordinates. It was hoped that the position of the global minimum could be determined from the resulting vibration heat map. After about one day of taking measurements for this new approach, it became apparent that the whole system was significantly too unstable to get reliable and repeatable measurements. The stability of the system was asserted twice by going through the whole process of changing a balancing weight but without actually changing anything, which nevertheless resulted in three different measurements for the same balancing condition. After it was established that the system was too unstable to reliably balance the target rotor complex in the current design, the balancing process was aborted, and the LFXT prototype was assembled without the target rotor complex being fully balanced. Overall, the balancing of the target rotor complex could not be

significantly improved, and only a rotational frequency of about 30 Hz is achievable with the current design of the LFXT prototype within safe margins of vibration amplitude.

## 12.2 Bake-out of vacuum chamber

After the final assembly of the vacuum chamber, the next objective of the commissioning procedure was to reach sufficiently high vacuum levels in the pressure range of  $10^{-8}$  mbar and below. Especially in the electron accelerator chamber, high vacuum levels are required to elongate the lifespan of the thermionic barium dispenser cathode and enable the insulation of the high acceleration voltages [44]. The conventional procedure for the preparation of UHV chambers comprises the so-called vacuum firing and the *in situ* bake-out [85]. During vacuum firing, all inner components of the vacuum chamber for which it is applicable are heated to about 1000 °C under high vacuum conditions, leading to gas molecules trapped within them diffusing to the surface to be pumped away [86]. In the case of the LFXT prototype, vacuum firing of the vacuum chamber and the target was done by their respective manufacturers. After the final assembly of a vacuum chamber, an *in situ* bake-out is performed to remove gas molecules, which diffused into the surfaces again after the vacuum firing. During the bake-out procedure, the vacuum chamber is evacuated and heated to about 200 °C for several days, reducing the out-gassing rate after the chamber is again at room temperature.

The design of the LFXT prototype posed some limitations on the bake-out procedure, as the quadrupole magnets situated around the electron beam pipe and the stator of the electric motor could not be removed and would have been damaged by temperatures greater than about 80 °C. To mitigate these limitations, the sensitive components were air-cooled and shielded from infrared (IR) radiation originating from the rest of the vacuum chamber by aluminium foil. Where possible, heating tape was fixed to the outside of the vacuum chamber, and the chamber was wrapped in several layers of aluminium foil to achieve an as homogeneous as possible temperature distribution. That way, temperatures of 200 °C could be reached in most areas of the vacuum chamber while maintaining safe temperatures at the sensitive components.

After slowly cooling the vacuum chamber down to room temperature again, the pressure stabilised at about  $2 \times 10^{-9}$  mbar in the electron accelerator chamber and about  $1 \times 10^{-8}$  mbar in the target chamber. The pressure in the target chamber was higher than in the accelerator chamber by about an order of magnitude, probably due to the target not being heated directly during the bake-out procedure but only by IR radiation from the inner surfaces of the vacuum chamber. Therefore, the bake-out was not as effective for the target as for the rest of the chamber, and additionally, the target posed a cold spot, potentially even absorbing gas molecules expelled from other components at higher temperatures.

## 12.3 High-voltage conditioning of electron accelerator

After the required UHV conditions in the vacuum chamber have been achieved, the last major step in the commissioning process of the LFXT prototype was the conditioning of the electron accelerator for the high acceleration voltages. The UHV conditions are necessary before applying the acceleration voltage as, according to Paschen's law [87], a vacuum is an excellent electrical insulator. The presence of UHV between the electron source complex on negative and the anode on positive voltage is, however, initially not sufficient to insulate the required acceleration voltage of up to 300 kV, due to the formation of vacuum arcs already at voltages significantly below the desired maximum voltage. The process of vacuum arcing is defined by the not fully understood formation of an electrically conductive plasma bridge between the two electrodes, leading to a short circuit disrupting the electrical acceleration field and potentially damaging components of the electron accelerator [88]. What is known is that defects and impurities on the surfaces of the electrodes, especially the cathode, like microscopic scratches and protrusions remaining even after elaborate polishing procedures, can produce plasma seeds that can lead to the formation of arcs [89, 90].

To increase the breakdown voltage of the accelerator of the LFXT prototype, the voltage between the electrodes is slowly increased during HV conditioning up to about 10% above the maximum operation

voltage, resulting in minor discharges, hopefully cleaning the surfaces but not leading to fully formed arcs. To protect the electron accelerator and the connected components from damage in the case of an electrical arc forming between the electron source complex and the anode during HV conditioning, a series of four HV resistors integrated into the cold-deck as presented in chapter 7 limits the maximum current. To enable conditioning at voltages above the maximum voltage of the HV generators, a low-powered HV source producing up to 30 kV is integrated into the cold-deck and can be wired in series to the main HV generators as explained in chapter 7.

During the first attempt to commission the LFXT prototype, the HV conditioning was initially controlled manually. However, it quickly became apparent that the HV conditioning procedure was significantly too slow and hard to control for a manual approach. Therefore, a simple program monitoring the vacuum within the electron accelerator and controlling the HV generators was devised to automate the HV conditioning procedure and enable it to run continuously, even without the presence of any operating personnel. The initial version of the conditioning program was very straightforward, as it simply monitored the vacuum pressure within the electron accelerator and increased the voltage by a defined step size if the pressure was below a set threshold for a given amount of time or deactivated the HV generators in case the pressure did rise above a defined threshold. Over the course of the conditioning process, the thresholds, wait time and step size of the conditioning program were adjusted numerous times, and the conditioning program evolved by adding and improving functionalities like a remote monitoring and emergency stop function.

During the HV conditioning procedure, frequent vacuum pressure spikes occurred whose prevalence decreased the longer a given voltage was constantly applied, indicating that the conditioning principle was working and surface impurities were evaporated. However, vacuum arcs also occurred regularly, with up to a handful of incidents per day, which slowed down the conditioning process as after each arc, the HV conditioning had to be restarted manually by carefully ramping the voltage up to a bit below the last applied voltage. This often meant idle times of several hours if the incident occurred, for example, at night. Additionally, HV conditioning had to be halted twice for a period of several weeks due to electro-magnetic pulses (EMPs) resulting from the abrupt voltage drop in the HV system in case of a vacuum arc damaging parts of the safety system, which needed to be repaired and better shielded against electro-magnetic influences. Nevertheless, the maximum applicable acceleration voltage increased slowly but steadily over the course of the HV conditioning procedure, indicating that the basic principle was working as planned. At about 260 kV, however, a catastrophic insulation failure caused by a mechanical problem with the locking mechanism of the HV plug supplying the electron source complex led to the destruction of both the HV plug and the ceramic insulator holding the electron source complex and acting as the socket for the plug. The necessary repairs not only took more than six months but required the near-full disassembly of the vacuum chamber of the LFXT prototype, meaning the bake-out procedure also had to be repeated. It was decided to combine the repairs of the electron accelerator with the replacement of the bearing of the target rotor complex as mentioned in section 12.1 and restart the commissioning process from zero. Additionally, the locking mechanism of the HV plug was reworked.

After the necessary repairs and the second iteration of the former commissioning steps, the HV conditioning process was started a second time. The autonomous conditioning program was further improved by adding the ability to automatically restart the HV conditioning after the occurrence of a vacuum arc, minimising the idle time after an incident. Additionally, the conditioning program was extended by an additional vacuum pressure threshold to not only be able to increase the voltage but also decrease it in case of too high vacuum pressure spikes. That way, in the occurrence of small pressure spikes, which are deemed safe, the voltage is kept constant until the prevalence of the spikes decreases far enough and the voltage is increased again, but in the occurrence of a higher pressure spike, which is not yet high enough to trigger an emergency shutdown but too high to be deemed safe, the voltage is immediately decreased by a defined amount, hopefully preventing an arc from forming. In fig. 12.2, the course of the second HV conditioning is presented, and in fig. 12.2 B, the explained behaviour of the conditioning program can be seen as well as the mentioned vacuum pressure spikes.

The second HV conditioning was halted at 180 kV to perform the first beam experiments at up to 150 kV before risking again any damage to the LFXT prototype. After the first beam, HV conditioning was con-

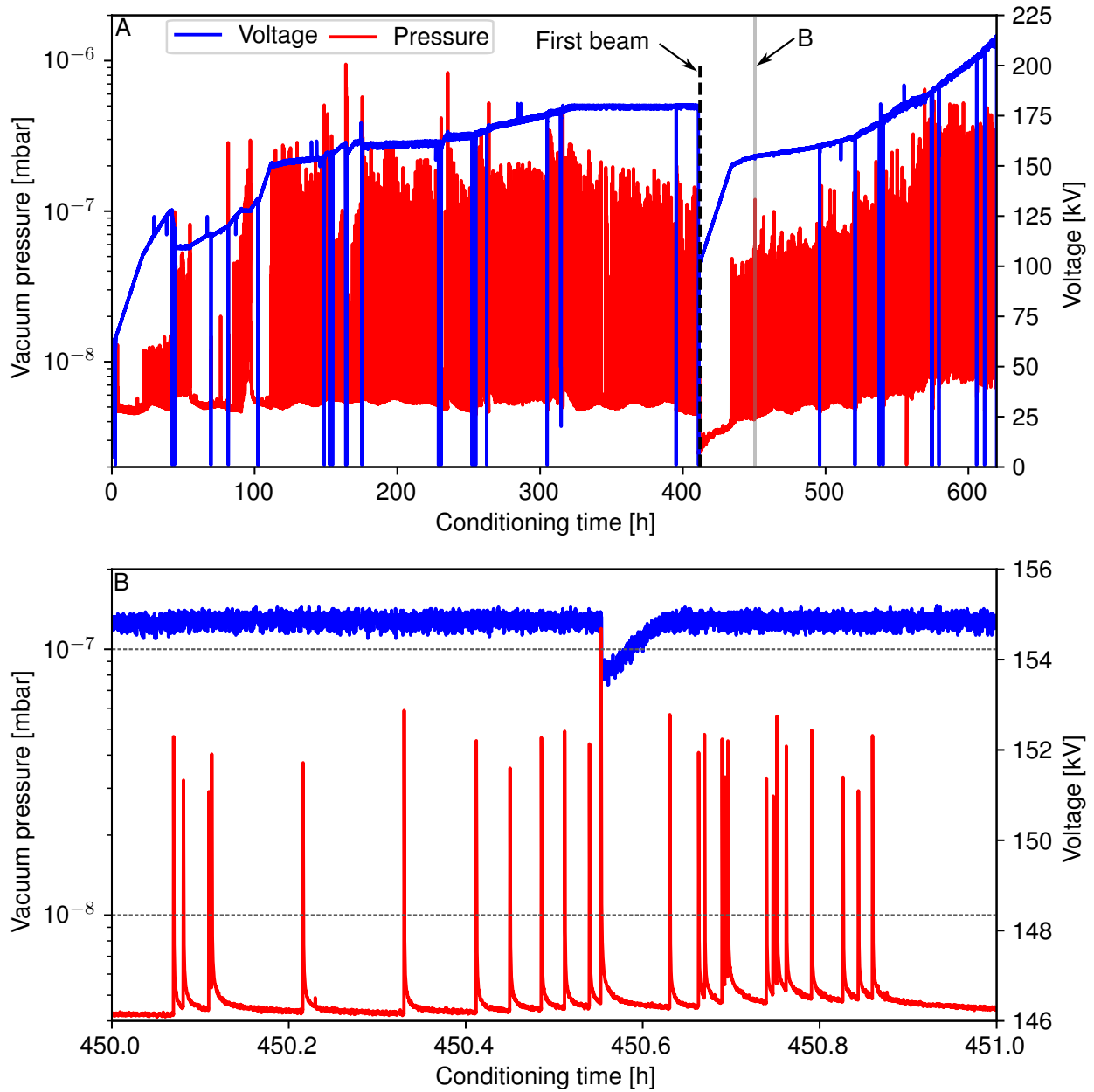


**Figure 12.2** Graphs depicting vacuum pressure in the accelerator chamber in red and applied acceleration voltage in blue over the course of the second HV conditioning process. In **A**, the progression over the entire HV conditioning process is presented, only incorporating times when the conditioning process was active. The time point at which the HV conditioning process was paused and the first beam was conducted is marked. In **B**, a zoom-in to one hour of the HV conditioning process is shown, sharing the same legend as **A**. Two dotted lines mark the vacuum thresholds applied at this time of HV conditioning. The location of the zoom-in is marked by a narrow grey rectangle in **A**.

tinued up to a voltage of about 220 kV, where a vacuum arc produced a so-called cold emitter. A cold emitter is a surface defect emitting free electrons even at room temperature via a process called field emission when a sufficiently high voltage is applied to it [91]. The free electrons get accelerated in the applied electric field and impinge on the wall of the accelerator chamber or the anode, generating X-ray photons and heat and, therefore, increasing the vacuum pressure. Additionally, the activity of a cold emitter may disturb the primary electron beam and deteriorate the electron beam focusing, effectively limiting the maximum applicable acceleration voltage. The presence of a cold emitter was experimentally verified by measuring the X-radiation emanating from the electron accelerator chamber. The results of the verification measurements are presented in fig. 12.3. The measurements were performed with a highly sensitive photon-counting X-ray imaging detector comprising a Cadmiumtellurid (CdTe) semiconductor sensor. Faulty influences from the applied HV or normal discharges occurring during HV conditioning were ruled out by repeating the measurements with a lead shielding layer positioned between the detector and the vacuum chamber. From the measurements, it can be seen that the cold emitter starts to become active at about 150 kV.

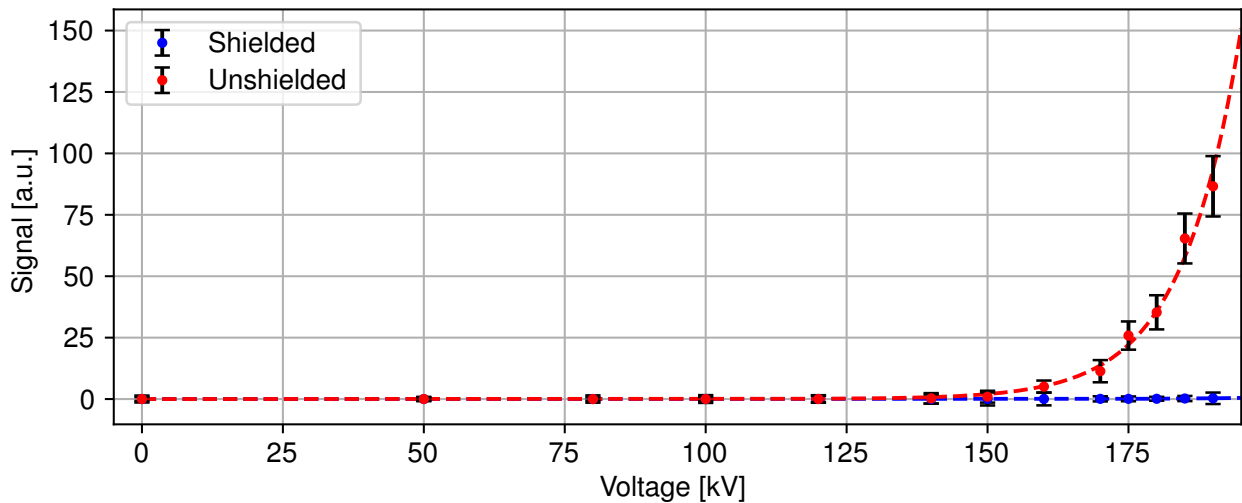


**Figure 12.3** Results of emitter verification measurement. The mean detector signal in arbitrary units is plotted against the applied voltage for the unshielded measurement in red and the shielded measurement in blue. The uncertainties of the measured points are registered on a confidence level of  $\sigma$  and an exponential function of the form  $S = \exp(a \cdot U + b)$  with the detector signal  $S$ , the voltage  $U$ , and the fit parameters  $a$  and  $b$  is fitted to the measured points for better visualisation.

Mechanically, a cold emitter is a sharp protrusion from the surface of the electrode and can be eliminated in the same manner as the defects which are targeted by HV conditioning. Another potential approach to deal with a cold emitter would be gas processing using Helium or Krypton, during which controlled amounts of the processing gas are introduced into the vacuum chamber [91]. During gas processing, the gas atoms are ionised in the applied electric field and accelerated towards the cold emitter, destroying it mechanically via sputtering and increasing its work function due to ion implantation. However, both the conventional HV conditioning and the gas processing approach include the risk of worsening the cold emitter or generating additional ones, effectively limiting the maximum acceleration voltage further. Therefore, it was decided to halt the HV conditioning procedure and operate the LFXT prototype at 150 kV until after the first biological experiments had been conducted.

## 12.4 Summary and discussion of commissioning process

In the preceding chapter, the three major steps in the commissioning process of the LFXT prototype have been presented. The commissioning process includes the balancing of the target rotor complex to min-

imise vibrations, the bake-out procedure of the vacuum system to achieve the required UHV conditions, and the HV conditioning to prepare the electron accelerator for the application of high acceleration voltages.

The commissioning process had to be carried out twice due to significant problems with the bearing of the target rotor complex and the insulation of the HV plug supplying the electron source complex. The initial approach using a liquid metal bearing for the target rotor complex, as explained by Dimroth A. [21], failed, probably due to manufacturing tolerances, leading to the target rotor complex getting stuck such that the electric motor propelling it could not start the rotation again. During the first attempt at HV conditioning of the electron accelerator, the insulation between the tip of the HV plug inserted into the ceramic insulator of the electron source complex and the flange at the back locking it to the vacuum chamber failed. As the tip of the HV plug is charged with the negative portion of the acceleration voltage and the flange with the positive portion during HV conditioning, this led to an electrical breakdown in the form of a discharge travelling on the surfaces of the HV plug and the ceramic insulator, destroying both. After the bearing of the target rotor complex was exchanged for conventional roller bearings and the ceramic insulator and HV cable were replaced, the commissioning process was started again.

During the second commissioning attempt, *in situ* balancing of the target rotor complex was attempted. Due to major problems with the design of the LFXT prototype, the balancing procedure was rendered extremely time-consuming, and no reliable measurements could be taken. Therefore, the balancing of the target rotor complex was aborted after multiple attempts without significantly reducing vibrations, effectively limiting the target rotor complex to a maximum rotational frequency of about 30 Hz. The efficiency of the bake-out procedure of the vacuum system was also limited by the design of the LFXT prototype due to heat-sensitive components, which could not be removed from the vacuum chamber, limiting the homogeneity of the bake-out temperature. Nevertheless, the bake-out procedure significantly improved the vacuum pressures in both the electron accelerator and the target chamber to about  $2 \times 10^{-9}$  mbar and  $1 \times 10^{-8}$  mbar respectively, fulfilling the initial requirements. The HV conditioning process mostly worked as intended up to about 220 kV using an elaborate automatic script monitoring and controlling the vacuum and HV systems of the LFXT prototype. At the maximum voltage, a vacuum discharge led to the appearance of a cold emitter, leading to field emissions and limiting the maximum acceleration voltage. While it would be possible to attempt a removal of the cold emitter, it was decided to suspend HV conditioning and operate the LFXT prototype at an acceleration voltage of 150 kV until the first biological experiments have been concluded in order to not jeopardise them.

Overall, the commissioning process of the LFXT prototype was concluded with less-than-ideal results due to significant problems, heavily limiting the maximum applicable power. Nevertheless, the LFXT prototype is operational and initial experiments both concerning characterisations of the X-ray beam and biological evaluations are possible. Additionally, many lessons were learned from the problems that occurred during the commissioning process that can be applied for future improvements of the LFXT prototype and especially for potential future iterations based on the LFXT concept.



# 13 Preparation for focal spot characterisation

The following chapter presents two standard approaches for characterising the X-ray focal spot of an X-ray source that have been adapted to suit the special requirements of the LFXT prototype, together with Monte Carlo simulations testing their validity. The contents of the following chapter are also published by Petrich et al. [25].

## 13.1 Introduction

For adjusting the magnetic electron optics during the first beam of the LFXT prototype, a method for visualising the spatial intensity distribution of the X-ray focal spot is required, as it is in good approximation a representation of the electron focal spot on the target. Additionally, a method for quantitatively characterising the X-ray focal spot is of importance also after the initial adjustments of the magnetic optics for monitoring the performance of the LFXT prototype and as input data for potential later simulations and calculations of the irradiation field.

A multitude of different approaches for characterising an X-ray focal spot have been developed over time, each with its own advantages and disadvantages. The two approaches adapted and tested for application at the LFXT prototype are the pinhole method [92] and the edge method [93]. Adaptation is necessary as the extremely eccentric focal spot with a planned width of only 50  $\mu\text{m}$  at a length of 20 mm and the angle of 45° between the target surface normal and the primary beam axis would introduce artefacts into the focal spot measured using the standard approaches.

In the following, the pinhole method and the edge method are presented, including the adaptations made to them. The validity of the two methods has been tested in Monte Carlo simulations. At last, a discussion of the two methods is given, including their potential applications during the first beam and the following operation of the LFXT prototype.

## 13.2 Materials and methods

Both the pinhole and the edge method rely on a special test object placed in the X-ray beam between the focal spot and an arbitrary X-ray detector. The image recorded by the detector is then, equivalent to X-ray imaging applications and under the negligence of refraction effects, the convolution between the projected spatial attenuation mask of the test object and the spatial intensity distribution of the focal spot represented by its point-spread-function (PSF). While it would theoretically be possible to deduce the focal spot PSF from an image taken with any arbitrary object in the X-ray beam, in the presence of noise in a real image, the required naive deconvolution is not possible anymore. Therefore, the test objects used in the pinhole and the edge method allow for the inference of the focal spot PSF without directly performing a deconvolution.

### 13.2.1 Pinhole method

The pinhole method utilises a thin but highly absorbing plate made, for example, from tungsten incorporating a narrow aperture allowing photons to pass as the test object. The plate is conventionally called a pinhole and is eponymous for the method. The pinhole is placed between the X-ray source and the X-ray detector to form a camera obscura, directly yielding a two-dimensional representation of the spatial intensity distribution of the focal spot within a single image acquisition and without requiring further reconstructions [92].

The simplicity of the pinhole method is its biggest advantage, as measurements can be performed on the fly. However, both the achievable resolution and the efficiency in terms of the fraction of photons that contribute to signal generation are highly dependent on the diameter of the aperture of the pinhole. Only for an infinitely narrow aperture in an infinitely thin plate that can be modelled by a Dirac delta distribution is the resulting image a perfect representation of the focal spot PSF. An aperture of finite diameter, however, leads to a dilation of the measured PSF and, therefore, a deterioration of the achievable resolution. On the other hand, the larger the diameter of the aperture, the higher the fraction of photons that can pass through and contribute to the measured signal, decreasing the required acquisition time. Overall, the diameter of the aperture of the pinhole is, therefore, a trade-off between the achievable resolution and the required acquisition time. Another effect that can not be neglected in the case of the LFXT prototype is caused by the thickness of the pinhole plate. Due to the long focal spot, the parallax angle between the apertures in the front and back surfaces of the pinhole plate and, therefore, the visible aperture changes depending on the starting point on the target surface, leading to distortions that must be corrected. Additionally, the ratio between the diameter of the aperture and the thickness of the plate of a pinhole influences the precision with which it needs to be aligned to the central X-ray beam, meaning pinholes with small diameter apertures but sufficiently thick and attenuating plates have to be aligned with very high precision.

For application at the LFXT prototype, it was decided that an analogous X-ray film could be used instead of a digital X-ray detector to maximise the achievable resolution. Combined with a suitable film scanner, digital images with a resolution of up to 2.54  $\mu\text{m}$  pixel size can be taken that way. Although more labour-intensive if applied in reality, it was decided to go with this approach for the validation simulations of the pinhole approach to gauge its maximum potential. To increase the resolution achieved by the pinhole approach above what would conventionally be possible, a Richardson-Lucy deconvolution algorithm [94, 95] is applied to the digital images. The mentioned distortions produced by the angle-dependent aperture are corrected by approximating the visible aperture for each pixel separately and scaling their intensities. To get a geometrically and quantitatively correct representation of the focal spot on the target surface, the PSF measured on the detector plane is projected in the last step back onto the tilted source plane, considering the pixel size and detector distance varying along the length of the focal spot.

### 13.2.2 Edge method

For the edge method, a thin but highly absorbing plate with a straight edge is used as the test object, which is called the knife edge and is eponymous for the method [93]. The knife edge is placed under a specified angle in the X-ray beam such that it shadows about half of the sensitive area of the X-ray detector, as depicted in fig. 13.1. The resulting intensity profile measured on the detector plane perpendicular to the edge is then the so-called edge-spread-function (ESF), which can be modelled as the convolution between the focal spot PSF and a Heaviside step function representing the knife edge. The derivative of the ESF is then the line-spread-function (LSF) according to

$$\begin{aligned}
\frac{\partial}{\partial x}ESF(x) &= \frac{d}{dx} \int_{-\infty}^{\infty} \int_{-\infty}^{\infty} \Theta(x-u) \cdot PSF(u,v) dudv \\
&= \int_{-\infty}^{\infty} \int_{-\infty}^{\infty} \delta(x-u) \cdot PSF(u,v) dudv \\
&= \int_{-\infty}^{\infty} PSF(x,v) dv \\
&= LSF(x)
\end{aligned} \tag{13.1}$$

with  $x$  and  $u$  perpendicular and  $v$  parallel to the knife edge, the Heaviside function  $\Theta(x)$  and the Dirac function  $\delta(x)$ . From eq. 13.1, it can be seen that the LSF is a line-integral projection of the PSF, similar to the Radon-transform for parallel beam geometry in computed tomography (CT) [96]. Therefore, the full two-dimensional focal spot PSF can be reconstructed from a suitable set of LSFs measured under different angles using equivalent methods as developed for CT reconstruction.

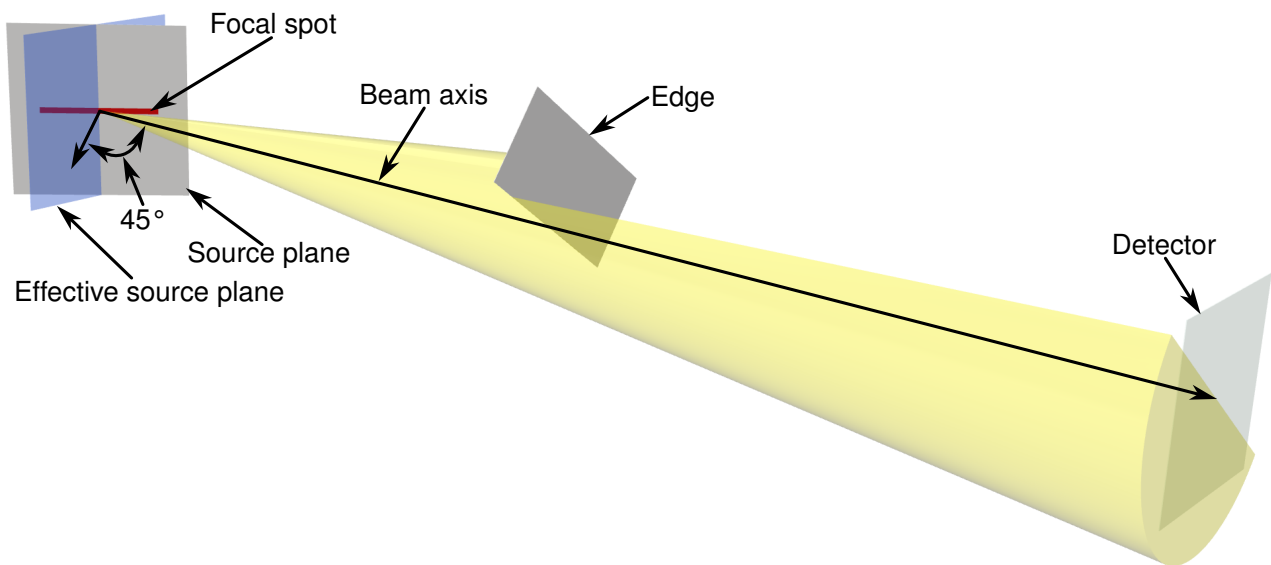


**Figure 13.1** Sketch depicting the basic principle of the edge method for focal spot characterisation. The source plane with the highly asymmetric focal spot in red is presented, as well as the effective source plane required for reconstruction. The central beam axis is denoted, and an exemplary X-ray beam is visualised in translucent yellow. The angle of  $45^\circ$  between the surface normal of the source plane and the beam axis is labelled. Between the focal spot and the detector plane, the knife edge is shown under an arbitrary angle. *Adapted from [25].*

Assuming a sufficiently straight and even knife edge, the resolution achievable with the edge method is only limited by the applied X-ray detector and the number of projections, allowing for significantly higher resolutions compared to the pinhole method explained above. Additionally, the efficiency in terms of the fraction of photons contributing to image generation is substantially better than with the edge method. However, a very large number of LSFs needs to be measured under various angles if high resolution and a large field-of-view (FOV) is desired according to the Nyquist criterion [96]. This renders the measurement not only very time-consuming but also very complex, as a suitable motorised setup is required to rotate the knife edge around and potentially even move it along the central beam axis to change the geometric magnification. Additionally, a complex reconstruction procedure is required during post-processing, further increasing the complexity of the method.

The first step in measuring the spatial intensity distribution of the focal spot of the LFXT prototype using the edge method is the acquisition of images under various angles of the knife edge rotated around the central beam axis. As an X-ray detector, a digital photon-counting detector with a nominal pixel size of  $100\ \mu\text{m}$  and a box-like PSF is assumed for the validation simulations. The distance between the knife edge and the focal spot is modified per projection depending on the edge angle to account for the asymmetry of the focal spot of the LFXT prototype, such that projections of the small dimension of the focal spot are magnified more than those of the long dimension, effectively maximising the achievable resolution while fitting the projected focal spot into the detector FOV. Conventionally, the projections for CT reconstruction need to be acquired in uniform angular sampling, which would lead to a very high number of projections if a resolution sufficient for depicting the small dimension of the focal spot and a reconstruction FOV sufficient to fit the long dimension of the focal spot are required. To circumvent this, anisotropic pixels with a width of  $1\ \mu\text{m}$  in the vertical and a length of  $100\ \mu\text{m}$  in the horizontal direction are defined for the reconstruction and angular sampling is done uniformly in reconstruction space instead of real space. The intensities of the separate projections need to be scaled according to the length of their integration paths to correct for the highly non-uniform sampling in real space. Due to the anisotropic pixels and the uniform sampling in reconstruction space, all projections contain the same amount of information for the reconstruction, and the number of required projections is minimised.

After all individual projections have been acquired, each image is processed separately, starting with detecting the precise angle and location of the edge. Especially the edge angle within the images must

be found with very high precision, as even a slight misalignment during the following steps would lead to a deterioration of the computed LSF. When the alignment of the edge is known, the distance of each pixel to it can be calculated, and the pixels are sorted accordingly, resulting in a low resolution ESF distorted by partial volume effects. On the low resolution ESF, an iterative back projection algorithm [97] adapted to one-dimensional data on a non-regular grid is applied, resulting in the high resolution ESF. The adapted iterative back projection algorithm intrinsically samples onto a regular grid, corrects for partial volume effects and reduces noise within the data. The high resolution ESF needs to be minimally filtered by a Gaussian filter to reduce the contained noise further and enable the following numeric derivation into the LSF.

After all individual LSFs are gathered on the detector plane, they are projected onto the effective source plane as depicted in fig. 13.1. Directly projecting the LSFs onto the real source plane is not reasonable, as for the following reconstruction, it needs to be assumed that the reconstruction plane is parallel to the detector plane. Distortions produced by this assumption are corrected later. On the effective source plane, the simultaneous algebraic reconstruction technique (SART) for parallel beam geometry [98] is used to reconstruct the effective focal spot PSF. In the final step, the effective focal spot PSF is projected onto the source plane, assuming all LSFs were acquired with the same geometric magnification and accounting for varying pixel sizes, resulting in the spatial X-ray intensity distribution of the focal spot.

### 13.2.3 Validation simulations

For the validation of the adapted focal spot measurement methods, Monte Carlo simulations using TOPAS (Version 3.9) [80, 81] and the physics list "g4em-penelope" with default settings have been conducted. For both methods, a rectangular focal spot with a width of 50  $\mu\text{m}$ , a length of 20 mm and a flat intensity distribution was used as the X-ray source emitting isotropically mono-energetic photons with an energy of 100 keV. The X-ray energy was chosen to be approximately the mean energy expected from the LFXT prototype at an acceleration voltage of 300 kV. The normal vector of the focal spot was tilted by 45° away from the defined central beam axis connecting the middle of the focal spot and the detector plane.

#### Pinhole method

For validation of the pinhole method, simulations with aperture diameters of 25  $\mu\text{m}$ , 50  $\mu\text{m}$ , and 100  $\mu\text{m}$  were conducted. The apertures were modelled as cylindrical holes punctured through a 1 mm thick tungsten plate. Additionally, a simulation for an ideal pinhole with an infinitesimal small diameter and an infinitely thin but fully absorbing plate was conducted. Scoring was done using a pixelated detector with a pixel size of 2.54  $\mu\text{m}$  and a FOV of  $2.5 \times 2.5 \text{ cm}^2$  imitating an analogous X-ray film in a distance of 150 cm to the focal spot. The pinhole was placed in the middle between the focal spot and the detector at a distance of 75 cm.

Phase-space sampling was used to reduce simulation time by only generating photons in the X-ray source that were directed towards a circle around the centre of the pinhole. The diameter of the targeting circle was chosen large enough that every point of the source fully illuminated the aperture of the pinhole and the area around it. Therefore, the applied phase-space sampling does not affect the simulation results. For each simulated pinhole, between  $10^9$  and  $10^{10}$  X-ray photons were generated to yield images with sufficiently low noise levels.

#### Edge method

For the simulation of the edge method, individual sub-simulations were performed for each angle of the knife edge. The knife edge was modelled by a simple 1 mm thick rectangular tungsten plate positioned under varying angles and distances to the focal spot between the X-ray source and the detector. The distance of the knife edge to the focal spot was adjusted based on the angle, such that the geometrically magnified focal spot PSF on the detector plane always had an optimal size. The detector was placed 150 cm away from the centre of the focal spot, and the distance between the focal spot and the knife

edge varied between 12 cm and 75 cm, resulting in the geometric magnification factor varying between 11.5 and 1.0. The detector was modelled by a pixelated scorer with a pixel size of 100  $\mu\text{m}$  and a FOV of  $2.5 \times 2.5 \text{ cm}^2$ . To circumvent the fact that the LSF can not be calculated if the edge is exactly parallel to the detector lines, the detector was rotated by  $10^\circ$  around the beam axis.

Similar to the simulations for the pinhole method, phase-space sampling was applied to reduce simulation time by only generating photons directed towards the detector FOV and the close surrounding area. Overall, about 800 projections were simulated with  $10^9$  photons generated per projection. Angular sampling was performed, as explained above, uniformly in reconstruction space instead of real space. Two additional simulations with the edge horizontally and vertically aligned to the focal spot were conducted with  $5 \cdot 10^{10}$  photons each to get the horizontal and vertical LSFs with higher signal-to-noise levels for comparison.

## 13.3 Results

For the validation of the two focal spot measurement methods, the simulated images were treated the same way as images taken with the real LFXT prototype and a real X-ray detector would be. The resolutions achieved by the two different approaches are defined by the full width at half maximums (FWHMs) of the Gaussian functions, which transform the ground truth into the respective measured focal spot PSFs by convolution. A least-squares optimisation is used to identify the Gaussian functions.

### 13.3.1 Pinhole method

In fig. 13.2, the results of the simulated pinhole measurements are presented. It can be seen that the results obtained using the ideal pinhole are in very good accordance with the ground truth, with only a minimal gradient remaining in the horizontal LSF. In the horizontal direction, all of the realistic pinholes also yield good representations of the focal spot PSF, with only minor ringing artefacts at the left and right boundaries of the focal spot produced from the Richardson-Lucy deconvolution algorithm at discontinuities. This leads to the conclusion that the applied corrections for the distortions produced due to the long and tilted focal spot function correctly. The ringing artefacts at the boundaries are not a significant problem, as any real focal spot would not have discontinuities like the box-like focal spot used for the simulations has. In the vertical direction, however, the results obtained with the realistic pinholes are not as satisfactory as in the horizontal direction. The vertical LSFs all yield similar nominal resolutions of 18  $\mu\text{m}$  but show a central overshoot, as can be seen in fig. 13.2B, which is present due to the Richardson-Lucy deconvolution algorithm not converging as it should but compressing and distorting the small dimension of the focal spot PSF. The severity of the distortions produced by the deconvolution algorithm is dependent on the chosen number of iterations. As the optimal number of iterations can not be defined unless the ground truth is already known, in which case the measurement would be futile, the Richardson-Lucy deconvolution algorithm can not be applied for quantitative measurements.

Overall, the pinhole method is able to yield a rough representation of the focal spot PSF without complex reconstructions and within a single image acquisition. The applied corrections for distortions in intensity and dimension caused by the long and tilted focal spot of the LFXT prototype are working well. However, the application of the Richardson-Lucy deconvolution algorithm significantly diminishes the quantitative validity of the measured focal spot intensity distribution.

### 13.3.2 Edge method

In fig. 13.3 the focal spot PSF reconstructed from the simulated edge measurement and the horizontal and vertical LSFs derived from the reconstructed PSF and directly simulated are presented. The reconstructed focal spot PSF exhibits an approximately homogeneous intensity distribution and reliably represents the ground truth. A slight intensity gradient of about  $\pm 11\%$  is visible along the horizontal dimension of the focal spot, and structured noise is present in the PSF. The intensity gradient is due to assumptions required

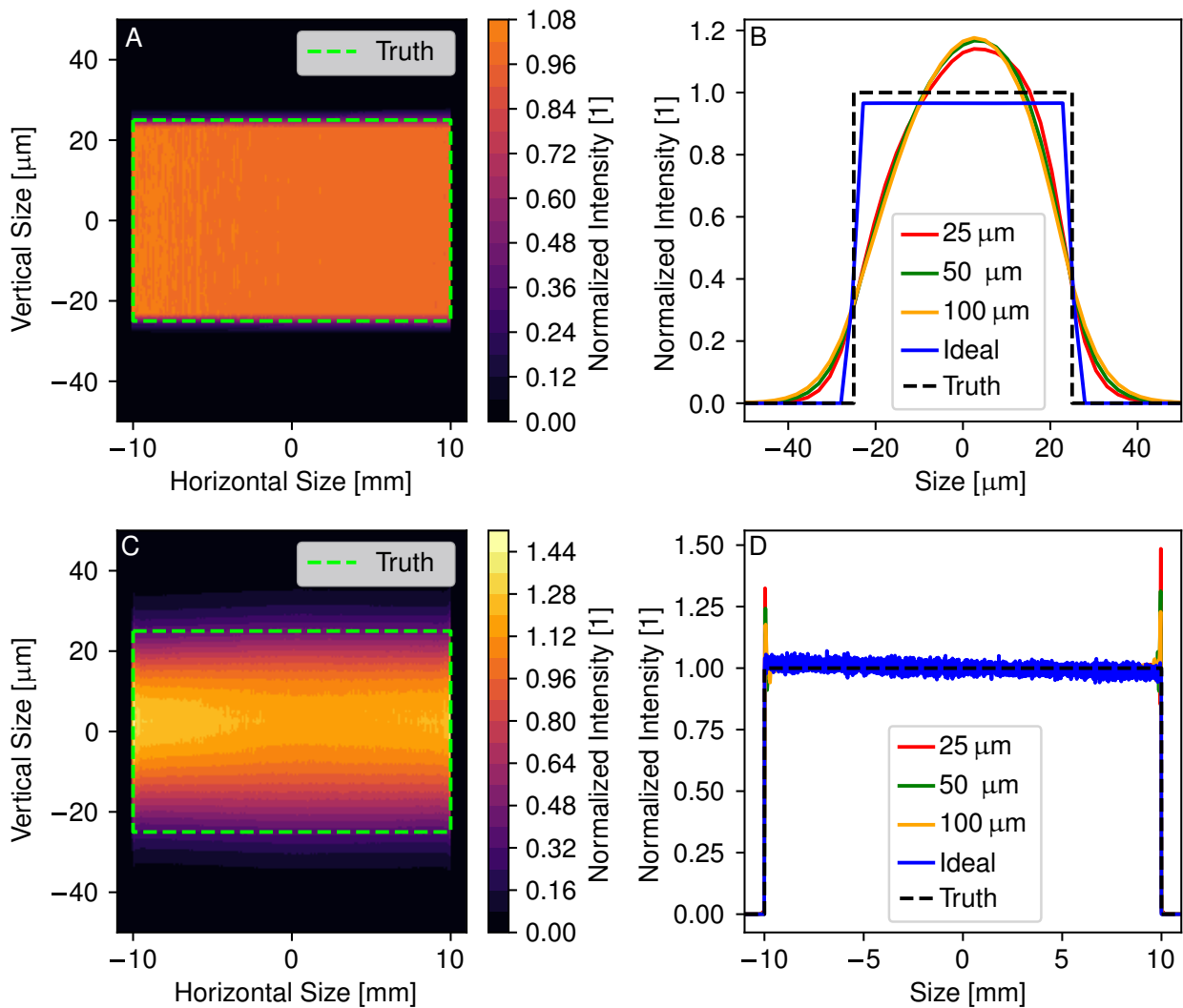


**Figure 13.2** Results of simulated pinhole measurements. In **A** and **C**, the resulting two-dimensional intensity distributions of the focal spot from simulations with the ideal and the 100  $\mu\text{m}$  wide pinholes are shown. In green, the outline of the ground truth is shown where the intensity outside should be zero and inside one. Both images share the same colour scale. In **B**, the vertical and in **D**, the horizontal LSFs are shown for different pinhole sizes of 25  $\mu\text{m}$ , 50  $\mu\text{m}$ , and 100  $\mu\text{m}$  together with the results for the ideal pinhole and the ground truth. Shown intensities are normalised to ground truth. Adapted from [25].

for the reconstruction and the back projection from the reconstruction plane to the source plane. The structured noise is a reconstruction artefact that could be improved upon by acquiring more projections and higher statistics per projection.

As the directly simulated LSFs were acquired with more statistics, a smaller Gaussian filter could be used during their analysis, suggesting they could achieve a higher resolution compared to the LSFs derived from the reconstructed PSF. However, the two vertical LSFs show no significant differences, and both achieve a resolution of about  $9\ \mu\text{m}$ , leading to the conclusion that the Gaussian filter required during reconstruction is not the limiting factor for the achievable resolution. The achievable resolution is, therefore, mainly limited by the used X-ray detector and by physical interactions within the knife edge like scattering.

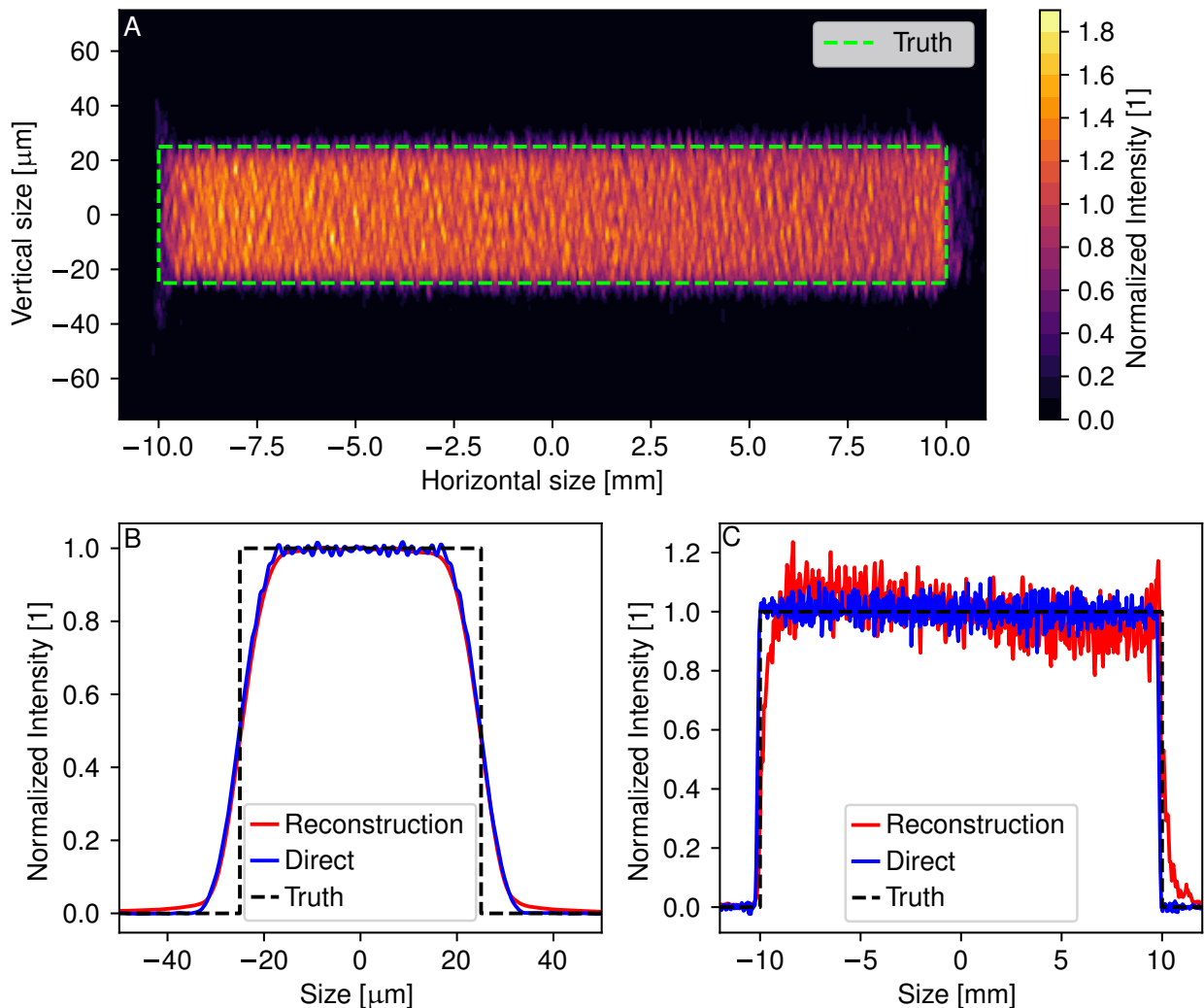


**Figure 13.3** Results of simulated edge measurement. In **A**, the focal spot reconstructed from the simulated edge projections is shown. In green, the outline of the ground truth is registered where the intensity outside should be zero and inside one. In **B** and **C**, the vertical and horizontal LSFs, as calculated from the reconstructed focal spot and as directly measured with the edge, are shown for comparison. All shown intensities are normalised to ground truth. Adapted from [25].

## 13.4 Discussion

In the validation simulations, both the pinhole and the edge method yielded a representation of the spatial intensity distribution of the focal spot used as ground truth. The pinhole method has been shown to be

able to yield a gross representation of the focal spot PSF without complex post-processing procedures and within a single image acquisition. However, the tested Richardson-Lucy deconvolution algorithm significantly diminished the quantitative validity of the measurement and is, therefore, deemed unsuitable for quantitative measurements of the focal spot dimensions achieved by the LFXT prototype. Without the deconvolution algorithm, the resolution achieved by the pinhole method heavily depends on the diameter of the aperture of the pinhole, and none of the tested realistic pinholes achieved a sufficiently high resolution to quantitatively represent the 50  $\mu\text{m}$  wide focal spot. Practical considerations limit the usage of smaller pinhole apertures as the demands on acquisition time and positioning accuracy, as well as the severity of artefacts, would increase non-linearly. Other deconvolution methods like Gold's ratio method or different relaxation-based methods [99] could be tested to potentially improve the resolution achieved with the pinhole method without diminishing its quantitative validity.

Application of the edge method requires an elaborate measurement setup for acquiring many projections under different angles of the knife edge and a sophisticated reconstruction and post-processing procedure, rendering it highly labour-intensive and complex. Nevertheless, the validation simulations for the edge method have shown that it is able to yield a quantitatively valid representation of a focal spot similar to that of the LFXT prototype with a resolution of about 9  $\mu\text{m}$  FWHM. Furthermore, the resolution achieved by the edge method could be improved by the application of a higher resolving X-ray detector compared to the one used for the validation simulations with a pixel size of 100  $\mu\text{m}$  and by increasing the number of projections according to the Nyquist criterion [96]. For real measurements, image statistics should be increased to improve the signal-to-noise ratio in the reconstructed PSF, which should not be a problem as during the validation simulations, image statistics were mainly limited by the already significant simulation time of about 20 min for only  $1 \times 10^9$  photons.

Overall, the pinhole method can be used during the adjustment of the magnetic electron beam optics for an easy on-the-fly visualisation of the focal spot of the LFXT prototype. The edge method is the superior approach concerning resolution and quantitative validity and can be used once all machine parameters have been adjusted to get an accurate characterisation of the spatial intensity distribution of the focal spot. The results obtained with the edge method are sufficiently precise to allow Monte Carlo modelling, dose prediction and treatment planning.

# 14 First Beam

In the following chapter, the very first beam of the LFXT prototype and the results of the experiments conducted during it are presented. The materials and methods used for the first beam experiments are shortly introduced, followed by the experimental results and a brief discussion.

## 14.1 Introduction

As mentioned before, the main purpose of the LFXT prototype is the generation of microbeam and minibeam radiation fields with steep beam penumbras and a high dose rate without the need for a synchrotron radiation facility. The requirements for MRT are explained in more detail in chapter 3 of part I. Additionally, the LFXT prototype is meant to lay the foundation for future advancements of the LFXT concept and enable the development of a first clinical version.

To achieve these objectives, the development of the LFXT prototype was started in prior works and concluded with the systems developed within the scope of this work presented in part II. The commissioning process of the LFXT prototype was described in chapter 12 and is concluded in the following by the first ever X-ray beam produced using not only the LFXT prototype but any X-ray source based on the LFXT concept. In this chapter, results of initial characterisations and experiments validating the functionality of the LFXT prototype will be presented. The presented results are preliminary, as the LFXT prototype was not fully functional when they were conducted. During the first beam, only low electron beam currents at an acceleration voltage of up to 150 kV instead of the designed voltage of 300 kV could be used due to problems with the bearing of the target-rotor complex. Additionally, the power supply of the steering magnets of the electron beam optics malfunctioned, meaning that no optimal electron beam focusing could be achieved during the first beam.

## 14.2 Materials and methods

During the first beam, various initial tests were made at the LFXT prototype. The spatial intensity distribution of the focal spot was characterised using three different approaches based on optical and radiological methods. Dosimetric measurements were conducted for a microbeam field and compared to a conventional X-ray source and a synchrotron facility. In the end, first preclinical *in-vitro* cell experiments were conducted.

### 14.2.1 Focal spot characterisation

The focal spot of an X-ray tube emits electromagnetic radiation over a broad range of wavelengths from the IR regime up to X-radiation. In chapter 13, two approaches utilising the produced X-ray photons are presented that will be applied during the first beam with minimal adaptations. The pinhole method is applied without any deconvolution algorithm using a 25  $\mu\text{m}$  diameter pinhole aperture in a 1 mm thick Tungsten plate. As the X-ray detector, a conventional flat-panel detector with a nominal pixel size of 20  $\mu\text{m}$  (Hamamatsu S15683-13) is used. The X-ray detector is positioned in the primary X-ray beam 50 cm from the focal spot and the pinhole in the middle between them, resulting in a geometrical magnification of 1. The acquired images are flat- and dark-field corrected and projected from the detector plane onto the source plane according to the methods developed in chapter 13. For every image type, multiple images were acquired and summed up to increase image statistics.

For the edge method, only projections in the horizontal and vertical directions of the focal spot were acquired instead of a full reconstruction. The same X-ray detector as for the pinhole measurements was used and positioned equally. As the knife edge, a 2 mm thick Tungsten plate with a straight edge was used and was positioned in the middle between the detector and the focal spot for the measurement of the horizontal dimension of the focal spot and closer to the focal spot for the measurement of the vertical dimension. The acquired images were again flat- and dark-field corrected and projected onto the real source plane. To find the optimal edge angle for pure measurements of the long and short dimensions of the focal spot, measurements were acquired for a range of angles around the approximate horizontal and vertical directions in steps of 1° and the best results were selected.

When accelerated electrons impinge on a metal surface, they not only produce X-ray photons but also transition radiation with wavelengths in the optical regime [100]. Using an optical camera, the transition radiation can be used to acquire a qualitative visualisation of the focal spot. For the first beam experiments, a conventional optical camera was installed at one of the viewports meant for the IR pyrometers, as explained in chapter 5. The camera had a distance to the focal spot of about 30 cm and a steep viewing angle, leading to perspective distortions but allowing a rough visualisation of the focal spot of the LFXT prototype in an even less complex way than with the pinhole method.

### 14.2.2 Dosimetry

Microbeam dose profiles were acquired using radiochromic films (Gafchromic EBT3 films, Ashland Advanced Materials), which darken when exposed to dose. Films were calibrated using a conventional X-ray source for which the dose rate was measured with a calibrated ionisation chamber directly prior to film irradiation. Irradiated MRT and calibration films were scanned with a conventional film scanner, achieving a nominal resolution of 2.54 µm. Due to the limited dynamic range of the used films, a single MRT profile is composed of a peak film irradiated such that the peaks are within the dynamic range and a valley film irradiated with a higher amount of dose. A sophisticated analysis procedure is used to extract the interesting parameters from the irradiated films. More information on dosimetry for MRT and film handling can be found in [101, 15].

For the measurements of depth dose curves, radiochromic films were placed between the layers of a phantom made from stacked 5 mm thick Polymethylmethacrylate (PMMA) plates. The phantom was positioned such that a field size of  $2 \times 2 \text{ cm}^2$  was achieved at the entrance surface.

### 14.2.3 Cell experiments

For the first preclinical experiments, A549 cells of the human lung carcinoma were irradiated with MRT *in-vitro*. After irradiation, double-strand breaks in the deoxyribonucleic acid (DNA) of the cells caused by high doses in the peak regions were made visible by fluorescent staining of the  $\gamma$ H2AX histone protein. The  $\gamma$ H2AX histone is a phosphorylated version of the H2AX histone produced when double-strand breaks occur in a cell. The marked cells were analysed using fluorescent microscopy. More detailed information on the staining protocol can be found in [102].

For the irradiations, 200 000 cells were seeded per cell slide and incubated overnight. During irradiation, the cell slides were filled with medium, and irradiation was performed through it. The used MRT field was characterised by 50 µm wide peaks and a centre-to-centre spacing of 400 µm. The seeding, staining and imaging protocol was performed by the radiobiology group of the Institute of Radiation Medicine at the Helmholtz Centre Munich.

## 14.3 Results

In fig. 14.1, the very first X-ray image acquired using photons produced by the LFXT prototype is presented. The image was taken at an acceleration voltage of 150 kV and with a minimal electron beam current of about 0.1 mA using a conventional Hamamatsu S15683-13 flat-panel detector with a nominal pixel size

of 20  $\mu\text{m}$ . As the image was acquired during the very first activation of the LFXT prototype, the electron optics were not adjusted at the time, and the image is neither flat- nor dark-field corrected.

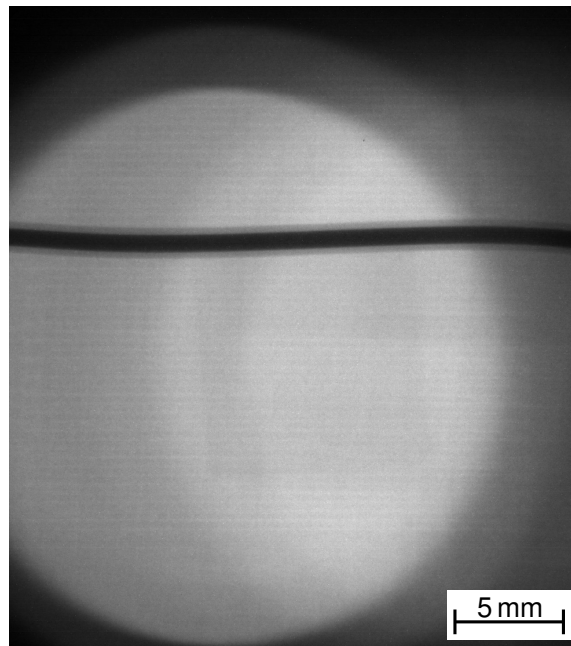


**Figure 14.1** First X-ray image acquired with the LFXT prototype during the first beam. The image was acquired using a conventional flat-panel detector. The boundaries of the radiation cone, due to the size of the primary beam exit window, are visible. Additionally, a copper wire surrounded by insulation material that was placed in front of the detector to add some contrast can be seen. The image is neither flat- nor dark-field corrected.

### 14.3.1 Focal spot characterisation

Using mainly the optical method explained before, the focal spot was visualised, and the magnetic electron beam optics were adjusted as far as possible for the applied acceleration voltage of 150 kV. The focal spot was then characterised using the pinhole method to get a two-dimensional representation of the intensity distribution and by the edge method to get the horizontal and vertical LSFs. The results of the focal spot measurements are presented in fig. 14.2.

Both the optical image and the pinhole image exhibit a highly asymmetric focal spot similar to a horizontal line. From the intensity distribution acquired using the pinhole, a length of the focal spot of about 6 mm can be derived. From the LSFs presented in fig. 14.2, the width of the focal spot can be calculated by fitting with a Gaussian function. With the pinhole, a width of  $(144.3 \pm 0.8) \mu\text{m}$  is measured, while the edge method results in a smaller width of  $(72.3 \pm 0.3) \mu\text{m}$ . The difference between the two measurements can be explained by the higher resolution of the edge method due to the dilating influence of the pinhole on the measurement.

The measured focal spot width is close to the designed focal spot width of 50  $\mu\text{m}$ , but does not fully achieve it yet. One reason for the larger focal spot width is the malfunction of the power supply of the steerer magnets, which prevented optimal focusing of the electron beam into a focal spot with a width of only 50  $\mu\text{m}$ . A second explanation could be the lower acceleration voltage of only 150 kV compared to the designed voltage of 300 kV. Potentially, the accelerator and electron optics are not able to achieve the designed focal spot width away from their optimised parameters.

In contrast to the width, the measured length of the focal spot is significantly smaller than the designed length of 20 mm. While noteworthy, this is not a problem for the generation of MRT irradiation fields, as the penumbras of the individual beamlets are only influenced by the width and not the length of the focal spot, as long as the alignment of the collimator is sufficiently accurate. Two potential effects could influence the length of the focal spot in this case. As only a very low beam current was used for the

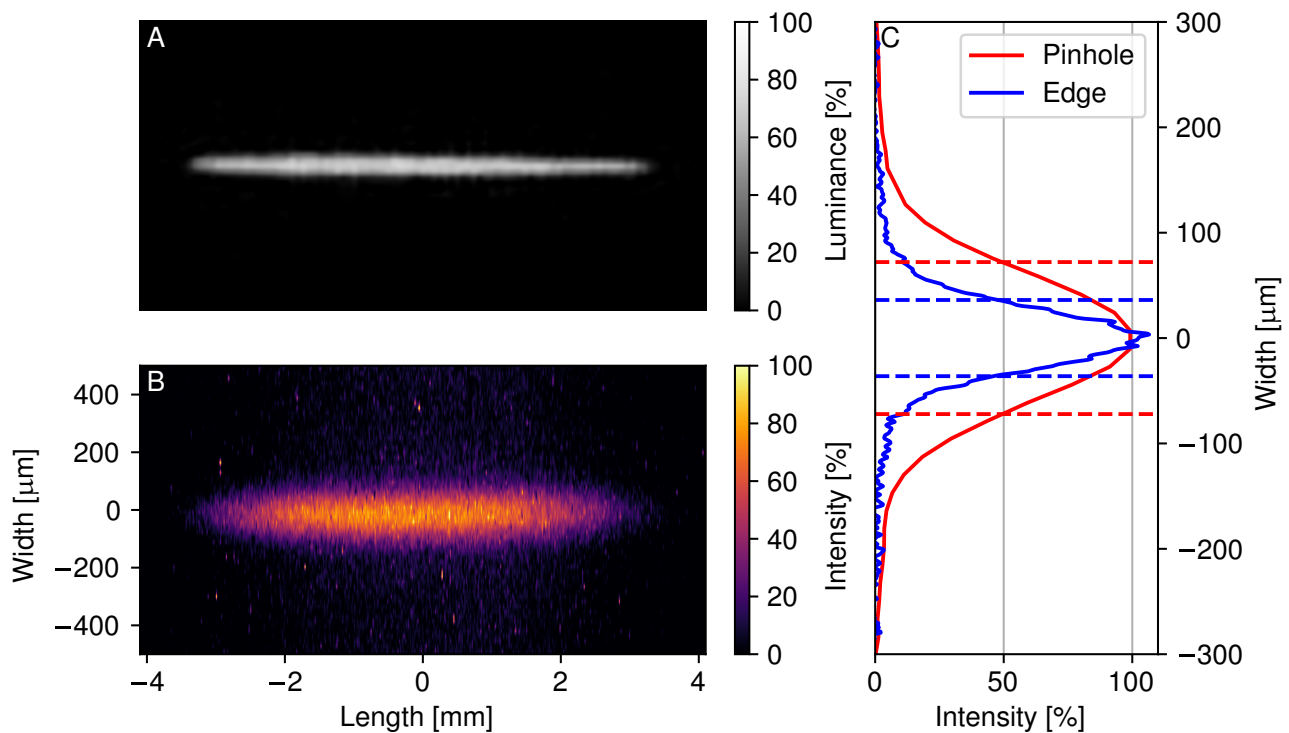


**Figure 14.2** Results of focal spot characterisations conducted during the first beam. In **A**, the normalised luminance of the optical image of the focal spot is shown. The pixels of the optical image have an aspect ratio of 1, but no dimensions are given due to an unknown zoom factor of the used camera. In **B**, the normalised focal spot intensity distribution measured using a 25  $\mu\text{m}$  pinhole is depicted according to the colorbar on the right. The dimensions of the measured distribution are scaled according to the axis labels. In **C**, the vertical LSFs as derived by integrating the PSF measured with the pinhole along the horizontal direction and as directly measured using the edge method are presented. The LSF derived from the pinhole measurement has a FWHM of  $(144.3 \pm 0.8) \mu\text{m}$  and the LSF directly measured with the edge method has a FWHM of  $(72.3 \pm 0.3) \mu\text{m}$  as signified by the horizontal dashed lines.

focal spot characterisation, the voltage of the Pierce electrode was set very close to the cut-off voltage, which would switch the beam fully off. Potentially, only electrons emitted from the central part of the heated cathode could escape the electrical Pierce electrode field, while the periphery parts of the cathode remained inactive. Another potential explanation would be an inhomogeneous temperature distribution in the cathode, leading to only a part of it emitting electrons.

### 14.3.2 Dosimetry of MRT field

After adjusting the magnetic electron beam optics, a microbeam collimator specifically designed for the LFXT prototype as presented in [25] was aligned in front of the primary beam exit. In fig. 14.3, a photograph of the collimator and the resulting MRT irradiation field is presented. The MRT field is characterised, as explained in detail in chapter 3, by sharp lines of high radiation doses called peaks, separated by low dose regions called valleys. The collimator used during the first beam was designed for a peak width of  $50\ \mu\text{m}$  and a centre-to-centre spacing of the peaks of  $400\ \mu\text{m}$ . Some defects are obvious in the MRT field presented in fig. 14.3. The defects are due to problems in the manufacturing process of the microbeam collimator that need to be corrected in future iterations.

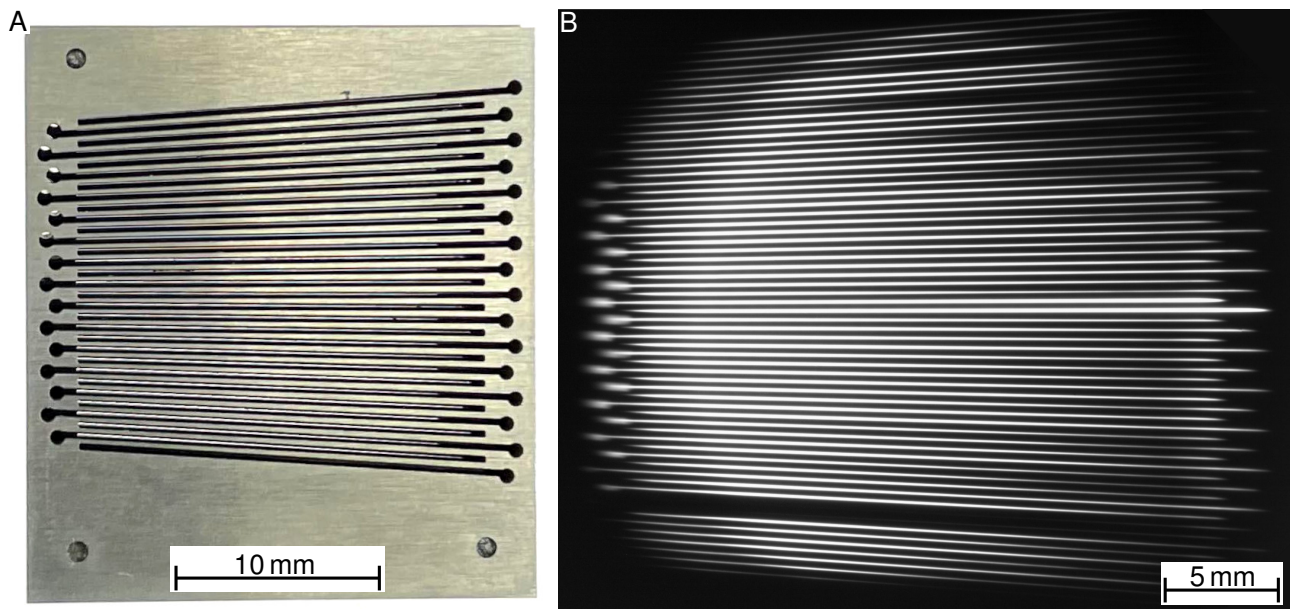


**Figure 14.3** Microbeam collimator with  $50\ \mu\text{m}$  slits and  $400\ \mu\text{m}$  centre-to-centre spacing and resulting MRT irradiation field. In **A**, a photograph of one of the microbeam collimators specifically designed for use with the LFXT prototype is shown. In **B**, the resulting MRT irradiation field measured with a flat-panel X-ray detector is presented. The detector was positioned directly behind the collimator and at a distance of about 20 cm from the focal spot.

To assess the ability of the LFXT prototype to produce MRT fields with sharp beam penumbras throughout a deeper volume, the peak-to-valley dose-ratio (PVDR) was measured at various depths of a PMMA phantom up to about 70 mm. The PVDR is the ratio between the peak and the valley dose and one of the most important parameters characterising the quality of a MRT irradiation field. The measurement was repeated at a conventional X-ray source called XenX manufactured by the company Xstrahl (Xstrahl GmbH, Ratingen, Germany) for comparison. Additionally, a measurement performed at the European Synchrotron Radiation Facility (ESRF) in France adapted from [101] is used as the gold standard. The results of the measurements are presented in fig. 14.4. For all measurements, an irradiation field size of  $2 \times 2\ \text{cm}^2$  at the entrance into the phantom was used.

It can be seen that the PVDR achieved at the ESRF is by far superior across the measured range, with its value staying above 20. This was to be expected due to the significantly higher spatial coherence and the mono-chromatic spectrum of the X-radiation produced by a synchrotron light source. Nonetheless, the PVDR measured at the LFXT prototype stays above 10 up to the maximum measured depth of

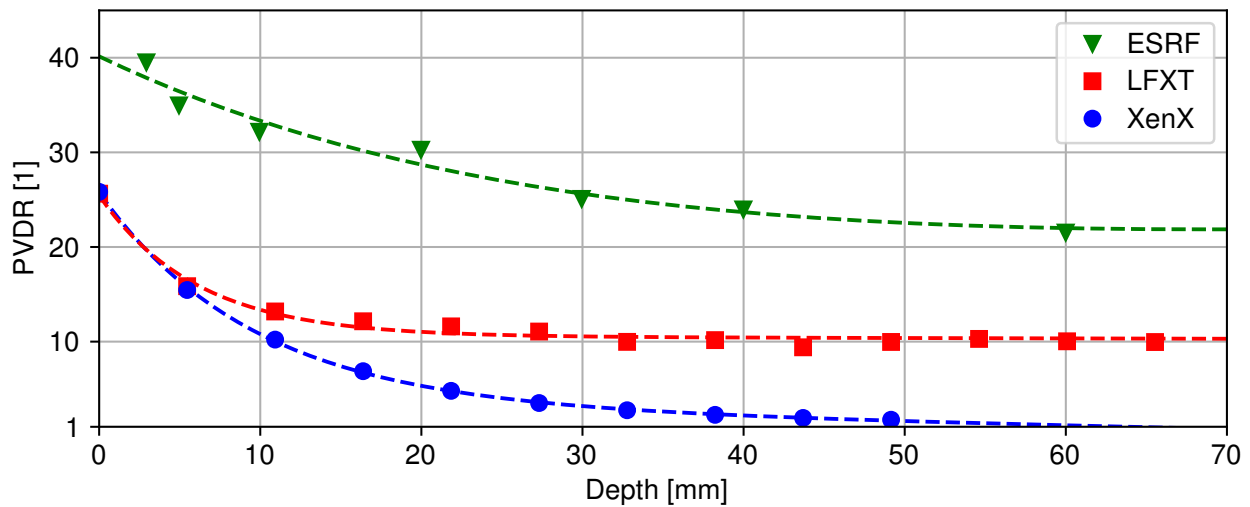


**Figure 14.4** Comparison of PVDRs over depth between the ESRF, the LFXT prototype, and the XenX. The measurement points are depicted, and functions of the form  $y = \exp(a \cdot x + b) + c \cdot x + d$  are fitted to them for better visualisation.

about 65 mm and is therefore only lower than that measured at the ESRF by about a factor of 2. A dose modulation with a PVDR of 10 is still sufficiently fractionated to do MRT irradiations with it. Compared to the XenX, the advantage of the LFXT prototype over a conventional X-ray source becomes obvious. The PVDR achieved with the XenX exhibits a quick decline after entry into the phantom, and within the first few centimetres, spatial fractionation is nearly fully lost, resulting in a more or less homogeneous irradiation field.

### 14.3.3 First preclinical experiments

With the MRT irradiation field produced by the LFXT prototype presented before, human lung carcinoma cells were irradiated *in vitro*. The cells were stained after irradiation to visualise radiation-induced DNA double-strand breaks and imaged using fluorescence microscopy. In fig 14.5, the resulting microscopy image is presented.

The individual cells are clearly visible in fig. 14.5 either in green if they suffered a DNA double-strand break or in blue if they did not. A double-strand break most likely leads to the death of the respective cell, while single-strand breaks are commonly repairable, and the concerned cells can likely survive and proliferate. The impact of the MRT irradiation is obvious in the irradiated cells exhibiting lines of heavily damaged cells in the peak regions separated by valley regions where the cells received less dose. This validates the functionality of the LFXT prototype also in a first preclinical experiment.

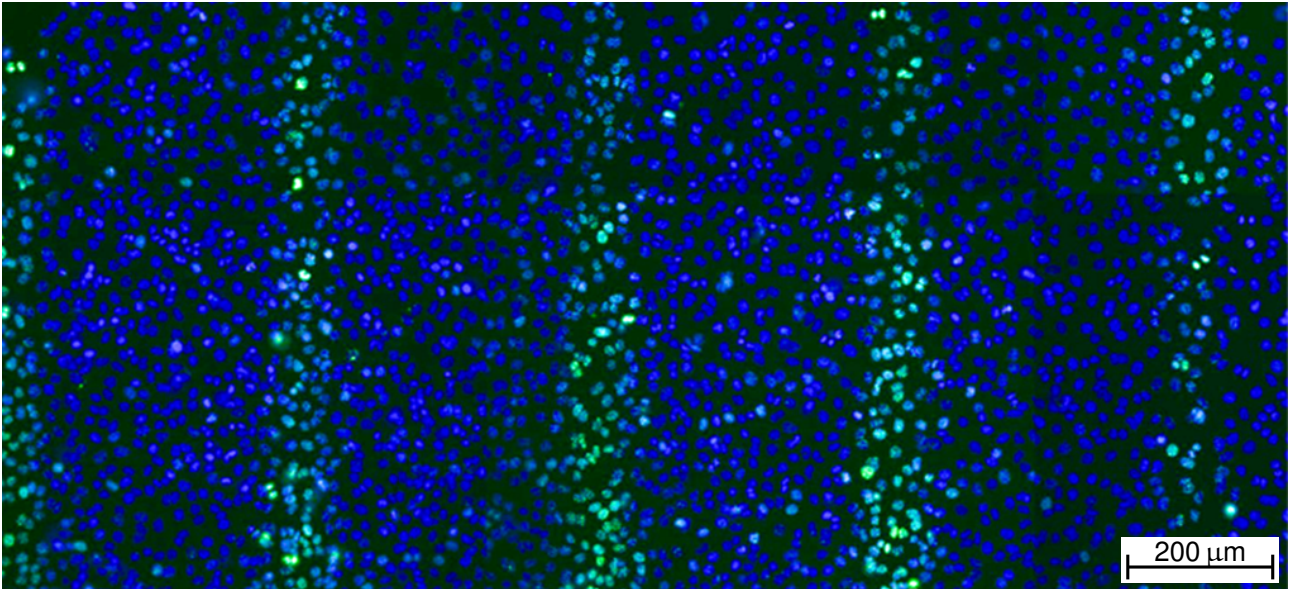


**Figure 14.5** Microscopy image of MRT irradiated cells. The  $\gamma$ H2AX histone produced in the occurrence of DNA double-strand breaks is stained green, and the cells are counter-stained in blue.

## 14.4 Discussion

In this chapter, the first experiments conducted during the first beam at the LFXT prototype were presented. The characterisation of the focal spot produced at 150 kV and with low electron beam current showed a highly asymmetric line-like focal spot with a width of about 72  $\mu\text{m}$  and a length of approximately 6 mm. Even without fully functional electron beam optics, the width of the focal spot is close to the designed width of 50  $\mu\text{m}$ , which makes it likely that the planned focal spot width is reachable once the power supply of the steerer magnets is repaired. The measured focal spot length is substantially below the designed length of 20 mm, which can probably be explained by the used low electron beam current and an insufficiently hot cathode. However, the focal spot length does not substantially influence the resulting MRT irradiation field and is, therefore, only of lower priority.

The MRT irradiation field produced with the characterised focal spot was presented, and the PVDR over depth in a PMMA phantom was measured. Comparison between the depth-dependant PVDR achieved by the LFXT prototype to that achieved using a conventional X-ray source and a synchrotron light source showed that the LFXT prototype in its current state is, as expected, inferior to a synchrotron facility but a significant improvement compared to a conventional X-ray source. The LFXT prototype allows for MRT irradiations of target volumes seated in up to several centimetres depth while fitting into a laboratory room. Future improvements could potentially increase the achievable PVDR and the quality of the MRT irradiation field altogether.

In *in vitro* cell experiments, the biological efficacy of the LFXT prototype was shown. A mono-layer of human cancer cells irradiated with the produced MRT field and stained for DNA double-strand breaks clearly showed the desired influence of the MRT irradiation.

With the first beam, the foundation for future physical and preclinical experiments at the LFXT prototype was laid. Although the LFXT prototype can not yet be operated at its full designed power, it is now operational and further improvements can be made partly simultaneously to more elaborate preclinical experiments.



## **Part IV**

# **Summary and Outlook**



## 15 Summary

In a multitude of preclinical studies, microbeam radiotherapy (MRT) has been shown to be able to widen the therapeutic window of cancer treatment by mitigating normal tissue toxicity and improving tumour control probability. Although the beneficial effects of MRT have been known for a comparably long time, it is still not applied clinically and not even the first clinical trials have been conducted. One of the major reasons for that are the strict requirements posed on the X-ray beam quality and, therefore, the radiation source used. In MRT, treatment is done using an irradiation field characterised by line-like high-dose regions with widths in the range of tens of micrometres called peaks separated with a centre-to-centre distance in the range of hundreds of micrometres by low-dose regions called valleys. The quality of a MRT irradiation field can be characterised by the peak-to-valley dose-ratio (PVDR), which is mainly influenced by three distinctive parameters of the X-ray beam used to generate it through the use of a multi-slit collimator (MSC). A high PVDR, corresponding to steep beam penumbras, is required for the successful application of MRT, especially to non-superficial target volumes. The sharpness of the beam penumbras is influenced directly by the X-ray energy, with higher energies leading to more dose scattering from the peak into the valley regions, and the spatial coherence of the X-ray beam, corresponding to the focal spot size of the X-ray source, geometrically blurring the MRT pattern. The dose rate indirectly influences the PVDR achieved in living target volumes, as the impact of organ motion is amplified by extended irradiation times.

In this work, the support systems for the first prototype of a line-focus X-ray tube (LFXT) were developed, concluding the design and setup of it, the commissioning process of the LFXT prototype was introduced, and the results gathered during the first beam were presented. The LFXT is a novel type of X-ray source mechanically similar to a conventional rotating anode X-ray tube utilising the heat-capacity limit to provide a high dose rate X-ray beam in the orthovoltage regime from a focal spot with a width of only 50  $\mu\text{m}$  for MRT. The LFXT prototype acts as a proof of concept and enables preclinical studies of MRT in a conventional laboratory setting without the need for a synchrotron light source. In chapter 3 of part I of this work, the background to MRT and the LFXT concept is explained in detail.

In part II, the design and setup of the LFXT prototype was presented from a systems engineering point of view, starting with an overview of the systems developed within prior works and their requirements needing to be fulfilled by the systems developed within the scope of this work in chapter 4. In chapter 5, the focal track temperature monitoring system was presented. Monitoring of the temperature of the rotating target in the area directly heated by the electron beam is required for reasons of machine safety and to assess the validity of the heat capacity limit and the efficacy of the LFXT prototype in general. The temperature in the electron focal spot is measured by two infrared (IR) pyrometers with a combined temperature range of 275  $^{\circ}\text{C}$  to 3000  $^{\circ}\text{C}$  and by an IR camera in combination with a complex optical setup providing a high-resolution spatial temperature distribution. A third IR pyrometer with a temperature range of 400  $^{\circ}\text{C}$  to 1500  $^{\circ}\text{C}$  is used to assess the temperature on the focal track opposite the focal spot. The point measurements provided by the IR pyrometers have been tested, although not up to their maximum temperatures, and are working as intended. However, the design of the optical system for the IR camera could not be finalised within this work due to a lack of time and projects with higher priority. The IR camera was tested without the optical system, yielding a visualisation of the spatial temperature distribution in the focal spot with a lower resolution.

In chapter 6, the cooling system designed to remove excess heat produced by the highly inefficient conversion from electron beam power to X-ray beam power and by power losses of the electric motor propelling the target was presented. The LFXT prototype is cooled by six individual cooling cycles, which are all supplied from a common water reservoir and cool individual components. Each cooling cycle contains its own water pump and piping and is optimised for the hydrodynamic and cooling requirements of the respective component. The water reservoir buffers the accumulated heat during the 20 s irradiation

pulses, and a seventh cycle containing an air-water heat exchanger dissipates it over the 20 min cooling periods. The volume of the water reservoir is chosen to be large enough to limit the temperature within it to a maximum of 10°C above room temperature during cyclic operation of the LFXT prototype, which was proven in a numerical simulation. Due to a lack of experience and associated large margins of safety and conservative calculations, the cooling system is more powerful than strictly required. At the time of writing, the cooling system was not yet filled with water and tested due to it being unnecessary at the power levels the LFXT prototype has been operated at.

The high-voltage (HV) system comprising all components concerned with the high acceleration voltage of up to 300 kV and the supply of the electron accelerator of the LFXT prototype was presented in chapter 7. The acceleration voltage is provided by two HV generators producing up to 150 kV each with opposite polarity. The negative part of the acceleration voltage is connected through the so-called cold-deck, where the cathode heating current and the pierce electrode voltage are modulated onto it before it is supplied to the electron source complex. Electrical insulation inside the cold-deck is achieved by nesting a metallic box within another and filling the gap with transformer oil. The positive part of the acceleration voltage is directly connected to the anode of the electron accelerator and, therefore, the vacuum chamber and the X-ray cabinet. The X-ray cabinet has to be insulated from the surrounding area through the air as it needs to be accessible. For that, the X-ray cabinet is built on top of specialised post insulators, the top of it is rounded and covered with Polyvinylchlorid (PVC) sheets, and a Faraday cage is built around it to homogenise the electrical fields. Connected to the X-ray cabinet is a small platform where components that need to be conductively connected to the LFXT prototype but are sensitive to radiation can be placed. A Faraday cage surrounds the platform to protect the contained components from strong electrical fields, and the combination of the X-ray cabinet and the platform is called hot-deck. Electrical energy is supplied to the hot- and cold-deck using two insulation transformers. At the time of writing, the HV system is fully tested and used during the regular operation of the LFXT prototype.

In addition to the systems required for the functionality of the LFXT prototype, the protection of personnel in the vicinity of the machine during operation needs to be ensured. The safety system charged with ensuring personal safety was presented in chapter 8. The outermost line of protection in the safety system is the fence surrounding the danger zone, preventing personnel not only from getting into the vicinity of electrically charged components but also from mechanical hazards due to the rapidly rotating target rotor complex and from X-radiation. An automatic grounding mechanism partly incorporated into the fence ensures that the hot-deck is fully discharged before the door of the fence is unlocked. Inside the danger zone, the X-ray cabinet surrounds the LFXT prototype, acting as a mechanical barrier against potential fragments of a fracturing target while fulfilling its main purpose of shielding the area around it from the high levels of X-radiation present within. The walls of the X-ray cabinet are made from 25 mm thick lead, which was proven in Monte Carlo simulations to reduce the dose a person could be exposed to in the two potential hotspots to  $(0.0552 \pm 0.0013)$  mSv/a and  $(0.0901 \pm 0.0009)$  mSv/a respectively according to the definition of a work-year in German radiation protection jurisdiction. The vacuum chamber of the LFXT prototype is also defined as part of the safety system, as it constitutes the first mechanical barrier against the potential hazards arising from a malfunction concerning the rapidly rotating target rotor complex. All electrical components and processes of the safety system are controlled by a dedicated programmable logic controller (PLC). Up to the time of writing, the safety system has been fully functional without any critical malfunctions and is in regular operation.

To control the interplay between all components and systems constituting the LFXT prototype and to provide an interface for operating personnel, the control system was developed and presented in chapter 9. Overall, the control system is built in a client-server architecture, which is reflected both on the hardware and software side. On the hardware side, two client-sided workstations, a dedicated server, and some auxiliary infrastructure make up the control system. On the software side, a simple client comprising little more than a network interface and a graphical user interface (GUI) and a highly parallelised server program containing most of the logic within its modular and hierarchical architecture exist. Due to a lack of time and other projects of higher priority, the control system is not fully implemented at the time of writing, and instead, a minimal version of it based on the same architecture is used. The hardware of the control

system is fully set up and operational, and the basic principles of the software have been successfully tested and applied.

In part III, the commissioning process of the LFXT prototype from the first start-up to the first beam was presented. In chapter 12, the three main steps of the commissioning process were laid out chronologically, starting with the balancing of the target rotor complex, followed by the bake-out of the vacuum chamber and the HV conditioning of the electron accelerator. During the commissioning process, flaws in the design of the LFXT prototype became obvious and led not only to the commissioning process needing to be executed twice but also significantly limited the achievable results. The balancing of the target rotor complex had to be aborted due to severe problems with the measurements and the adjustment of the state of balance, limiting the target to a rotational frequency below about 30 Hz. The bake-out procedure was limited due to temperature-sensitive components, but nevertheless, vacuum pressures of about  $2 \times 10^{-9}$  mbar and  $1 \times 10^{-8}$  mbar were achieved in the accelerator and target chambers respectively. The HV conditioning procedure using an elaborate automatic protocol worked as intended up to a voltage of about 220 kV, where a vacuum discharge led to the occurrence of a cold emitter, effectively limiting the maximum acceleration voltage. While it would have been possible to attempt a removal of the cold-emitter, the HV conditioning was suspended to not jeopardise the first preclinical experiments with a potentially risky procedure.

In chapter 13, two standard approaches for the radiological characterisation of the focal spot of an X-ray source adapted to the specific requirements of the LFXT prototype were presented. In Monte Carlo simulations, the adapted pinhole method has proven to be able to yield a rough representation of the focal spot within a single image acquisition and without complex post-processing but lacked quantitative validity. The adapted edge method requiring an elaborate reconstruction and post-processing procedure has been proven to be able to yield a quantitative representation of the spatial intensity distribution of the eccentric focal spot of the LFXT prototype with a resolution of about 9  $\mu\text{m}$ .

The culmination point of this work, the results of the first X-ray beam produced by the LFXT prototype, was presented in chapter 14. Results of initial characterisations of the focal spot of the LFXT prototype were presented and despite problems with the magnetic electron optics, measurements showed a width of the focal spot of only  $(72.3 \pm 0.3) \mu\text{m}$ , which is already close to the designed width of 50  $\mu\text{m}$ . Using a MSC, a MRT irradiation field was formed from the primary X-ray beam of the LFXT prototype and the depth-dependant PVDR was assessed. In comparison to a conventional X-ray source, the LFXT prototype proved to be superior, with the PVDR staying above 10 up to the maximum measured depth of about 65 mm. During the first beam, the efficacy of the LFXT prototype for preclinical MRT experiments was also tested by irradiating human cancer cells *in vitro* with promising results.

Overall, the LFXT prototype was brought from the design phase to an operational machine within this work, fulfilling the main aim as stated in chapter 2. However, the LFXT prototype is still in the prototype stage, with inherent flaws and, at the time of writing, unable to meet its originally targeted parameters. The maximum sustainable electron beam power is especially limited due to the limited rotational speed of the target. This also means the LFXT prototype will most probably never be able to experimentally prove the heat capacity limit. Nevertheless, the LFXT prototype is in many aspects superior to a conventional X-ray source and can be used for future preclinical studies of MRT. A multitude of lessons were learned from the problems arising during the setup and commissioning of the LFXT prototype, which will be invaluable for the design of future versions of the LFXT and which, in the end, is the main purpose of any prototype.



## 16 Outlook

Within the scope of this work, the first prototype implementing the LFXT concept was successfully brought to the point where a first X-ray beam could be produced from it, and initial experiments could be conducted. But of course, this is not the final conclusion of the application and development of the LFXT prototype or the general LFXT concept. To further improve our understanding of MRT and simultaneously assess the functionality of the LFXT prototype, preclinical studies both *in vitro* and *in vivo* are planned for the near future. In the first *in vivo* study, brain tumours in mice will be irradiated with MRT and the tumour growth delay and normal tissue toxicity in terms of behavioural changes will be assessed. Aside from the application to preclinical MRT as its main purpose, other potential applications of the LFXT concept should be gauged with the LFXT prototype, like X-ray phase contrast imaging. The thin focal spot of the LFXT prototype, especially if viewed from a shallow angle through the downwards-facing tertiary beam exit, potentially yields a sufficiently high spatial coherence in one dimension for grating-based phase contrast imaging without a source grating. The length of the focal spot, however, renders image acquisition and reconstruction similar to tomographic methods necessary, which would need to be investigated further.

In addition to making use of the LFXT prototype, also its characterisation and improvement will be of interest in the future. Work on the LFXT prototype should not only continue to optimise it for ongoing experiments but also to deepen knowledge and identify areas for improvement in future LFXT iterations. For example, the longevity of the cathode should be assessed, gas processing followed by further HV conditioning could be tested to reach the designed acceleration voltage of 300 kV, and the resilience of the target to different electron beam pulse lengths and powers may be investigated.

While work on and with the LFXT prototype is continued, the development of the next version of the LFXT has already been started, which should facilitate the first clinical studies of MRT, taking a leap towards potential regular clinical application. The first clinical LFXT version is currently being designed for an acceleration voltage between 300 kV and 600 kV at an electron beam power of up to 1.5 MW. The lessons which have already been and will in the future potentially be learned from the LFXT prototype will prove to be invaluable during the design of the clinical LFXT version. The target rotor bearing concept should be rethought most carefully, as it is the most limiting problem which occurred with the LFXT prototype, and the heated cathode could potentially be exchanged for a more conventional and robust tungsten cathode instead of the barium dispenser cathode used in the LFXT prototype. The bipolar concept of HV delivery to the electron accelerator needs to be replaced by a monopolar supply, not only due to the significant reduction in complexity this would bring but also because it would not be feasible for obvious safety reasons in a clinical setting. Additionally, the manufacturing and preparation procedures concerning all components in contact with the vacuum should be improved, for example, by high-temperature burning, to improve the vacuum conditions further.



# List of Abbreviations

<b>CAD</b>	computer aided design
<b>CdTe</b>	Cadmiumtellurid
<b>CT</b>	computed tomography
<b>DNA</b>	deoxyribonucleic acid
<b>EMP</b>	electro-magnetic pulse
<b>ESF</b>	edge-spread-function
<b>ESRF</b>	European Synchrotron Radiation Facility
<b>FEA</b>	finite element analysis
<b>FOV</b>	field-of-view
<b>FWHM</b>	full width at half maximum
<b>GUI</b>	graphical user interface
<b>HLD</b>	high-level driver
<b>HTTP</b>	hypertext transfer protocol
<b>HV</b>	high-voltage
<b>IR</b>	infrared
<b>LAN</b>	local area network
<b>LFXT</b>	line-focus X-ray tube
<b>LSF</b>	line-spread-function
<b>MRT</b>	microbeam radiotherapy
<b>MSC</b>	multi-slit collimator
<b>PLC</b>	programmable logic controller
<b>PMMA</b>	Polymethylmethacrylate
<b>PSF</b>	point-spread-function
<b>PVC</b>	Polyvinylchlorid
<b>PVDR</b>	peak-to-valley dose-ratio
<b>SART</b>	simultaneous algebraic reconstruction technique
<b>SFRT</b>	spatially fractionated radiotherapy
<b>TCP</b>	transmission control protocol
<b>TZM</b>	titanium–zirconium–molybdenum alloy
<b>UDP</b>	user datagram protocol
<b>UHV</b>	ultra-high vacuum



# List of Figures

3.1	Exemplary MRT dose profile . . . . .	9
3.2	Sketch of basic principle of MRT . . . . .	10
3.3	Basic principle of LFXT . . . . .	13
3.4	Simulated maximum temperature increase in focal spot . . . . .	15
4.1	Horizontal section view of LFXT prototype . . . . .	19
4.2	Requirement diagram for experiments with LFXT prototype . . . . .	21
5.1	Photograph of exemplary pyrometer . . . . .	24
5.2	CAD rendering of pyrometer setup . . . . .	25
5.3	CAD rendering of IR camera setup . . . . .	27
6.1	Heat deposition by backscattered electrons . . . . .	32
6.2	Horizontal section view through steady axis cooling cycle . . . . .	34
6.3	Overview of cooling cycles of the vacuum chamber . . . . .	35
6.4	Cooling cycles integrated into the lid of the vacuum chamber . . . . .	36
6.5	Cooling cycle of primary beam exit . . . . .	37
6.6	Cooling channels within motor . . . . .	38
6.7	Cooling cycle of target motor . . . . .	39
6.8	Simulated temperature increase in water tank . . . . .	40
6.9	Overview graph of cooling system . . . . .	41
6.10	Annotated photos of the cooling system . . . . .	42
7.1	CAD rendering of electron accelerator . . . . .	45
7.2	Wiring diagram of high-voltage generation . . . . .	47
7.3	Insulation principle of cold-deck . . . . .	50
7.4	Circuit diagram of cold-deck insulation . . . . .	51
7.5	Insulation principle of hot-deck . . . . .	52
7.6	Components for shielding and discharging of hot-deck . . . . .	53
7.7	Circuit diagram of hot-deck insulation . . . . .	54
7.8	Overview of HV system . . . . .	55
7.9	Annotated photographs of HV system . . . . .	56
8.1	Laboratory layout for radiation safety . . . . .	61
8.2	Simulated dose distribution around LFXT prototype . . . . .	62
8.3	Laboratory layout depicting hazard from target rotation . . . . .	64
8.4	Laboratory layout depicting hazard from high voltage . . . . .	65
8.5	Annotated photographs of safety system . . . . .	67
9.1	Overview graph of software architecture . . . . .	70
9.2	Simplified sequence diagram of command thread in high-level driver . . . . .	71
9.3	Simplified sequence diagram of command execution in server . . . . .	73
9.4	Overview graph of physical network architecture . . . . .	74
10.1	Laboratory overview with main components highlighted . . . . .	79
12.1	Annotated CAD rendering and photograph of target rotor complex . . . . .	89

12.2 Graphs of second HV conditioning . . . . .	93
12.3 Results of emitter verification measurement . . . . .	94
13.1 Measurement sketch of edge method . . . . .	99
13.2 Results of simulated pinhole measurement . . . . .	102
13.3 Results of simulated edge measurement . . . . .	103
14.1 First X-ray image acquired with LFXT prototype . . . . .	107
14.2 Results of focal spot characterisation . . . . .	108
14.3 Microbeam collimator for LFXT prototype . . . . .	109
14.4 Comparison of PVDR over depth . . . . .	110
14.5 Microscopy image of MRT irradiated cells . . . . .	111

## List of Tables

5.1	Properties of pyrometers . . . . .	25
6.1	Parameters of vacuum chamber cooling cycles . . . . .	36



# Own publications

## Journal articles

J. Winter, A. Dimroth, S. Roetzer, Y. Zhang, K. Krämer, C. Petrich, C. Matejcek, K. Aulenbacher, M. Zimmermann, S. E. Combs, M. Galek, G. Natour, M. Butzek, J. J. Wilkens, and S. Bartzsch. "Heat management of a compact x-ray source for microbeam radiotherapy and FLASH treatments". In: *Medical Physics* 49 (2022). DOI: 10.1002/mp.15611

C. Petrich, J. Winter, A. Dimroth, J. J. Wilkens, and S. Bartzsch. "The compact line-focus X-ray tube for microbeam radiation therapy — focal spot characterisation and collimator design". In: *Physica Medica* 129 (2025). DOI: 10.1016/j.ejmp.2024.104861

C. Petrich, J. Winter, A. Dimroth, T. Beiser, M. Dehn, J. Stolz, S. E. Combs, T. E. Schmid, K. Aulenbacher, J. J. Wilkens, S. Bartzsch. "Commissioning, characterization and first high dose rate microbeam and minibeam irradiation at a compact X-ray source". *Currently in progress*

## Conference proceedings

S. Bartzsch, A. Dimroth, J. Winter, C. Petrich, C. Matejcek, Y. Zhang, J. Rieser, S. Roetzer, K. Krämer, M. Zimmermann, M. Galek, M. Butzek, K. Aulenbacher, J. Wilkens, S. E. Combs. "THE LINE FOCUS X-RAY TUBE: AN X-RAY SOURCE FOR FLASH AND SPATIALLY FRACTIONATED RADIATION THERAPY". In: *Physica Medica: European Journal of Medical Physics* 94 (2022). DOI: 10.1016/S1120-1797(22)01595-2

C. Petrich, J. Winter, A. Dimroth, C. Matejcek, S. Roetzer, Y. Zhang, M. Ravichandran, M. Zimmermann, M. Butzek, K. Aulenbacher, J. J. Wilkens, and S. Bartzsch. "PROTOTYPE OF A LINE-FOCUS X-RAY TUBE (LFxT) AS COMPACT SOURCE FOR MICROBEAM AND FLASH RADIOTHERAPY". In: *Physica Medica: European Journal of Medical Physics* 104 (2022). DOI: 10.1016/S1120-1797(22)02257-8

C. Petrich, J. Winter, A. Dimroth, C. Matejcek, M. Ravichandran, M. Zimmermann, K. Aulenbacher, M. Butzek, S. E. Combs, J. J. Wilkens, and S. Bartzsch. "Eine kompakte Hochleistungs-Röntgenquelle für die Mikrostrahltherapie". In: *Jahrestagung der Deutschen Gesellschaft für Medizinische Physik* 56 (2023)

C. Petrich, A. Dimroth, K. M. Kraus, J. Winter, C. Matejcek, M. Butzek, G. Natour, M. Ravichandran, M. Zimmermann, K. Aulenbacher, M. Galek, J. J. Wilkens, S. E. Combs, S. Bartzsch. "Towards Clinical Translation of Microbeam Radiation Therapy (MRT) with a Compact Source". In: *International Journal of Radiation Oncology \* Biology \* Physics* 117 (2023). DOI: 10.1016/j.ijrobp.2023.06.308

## Patents

J. Winter, S. Bartzsch, C. Petrich. "Beam Collimator". *Patent pending*



# Bibliography

- [1] W. C. Röntgen. "Ueber eine neue Art von Strahlen". In: *Annalen der Physik* 300 (1898). DOI: 10.1002/andp.18983000102.
- [2] H. D. Kogelnik. "Inauguration of radiotherapy as a new scientific speciality by Leopold Freund 100 years ago". In: *Radiotherapy and Oncology* 42 (1997). DOI: 10.1016/S0167-8140(96)01887-7.
- [3] S. Gianfaldoni et al. "An Overview on Radiotherapy: From Its History to Its Current Applications in Dermatology". In: *Macedonian Journal of Medical Sciences* 5 (2017). DOI: 10.3889/oamjms.2017.122.
- [4] J. Ferlay et al. *Global Cancer Observatory: Cancer Today*. 2024. URL: <https://gco.iarc.who.int/today>, (visited on 04/29/2024).
- [5] G. P. Delaney and M. B. Barton. "Evidence-based Estimates of the Demand for Radiotherapy". In: *Clinical Oncology* 27 (2015). DOI: 10.1016/j.clon.2014.10.005.
- [6] J. A. Laissue, H. Blattmann, and D. N. Slatkin. "Alban Köhler (1874-1947): Erfinder der Gittertherapie". In: *Zeitschrift für Medizinische Physik* 22 (2012). DOI: 10.1016/j.zemedi.2011.07.002.
- [7] E. Bräuer-Krisch et al. "Effects of pulsed, spatially fractionated, microscopic synchrotron X-ray beams on normal and tumoral brain tissue". In: *Mutation Research/Reviews in Mutation Research* 704 (2010). DOI: 10.1016/j.mrrev.2009.12.003.
- [8] C. Fernandez-Palomo et al. "Animal Models in Microbeam Radiation Therapy: A Scoping Review". In: *Cancers* 12 (2020). DOI: 10.3390/cancers12030527.
- [9] D. N. Slatkin et al. "Subacute neuropathological effects of microplanar beams of x-rays from a synchrotron wiggler." In: *Proceedings of the National Academy of Sciences* 92 (1995). DOI: 10.1073/pnas.92.19.8783.
- [10] J. A. Laissue et al. "Neuropathology of ablation of rat gliosarcomas and contiguous brain tissues using a microplanar beam of synchrotron-wiggler-generated X rays." In: *International journal of cancer* 78 (1998). DOI: 10.1002/(sici)1097-0215(19981123)78:5<654::aid-ijc21>3.0.co;2-l.
- [11] J. A. Laissue et al. "Prospects for microbeam radiation therapy of brain tumours in children to reduce neurological sequelae". In: *Developmental Medicine and Child Neurology* 49 (2007). DOI: 10.1111/j.1469-8749.2007.00577.x.
- [12] R. Serduc et al. "Characterization and quantification of cerebral edema induced by synchrotron x-ray microbeam radiation therapy". In: *Physics in Medicine and Biology* 53 (2008). DOI: 10.1088/0031-9155/53/5/001.
- [13] A. Bouchet et al. "Better Efficacy of Synchrotron Spatially Microfractionated Radiation Therapy Than Uniform Radiation Therapy on Glioma". In: *International Journal of Radiation Oncology \* Biology \* Physics* 95 (2016). DOI: 10.1016/j.ijrobp.2016.03.040.
- [14] L. Eling et al. "Neuro-Oncologic Veterinary Trial for the Clinical Transfer of Microbeam Radiation Therapy: Acute to Subacute Radiotolerance after Brain Tumor Irradiation in Pet Dogs". In: *Cancers* 16 (2024). DOI: 10.3390/cancers16152701.
- [15] M. Ahmed et al. "In Vivo Microbeam Radiation Therapy at a Conventional Small Animal Irradiator". In: *Cancers* 16 (2024). DOI: 10.3390/cancers16030581.

- [16] F. Treibel et al. "Establishment of Microbeam Radiation Therapy at a Small-Animal Irradiator". In: *International Journal of Radiation Oncology \* Biology \* Physics* 109 (2021). DOI: 10.1016/j.ijrobp.2020.09.039.
- [17] M. Hadsell et al. "A first generation compact microbeam radiation therapy system based on carbon nanotube X-ray technology". In: *Applied Physics Letters* 103 (2013). DOI: 10.1063/1.4826587.
- [18] A. C. Dombrowsky et al. "A proof of principle experiment for microbeam radiation therapy at the Munich compact light source". In: *Radiation and Environmental Biophysics* 59 (2020). DOI: 10.1007/s00411-019-00816-y.
- [19] S. Bartzsch and U. Oelfke. "Line focus x-ray tubes—a new concept to produce high brilliance x-rays". In: *Physics in Medicine and Biology* 62 (2017). DOI: 10.1088/1361-6560/aa910b.
- [20] S. Bartzsch et al. "Technical advances in x-ray microbeam radiation therapy". In: *Physics in Medicine and Biology* 65 (2020). DOI: 10.1088/1361-6560/AB5507.
- [21] A. Dimroth. "Auslegung einer Lager- und Antriebseinheit für ein neuartiges Röntgentarget zur Strahlentherapie - Design of a Bearing and Drive Train Unit for a Novel X-Ray Target for Radiotherapy". Dissertation. RWTH Aachen University, 2023. DOI: 10.18154/RWTH-2023-02240.
- [22] J. Winter. "Microbeam radiotherapy on the path to clinical application: A powerful compact x-ray source and microbeam treatment planning". Dissertation. Technical University of Munich, 2023. URL: <https://nbn-resolving.de/urn/resolver.pl?urn:nbn:de:bvb:91-diss-20230419-1687953-1-7>.
- [23] H. Zhang and N. A. Mayr. *Spatially Fractionated, Microbeam and FLASH Radiation Therapy*. IOP Publishing, 2023. ISBN: 978-0-7503-4046-5. DOI: 10.1088/978-0-7503-4046-5.
- [24] E. Bräuer-Krisch et al. "New technology enables high precision multislit collimators for microbeam radiation therapy". In: *Review of Scientific Instruments* 80 (2009). DOI: 10.1063/1.3170035/352070.
- [25] C. Petrich et al. "The compact line-focus X-ray tube for microbeam radiation therapy — focal spot characterisation and collimator design". In: *Physica Medica* 129 (2025). DOI: 10.1016/j.ejmp.2024.104861.
- [26] D. N. Slatkin et al. "Design of a multislit, variable width collimator for microplanar beam radiotherapy". In: *Review of Scientific Instruments* 66 (1995). DOI: 10.1063/1.1145940.
- [27] C. Stengl et al. "Development and characterization of a versatile mini-beam collimator for pre-clinical photon beam irradiation". In: *Medical Physics* 50 (2023). DOI: 10.1002/MP.16432.
- [28] W. Zeman, H. J. Curtis, and C. P. Baker. "Histopathologic Effect of High-Energy-Particle Microbeams on the Visual Cortex of the Mouse Brain". In: *Radiation Research* 15 (1961). DOI: 10.2307/3571293.
- [29] J. C. Crosbie et al. "Tumor Cell Response to Synchrotron Microbeam Radiation Therapy Differs Markedly From Cells in Normal Tissues". In: *International Journal of Radiation Oncology \* Biology \* Physics* 77 (2010). DOI: 10.1016/j.ijrobp.2010.01.035.
- [30] C. B. Seymour and C. Mothersill. "Radiation-induced bystander effects — implications for cancer". In: *Nature Reviews Cancer* 4 (2004). DOI: 10.1038/nrc1277.
- [31] M. V. Sokolov and R. D. Neumann. "Radiation-Induced Bystander Effects in Cultured Human Stem Cells". In: *PLoS ONE* 5 (2010). DOI: 10.1371/journal.pone.0014195.
- [32] V. Trappetti et al. "Microbeam Radiotherapy-A Novel Therapeutic Approach to Overcome Radioreistance and Enhance Anti-Tumour Response in Melanoma." In: *International journal of molecular sciences* 22 (2021). DOI: 10.3390/ijms22147755.
- [33] A. Bouchet et al. "Identification of AREG and PLK1 pathway modulation as a potential key of the response of intracranial 9L tumor to microbeam radiation therapy". In: *International Journal of Cancer* 136 (2015). DOI: 10.1002/IJC.29318.

- [34] M. J. Ibahim et al. “Eosinophil-Associated Gene Pathways but not Eosinophil Numbers are Differentially Regulated between Synchrotron Microbeam Radiation Treatment and Synchrotron Broad-Beam Treatment by 48 Hours Postirradiation”. In: *Radiation Research* 185 (2015). DOI: 10.1667/RR14115.1.
- [35] C. Fernandez-Palomo et al. “Complete Remission of Mouse Melanoma after Temporally Fractionated Microbeam Radiotherapy”. In: *Cancers* 12 (2020). DOI: 10.3390/cancers12092656.
- [36] E. Dagueuet et al. “Radiation-induced bystander and abscopal effects: important lessons from preclinical models”. In: *British Journal of Cancer* 123 (2020). DOI: 10.1038/s41416-020-0942-3.
- [37] R. Serduc et al. “In vivo two-photon microscopy study of short-term effects of microbeam irradiation on normal mouse brain microvasculature”. In: *International Journal of Radiation Oncology \* Biology \* Physics* 64 (2006). DOI: 10.1016/j.ijrobp.2005.11.047.
- [38] A. Bouchet et al. “Effects of microbeam radiation therapy on normal and tumoral blood vessels”. In: *Physica Medica* 31 (2015). DOI: 10.1016/j.ejmp.2015.04.014.
- [39] A. Bouchet et al. “Synchrotron microbeam radiation therapy induces hypoxia in intracerebral gliosarcoma but not in the normal brain”. In: *Radiotherapy and Oncology* 108 (2013). DOI: 10.1016/j.radonc.2013.05.013.
- [40] S. Sabatasso et al. “Transient and Efficient Vascular Permeability Window for Adjuvant Drug Delivery Triggered by Microbeam Radiation”. In: *Cancers* 13 (2021). DOI: 10.3390/cancers13092103.
- [41] R. Behling and F. Grüner. “Diagnostic X-ray sources—present and future”. In: *Nuclear Instruments and Methods in Physics Research Section A: Accelerators, Spectrometers, Detectors and Associated Equipment* 878 (2018). DOI: 10.1016/j.nima.2017.05.034.
- [42] J. Winter et al. “Heat management of a compact x-ray source for microbeam radiotherapy and FLASH treatments”. In: *Medical Physics* 49 (2022). DOI: 10.1002/MP.15611.
- [43] W. J. Oosterkamp. “The heat dissipation in the anode of an X-ray tube”. In: *Philips Research Reports* 3 (1948).
- [44] C. Matejcek et al. “A novel electron source for a compact x-ray tube for microbeam radiotherapy with very high dose rates”. In: *Physica Medica* 106 (2023). DOI: 10.1016/j.ejmp.2023.102532.
- [45] W. Schlegel, C. P. Karger, and O. Jäkel. *Medizinische Physik*. 1st ed. Springer Spektrum Berlin Heidelberg, 2018. ISBN: 978-3-662-54800-4. DOI: 10.1007/978-3-662-54801-1.
- [46] A. Holmes-Siedle and L. Adams. *Handbook of Radiation Effects*. Oxford University Press Oxford, 2002. ISBN: 9780198507338. DOI: 10.1093/oso/9780198507338.001.0001.
- [47] D. Ketui, F. Chi, and G. Shan. “Single wavelength and ratio pyrometry reflection errors in temperature measurement of gas turbine blade”. In: *Measurement* 86 (2016). DOI: 10.1016/j.measurement.2016.02.054.
- [48] Micro-Epsilon Messtechnik GmbH & Co KG. *Basics of non contact temperature measurement*. 2021.
- [49] M. Vollmer and K. Möllmann. *Infrared Thermal Imaging: Fundamentals of Infrared Thermal Imaging*. 2nd ed. Wiley, 2017. ISBN: 9783527693306. DOI: 10.1002/9783527693306.ch1.
- [50] M. Planck. *The Theory of Heat Radiation*. P. Blakiston’s Son & Co., 1914.
- [51] F. P. Incropera et al. *Fundamentals of Heat and Mass Transfer*. 6th ed. John Wiley & Sons, 2006. ISBN: 978-0-471-45728-2.
- [52] Advanced Energy Industries Inc. *Understanding Two-Color (Ratio) Pyrometer Accuracy*. 2020. URL: <https://www.advancedenergy.com/getmedia/05a3d488-d3c0-4f71-87e5-4e23ba44e06b/en-op-understanding-two-color-accuracy-technical-note.pdf> (visited on 06/11/2024).

- [53] Fluke Process Instruments. *Emissivity - Metals*. URL: <https://www.flukeprocessinstruments.com/en-us/service-and-support/knowledge-center/infrared-technology/emissivity-metals> (visited on 05/30/2024).
- [54] Fluke Process Instruments. *What is Thermal Imaging? Thermal Cameras and How They Work*. URL: <https://www.fluke.com/en-us/learn/blog/thermal-imaging/how-infrared-cameras-work> (visited on 06/06/2024).
- [55] F. R. S. Lord Rayleigh. "Investigations in optics, with special reference to the spectroscope". In: *The London, Edinburgh, and Dublin Philosophical Magazine and Journal of Science* 8 (1879). DOI: 10.1080/14786447908639684.
- [56] W. Demtröder. *Experimentalphysik 2*. 6th ed. Springer Berlin Heidelberg, 2013. ISBN: 978-3-642-29943-8. DOI: 10.1007/978-3-642-29944-5.
- [57] N. A. Baily. "Electron backscattering". In: *Medical Physics* 7 (1980). DOI: 10.1118/1.594750.
- [58] J. I. Goldstein et al. *Scanning Electron Microscopy and X-Ray Microanalysis: Backscattered Electrons*. 4th ed. Springer New York, 2018. ISBN: 978-1-4939-6676-9. DOI: 10.1007/978-1-4939-6676-9\_2.
- [59] Diamond Materials GmbH. *CVD Diamond for Synchrotron Beamlines*. URL: [https://www.diamond-materials.com/site/assets/files/1096/cvd\\_diamond\\_synchrotron\\_windows.pdf](https://www.diamond-materials.com/site/assets/files/1096/cvd_diamond_synchrotron_windows.pdf) (visited on 06/13/2024).
- [60] EMOD Motoren GmbH. *Data sheet for threephase induction-motor*. 2020.
- [61] W. Demtröder. *Experimentalphysik 1*. 9th ed. Springer Berlin Heidelberg, 2021. ISBN: 978-3-662-62727-3. DOI: 10.1007/978-3-662-62728-0.
- [62] E. H. Lieb and J. Yngvason. "The physics and mathematics of the second law of thermodynamics". In: *Physics Reports* 310 (1999). DOI: 10.1016/S0370-1573(98)00082-9.
- [63] L. Boltzmann. "Ableitung des Stefan'schen Gesetzes, betreffend die Abhängigkeit der Wärmestrahlung von der Temperatur aus der electromagnetischen Lichttheorie". In: *Annalen der Physik* 258 (1884). DOI: 10.1002/andp.18842580616.
- [64] P. Stephan. *VDI-Wärmeatlas: B1 Die Energieform Wärme und verschiedene Arten der Wärmeübertragung*. 12th ed. Springer Vieweg Berlin Heidelberg, 2019. ISBN: 978-3-662-52989-8. DOI: 10.1007/978-3-662-52989-8\_3.
- [65] P. Stephan. *VDI-Wärmeatlas: B2 Grundlagen der Berechnungsmethoden für Wärmeleitung, konvektiven Wärmeübergang und Wärmestrahlung*. 12th ed. Springer Vieweg Berlin Heidelberg, 2019. ISBN: 978-3-662-52989-8. DOI: 10.1007/978-3-662-52989-8\_4.
- [66] H. Nirschl. *VDI-Wärmeatlas: L1.2 Druckverlust in durchströmten Rohren*. 12th ed. Springer Vieweg Berlin Heidelberg, 2019. ISBN: 978-3-662-52989-8. DOI: 10.1007/978-3-662-52989-8\_75.
- [67] S. Rötzer. *Unpublished report on cooling calculations*. 2021.
- [68] KSB SE & Co. KGaA. *Datasheet KSB Movitec*. 2021.
- [69] Schwämmle GmbH & Co. KG. *Datasheet Heatexchanger S1N to S3N*.
- [70] Schwämmle GmbH & Co. KG. *Datasheet Heatexchanger ELW*.
- [71] S. Dushman. "Thermionic Emission". In: *Reviews of Modern Physics* 2 (1930). DOI: 10.1103/RevModPhys.2.381.
- [72] Technix. *Operator Manual - SR150KV45KW*. 2021.
- [73] FuG Elektronik GmbH. *Datasheet Highvoltage power supply HCP*.
- [74] C. Matejcek. *Unpublished report on electron accelerator of linefocus X-ray tube*. 2019.
- [75] Heat Wave Labs Inc. *Internal communication with Heat Wave Labs Inc*.

- [76] W. M. Haynes, D. R. Lide, and T. J. Bruno. *CRC Handbook of Chemistry and Physics*. 97th ed. CRC Press, 2016. ISBN: 9781498754293.
- [77] Essex X-Ray & Medical Equipment Ltd. *Datasheet - HV cables*. 2020.
- [78] H. Vogt and J. Vahlbruch. *Grundzüge des praktischen Strahlenschutzes*. 7th ed. Carl Hanser Verlag München, 2019. ISBN: 978-3-446-44919-0.
- [79] H. Veith. *Strahlenschutzgesetz mit Verordnungen*. 12th ed. Reguvis, 2022. ISBN: 978-3-8462-1337-7.
- [80] J. Perl et al. "TOPAS: an innovative proton Monte Carlo platform for research and clinical applications." In: *Medical physics* 39 (2012). DOI: 10.1118/1.4758060.
- [81] B. Faddegon et al. "The TOPAS tool for particle simulation, a Monte Carlo simulation tool for physics, biology and clinical research." In: *Physica medica* 72 (2020). DOI: 10.1016/j.ejmp.2020.03.019.
- [82] T. Schoonjans et al. "The xraylib library for X-ray-matter interactions. Recent developments". In: *Spectrochimica Acta Part B: Atomic Spectroscopy* 66 (2011). DOI: 10.1016/j.sab.2011.09.011.
- [83] M. S. Darlow. "Balancing of high-speed machinery: Theory, methods and experimental results". In: *Mechanical Systems and Signal Processing* 1 (1987). DOI: 10.1016/0888-3270(87)90087-2.
- [84] E. J. Gunter and C. Jackson. *Handbook of Rotor Dynamics: Balancing of rigid and flexible rotors*. 1st ed. McGraw-Hill, 1992. ISBN: 9780070193307.
- [85] K. Jousten. "Dependence of the outgassing rate of a "vacuum fired" 316LN stainless steel chamber on bake-out temperature". In: *Vacuum* 49 (1998). DOI: 10.1016/S0042-207X(98)00002-5.
- [86] R. Calder and G. Lewin. "Reduction of stainless-steel outgassing in ultra-high vacuum". In: *British Journal of Applied Physics* 18 (1967). DOI: 10.1088/0508-3443/18/10/313.
- [87] F. Paschen. "Ueber die zum Funkenübergang in Luft, Wasserstoff und Kohlensäure bei verschiedenen Drucken erforderliche Potentialdifferenz". In: *Annalen der Physik* 273 (1889). DOI: 10.1002/andp.18892730505.
- [88] A. Korsbäck et al. "Vacuum electrical breakdown conditioning study in a parallel plate electrode pulsed dc system". In: *Physical Review Accelerators and Beams* 23 (2020). DOI: 10.1103/PhysRevAccelBeams.23.033102.
- [89] R. V. Latham. "High voltage vacuum insulation: new horizons". In: *Conference on Electrical Insulation and Dielectric Phenomena*. IEEE, 1988. DOI: 10.1109/CEIDP.1988.26305.
- [90] R. V. Latham. *High Voltage Vacuum Insulation: Basic Concepts and Technological Practice*. Academic Press Inc., 1995. ISBN: 0-12-437175-2.
- [91] M. BastaniNejad et al. "Improving the performance of stainless-steel DC high voltage photoelectron gun cathode electrodes via gas conditioning with helium or krypton". In: *Nuclear Instruments and Methods in Physics Research Section A: Accelerators, Spectrometers, Detectors and Associated Equipment* 762 (2014). DOI: 10.1016/j.nima.2014.05.114.
- [92] DIN German Institute for Standardization. *DIN EN 12543-2: Non-destructive testing - Characteristics of focal spots in industrial X-ray systems for use in non-destructive testing - Part 2: Pinhole camera radiographic method*. 2021.
- [93] DIN German Institute for Standardization. *DIN EN 12543-4: Non-destructive testing - Characteristics of focal spots in industrial X-ray systems for use in non-destructive testing - Part 4: Edge method*. 1999.
- [94] W. H. Richardson. "Bayesian-Based Iterative Method of Image Restoration". In: *Journal of the Optical Society of America* 62 (1972). DOI: 10.1364/JOSA.62.000055.

- [95] L. B. Lucy. "An iterative technique for the rectification of observed distributions". In: *The Astronomical Journal* 79 (1974). DOI: 10.1086/111605.
- [96] T. Buzug. *Computed Tomography*. 1st ed. Springer Berlin Heidelberg, 2008. ISBN: 978-3-540-39407-5. DOI: 10.1007/978-3-540-39408-2.
- [97] C. P. Sung, K. P. Min, and G. K. Moon. "Super-resolution image reconstruction: a technical overview". In: *IEEE Signal Processing Magazine* 20 (2003). DOI: 10.1109/MSP.2003.1203207.
- [98] A. Andersen. "Simultaneous Algebraic Reconstruction Technique (SART): A superior implementation of the ART algorithm". In: *Ultrasonic Imaging* 6 (1984). DOI: 10.1016/0161-7346(84)90008-7.
- [99] P. B. Crilly. "A quantitative evaluation of various iterative deconvolution algorithms". In: *IEEE Transactions on Instrumentation and Measurement* 40 (1991). DOI: 10.1109/19.87019.
- [100] N. Yamamoto et al. "Light emission from surfaces, thin films and particles induced by high-energy electron beam". In: *Surface and Interface Analysis* 31 (2001). DOI: 10.1002/sia.958.
- [101] S. Bartzsch et al. "Micrometer-resolved film dosimetry using a microscope in microbeam radiation therapy". In: *Medical Physics* 42 (2015). DOI: 10.1118/1.4922001.
- [102] O. Zlobinskaya et al. "Induction and repair of DNA double-strand breaks assessed by gamma-H2AX foci after irradiation with pulsed or continuous proton beams". In: *Radiation and Environmental Biophysics* 51 (2012). DOI: 10.1007/s00411-011-0398-1.